Large Scale Anisotropy Studies of Ultra High Energy Cosmic Rays Using Data Taken with the Surface Detector of the Pierre Auger Observatory

Der Fakultät für Mathematik, Informatik und Naturwissenschaften der RWTH Aachen University vorgelegte Dissertation zur Erlangung des akademischen Grades eines Doktors der Naturwissenschaften

von

Diplom-Physiker

Marius Grigat

aus Waldbröl

Berichter: Prof. Dr. Thomas Hebbeker
Prof. Dr. Martin Erdmann

Tag der mündlichen Prüfung: 10.06.2011

”Fast is fine, but accuracy is everything.”
Wyatt Earp

for Julia, Paula and Till

Abstract

The distribution of arrival directions of cosmic rays is remarkably uniform over the complete spectrum of energies. At large angular scales only tiny deviations from isotropy have been observed and huge statistics are required to quantify the corresponding amplitudes. The measurement of cosmic rays with energies above 10^{15} eV is only feasible with large, earthbound observatories: The cosmic ray primary particles initiate cascades of secondary particles in the Earth's atmosphere. Every aspect of the development of these air showers down to the measurement of the resulting particles at ground level needs to be well understood and controlled in order to precisely reconstruct the properties of the primary particle. The development of air showers is subject to systematic distortions caused by the magnetic field of the Earth. Both this and other local effects are capable of inducing false anisotropy into the distribution of arrival directions. In this thesis, the effect of the geomagnetic field on the energy measurement is modelled and quantified; consequently, a correction of the energy estimator is derived. Furthermore, a method is introduced to fit dipolar patterns to the distribution of arrival directions of cosmic rays as observed from the field of view of the surface detector of the Pierre Auger Observatory. After correcting for all relevant local effects the method is applied to data and the parameters of a potentially underlying dipole are determined and evaluated.

Zusammenfassung

Die Verteilung der Ankunftsrichtungen kosmischer Teilchen ist auffallend gleichförmig im gesamten Energiebereich. Bei großen Winkelskalen wurden nur kleine Abweichungen von Isotropie beobachtet und eine Vielzahl von Einzelmessungen ist erforderlich um die entsprechenden Amplituden zu quantifizieren. Die Messung kosmischer Teilchen mit Energien oberhalb von 10^{15} eV ist nur möglich mit großen, erdgebundenen Observatorien: Kosmische Primärteilchen lösen Kaskaden von Sekundärteilchen in der Erdatmosphäre aus. Jeder Aspekt der Entwicklung dieser Luftschauer bis zur Messung der resultierenden Teilchen auf Bodenhöhe bedarf guten Verständnisses, um die Eigenschaften des Primärteilchens präzise rekonstruieren zu können. Die Entwicklung von Luftschauern unterliegt systematischen Verzerrungen durch das Magnetfeld der Erde. Dieser und andere lokale Effekte sind imstande unechte Anisotropie in der Verteilung der Ankunftsrichtungen hervorzurufen. In dieser Arbeit wird der Effekt des Erdmagnetfeldes auf die Energiemessung modelliert und quantifiziert; eine entsprechende Korrektur des Energieschätzers wird abgeleitet. Des weiteren wird eine Methode eingeführt zur Anpassung eines Dipols an die Verteilung der Ankunftsrichtungen kosmischer Teilchen aus Sicht des Oberflächendetektors des Pierre Auger Observatoriums. Nach der Korrektur sämtlicher relevanter lokaler Effekte wird diese Methode auf Daten angewendet und die Parameter eines möglicherweise zugrundeliegenden Dipols werden ermittelt und bewertet.

Contents

Chapter 1

Introduction

Cosmic rays have been discovered almost one century ago by Victor Hess in 1912. They are known to induce particle cascades commonly referred to as air showers which can be measured by ground based detectors. The largest earthbound cosmic ray experiment is the Pierre Auger Observatory. It started taking data in January 2004 and construction was completed in 2007. The surface detector has accumulated more than two and a half million records of extensive air showers in the EeV regime.

Due to the steeply falling particle flux, only a few percent of these showers exceed the energy threshold of $E > 10^{18.5}$ eV above which the detection of air showers with the surface detector is fully efficient. They are of particular interest when it comes to anisotropy studies for two main reasons: Firstly, the exposure of the fully efficient detector can be calculated from purely geometric considerations. Secondly, the larger the energy of the cosmic ray primary particle the smaller its deflection by galactic and extra-galactic magnetic fields it is exposed to on its way from source to Earth. This may allow for performing astronomy with cosmic rays of highest energies knowing that the angular resolution of the detector is of the order of few degrees.

Large scale anisotropy studies aim at quantifying potential anisotropy in the distribution of arrival directions at rather large angular scales. The largest angular scale is given by the definition of the dipole on the sphere. These large scale studies are especially attractive in the absence of exact knowledge of the actual strengths of turbulent magnetic fields cosmic rays propagate through. These fields may disperse the measured arrival directions to large patterns on the sky although the corresponding cosmic rays might originate in the same source. Furthermore, some models of the ordered galactic magnetic field predict a dipolar anisotropy from the point of view of an earthbound detector due to a magnetic lensing effect. Consequently, the cosmic rays may arrive isotropically at our galaxy and still cause detectable anisotropy on Earth. The same applies in the presence of the Compton-Getting effect which predicts a dipolar anisotropy derived from the fact that an earthbound detector travels through the reference frame in which cosmic rays are isotropic.

The irregularly growing detector in the deployment phase until mid-2007 as well as its uptimes and downtimes introduce a modulation of the size of the detector over time which must be carefully accounted for when performing anisotropy studies. Besides, the measurement of cosmic rays with the Pierre Auger Observatory occurs indirectly by means of the particles produced in the air shower cascades that they have initiated. This makes the observables sensitive to external conditions in terms of local effects such as atmospheric variations and the geomagnetic field. If not accounted for adequately, the unsteady size of

the detector as well as these external conditions will be capable of mimicking anisotropy in the distribution of arrival directions of cosmic rays.

In chapter 2, the history and theory of ultra high energy cosmic rays and air showers as well as the current status and results of extensive air shower experiments is introduced. An overview of the Pierre Auger Observatory is given in chapter 3, the basic properties of the detectors and the respective reconstruction methods of air showers are discussed. The angular resolution of the surface detector is analysed in chapter 4. In chapter 5, the impact of external conditions on large scale anisotropy studies is quantified and the respective corrections are described. Methods to study dipolar patterns in the distribution of arrival directions as recorded with the surface detector of the Pierre Auger Observatory are presented in chapter 6 and tested on sky maps generated by means of Monte Carlo simulations in chapter 7. These methods are applied to real data taken with the surface detector of the Pierre Auger Observatory in chapter 8 after having applied the necessary corrections to get rid of local effects.

Chapter 2

Ultra High Energy Cosmic Rays and Extensive Air Showers

2.1 Cosmic Rays

Highly energetic particles coming from outer space are permanently hitting and penetrating the Earth's atmosphere. The charged part of these is commonly referred to as cosmic radiation which mainly consists of ionized nuclei (98 %), thereof 87 % protons, 12 % α-particles and 1 % heavier nuclei; electrons yield the remaining 2 %. Neutrinos and photons finally make up the neutral part of the incoming particles [Lon92]. These values rely on direct measurements of the huge particle fluxes at energies below $\sim 10^{15}$ eV which yield far more than 99 % of the integrated flux of cosmic rays.

History

In 1785, Charles-Augustin de Coulomb unsuspectingly observed the ionizing effect of cosmic radiation when he found that a simple electroscope loses its charge though being well insulated. After the discovery of radioactivity in 1896 by Henri Becquerel it was believed that ionization by naturally radioactive material could explain the charge leakage.

A series of experiments followed investigating this phenomenon and its dependence on altitude above ground, i.e. distance to the potential, earthbound sources. Measurements on the Eiffel tower [Wul09] showed a significant drop of the ionization rate. In order to increase the distance to ground Victor Hess performed balloon flights in 1912 reaching altitudes of 5300 m. He found out that the ionizing radiation indeed diminished up to 1500 m. However, then it started to increase again finally reaching even larger rates at 3600 m compared to ground level [Hes12]. This led to the idea of an extraterrestrial origin of the radiation. Further experiments could establish this idea and even show that the radiation was of extrasolar origin.

In 1925 Robert Millikan discovered that this cosmic radiation was capable of causing changes of the atmospheric composition; the interactions of cosmic rays and particles of the Earth's atmosphere, i.e. usually nitrogen or oxygen nuclei, produce secondary particles which themselves may interact with atmospheric constituents. The particles produced during this process are referred to as secondary cosmic rays. A few years after Millikan's explorations of cosmic rays and secondary particles the first individual particles could be identified

Table 2.1: Typical particle fluxes at various orders of magnitude in lower limit of energy. These values have been estimated from the results of the Pierre Auger Collaboration [Abr10a] and the famous spectrum by Swordy *et al.* [Swo01].

energy	10^{11} eV	3×10^{13} eV	3×10^{15} eV	3×10^{18} eV	10^{20} eV
flux	$1/(\mathrm{m}^2\ \mathrm{s})$	$1/(\mathrm{m}^2\ \mathrm{d})$	$1/(\mathrm{m}^2\ \mathrm{y})$	$5/(\mathrm{km}^2\ \mathrm{y})$	$5/(1000\ \mathrm{km}^2\ \mathrm{y})$

by means of photographic plates and cloud chambers, e.g. the pion, the muon, the kaon and the positron.

In the late 1930s, while the Nobel prize was given to Victor Hess in 1936, Pierre Auger observed time coincidences of particle detections in horizontally separated detectors on ground level [Aug38]. Relying on Millikan's investigations his conclusion was to assume a common origin of these coincidently measured particles. Cosmic ray primaries initiate cascades of secondary particles originating from the point of interaction with an atmospheric constituent. These cascades are commonly referred to as air showers. Additionally, the measurement of coincidences caused by secondary particles in spatially separated detectors provided a first means to estimate the energy of cosmic rays.

While Pierre Auger was capable of measuring energies to an upper limit of 10^{15} eV, the energy range of cosmic particles as being measured in several air shower experiments during the previous decades continuously grew up to 10^{20} eV. The highest energetic cosmic ray event reported so far was recorded in 1991 by the HiRes experiment at an energy of 3.2×10^{20} eV. However, cosmic rays become less frequent with increasing energy; in fact, their flux has been shown to follow a steeply falling power law. Some values of the flux of cosmic rays are given in table 2.1 for typical energies. For comparison, the energy reachable by state-of-the-art man made particle accelerators amounts to $\sim 10^{13}$ eV in the centre of mass system corresponding to $\sim 10^{17}$ eV in the cosmic ray case. And maybe even more tangible, the energy of a tennis ball played at a speed of 100 km/h has a kinetic energy of 1.4×10^{20} eV.

The altitude of first interaction of a primary cosmic particle with atmospheric constituents typically amounts to $\mathscr{O}(10)$ km. Therefore, only satellite and balloon experiments are applicable to measure cosmic rays directly. For obvious reasons, this limits the detection area, so that only primaries below 10^{15} eV arrive with fluxes large enough to be measured directly with reasonably high statistics. Alternatively, ground experiments are suitable to detect secondary particles that yield information about their "immediate" origin, i.e. the cosmic ray primary. On ground level, huge detection areas allow to access energies up to $\sim 10^{21}$ eV with sufficient statistics. Therefore, it is necessary to investigate and understand the properties of Extensive Air Showers (EAS).

2.2 Extensive Air Showers

When a cosmic ray particle hits the Earth's atmosphere, it undergoes a nuclear reaction with an atmospheric constituent. In case of a hadronic primary particle, its strong interaction partner is a nucleus of a nitrogen or oxygen atom, according to the composition of the atmosphere. This first interaction forms a multitude of secondary particles which themselves may interact with atmospheric constituents, thus initiating a cascade (see figure 2.1, left).

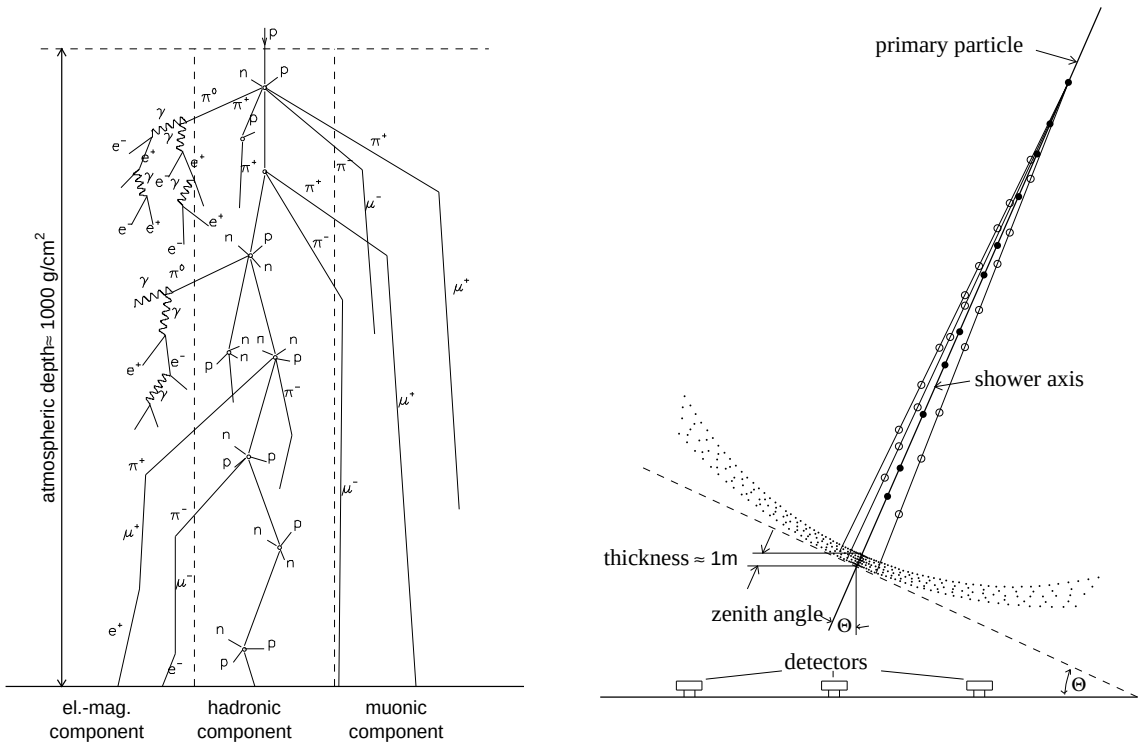

Figure 2.1: Schematic view of an extensive air shower [Alk75]: The left plot shows typical particle interactions and decays leading to the development of the three dominant components of an air shower. The right plot schematically indicates the geometric properties of an air shower; the dimensions are not to scale, the first interaction typically occurs at an altitude of ~ 10 km and while the longitudinal thickness of the shower disc is of the order of 1 m, the lateral spread of the shower amounts to several kilometres.

The particles in such an air shower form a disc with a thickness of a few meters and a lateral diameter of up to some kilometres (see figure 2.1, right), depending on energy and type of the primary particle. Furthermore, the thickness of this disc is small at the shower centre, $\mathcal{O}(1)$ m, while increasing to its edge, ~ 100 m. The shower disc propagates through the atmosphere with the speed of light, virtually; since the secondary particles have the same spatial direct or indirect origin, i.e. the point of first interaction, the shower front is slightly curved. However, it can be considered as plane in good approximation.

The number of secondary particles produced rises with the total energy of the primary. A proton at an energy of 10^{15} eV for example produces $\sim 10^6$ secondary particles [Gru00]. Air shower simulations show that protons of $E = 10^{19}$ eV produce even more than $\sim 10^9$ secondary particles. The instantaneous number of particles varies while the air shower propagates in the atmosphere. It firstly rises as described by a cascade like process of particle production. As soon as the particle energies drop below the production limit of new secondaries, the number of particles falls exponentially with atmospheric depth.

Cosmic rays at high energies generate extensive air showers, whose secondary particles are capable of reaching the Earth's surface. The integral composition of secondary particles, as being produced during the development of an air shower, is given by table 2.2. These particles are not only created by hadronic, but also by electromagnetic interactions. The dominant decay modes of mesons responsible for the generation of the muonic and electromagnetic component of air showers are given in table 2.3. The basic properties of these

Table 2.2: Integral composition of secondary particles: Relative amount of particles produced in air showers in the atmosphere.

particle type	photons	electrons	muons	hadrons
percentage	80 %	18 %	1.7 %	0.3 %

Table 2.3: The table shows decay modes of charged mesons produced in the development of an air shower. The most relevant processes responsible for the production of the main components of the shower are indicated.

Production of electromagnetic component

$$K^{\pm} \rightarrow \pi^{\pm} + \pi^0 , \quad \pi^0 \rightarrow \gamma + \gamma$$

Production of muonic component

$$\pi^- \rightarrow \mu^- + \bar{\nu}_\mu , \quad \pi^+ \rightarrow \mu^+ + \nu_\mu$$
$$K^- \rightarrow \mu^- + \bar{\nu}_\mu , \quad K^+ \rightarrow \mu^+ + \nu_\mu$$

components will be described in the following subsections. The aspects of air shower simulations including the display of tracks of secondary particles is given in appendix B.

2.2.1 Electromagnetic Component

The decay of neutral pions, themselves generated e.g. from Kaon decay or other hadronic interaction processes, initiates an electromagnetic (EM) cascade; the photons produced generate electron-positron pairs (pair production) that in turn create new γs via bremsstrahlung, thus forming a cascade. Of course, this type of cascade can also be initiated by an electromagnetic primary particle. Other EM interactions like photo-electric effect, Compton effect (photons) and ionization (electrons) can be neglected with respect to the high energies necessary for the cascade development [Rao98]. Based on these interactions, Walter Heitler introduced a model for the characterisation of an electromagnetic shower [Hei36]. This model will be reviewed briefly in the following.

The short radiation length of electrons and photons in air, $\lambda_r \approx 36.7$ g/cm^2, results in a rapid absorption of EM particles; therefore, the EM component is commonly referred to as the soft component of an air shower. The development of the EM cascade can be modelled in steps of splittings. Splittings are the interaction processes available in the EM component, see figure 2.2(a). They occur every

$$d = \lambda_r \ln 2 = 25.4 \text{ g/cm}^2 \tag{2.1}$$

with d the average distance after which a photon splits into an $e^+ e^-$ pair or the distance over which an electron loses half of its energy by radiation. In fact, d is the distance after which an electron loses on average half its energy due to radiation; equivalently, according to the definition of the radiation length, a photon has travelled approximately half of its mean free path for pair production. After n splitting lengths, a distance of $x = nd$ has been travelled and the total number of particles, also known as the shower size, is $N = 2^n = e^{x/\lambda_r}$. In air the critical energy below which radiative energy loss falls below the loss due to ionizations is

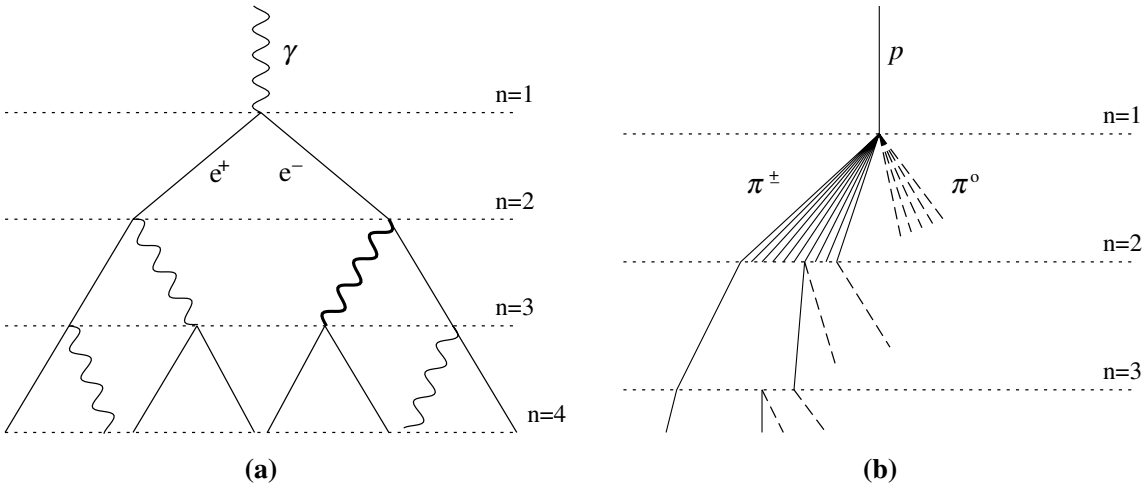

Figure 2.2: Cascade steps of an extensive air shower [Hei36]: (a) shows typical alternation of bremsstrahlung and pair production of the electromagnetic cascade. (b) indicates a hadronic cascade eventually feeding the muonic component from $\pi^{\pm}$-decays next to the contribution to the electromagnetic part of the shower via the generation of neutral pions. The drawings are not to scale.

$E^{\gamma}_{crit} = 85$ MeV. In case the cascade initiator was a photon of energy E_0, the shower reaches its maximum number of coexisting secondary particles N_{max} when all particles have reached the critical energy, so that

$$E_0 = E^{\gamma}_{crit} \cdot N_{max} \; . \tag{2.2}$$

The corresponding depth of penetration of the shower at its maximum is reached after n_{crit} splitting lengths. Using equation 2.2, the relation $N_{max} = 2^{n_{crit}} \Leftrightarrow n_{crit} = \ln[N_{max}]/\ln 2$ leads to $n_{crit} = \ln[E_0/E^{\gamma}_{crit}]/\ln 2$. Finally, with $x = nd$ and equation 2.1, purely electromagnetic cascades reach their maximum at

$$X^{\gamma}_{max} = n_{crit} d = \lambda_r \ln[E_0/E^{\gamma}_{crit}] \; . \tag{2.3}$$

The elongation rate Λ^{γ} is defined as the "rate" at which X^{γ}_{max} increases with primary energy E_0,

$$\Lambda^{\gamma} = \frac{dX^{\gamma}_{max}}{d\log_{10} E_0} = 2.3\lambda_r = 85 \text{g/cm}^2 \; . \tag{2.4}$$

The Heitler model of EM cascades has proven to produce reasonable predictions when it comes to order of magnitude estimates. More precisely, it reproduces two important features of EM shower development which have been confirmed by both detailed simulations and experiments: The maximum size of the shower N_{max} is proportional to the primary energy E_0 and the depth of maximum grows logarithmically with E_0 at a rate of 85 g/cm^2 per decade of primary energy. However, testing the model predictions against simulations also shows that it is inadequate to some extent: As already pointed out by its author, the model underestimates the ratio of photons to electrons; it does not take into account multiple photon generation via bremsstrahlung and in turn neglects the quick absorption of electrons. In order to correct for this inadequateness, the actual number of electrons N_e can be estimated to be a tenth of the total number of EM particles, e.g. the charged fraction of the shower size at the maximum becomes $N_e = N_{max}/10$ [Mat05].

The lateral spread of the electromagnetic component of an air shower reaches values of up to several kilometres depending on energy. This lateral development is due to multiple Coulomb scattering; the corresponding lateral density function (LDF) models the lateral distribution of EM particles; this is commonly done by the Nishimura-Kamata-Greisen (NKG) approach [Gre56, Kam58, Gre60],

$$\triangle(N_e, r) = \frac{N_e}{2\pi r_0^2} C_e(s) \left(\frac{r}{r_0}\right)^{(s-1)} \left(1+\frac{r}{r_0}\right)^{(s-4.5)}, \tag{2.5}$$

where N_e is the number of charged particles in the EM shower and $\triangle(N_e, r)$ is the area density of particles (per m^2) at distance r from the shower axis in a plane perpendicular to this axis; C_e is constant for a fixed shower age, parametrised by s and r_0 is the Molière radius, i.e. a measure of the transverse dimension of the EM shower. Approximately, the Molière radius relates to the radiation length like $r_0 \approx 0.0265\lambda_r(Z+1.2)$ with Z the atomic number of the material penetrated. This expression is meaningful for a fixed atmospheric depth, i.e. fixed air density, and λ_r given in m. According to Greisen referring to the exponential nature of the atmosphere in pressure, r_0 should be taken at two radiation lengths $2\lambda_r$ above observation level, e.g. at sea level this is 81 m. The shower age is $s = 0$ at the point of shower initiation, $s = 1$ at the shower maximum and $s = 2$ at the point where the shower dies out. The validity of the NKG function has been tested with simulations extensively and ranges from $0.8 < s < 1.6$, [Gai90].

2.2.2 Hadronic Component

When a hadron (most likely a proton) enters the atmosphere, it collides with atmospheric constituents being subject to strong interaction. In case the primary is a proton this first collision will take place in an altitude of 15 to 20 km because of the proton interaction length of $\lambda_I^p = 90$ g/cm^2 [Gru05]. Thus a hadronic cascade is initiated producing secondary particles, mostly pions. Kaon production on the other hand is less likely with a relative probability of 10 % compared to pions. The interaction length of pions amounts to $\lambda_I^\pi = 120$ g/cm^2. Charged pions are supposed to be subject to further hadronic interaction, whereas neutral pions decay most likely $\pi^0 \rightarrow 2\gamma$ as the life time of the latter is much shorter than the interaction length: Since they decay electromagnetically, their life time is a factor of $\sim 10^{-9}$ times shorter compared to the weakly decaying charged pions. In principle, a hadronic cascade can also be initiated by an electromagnetic primary or by the EM component originally produced by a π^0; though not very likely, the probability of this to happen increases with the primary's energy.

The Heitler model of electromagnetic showers has been adapted to produce a depiction of the cascade induced by a hadronic primary [Mat05]. In the following this model will be reviewed briefly. There is need to account for not only hadronic interactions of charged pions but also EM processes initiated by neutral pions, see figure 2.2 (b). The model of the purely hadron driven cascade can be designed similar to the EM case. The analogous of the radiation length for EM particles is the (strong) interaction length λ_I. In every interaction step, roughly $N_{ch} = 10$ charged pions are produced. Since there are three pions, with two of them charged, two third of the total energy E_0 can be assumed to be transferred to charged

pions. After n interactions, $N_\pi = (N_{ch})^n$ charged pions exist and their average energy is

$$E_\pi = \frac{E_0}{\left(\frac{3}{2}N_{ch}\right)^n} \,. \tag{2.6}$$

The critical energy of charged pions is the energy at which they have equal probability to interact or decay. It can be estimated applying equation 2.6 and amounts to $E^\pi_{crit} \approx 20$ GeV. The number of interactions necessary to make the energy of charged pions drop to the critical value E^π_{crit} can now be calculated,

$$n_{crit} = \frac{\ln[E_0/E_{crit}]}{\ln\left[\frac{3}{2}N_{ch}\right]} = 0.85\log_{10}[E_0/E_{crit}] \,, \tag{2.7}$$

leading to $n_{crit} = 3,\ 4,\ 5,\ 6$ for $E_0 = 10^{14},\ 10^{15},\ 10^{16},\ 10^{17}$ eV, respectively. The full set of five parameters for the Heitler model of hadronic showers then is:

$$\lambda_r = 37 \text{ g/cm}^2 \,,\ E^\gamma_{crit} = 85 \text{ MeV} \,,\ N_{ch} = 10 \,,\ \lambda_I = 120 \text{ g/cm}^2 \,,\ E^\pi_{crit} = 20 \text{ GeV} \,. \tag{2.8}$$

With these parameters and using $N_\mu = N_\pi$, the total energy E_0 is given by the number of hadronic and electromagnetic particles and their respective critical energy,

$$E_0 = 10N_eE^\gamma_{crit} + N_\mu E^\pi_{crit} \approx 0.85 \text{ GeV } (N_e + 24N_\mu) \,. \tag{2.9}$$

The electron and muon numbers N_e and N_μ can be computed from the total and critical energies. N_μ is obtained from equation 2.7 as $\ln N_\mu = n_{crit}\ln N_{ch} = 0.85\ln[E_0/E^\mu_{crit}]$ and N_e is estimated under the observation of energy conservation, $E_{em} = E_0 - N_\mu E^\mu_{crit}$, so that

$$N_\mu = \left(\frac{E_0}{E^\mu_{crit}}\right)^{0.85} \,, \quad N_e = \frac{1}{10}\frac{E_{em}}{E^\gamma_{crit}} \,. \tag{2.10}$$

For the estimation of the atmospheric depth of the shower maximum of a hadronic shower initiated by a proton, the EM cascades must be considered for every step of π^0 creation. The first interaction occurs at an atmospheric depth $X_0 = \lambda_I \ln 2$ and yields N_{ch} photons produced from the decay of the $N_{ch}/2$ neutral pions available. The EM shower initiated in turn by each of these photons carries an energy of $E_0/(3N_{ch})$. Similar to equation 2.3 the depth of maximum is obtained as

$$X^p_{max} = \ln 2\lambda_I + \lambda_r \ln[E_0/(3N_{ch}E^\gamma_{crit})] = X^\gamma_{max} + \ln 2\lambda_I - \lambda_r \ln[3N_{ch}] \,. \tag{2.11}$$

Finally, the elongation rate for proton induced showers is

$$\Lambda^p = \Lambda^\gamma + \frac{d}{d\log_{10}E_0}\{\ln 2\lambda_I - \lambda_r \ln[3N_{ch}]\} \approx 58 \text{ g/cm}^2 \,. \tag{2.12}$$

The transverse momenta of highly energetic hadrons on average is rather low compared to their total momenta; thus, they are concentrated within a radius of ~ 10 m around the shower axis. When the energy of a hadron drops below the pion production threshold, it loses energy through ionization until it decays or is stopped.

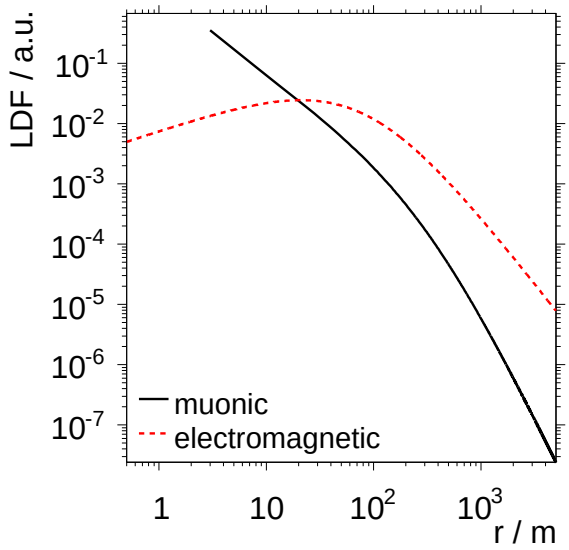

Figure 2.3: Comparison of lateral profiles of muonic and electromagnetic LDF: The functions are taken from equations 2.5 and 2.13, for the qualitative comparison they have been scaled to match with the same y-axis range.

2.2.3 Muonic Component

80 % of the charged particles reaching sea-level are muons. They are produced by the decay of charged mesons; the production modes via the decays of pions and kaons as given in table 2.3 are dominant. Muons live 100 times longer than pions in their respective rest frames; moreover, their range is extended by relativistic time dilatation enabling most of them to reach the Earth's surface. Muons gain less lateral momentum on their way through the atmosphere than multi-scattering electrons. Similarly to equation 2.5, Greisen has introduced a parametrisation of the lateral distribution of muons [Gre60]:

$$\triangle(N_\mu, r) \propto \frac{N_\mu}{2\pi r_0^2} \left(\frac{r}{r_0}\right)^{-1.25} \left(1+\frac{r}{r_0}\right)^{-2.5} , \tag{2.13}$$

where N_μ is the number of muons in the shower, $\triangle(N_\mu, r)$ is the area density of muons at distance r from the shower axis in the shower plane; r_0 is again a measure of the transverse dimension of the muonic component. According to Greisen, r_0 has to be obtained experimentally and a value of $r_0 = 320$ m is adequate for the observation at sea level. A qualitative comparison of the LDFs for the muonic and electromagnetic component of the shower, see equations 2.13 and 2.5, is given in figure 2.3; it shows the expected behaviour of a smaller spreading of the muons compared to the EM component. Muons are concentrated around the shower axis, while EM particles tend to spread more strongly.

Neutrinos in air showers are mainly generated by both pion and muon decay. On the one hand, they play an inferior role in the measurement of secondary particles in EASs as they interact only weakly and the corresponding cross section is small. On the other hand, these atmospheric neutrinos make up a huge background for experiments aiming at the detection of primary neutrino particles such as IceCube [Hul11] and KM3Net [HR09]. With IceTop [Sta09] the former even makes use of an air shower detector to veto atmospheric neutrinos originating in extensive air showers.

2.3 Flux of Cosmic Rays

The flux of cosmic rays is described as the particle flux I depending on the energy E. The differential expression commonly used as an approximation for several orders of magnitude is the following power law:

$$\frac{dI}{dE} \propto E^{-\xi}, \tag{2.14}$$

where ξ is called the spectral index. Accordingly, the flux is often referred to as the energy spectrum of cosmic rays, especially when emphasis is laid on the energy. At first sight, the energy spectrum looks almost featureless. This property can be interpreted as the result of a mechanism of stochastical acceleration of charged particles as proposed by Fermi [Fer49]. The acceleration mechanism could for example apply to what happens during supernova explosions: Material of several solar masses is ejected with velocities beyond the speed of sound into the interstellar medium. Strong shock waves created this way propagate radially and could accelerate a particle every time it passes the shock front.

The flux of cosmic rays is described by a broken power law with few but apparent changes of the spectral index, see figure 2.4. For energies starting from 10^{11} eV ξ equals 2.7. A convex bent in the spectrum around $\sim 3 \times 10^{15}$ eV, commonly referred to as the *knee*, corresponds to an increasing spectral index: ξ changes to 3.3. At $\sim 3 \times 10^{18}$ eV it falls to a value of 2.6 corresponding to a concave bent of the spectrum curve, the *ankle*. For energies beyond several 1×10^{19} eV, the spectrum experiences the feature of the *toe*, another convex bent changing the spectral index to $\xi = 4.3$. In general, possible interpretations of the features in the spectrum cover changes of the acceleration mechanisms at the sources, an effect of cosmic ray propagation and energy dependent changes in the hadronic interaction cross-sections (see [Blu09] and references therein).

There are three concurrent scenarios attempting to explain the *knee*. Firstly, it may be a feature generated by the limitations of thinkable acceleration processes. More precisely, the energy of the cosmic ray is proportional to the charge of the particle; the maximum energy the cosmic ray can be accelerated to is determined by the size of the accelerator which must be larger than the gyroradius of the particle. Therefore, the *knee* could be explained by limitations of the spatial extent of accelerating regions. Then, the energy of the *knee* would be proportional to the cosmic ray particle charge Z. Another possible explanation of the *knee* is a change in the regime of diffusion in the galactic magnetic field [Can02]. Appropriately parametrised, these changes can impact the energy dependence of the escape probability of cosmic rays from the galaxy. Thirdly, the *knee* is possibly not a genuine feature of the cosmic ray flux itself but rather of its observation on Earth. This could be caused by a change of the hadronic interactions at highest energies, e.g. new types of heavy particles might be created which in turn escape undetected [Erl02]. In this scenario the energy of the *knee* would scale with the particle mass number A.
There is another feature in the cosmic ray energy spectrum at $\sim 3 \times 10^{17}$ eV, the *second knee*. Common interpretations relate it to composition-specific properties of cosmic rays in the context of the transition of their origins from galactic to extragalactic.

The most commonly believed explanation for the *ankle* in the energy spectrum would be the transition from a dominantly galactic to an extragalactic component [DM05, Hil06]. The *ankle* is the energy at which both components contribute in equal measure to the particle flux. Different elaborations of this scenario exist concerning the extragalactic composition and

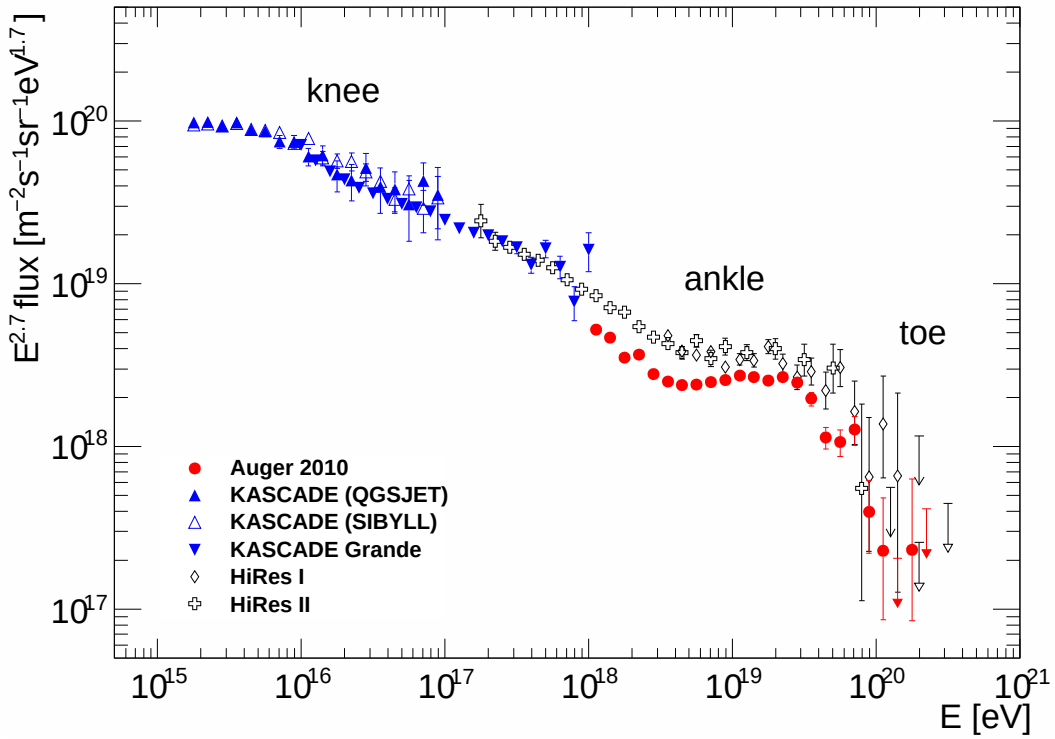

Figure 2.4: The flux of UHECRs as obtained from measurements by the Pierre Auger Observatory (PAO) [Abr10a], HiRes [Abb08b], KASCADE [Ant05] and KASCADE Grande [Hau09]. The flux has been scaled by a power of 2.7 of the energy to emphasize deviations of the gradient from a pure power law. Three features can be identified in the plot: In analogy to the anatomy of a human leg, they are commonly referred to as *knee*, *ankle* and *toe* within the astrophysics community. The plot was provided by Stefan Fliescher, Dr Christine Meurer and Tobias Winchen.

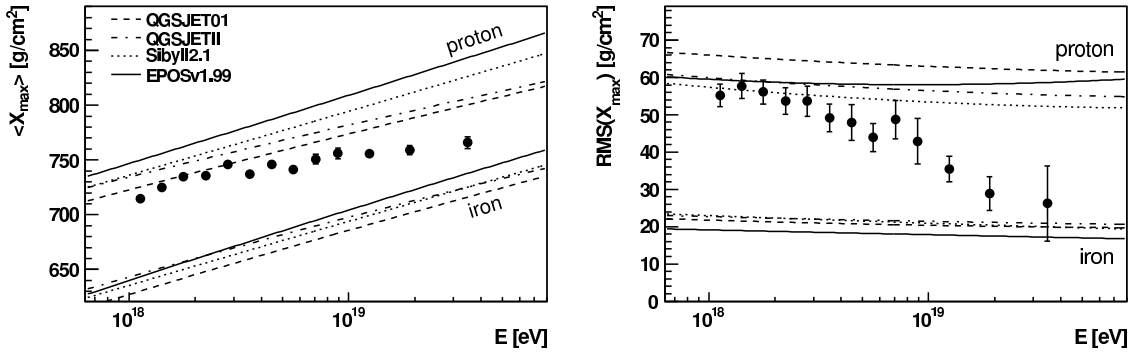

Figure 2.5: The composition of cosmic rays is measured indirectly making use of the observable of the shower maximum X_{max}. Measurements by the Pierre Auger Observatory imply a change in the composition from rather light particles to moderately heavy nuclei or a mixed composition. Plot taken from [Rou11].

relatedly the actual energy at which the transition occurs. For example, extragalactic protons dominantly contributing to the flux already at lower energies produce e^+e^--pairs with CMB photons [Ber06a]; consequently, these protons lose energy and their flux is suppressed at higher energies while being enlarged at lower energies. This explanation would make the ankle a pure propagation effect, it is called the dip model.

Above energies of 6×10^{19} eV, proton primary particles are supposed to lose energy via the production of pions when interacting with photons of the cosmic microwave background (CMB), $N + \gamma_{CMB} \rightarrow \Delta \rightarrow N' + \pi$. This prediction is commonly referred to as the Greisen, Zatsepin and Kuzmin (GZK) cut-off [Gre66, Zat66] and was made shortly after the detection of the CMB in the 1960s [Pen65]. Essentially, this prediction is supported by the clear kink in the flux of cosmic rays at several 10 EeV, the *toe*; it has been measured consistently by both the Pierre Auger Observatory and the HiRes experiment. In fact it was shown that the spectral index changes at ~ 30 EeV from -2.6 to -4.3 with a significance of $\sim 5\sigma$ [Abr08b, Abr10a]. However, other explanations of the *toe* exist such as a drop of the acceleration power at the sources and its true origin remains uncertain.

2.4 Composition

Below 10^{14} eV the elemental abundance in the flux of cosmic rays can be measured directly using detectors above the atmosphere. This is not applicable to higher energies due to the steep decrease of the flux with growing energy. Ground based experiments can make a statement about the mass of the cosmic ray primary particle by measuring the secondary particles and estimating the altitude of first interaction. Heavy nuclei are supposed to interact higher in the atmosphere than light particles. Often, the point of first interaction is not accessible with the detector, or more precisely out of the field of view of the detector. However, with a detector capable of measuring the longitudinal development of the particle cascade it is possible to determine the shower maximum X_{max}, the depth at which the number of secondary particles is largest. It is connected to the depth of first interaction and thus, to the primary particle mass.

Both the mean and the RMS of the shower maximum distribution in a specific energy bin contain information on the composition of the cosmic rays populating this bin. The

measurements can be compared to the expectations derived from simulations of air showers which make use of different hadronic interaction models at highest energies. As shown in figure 2.5, these different model predictions produce rough agreement for the extreme cases of the lightest charged hadron, the proton, and the heaviest nucleus thinkable as a cosmic ray primary particle. The results obtained with fluorescence detector measurements by the Pierre Auger Observatory imply a change in the composition from rather light particles at energies of 10^{18} eV to moderately heavy nuclei or a mixed composition beyond 10^{19} eV [Rou11]. In the overlapping energy range of the measurements, these results agree with HiRes data published in [AZ00].

Also uncharged cosmic particles such as photons and neutrinos are capable of initiating extensive air showers. Photons are investigated with respect to their contribution to the total cosmic ray flux since their abundance provides information on the composition of dark matter. For example, several models predict dark matter to be made up of Weakly Interacting Massive Particles (WIMPs) [Pri88]; if WIMPs were majorana particles [Maj37], the annihilation of a pair of these would possibly generate photons. Depending on the respective dark matter model, predictions of the photon abundance at highest energies can be derived and tested by corresponding experiments. Furthermore, the photon abundance is sensitive to the type of process of cosmic ray particle acceleration: Top down models predict cosmic rays at highest energies to be generated by decay processes from topological defects and relics of the early universe. This is opposed to the bottom up models which claim that charged particles of the interstellar matter are accelerated to highest energies e.g. by shock waves. Top down models predict a larger photon fraction since photons are likely to be produced in the decays of cosmological relics where the energy of the photons is generated instantaneously. It is unlikely that photons are accelerated in bottom up scenarios. Some of these models have been excluded recently by measurements of in particular cosmic ray experiments such as the Pierre Auger Observatory, see figure 2.6(a). Another potential source of highest energy photons and also neutrinos is the GZK process described earlier: The pions produced by the interaction of cosmic rays with the CMB photons decay into two gammas or muons and neutrinos (see table 2.3) which in turn would lead to a mensurable fraction of these in the cosmic ray flux.

Measurements at energies around 10^{18} eV and above have been able to set limits on the flux of neutrinos and photons, see figures 2.6. These limits already exclude the super heavy dark matter and hot dark matter models with the latter providing the necessary basis for top-down models of cosmogenesis, figure 2.6(a), [Ber05]. In case the cosmic rays at highest energies are protons, both limits obtained by the Pierre Auger Observatory [Abr09b, Abr09d] are supposed to become sensitive to the GZK photon and neutrino prediction within the next years of data taking.

2.5 Anisotropy of Arrival Directions of Cosmic Rays

The distribution of arrival directions of cosmic ray primaries is remarkably uniform. Especially for the huge statistics of particles with energies below 10^{14} eV no significant deviation from isotropy was observed. Observations related to the spatial distribution of arrival directions of cosmic rays can have implications on their sources in terms of spatial distribution and models of acceleration and theories of the propagation and magnetic deflection of these

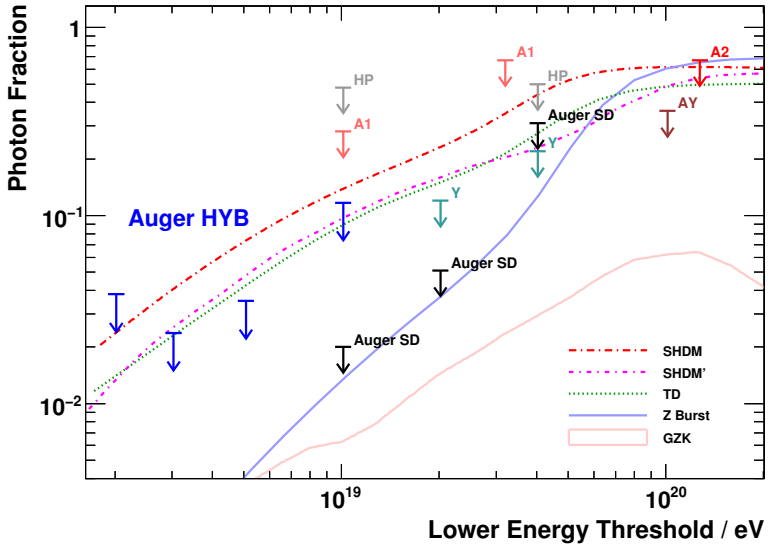

(a)

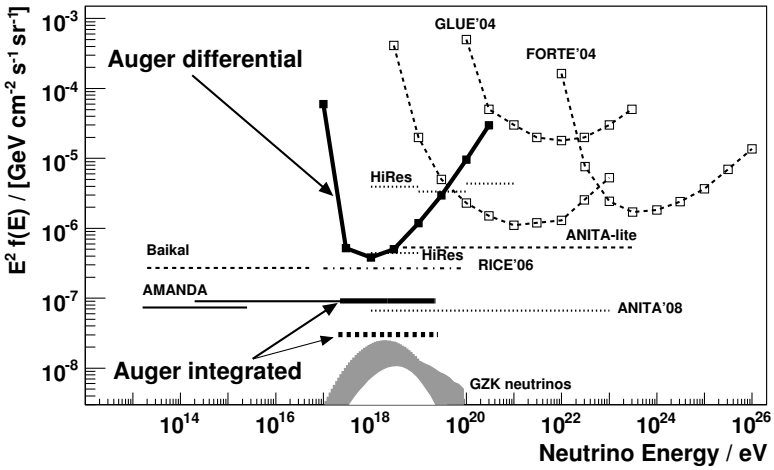

(b)

Figure 2.6: Upper plot: Limits (95 % confidence) on the photon abundance in UHECRs by the Pierre Auger Collaboration exclude super heavy dark matter (SHDM) and top down (TD) models (adapted from [Abr09d]). Both plots: Both photon and neutrino limits are close to becoming sensitive to the predictions derived from GZK interaction with CMB photons (lower plot taken from [Abr09b]).

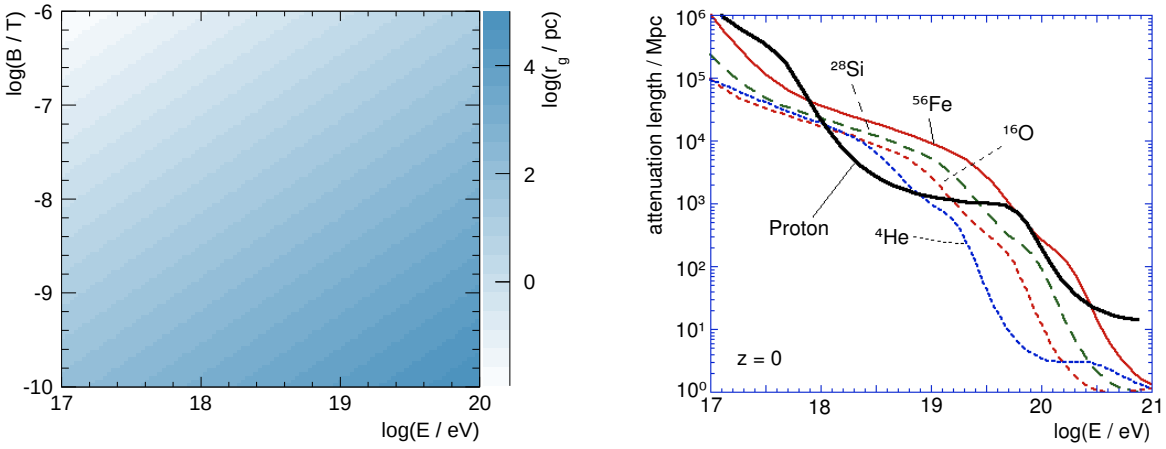

(a) (b)

Figure 2.7: Aspects of the propagation of cosmic rays. (a) Gyroradius r_g as a function of magnetic field strength B and cosmic ray energy E, see equation 2.15. (b) Attenuation length versus energy of the cosmic ray primary for various particle types at redshift $z = 0$ [All06], see text for details.

particles. Anisotropies at small angular scales may pinpoint the directions of point sources while large scale anisotropies are supposed to yield information on propagation and deflection aspects the cosmic rays are subject to.

2.5.1 Propagation and Magnetic Deflection

As cosmic rays are charged particles, they are deflected by galactic and extragalactic magnetic fields while travelling through outer space. Thus, directional information originally carried by the particles may be lost, depending on the energy of the primary, the distance of its origin and strength and topology of the magnetic fields it is exposed to. The gyroradius, also Larmor radius, is given as $r_g = p_T/(|q|B)$ with the transverse momentum p_T of the particle, its charge q and the B-field B it is exposed to; in the relativistic case it can be written as a rule-of-thumb expressing the physical quantities in appropriate units:

$$r_g \approx (108\text{pc})\frac{E/\text{EeV}}{Z(B/\text{nT})}\,, \tag{2.15}$$

with E the energy of the particle, Z its number of charge carriers and B the magnetic field strength; 1 pc = 30.857×10^{15} m. Figure 2.7(a) shows the development of the gyroradius for varying magnetic field strength and cosmic ray energy. Since the deflection decreases at higher energies, it is not too unlikely, that the arrival directions of highest energy cosmic ray primaries point back almost directly to their sources. The fact, that gyration radii are expected to be rather large at these high energies (e.g. equation 2.15 yields $r_g \approx 100$ pc at a particle energy of $E = 1$ EeV $= 10^{18}$ eV and for a field strength of the order of B = 1 nT), does not reduce the necessity to take into account the magnetic fields and even their evolution through the last tens of million years; sources may easily reside at distances larger than 10 Mpc corresponding to 32.6×10^6 ly [Gru00].

Unfortunately, only little is known about the topology of such fields. There is no consensus on the size of the magnetic field strength within our galaxy. Estimates and measurements

differ by several orders of magnitude ($B = (10^{-7} - 10^{-9})$ T) [Bec09, Han09]. Finally, it is worth noting that the observation of (small scale) anisotropy may not only indicate possible sources but also yield an upper limit on the influence of magnetic fields in turn providing information on their strength and shape.

Next to magnetic deflection, cosmic rays are supposed to be subject to attenuation during their propagation. According to the GZK effect described earlier, protons of energies beyond $E \approx 5 \times 10^{19}$ eV will suffer energy loss when producing Δ-resonances with photons of the CMB. In case of primary particles heavier than protons, this procedure will not only lead to energy loss processes but also result in spallation of the nuclei. Further interactions with photons of the CMB, but also in the infrared (IR), visible and ultraviolet (UV) wavelength range, are supposed to occur at lower energies and thus, contribute to the attenuation of cosmic rays. In figure 2.7(b), the attenuation length is given versus the primary energy for different primary particles at a redshift of $z = 0$ [All06]. It shows for example that if cosmic primaries at energies $E \approx 10^{18}$ eV (10^{20} eV) are protons or iron nuclei, their sources will likely reside at distances closer than 5×10^4 Mpc (10^3 Mpc). In the range between, however, iron nuclei are allowed to travel larger distances than protons. Finally, at energies above $E \approx 10^{20}$ eV the attenuation length falls quickly below ~ 100 Mpc for any particle type.

2.5.2 Sources of Cosmic Rays

There is a fundamental restriction to the possible sites of particle acceleration[1]: Given the size of the magnetic field at the site of acceleration and the charge of the particle that is subject to this acceleration, the diameter L of the accelerating region must be two times larger than the gyroradius of the particle. This is necessary to keep the particle inside the region until it has gained a certain energy. Mathematically, it can be written as $L \cdot B \gtrsim 2r_g \cdot B$ and accordingly we derive from equation 2.15:

$$L/\mathrm{pc} \cdot B/\mathrm{nT} \gtrsim 108 \frac{E/\mathrm{EeV}}{Z} \,. \tag{2.16}$$

A summary of known astrophysical objects and their position in a plot *magnetic field* versus *size* is given in figure 2.8. Apparently, none of the known objects fulfils the fundamental conditions to accelerate protons to 10^{20} eV. However, some of them are capable to accelerate heavier nuclei (with larger Z) to such energies, e.g. Active Galactic Nuclei (AGN) and Gamma Ray Bursts (GRB).

2.5.3 Point Source Searches

At highest energies the gyroradii of cosmic rays become large, e.g. $r_g \gtrsim 100$ kpc for particle energies of $E \gtrsim 10^{19}$ eV and magnetic fields $B \lesssim 1$ nT. In this case there is a chance that cosmic rays point back to their origin, and thus make UHECR astronomy feasible. However, the small flux of these UHECRs leads to the task of deriving conclusions from only little information available. This can make it difficult to produce significant results with regard to anisotropy studies.

[1] Note that the sites of particle acceleration are often referred to as the sources of the cosmic particles. Even though that may not necessarily be the case, the main focus and interest of astroparticle physicists lies on the particle acceleration process, not the generation process.

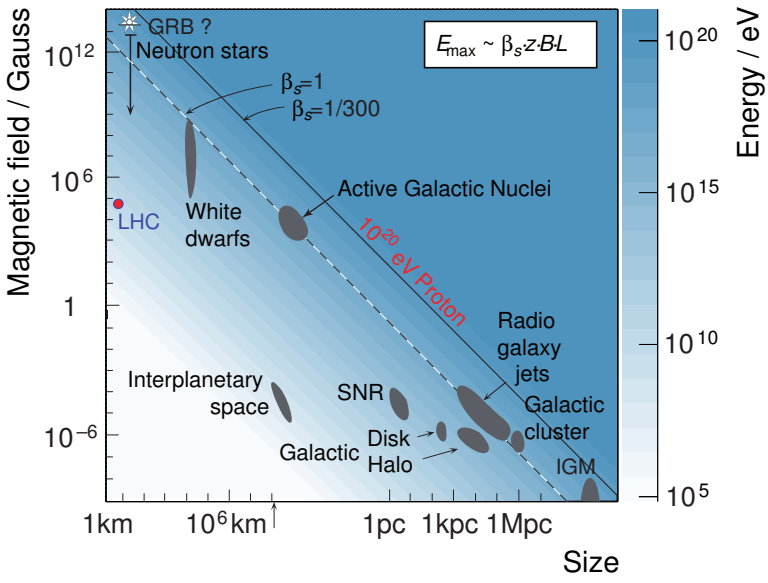

Figure 2.8: The Hillas diagram shows the relation of size and magnetic field of possible sites of particle acceleration, see equation 2.16. Objects below the diagonal solid line cannot accelerate protons to 10^{20} eV [Hil84]. β_s indicates the relativistic velocity of the accelerating shock. Larger shock velocities correspond to smaller B-fields and sizes of the regions necessary to accelerate particles to the same energy as indicated by the dashed line. The same applies to nuclei heavier than protons. Adapted from [Blu09], originally in [Hil84].

The AGASA collaboration has reported a clustering at angular scale of $< 2.5^\circ$ at energies above 4×10^{19} eV [Hay96]. This finding was based on only three pairs of events out of a total of 36 events and its chance probability to have been caused by an isotropic distribution was computed to be 2.9 %. The HiRes collaboration could not confirm the observation of clustering [Abb04] based on the analysis of a data set of similar size.

In order to produce a larger set of arrival directions of UHECRs, published data sets of AGASA, HiRes, SUGAR, Yakutsk, Haverah Park, Volcano Ranch and Fly's Eye have been combined to a set of 107 events in total [Kac06]. This has been made feasible by adjusting the energy scales to make the positions of the knees in the spectra of the respective experiments coincide. The analysis produces a signal at an angular scale of 25° (in the autocorrelation function) with a chance probability of 0.3 % to have occurred from isotropy. An autocorrelation analysis on data taken at the Pierre Auger Observatory shows to peak at a similar intermediate angular scale in the range $9^\circ - 22^\circ$; here, the chance probability is 2 % [Mol09].

Next to the investigation of clustering, correlation searches of arrival directions of cosmic rays with positions of astrophysical objects such as Gamma Ray Bursts (GRBs) and Active Galactic Nuclei (AGN) have been performed but remained unfruitful until recently: The arrival directions measured by the PAO have been found to correlate with the positions of AGN catalogued by Veron-Cetty and Veron [Abr07, Abr08a], see figure 2.9. Technically, this has been achieved by defining a prescription on the set of events collected from start of 2004 until mid 2006. Three parameters have been scanned to tune the significance of the correlation: A lower energy cut for the cosmic rays ($E_{th} > 5.6 \times 10^{19}$ eV), the maximum angular radius within which points on the sphere are considered to be correlated ($\psi = 3.1^\circ$)

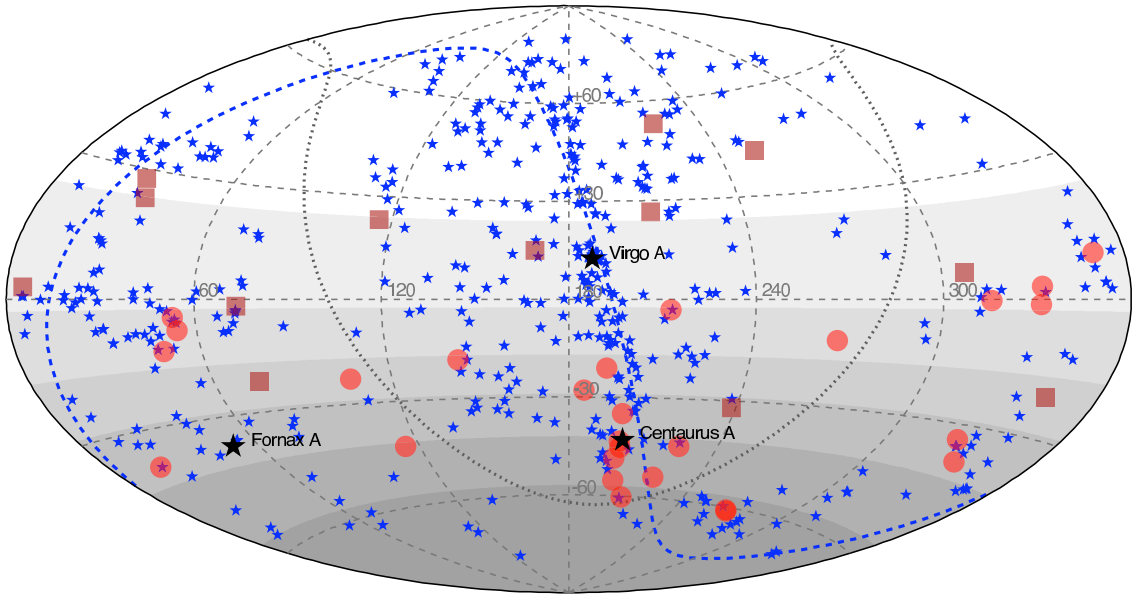

Figure 2.9: Equatorial sky map of UHECRs and AGN. Measurements of arrival directions by the PAO (circles) [Abr07, Abr08a] and HiRes (squares) [Abb08a], asterisks indicate the positions of AGN closer than 75 Mpc according to the Veron-Cetty and Veron catalogue [VC06] and the shaded regions display the relative exposure of the PAO. Plot taken from [Blu09].

and the maximum redshift of AGN contributing to the correlation ($z_{max} = 0.018$ corresponding to distances of less than 75 Mpc). These values have been obtained by minimising the probability that the correlation was caused by an isotropic sky. In the resulting parameter scenario, 12 out of 15 events correlated while 3.2 where expected from isotropy. Apparently, this observation was made a posteriori; the computation of a significance from these results would need to account for this fact in terms of the penalisation via trial factors. This procedure can be avoided by defining a running prescription which only allows to evaluate new data accumulated after the exploratory scan. With the fixed set of parameter values the arrival directions of cosmic rays collected after mid 2006 have been investigated with respect to whether or not they would contribute to and confirm the correlation: Do they have energies beyond 5.6×10^{19} eV and do they spatially coincide within a radius of 3.1° with AGN closer than 75 Mpc. Until mid 2007 another 6 out of 8 events fulfilled the criteria and the signal found in the exploratory scan was considered to be confirmed. Before publication in September 2007, the number of correlating events in the new data set grew to 8 out of 13 with 2.7 expected from the hypothesis of isotropy; this lead to a chance probability of 0.17 % that an isotropic flux had produced the correlation observed. In an update including data up to end of 2009 [Abr10c], the chance probability increased slightly to 0.3 %. Although the significance of the observation of the correlation did not improve (as would have been expected from the extrapolation of the numbers obtained until the time of publication), the result is still capable of excluding isotropy at the percent level. As sort of a cross-check, the HiRes collaboration has analysed UHECR data making use of the same set and values of parameters [Abb08a], see figure 2.9. The correlation found occurred with a chance probability of 82 %. Thus, HiRes data is not distinguishable from isotropy in this context. Whether or not this result contradicts the observation of a correlation by the PAO is debatable. Ac-

counting for different systematic uncertainties in the direction and energy reconstruction of the two experiments could in principle explain the discrepancy. In any case, it is worth emphasising that the two experiments cover a different field of view since they are located on different hemispheres. Based on measurements on one hemisphere, no safe expectations nor extrapolations can be derived with respect to the other hemisphere.

2.5.4 Large Scale Anisotropy Searches

Motivation

Large Scale Anisotropy (LSA) studies aim at quantifying potential anisotropy at rather large angular scales. The results of large scale anisotropy studies are expected to provide hints with respect to the origin and nature of UHECRs as well as to the (extra-) galactic magnetic fields they propagate through. The energy dependence of measures of (large scale) anisotropy can provide information connected to features in the energy spectrum: A possible explanation of the *ankle* in the energy spectrum as a signature of the transition from galactic to extragalactic UHECRs could result in a dipolar pattern in the event rate distribution measured on Earth [Lin63]. Theoretical expectations for the amplitude of such a dipolar anisotropy can be derived from predictions by galactic magnetic field models with different geometries [Can03]. Another possible interpretation of the *ankle* is the distortion of an extragalactic spectrum dominated by protons which suffer energy losses due to $e^{\pm}$-production with photons of the Cosmic Microwave Background (CMB) [Hil67]. The latter scenario is expected to result in a dipolar pattern due to the movement of the Earth within the CMB rest frame as described by the Compton-Getting effect with an amplitude of the order of ~ 0.6 % [Com35].

Compton-Getting Effect

If a cosmic ray detector moves at a velocity v_{det} equalling a significant fraction of the speed of cosmic rays, i.e. the speed of light c, it will experience an excess of cosmic ray detections peaking in the direction of travel. This is true in case the reference frame in which cosmic rays are isotropic is at rest compared to the moving detector. Together with the deficit in the opposite direction of the excess peak, both features will lead to a dipolar pattern in the distribution of arrival directions of cosmic rays as measured by the moving detector. This has been found as early as 1935 [Com35] and is commonly referred to as the *Compton-Getting effect*.

Arrival directions relative to the direction of travel shall be defined by the polar angle θ with $\theta = 0^\circ$ indicating the direction of travel. As an order of magnitude estimate, the amplitude of the dipole D can be derived from the velocity of the detector by simply computing the ratio $D \approx v_{det}/c = \beta$. In order to derive the exact amplitude of the dipole from the velocity of the detector, use of the analogy to the relativistic Doppler effect can be made:

$$E' = E\frac{\sqrt{1-\beta^2}}{1-\beta\cos\theta} \quad \xrightarrow{\beta \ll 1} \quad E/(1-\beta\cos\theta)\ . \tag{2.17}$$

The measurement of the energy E' of a particle by a moving detector is systematically changed compared to the energy E measured by a detector at rest depending on the incident direction of the particle. In this context, the primed quantities indicate the measurements by the moving observer. E' will be overestimated for incident directions from the front, $\theta < 90^\circ$,

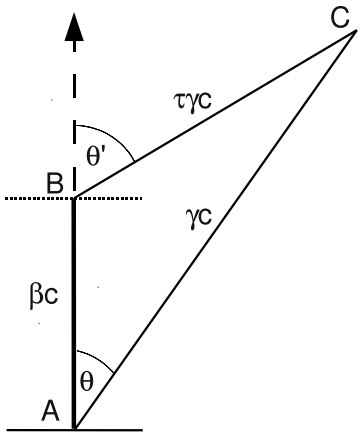

Figure 2.10: Geometry of the Compton-Getting effect: A detector moving from A to B at a speed βc will measure different energies for different incident angles θ of cosmic rays originating in C, see text for details. Adapted from [Com35].

underestimated for incident directions from the back, $\theta > 90^\circ$, and it will not be changed for $\theta = 90^\circ$. Intuitively, the modulation of the energy behaviour is expected to be described by a cosine of the incident direction θ relative to the direction of travel.
The detector is assumed to be fully acceptant in a plane normal to the direction of flight. To calculate the increase of the rate of cosmic particles penetrating this plane, AC$= \gamma c$ is defined as the distance travelled by a particle in unit time. The number τ of time units necessary for a particle to travel from C to B then can be estimated from the comparison of the velocities denoted in figure 2.10 by following the cosine rule,

$$\tau = \sqrt{\frac{(\beta c)^2 + (\gamma c)^2 - 2(\beta c)(\gamma c)\cos\theta}{(\gamma c)^2}} \quad \xrightarrow[\beta \ll 1]{\gamma \approx 1} \quad 1 - \beta\cos\theta \ . \tag{2.18}$$

At a constant velocity of the detector the same number of particles are detected per unit path. The purely geometrical acceptance of a flat detector is accounted for with a factor $\cos\theta$. The number of particles hitting the surface of a stationary detector at B within a range of $d\theta$ and in the time interval of τ units is proportional to

$$n = (1 - \beta\cos\theta) \cdot \cos\theta \cdot 2\pi \sin\theta d\theta \ , \tag{2.19}$$

whereas the detector moving from A to B will measure

$$n' = (1) \cdot \cos\theta' \cdot 2\pi \sin\theta' d\theta' \ . \tag{2.20}$$

Again with figure 2.10 the following relations are obtained:

$$\sin\theta = \sin\theta'/(1 - \beta\cos\theta) \ , \ \ d\theta = d\theta'/(1 - \beta\cos\theta) \ . \tag{2.21}$$

Therefore, within the same ranges of observed angles θ and θ' the ratio of the rates measured by the moving and stationary detectors is

$$n'/n = 1/(1 - \beta\cos\theta)^3 \quad \xrightarrow{\beta \ll 1} \quad 1 + 3\beta\cos\theta \ . \tag{2.22}$$

which represents the very basic formula of a dipole with the direction $\theta = 0^\circ$ given by the moving direction of the detector and the amplitude amounting to 3β. Finally, the cosmic ray flux $dN/dE \propto E^{-\xi}$ with spectral index ξ leads to an additional contribution $\xi - 1$ producing the following expression for the total dipole amplitude D as a function of β [Com35, Har10]:

$$D \approx (\xi + 2)\beta \ . \tag{2.23}$$

In order to compute the dipole amplitude of a specific scenario, the question in which frame of reference cosmic rays actually are isotropic needs to be answered. Then the problem can be reduced to the vector additions of known (relative) velocities. Expressed invertedly, an experiment observing a dipole amplitude and direction will be able to confirm or exclude certain scenarios. For the reality of cosmic rays, three scenarios that may lead to dipoles as described by the Compton-Getting effect will be considered in the following.

The first one is caused by the orbital motion of the solar system around the galactic centre. In case UHECRs are isotropic in the rest frame of the galaxy, the relative motion of the solar system would cause a dipole in the distribution of galactic UHECRs. The velocity of the solar system is $v_{det}^{sun} \approx 200$ km/s with a direction of $(\alpha, \delta) = (270^\circ, 30^\circ)$ in equatorial coordinates. Together with the spectral index $\xi = 3.3$ above the *knee* this leads to an amplitude of $D^{sun} \approx 0.35$ %, see equation 2.23. In case the UHECR rest frame co-rotates with the solar system, the overdensity of UHECRs arriving from the direction of travel might be partially diminished and so might the dipole amplitude. In any event, this scenario is especially applicable as a possible expectation for dominantly galactic UHECRs at energies below $E \lesssim 10^{17}$ eV.

The Compton-Getting effect is supposed to occur also in the cosmological context at energies above $E \gtrsim 10^{18}$ eV, commonly referred to as the extragalactic Compton-Getting effect: Astronomers believe the Milky Way galaxy is moving at a speed of approximately $v_{det}^{gal} \approx 630$ km/s relative to the local co-moving frame of reference that moves with the Hubble flow [Jon04]. It is supposed to move towards the Great Attractor at $(\alpha, \delta) = (241^\circ, 61^\circ)$. This motion of our galaxy through intergalactic space can produce a relative motion of the reference frame where extragalactic cosmic rays are isotropic. This relative motion would lead to a dipole in the distribution of extragalactic UHECRs as measured by a detector within the solar system, e.g. on Earth. If UHECRs are isotropic in the rest frame of the Great Attractor, the total velocity $\mathbf{v}_{det}^{tot}$ is obtained from the vector addition of $\mathbf{v}_{det}^{sun} + \mathbf{v}_{det}^{gal}$. It gives $v_{det}^{tot} \approx 800$ km/s corresponding to an amplitude of $D^{tot} = 1.3$ % and a direction of $(\alpha, \delta) = (251^\circ, 54^\circ)$. Note that this scenario has been chosen to exemplify the principle of computing the predicted dipole parameters for the Compton-Getting effect; many further scenarios are generally thinkable though more or less well motivatable.

The third scenario presented here is the one most commonly referred to at energies around the *ankle*. It describes the situation where the frame of reference of isotropic extragalactic UHECRs coincides with the CMB rest frame. The velocity of the solar system with respect to the rest frame of the CMB can be computed from the dipole measurement in the CMB data by e.g. the COBE experiment [Fix96] leading to $v_{det}^{cmb} \approx 370$ km/s, the direction is $(\alpha, \delta) = (168^\circ, -7^\circ)$. With a spectral index of $\xi = 2.7$ the expected amplitude of the dipole then is $D^{cmb} \approx 0.6$ %.

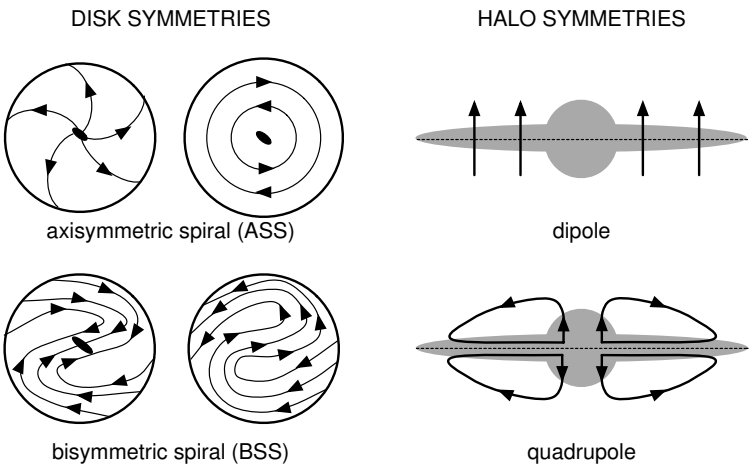

Figure 2.11: Galactic magnetic field geometries. On the left the symmetries of the field within the galactic disk, *ASS* and *BSS*, are shown. On the right the scenarios for the field directions below and above the disk are indicated: Dipole means parallel directions (same direction below and above), referred to as *S*, and quadrupole means antiparallel directions, referred to as *A*. The possible combinations lead to four scenarios, *ASS-S*, *ASS-A*, *BSS-S*, *BSS-A*. Taken from [Bro10], originally in [Zwe97].

Magnetic Fields

Even though it is still uncertain which model describes best the magnetic field in our galaxy [Han09], many of them exist producing a variety of predictions. The predictions of interest for this work are those relevant for the study of anisotropy or even responsible for the generation of anisotropy. In [Ptu93] a model of cosmic ray deflection in the galactic magnetic field has been proposed aiming at the explanation of the *knee* in the energy spectrum of UHECRs. Phenomenologically, the model makes use of the Hall-effect introducing a drift into the propagation of galactic cosmic rays. While this additional effect of systematic diffusion is expected to be negligible compared to the random walk diffusion below $E \lesssim 10^{15}$ eV, the model predicts the drift to become dominant possibly at the energy of the *knee*. Concerning the amplitudes of anisotropies induced by the systematically larger leakage of cosmic rays from the galaxy, predictions vary depending on the model parameters from 0.01 % to 10 % at 10^{17} eV. This model has been slightly adapted and tested with two standard geometries (ASS and BSS, see figure 2.11) of the galactic magnetic field [Can03]. This model yields expectation values for the parameters of dipole anisotropies caused by cosmic rays at energies below $E < 10^{18}$ eV generated within the galaxy.

Another possible cause of a dipolar pattern is the potential existence of a lensing effect of the galactic magnetic field: The coherent part of the field could lead to a focussing of extragalactic UHECRs and an excess of measurements from corresponding directions which in turn could induce a dipole anisotropy. The size of the amplitude and the direction of a dipole generated by magnetic lensing strongly depends on the parameters of the respective model describing the galactic magnetic field. Recent analyses of this effect concerning its impact on the (CMB-related) Compton-Getting dipole have shown that the predicted amplitude of 0.6 % may be suppressed at energies below $E \lesssim 5 \times 10^{18}$ eV and could reach down to $D^{cmb} \approx 0.45$ % at $E = 3 \times 10^{18}$ eV and $D^{cmb} \approx 0.3$ % at $E = 10^{18}$ eV [Har10].

Finally, and even simpler, a strong single source of cosmic rays could result in a large

scale pattern in the distribution of UHECRs which might be described at best by a dipole. If one assumes that the source produces cosmic rays at rates and energies similar to the overall flux measurement, see figure 2.4, the following considerations apply: The highest energetic particles would probably point back rather directly to the source and could be analysed by cluster and autocorrelation methods mentioned earlier in this section. The dominant fraction of UHECRs produced in the source, however, are comparably low energetic particles which are expected to be subject to significant deflections by magnetic fields with the angular distortion increasing with decreasing primary energy. The diffuse part of the magnetic fields would lead to a larger spread of the arrival directions measured on Earth around the source. This scenario could result in a dipolar pattern in the distribution of arrival directions of UHECRs. However, it is clear that again the amplitude and direction of a dipole generated this way do not only depend on the source itself but also on the size and direction of the coherent component of the magnetic field.

Status of Experimental Results

Large scale anisotropy studies by means of the Rayleigh formalism (see chapter 6) applied to the right ascension distributions have been performed at several air shower experiments in the knee energy range. The Akeno air shower array did not find a significant amplitude of the first harmonic modulation [Kif86]. Ten years later, the EAS-TOP collaboration claimed the observation of the Compton-Getting effect with an amplitude of $D^{sun} = (0.036 \pm 0.006)$ % and a direction compatible with the direction of travel of the solar system within the galaxy [Agl96]. KASCADE obtained upper limits on the flux of cosmic rays for Rayleigh amplitudes between 0.1 % and 1 % [Ant04].

The SuperKamiokande experiment [Oya06] has searched for large scale anisotropies in the distribution of cosmic rays with energies around 10^{13} eV. An excess of (0.104 ± 0.020) % (Taurus excess at a right ascension phase of $(75 \pm 7)^\circ$) and a deficit of (-0.094 ± 0.014) % (Virgo deficit) were found with directions on the sphere almost opposite ($(130 \pm 20)^\circ$). This observation will be compatible with the prediction due to the Compton-Getting effect [Com35] if the cosmic ray rest frame partially co-rotates with the galaxy, so that the relative velocity will be $v^{det} \approx 50$ km/s. Remember that the actual speed of the solar system about the galactic centre amounts to $v^{sun} \approx 200$ km/s. The IceCube experiment has reported dipolar anisotropy supporting this observation both in amplitude and phase, essentially [Abb09]: In the energy range around $E \sim (10^{13} - 10^{14})$ eV an amplitude of (0.064 ± 0.002) % has been found at a right ascension phase of $(66.4 \pm 2.6)^\circ$. It is remarkable that the observations of SuperKamiokande and IceCube agree well while being detected with experiments covering independent (disjoint) fractions of the sky. On the other hand, the Tibet experiment has detected cosmic rays at energies around $E = 3 \times 10^{14}$ eV [Ame06]. The investigation of a potential modulation of first order from isotropy yields an anisotropy amplitude of (0.03 ± 0.03) % which is consistent with isotropic arrival directions of galactic cosmic rays. Thus, there is no clear evidence for the galactic Compton-Getting effect and a co-rotating rest-frame of the UHECRs which originate in the galaxy is likely.

The Yakutsk collaboration has searched for a dipole amplitude in a set of 135000 arrival directions at energies between knee and ankle $E \sim (10^{16.5} - 10^{17.5})$ eV. These directions have been found to be distributed in a way compatible with isotropy [Glu01]. The AGASA experiment has not found anisotropy within a similar energy range, $E \sim (10^{17} - 10^{17.5})$ eV,

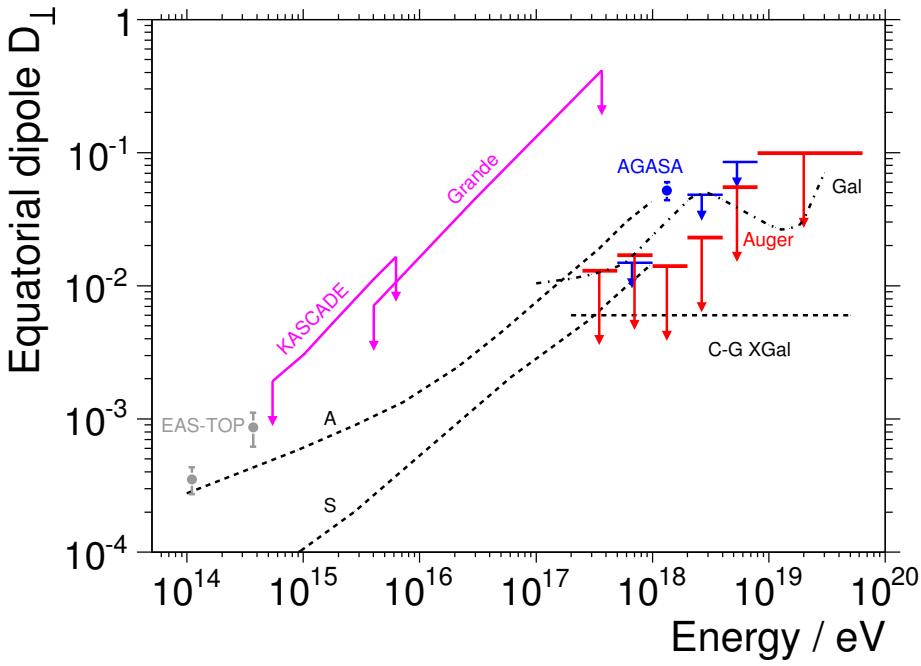

Figure 2.12: Amplitudes and upper limits of the dipole amplitude as a function of energy. The amplitudes and upper limits of dipole analyses on the right ascension distribution are shown for several experiments. For the sake of comparability of results obtained with experiments located at different geographical latitudes or even on different hemispheres the amplitude measurements are scaled to the value the potentially measured dipole would have in case it points to the equator. To do so, the amplitudes originally measured are divided by the cosine of the average declination value of all arrival directions involved. Predictions are displayed from two different galactic magnetic field models with different symmetries (A and S) up to 1 EeV, from a purely galactic origin of UHECRs up to a few tens of EeV (Gal) and the expectations from the Compton-Getting effect for an extragalactic component of UHECRs that are isotropic in the CMB rest frame (C-G Xgal). Plot taken from [Abr11c].

but reported an excess around the galactic centre and Cygnus region at ankle energies around $E = 10^{18}$ eV [Hay99]. The amplitude of the dipolar structure found by AGASA amounts to $D = 4$ % and can have occurred by chance with a probability of 0.2 %. While data taken with the SUGAR experiment could confirm the AGASA measurement [Bel01], it was not confirmable by Haverah Park and Yakutsk because they are too far north. However, a dedicated search for a dipolar anisotropy originating in the galactic centre with the PAO could not confirm the AGASA excess [Agl07]. Recently, upper limits for first harmonic dipolar modulations on the basis of studies of the right ascension distribution at energies above $10^{17.3}$ eV have been derived by the Pierre Auger Collaboration [Abr11c, Gri11]. These limits range from $D = 1.3$ % at $E = (10^{17.3} - 10^{17.7})$ eV to $D = 9.9$ % above $E = 10^{18.9}$ eV and were computed at a confidence level of 95 %. The upper limit found at the PAO at $E \approx 10^{18}$ eV amounts to $D = 1.5$ %, which does not confirm the AGASA excess. However, it must be kept in mind that different parts of the sky are covered by the two experiments.

Chapter 3

The Pierre Auger Observatory

The southern part of the Pierre Auger Observatory (PAO) is located in the Pampa Amarilla near Malargüe in the province of Mendoza, Argentina. It is an air shower experiment dedicated to the measurement of extensive air showers (EAS) as being initiated by ultra high energy cosmic rays (UHECR), which carry energies ranging from 10^{17} eV (0.1 EeV) to 10^{21} eV (1000 EeV). The PAO combines two complementary observation techniques to a hybrid approach: the detection of particles at ground and the observation of associated fluorescence light generated in the atmosphere above the ground. Experimentally, this is realised by employing an array of 1600 water Cherenkov detectors, distributed over an area of 3000 km^2, and operating 24 wide-angle Schmidt telescopes, positioned at four sites at the border of the ground array. The surface detector (SD, the former) measures the lateral footprint of the shower at ground level and the fluorescence detector (FD, the latter) records the longitudinal development of the particle cascade in the atmosphere.

Several almost unique conditions resulted in the selection of the Pampa as the optimum place for such a measurement. The experiment is set up on an elevated plain at the base of the Andes mountains. The plateau has an altitude of 1400 m above sea-level, corresponding to an atmospheric depth of $X_0 = 875$ g/cm^2. The Andes act as a shield against clouds, thus forwarding almost perfect weather conditions during the entire year. Only little precipitation can be measured, while Malargüe weather statistics promise mostly clear sky. The advantage of the altitude of the observatory is the decrease of distance to the shower maximum. The number of particles at a given point or time in the development of the shower reaches its maximum typically at a few kilometers height above sea level, depending on energy and inclination. This facilitates the observation of the shower maximum with the FD on the one hand and also allows enough particles to reach ground level and be detected by the SD on the other hand. Being on this elevated height, EAS are recorded with high statistics and quality.

The Pierre Auger Collaboration intends to build a similar observatory on the northern hemisphere. The purpose of this second hybrid observatory, called Auger Next, is to provide full sky information for cosmic ray research complementary to the Pampa site. Both will, and the southern observatory already does, yield an unprecedented level of statistics at highest energies. The full sky coverage of two observatories operated by the same collaboration is as well unprecedented and is supposed to provide ideal conditions for cosmic ray analyses of all kinds. The sky coverage both sites will have in common ($\sim \pm 25^\circ$ about the Earth's equator) allows cross-checks e.g. for anisotropy searches. All in all, Auger North is considered to be a promising complement of the southern part of the PAO. However, while Auger North has reached the status of thouroughly conducted R&D [Nit10], precise plans for the construction

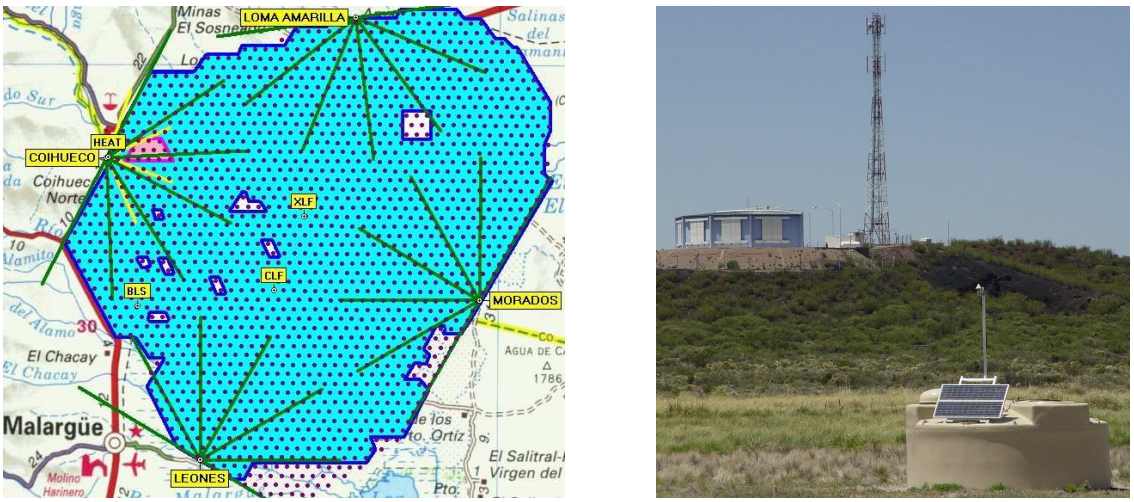

(a) (b)

Figure 3.1: (a) Geographical map showing the positions of the detectors at the site of the Pierre Auger Observatory. The positions of the stations of the SD are indicated by red dots while the locations and fields of view of the FD cameras are displayed by green lines. Starting with the lower left and going anticlockwise their names are *Los Leones*, *Los Morados*, *Loma Amarilla* and *Coihueco*. At the Coihueco site, the *HEAT* extension (yellow lines show field of view) is installed and the magenta trapezium indicates the position of the *AMIGA* and *AERA* detectors, see 3.3. (b) Picture of an SD station in front of one of the FD buildings; the tower in the upper middle is used for wireless data transmission.

phase and location lack the igniting spark from funding commitments.

In this chapter the different detector types are presented. Physical measurement principles are discussed and the reconstruction of shower parameters is explained. After the introduction of the fluorescence detector in section 3.1, the main focus of this chapter lies on the surface detector, section 3.2, which will be the prominent source of data that is used throughout this work. Emphasis is laid on properties of the detector that relate to anisotropy studies. Finally, further detectors conceptually designed to enhance and/or complement the hybrid detector are briefly described.

3.1 Fluorescence Detector FD

As described in chapter 2, cosmic rays initiate a cascade of secondary particles when they hit a nucleus of an atom in the uppermost layers of the Earth's atmosphere. Depending on energy and type, the individual secondary particle can contribute to the generation of new particles or excite atmospheric particles. The electromagnetic component of the air shower is capable of exciting nitrogen molecules. In turn, fluorescence light in the ultra-violet (UV) range is emitted isotropically in the process of de-excitation of these nitrogen molecules. According to [Per03], ~ 5000 photons are produced per ionising particle and km of distance travelled. This light can be detected by UV-sensitive cameras.

The fluorescence detector consists of 4 telescope buildings located at the perimeter of the SD array. Each telescope building (also called "eye") houses 6 cameras in turn consisting of 440 pixels realised by photo multiplier tubes (PMTs). The field of view (f.o.v.) of a

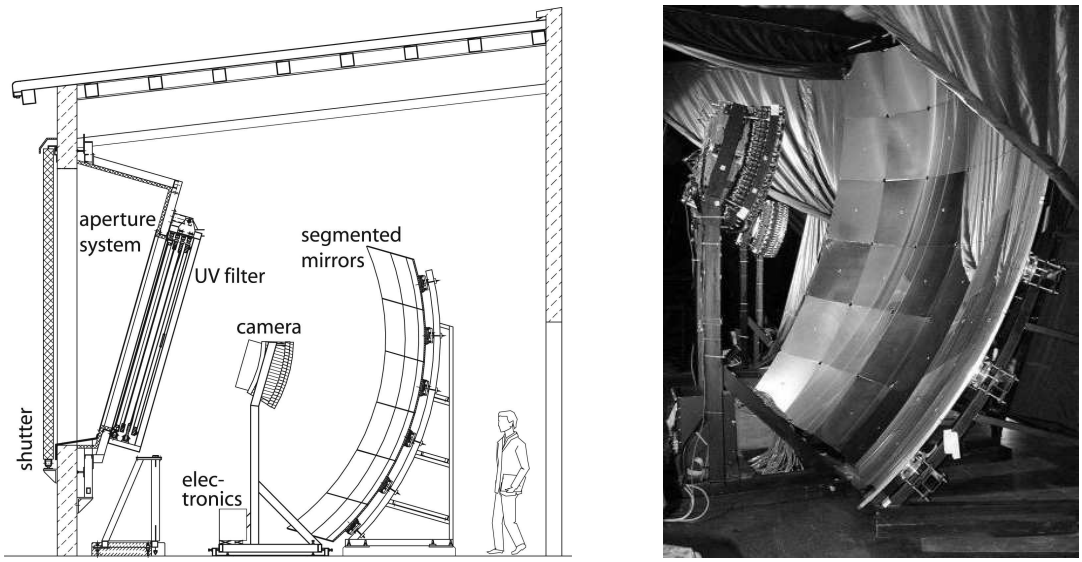

(a) (b)

Figure 3.2: Schematic setup (a) and picture (b) of a fluorescence camera in an FD building (taken from [Abr10b]), see text for details.

single camera comprises an angular area of $30^\circ \times 30^\circ$, so that each telescope building covers a region of 180° in azimuth and 30° in elevation starting at the horizon. The four FD sites together allow for the observation of the atmosphere above the SD array.

Figure 3.2 indicates a schematic view of the setup of a camera. In clear, moonless nights the shutters of the FD buildings are opened. Fluorescence light in the UV range passes the aperture system and the UV filter and is collected on a segmented mirror and concentrated on the camera. The light observed is transformed into an analog signal by the PMTs and digitised in the local electronics. The digital signal is preprocessed and transmitted to the central data acquisition system (CDAS) at the central campus of the PAO.

In this section overviews of several aspects of the fluorescence detector and the reconstruction are presented. Subsection 3.1.1 covers the angular reconstruction of EAS by means of data taken with the FD. In subsection 3.1.2 the energy measurement will be described and finally the principle of determining the composition of the primary particle is briefly illuminated.

3.1.1 Angular Reconstruction of the FD

Thorough characterisations of the angular reconstruction of the fluorescence detector can be found in [Kue08] and [Abr10b]. Here, however, the basic principles are elucidated to equip the reader with a qualitative picture of the method starting at the level of triggered pixels. The angular reconstruction of FD data makes use of the geometric alignment of these pixels in the camera and of the timing information of the signal of each pixel.

Fundamental types of patterns of 5 triggered pixels geometrically regarded as straight track segments are defined. To make a set of triggered pixels provide a fair basis for the reconstruction of the projection of the shower direction onto the camera it has to match one of these fundamental patterns. This projection together with the position and f.o.v. of the camera defines the orientation of the shower detector plane (SDP) that is illustrated in figure

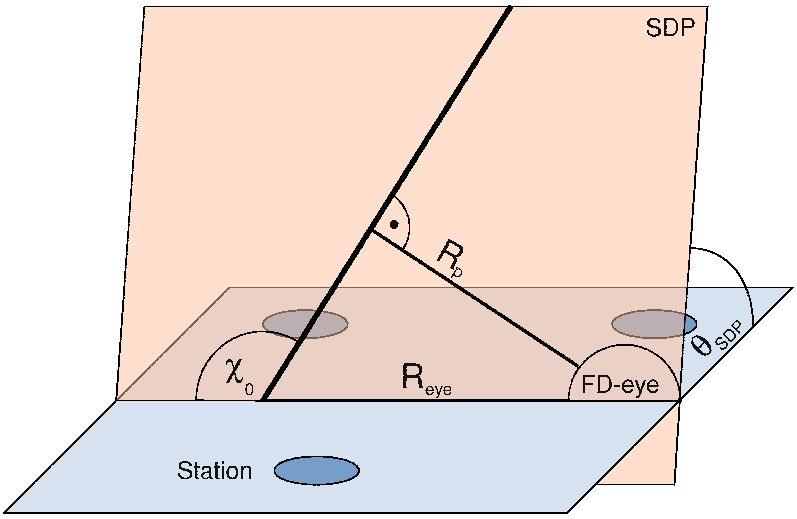

Figure 3.3: Coordinate system of the fluorescence detector. Angle definitions relevant for the measurement of the arrival direction of an air shower with the FD: SDP = Shower Detector Plane, $0° \leq \theta_{SDP} \leq 180°$ = inclination of the SDP, $0° \leq \chi_0 \leq 180°$ = inclination of the shower within the SDP, R_p = shower impact parameter, R_{Eye} = eye to core distance.

3.3: Both the inclination of the SDP, θ_{SDP}, and the azimuthal orientation of the SDP can be derived from the geometry of the aligned pixels and their viewing directions. A third angle is needed for the shower direction to be completely described. This angle is obtained from the time information of the pixel signals.

The signal start times of all pixels within one shower trigger are required to lie within a reasonably small time window. This interval is chosen assuming that both shower particles and fluorescence photons travel with the speed of light in vacuum. In principle, this information should fix the inclination χ_0 of the shower within the SDP. However, the camera pixels can only provide a relative measurement: The absolute distance of the shower to the FD camera, R_p, is unknown. Since R_p closely relates to the inclination angle χ_0 both are difficult to reconstruct. In [Kue08] it is shown, that a global fit of R_p, χ_0 and the pixel signal times can solve the issue. Nevertheless, the uncertainty of the reconstructed χ_0 for directions measured only with data from the FD can easily be of the order of $\sim 10°$. This is why whenever applicable the position and time information of the surface detector station with the largest signal (the *hottest station*) triggered by the same shower is considered in addition. Typically, the SD station used in this procedure is located far away from the FD building compared to the relative pixel timing. Therefore, given the correct time offset between the SD and the FD systems, it can provide a huge lever arm to limit the uncertainty of χ_0 of the same shower to the $\sim 1°$-level. Air shower events making use of the FD and one detector station of the SD are called reconstructed in *hybrid* mode[1].

3.1.2 Energy and Composition Reconstruction of the FD

With the complete angular reconstruction of the shower also the core position is known. After the determination of the SDP it is given by the shower impact parameter R_p and χ_0 or

[1] In this work, the terms *FD* and *hybrid* are used equivalently in fact always meaning the *hybrid* case.

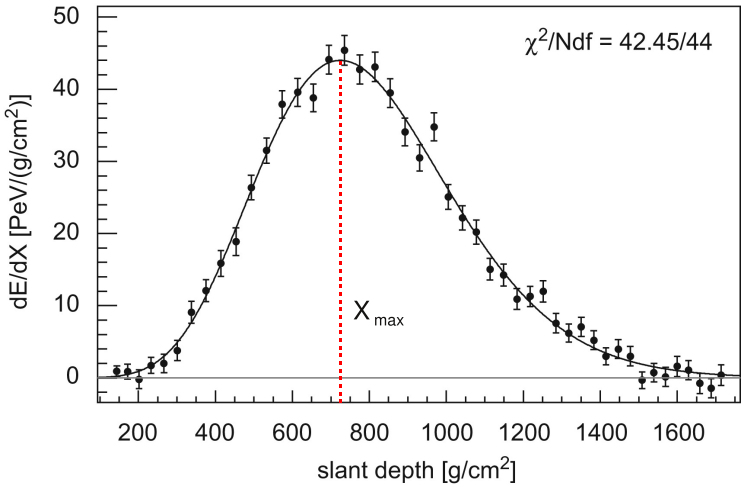

Figure 3.4: Energy deposit over slant depth and Gaisser-Hillas fit for a shower of (3.0 ± 0.2) EeV (adapted from [Abr10b]): The points and error bars show the signals in time bins of pixel traces involved in the reconstruction after transforming the time information to slant depth. The red dashed line indicates the position of the shower maximum X_{max}. To guide the eye, a grey horizontal line has been plotted indicating the null position on the dE/dX-axis.

equivalently by the distance R_{Eye} of the core to the FD building. This information is essential to correctly relate the number of collected photons in the camera pixels to the converted energy in the atmosphere along the track of secondary particles of the recorded shower.

The pixels (i.e. PMTs) measure the number of photons collected in time bins of 100 ns. With the knowledge of an individual pixel's viewing direction and its distance to the shower, the time measurement can be translated into an altitude measurement. Typically, the altitude is expressed by means of the so-called slant depth: Starting at the "boundary" of the atmosphere, the slant depth grows with decreasing altitude; it is measured in units of areal density and reaches a value of ~ 875 g/cm^2 at the altitude of 1400 m of the PAO.

The atmosphere acts as a calorimeter: The signal in a certain time bin of the pixel is a measure of the energy deposit $dE(X)/dX$ at a certain slant depth X. Using the number of photons measured in relevant time bins in all triggered pixels, a profile of the energy loss over slant depth of the shower is sampled, figure 3.4. For this purpose, the conversion between the locally counted number of photons and the energy deposit of secondary particles in the line of sight of the respective pixel must be known. The most substantial parameters for this conversion are the fluorescence yield and atmospheric properties influencing the propagation of these isotropically emitted fluorescence photons. The fluorescence yield indicates the fraction of deposited energy that is transferred to fluorescence photons in the process of interaction of secondary particles with nitrogen molecules. The atmospheric properties such as pressure, air-density and temperature dictate the interaction probability both of secondary particles with nitrogen molecules and of photons with aerosols. This is why it essential to have a good knowledge and / or parametrisation of the atmosphere, i.e. the calorimeter material.

The sampled longitudinal profile of the energy loss given in figure 3.4 can be described theoretically by means of the Gaisser-Hillas function [Gai77, Gai90],

$$f_{GH}(X) = (dE/dX)_{max} \left(\frac{X - X_0}{X_{max} - X_0} \right)^{(X_{max}-X_0)/\lambda} \exp((X_{max} - X)/\lambda), \qquad (3.1)$$

with the free parameters $(dE/dX)_{max}$, X_{max}, X_0 and λ. Fitting this function to the profile sample and computing the integral gives the total energy dissipated electromagnetically, which is approximately 90 % of the total energy of the primary cosmic ray [Abr10b]. (The total shower energy is obtained after the necessary correction for the invisible energy carried away by high energy muons and neutrinos.) Currently, the systematic uncertainties of the energy measurement with the FD add up to a total of 22 %. The dominant contributions come from the systematic uncertainties of fluorescence yield (14 %), reconstruction method (10 %) and absolute calibration of the FD telescopes (9 %) [Abr10b].

The composition reconstruction of the FD relies on the same measurement of the longitudinal profile of the air shower. Having obtained the shower maximum X_{max} as a fit parameter from the Gaisser-Hillas parametrisation, equation 3.1, the measurement needs to be related to the primary particle type. As already mentioned in chapter 2, this is typically achieved making extensive use of air shower simulations. From these simulations predictions can be derived with respect to what particle types do make the shower reach its maximum at what slant depth.

3.2 Surface Detector SD

After reaching the maximum of the number of particles in the slant depth range of $600 < X_{max}/(\mathrm{g/cm^2}) < 850$, the lateral extent of the shower decreases and the particle density within the shower front is thinned out. As less secondary particles exceed the necessary energy limits, the generation of new particles loses the prevalence with respect to absorption processes, see also chapter 2. Given the exposed position of the PAO at an altitude of 1400 m a.s.l., the diameter of the lateral distribution of particles at ground level amounts to several kilometers. The surface detector array measures this lateral footprint of the particle cascade of an EAS at ground level. By sampling the extended shower front at several discrete positions aligned in a hexagonal grid of 1.5 km spacing it records a snapshot of the amount and the time of particles reaching ground.

Each of the 1600 SD stations is self-sufficient in terms of producing and storing their own electric energy by means of a solar panel and a 12 V battery, see figure 3.5. Data is transmitted via the communications antenna and the GPS system provides time and position information which is of capital relevance for the reconstruction. Each detector station consists of a plastic tank containing 12 tons of purified water. Three PMTs are installed in the top cover of the tank facing downward and observe the water. Charged relativistic shower particles travelling through the water produce Cherenkov radiation ranging from UV to visible blue. Since mostly downgoing particles are expected, the narrowly emitted Cherenkov photons need to be reflected from the walls and bottom of a tank in order to be detectable for the PMTs. To this end the tank is lined with Tyvek® which provides uniform reflectivity at UV wavelengths. The measured light is converted into an analog PMT signal which in turn is sampled by 40 MHz FADCs.

The first part of this section is dedicated to the trigger system and trigger probability of the surface detector (subsection 3.2.1). In subsection 3.2.2 the size of the SD is discussed

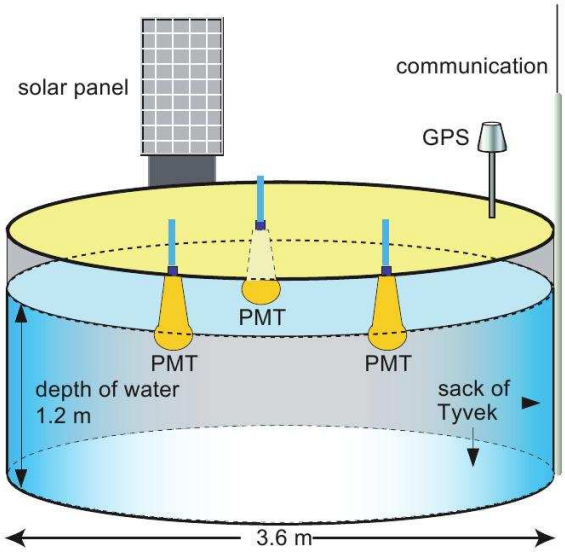

Figure 3.5: Schematic layout of a water Cherenkov station of the SD (taken from [Dem09]), see text for details.

and measures of the effective area and exposure are presented. Most emphasis is put on subsection 3.2.3 which covers the discussion of the principles of directional reconstruction with the SD. The arrival direction of the respective shower is obtained by the measurement of the rise times and sizes of the signals caused in the stations by the penetrating particles of the shower front. Finally, in subsection 3.2.4 the energy estimator of the SD is presented and the calibration procedure for the energy assignment is elucidated.

3.2.1 Trigger System of the SD

A uniform background flux of atmospheric muons constantly generated by cosmic rays of a few GeV produces a high rate of muon hits of roughly 2.5 kHz in each station. On the one hand, this flux is used for self-calibration purposes in every individual station [Ber06b]: It is reasonable to express the signals measured in the individual stations in units of vertical equivalent muons (VEMs). This unit is defined as the charge (Q_{VEM}) or current (I_{VEM}) signal produced in the respective station by a vertically downgoing atmospheric muon. The size of this signal is subject to several parameters determining the individual station's data taking characteristics, such as water quality, amplification of the PMTs and alike. Since these parameters differ from station to station, the large flux of atmospheric muons is an ideal and natural source for calibrating the SD stations and making their signals quantitatively comparable. On the other hand, this rate needs to be suppressed to e.g. 1 shower every 5 days at energies above 3 EeV for an individual station. These numbers can be estimated from the values given in 2.1 assuming on average 4 stations involved in a shower measurement above 3 EeV.

The trigger system of the surface detector has been designed to allow for the operation at a wide range of primary energies with full efficiency for cosmic rays above $10^{18.5}$ eV. It aims at selecting events of interest and rejecting background on the one hand and keeping the rate constraints imposed by the communication and data acquisition system on the other hand. In the following the trigger system is presented differentiating between local station trigger levels (*T1* and *T2*) and event trigger levels (*T3*, *T4* and *T5*).

Local Triggers

The local electronics of the SD stations continuously record the signals of the PMTs. The signals are temporarily stored into buffers as digitised traces with a time binning of 25 ns. These traces are preprocessed and analysed locally by means of FPGAs. The trigger logic searches for two different trigger modes. Firstly, a Time over Threshold (ToT) trigger is implemented, requiring a coincidence of two PMTs with signals above $0.2 I_{VEM}$ in 13 bins (325 ns) within a time interval of 3000 ns. The measured ToT rate of 1.6 Hz matches the expectation for the rate of double muons in an SD station. The technique of checking a bin window instead of a single bin is extremely efficient for the suppression of single atmospheric muons and for the detection of both high energy distant EAS and low energy showers; these showers typically provide rather small but spread signals corresponding to the longitudinal particle distribution within their shower fronts. In parallel, the second trigger within the T1 level requires a three PMT coincidence of a simple $1.75 \cdot I_{VEM}$ threshold. At a rate of 100 Hz it is more noisy; nevertheless it is essential in order to detect the muonic component of very inclined air showers which generates fast signals ($T_{sig} < 200$ ns, corresponding to 8 bins at most).

A ToT at T1 level is directly promoted to T2 status, whereas only 20 % of the T1 single bin threshold triggers fulfill the T2 requirement of a three-fold coincidence at a higher threshold of $3.2 \cdot I_{VEM}^{est}$ [LY05]. Thus, the T2 rate is reduced to about 20 Hz. Only triggers passing the T2 level are used to define the basic event trigger, T3. Besides, monitoring the T2 rate for each station individually, provides both a valuable tool to monitor the SD array performance and a means to calculate the array exposure which is discussed in subsection 3.2.2.

Event Triggers

The T3 trigger level is based on the implementation of two different trigger modes. Firstly, the time coincidence of three stations meeting the ToT requirement defines the so-called 3ToT; these stations need to be spatially aligned in the sense that they are next or next-to-next neighbours. Based on the local low-background ToT, the 3ToT selects 90 % physical events. The other trigger within the T3, being applied in parallel again, is more permissive: Indeed, four stations must pass the T2 level coincidently in time, but they are allowed to be spread spatially up to 6 km distant. Although the time window for coincidence is chosen under the assumption that secondary particles travel with the speed of light, only 2 % of the events selected by this T3 are real air showers; nevertheless it is needed to allow for the detection of strongly inclined showers, that produce both fast signals and spread footprints.

T2 triggers are communicated to the closest FD building where the T3 decision is taken. All data obtained from events that meet the T3 requirements are transmitted to the central data acquisition system (CDAS) and stored. A physical trigger (T4) performs real shower selection on this T3 data offline. Again one out of two different requirements has to be met. The simple application of the "standard" zenith angle cut ($\theta \leq \theta_{max} 60^{\circ}$) improves the selection efficiency for the 3ToT criterion on T3 level from 90 % to 99 %. Consequently, the 3ToT simply advances to T4 level. Alternatively, the so-called 4C1 trigger condition has to be fulfilled. Among the stations triggered, at least one station must be surrounded by three stations with T2 out of its six closest neighbors. In any case, reasonable timing conditions have to be obeyed: Secondary particles are assumed to travel with the speed of light and thus, the time differences between signals measured by neighbouring stations ($D = 1500$ m) detecting the

same shower must be smaller than $\Delta t < D/c = 5\ \mu$s. A tolerance of at most 200 ns for deviations from this assumption is defined; in fact, only strongly inclined so-called horizontal showers necessitate this reduction due to larger fluctuations in the longitudinal distribution of particles in the shower front. Due to chance coincidences, some accidental stations not fitting into the spatial and time conditions still have to be removed in most selected events. The two trigger methods work somewhat complementarily, as the few showers lost by the 3ToT are likely to be recorded by the 4C1 [LY05].

Finally, a quality trigger T5 is defined to facilitate acceptance calculations and energy spectrum studies. The angular and energy reconstruction of air showers need to be precise. For this purpose, the T5 ensures the shower-core to lie within the array of the SD stations. It is obvious, that in case e.g. the shower core lies (just) outside the array, a T4 condition may still be possible, but a lot of the available lateral information of the shower is not accessible for the measurement. Therefore, the T5 requires the reconstructed core to lie within an equilateral triangle of working stations and, moreover, the station closest to the core to have at least 5 direct neighbours available for data taking. Two definitions of the T5 are commonly used for the SD, the mild T5 (5 direct neighbours working) and the strict T5 (all 6 direct neighbours working). These neighbours do not have to be relevant for the fulfilment of the actual T4 condition. In other words, they do not need to have seen the shower but need to have been able to see it. Within this context it is worth noting that it is possible to effectively make use of the information that a working station has not measured the minimum signal necessary to pass the local trigger conditions. This information of an upper limit on the local signal is useful for the estimation of the energy of the EAS with the SD, 3.2.4.

Full Trigger Efficiency

In order to compute the effective size of the SD for a given configuration of the array the trigger probability needs to be known. It is determined by the energy and arrival direction of the shower. Several methods are available to investigate the probability of a shower with given parameters to produce a physics trigger (T4) on the SD array. On the one hand a purely data driven approach can be realised by making use of Golden Hybrid and hybrid data. It is possible to estimate the hybrid trigger probability and derive the SD trigger probability from the comparison of events that are detected by the FD at full efficiency but are not recorded in the set of Golden Hybrid data [Rov03]. On the other hand, the trigger probability of a single station can be estimated from data as a function of the distance to the shower axis [Lhe03] and can be used to compute the event trigger probability [Nel04]. Finally, simulations can be considered the intuitively obvious way to study shower trigger efficiencies at various energies and zenith angles [Mar08]. A detailed discussion of these methods and their results lies outside the scope of this thesis. However, the results obtained with the different approaches agree well and predict 100 % trigger efficiency above an energy of $E \gtrsim 3$ EeV for the typical zenith angle cut $\theta > \theta_{max} = 60^\circ$. The results obtained from the complete chain of shower and detector simulations in [Mar08] state that the threshold to full efficiency is in fact slightly higher than 3 EeV; it occurs rather at $E \gtrsim 10^{18.5}$eV ≈ 3.2 EeV. This is the energy threshold that will be used for the anisotropy studies in this thesis.

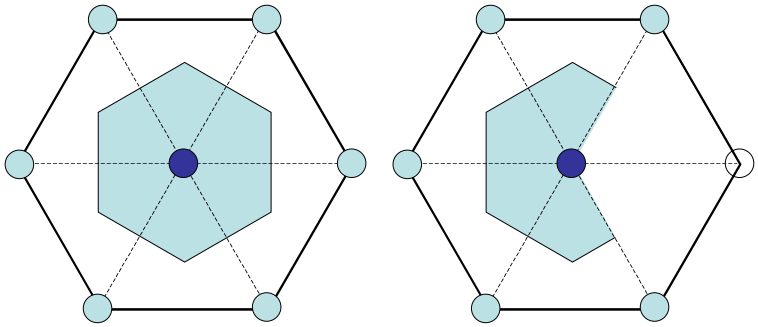

Figure 3.6: Definition and size of an elementary cell of the area of the SD: In case of full trigger efficiency of the SD, the area of an elementary cell can be computed from purely geometric considerations. For a central station surrounded by six working stations (strict T5, left drawing) the area of an elementary cell A_{cell}^{SD} is indicated by blue shade and can be calculated as $A_{cell}^{SD} = \mathrm{D}^2 \cdot \sqrt{3}/2 \approx 1.95$ km^2. Similarly, in case of five working direct neighbours (mild T5, right drawing) the cell size is $2/3 A_{cell}^{SD} = \mathrm{D}^2 \cdot \sqrt{3}/3 \approx 1.3$ km^2. Figure taken from [Par05].

3.2.2 Measures of the Size of the SD

The basic measures of the size of the surface detector are presented and quantified. Starting at the simplest level of area, the definition and computation of aperture and exposure is elucidated.

The *area* of the SD is the ground area equipped with SD stations sensitive to the detection of air showers. The case of full detection efficiency of the SD (i.e. primary energies above $\log(E/\mathrm{eV}) > 18.5$) will be considered in the following. In this case a shower is always measured with the SD. It does not matter where (within the array) the shower core is located nor what direction (up to a zenith of 60°) the shower arrives from.

An SD hexagon consists of a central detector station and its six closest neighbours. An elementary cell of the SD is defined as the sensitive detection area that can be assigned to the central station in case all surrounding stations have been in the DAQ ($\rightarrow$ strict T5). This area is illustrated in figure 3.6 [Par05], its size can be computed easily as $A_{cell}^{SD} = \mathrm{D}^2 \cdot \sqrt{3}/2 \approx 1.95$ km^2 with D = 1.5 km the distance of neighbouring stations of the SD. In case one of the six next neighbours has not been online or simply does not exist ($\rightarrow$ mild T5), $2/3$ of the elementary cell are counted to be part of the detector: Two out of the six equilateral triangles do not contribute to the SD area anymore, because showers with cores inside these two triangles do not fulfill the T5 trigger condition, see above. Note that in the limit of a very large array with a small ratio of the length of the borderline to the area covered, these values can be roughly confirmed by the simple computation of the ratio of ~ 3000 km$^2/1600 \approx 1.9$ km^2. Consequently, in an ideal senario the sensitive area of the SD is approximately as large as the area of the whole array, i.e. ~ 3000 km^2.

The *aperture* of an elementary cell is defined as its area multiplied with the integral solid angle covered. In case of full trigger efficiency up to zenith angles of 60° the computation goes

$$a_{cell}^{SD} = A_{cell}^{SD} \cdot \int_{\theta=0^\circ}^{60^\circ} d\theta \cos\theta \sin\theta = 4.59 \text{ km}^2 \text{ sr} \qquad (3.2)$$

Technically, to compute the *exposure*[2] of the whole SD array the aperture needs to be integrated over time. The number of elementary cells instantaneously active must be known. This is achieved by monitoring the T2 trigger rates of all stations and determining the spatial arrangement of those stations which are in the DAQ. Doing so, the number of elementary hexagonal cells is recorded every second. Consequently, for the computation of the integrated exposure over time of the SD, Λ^{SD}, the number of "cell-seconds" N_{cell} must be multiplied with the aperture of the elementary cell

$$\Lambda^{SD} = N_{cell} \cdot a_{cell}^{SD} \tag{3.3}$$

The *relative exposure* ω of a fully efficient surface detector after the application of the typical zenith angle cut, $\theta \leq \theta_{max} = 60^\circ$ has been computed in [Som01]. In this context, full efficiency means the flat detector only introduces a purely geometric zenith angle dependence into the exposure according to the scaling of the area visible to cosmic rays, similar to $a_{cell}^{SD} \propto \cos\theta$. Given these conditions and the geographical latitude of the detector, $lat_{\mathrm{PAO}} = -35.25^\circ$, the relative exposure ω does only depend on the declination δ:

$$\omega(\delta) \propto \cos(lat_{\mathrm{PAO}}) \sin\zeta \cos\delta + \zeta \sin(lat_{\mathrm{PAO}}) \sin\delta, \tag{3.4}$$

with ζ given by

$$\zeta = \begin{cases} 0 & \text{if } \xi > 1 \\ \pi & \text{if } \xi < -1 \\ 1/\cos\xi & \text{otherwise} \end{cases} \tag{3.5}$$

and

$$\xi = \frac{\cos\theta_{max} - \sin(lat_{\mathrm{PAO}}) \sin\delta}{\cos(lat_{\mathrm{PAO}}) \cos\delta} \tag{3.6}$$

The definition of ξ and its utilisation in the intermediate step is needed to account for the sharp zenith angle cut at $\theta_{max} = 60^\circ$. For convenience, the relative exposure has been plotted alongside a full sky plot in equatorial coordinates in figure 3.7. The sharp increase around $\delta \lesssim -85^\circ$ indicates the transition to the part of the sky that is covered uninterruptedly. It consists of a cone of $\sim 5^\circ$ radius about the south pole. This feature can be understood given the geographical latitude of the PAO $lat_{\mathrm{PAO}} \approx -35^\circ$ and the maximum zenith angle $\theta_{max} = 60^\circ$. Even though the cone lies at the edge of the exposure and correspondingly the weight derived from the area of the SD visible from this region is diminished by a factor $\sim \cos\theta_{max} = 0.5$, the fact that this part of the sky is always covered by the field of view of the SD leads to a peak in the relative exposure function.

More intuitively, the relative exposure on the sphere of equatorial coordinates can be derived from the local acceptance of the SD. According to equation 3.2, it is given by $\cos\theta \cdot \sin\theta$ with the former coming from the scaled size of the projected area of the SD and the latter accounting for the solid angle in (local) spherical coordinates. In the local system this produces a field of view defined by a cone of angular radius of $\theta_{max} = 60^\circ$, see figure 3.8(a). By rotation this cone can be transformed to equatorial coordinates, see appendix A, using the position of the observatory $(lon_{PAO}, lat_{PAO}) = (-69^\circ, -35^\circ)$ and introducing an arbitrarily chosen point in (local sidereal) time, see figure 3.8(b). Finally, this cone needs to travel 360° in right ascension α, corresponding to the integration over one sidereal day in time, in order to produce the correct relative exposure $\omega(\delta)$ as displayed in 3.7 (b).

[2] Note that the terms exposure and coverage are used ambiguously throughout this work; they place emphasis on the passive and active properties, respectively, of the detector.

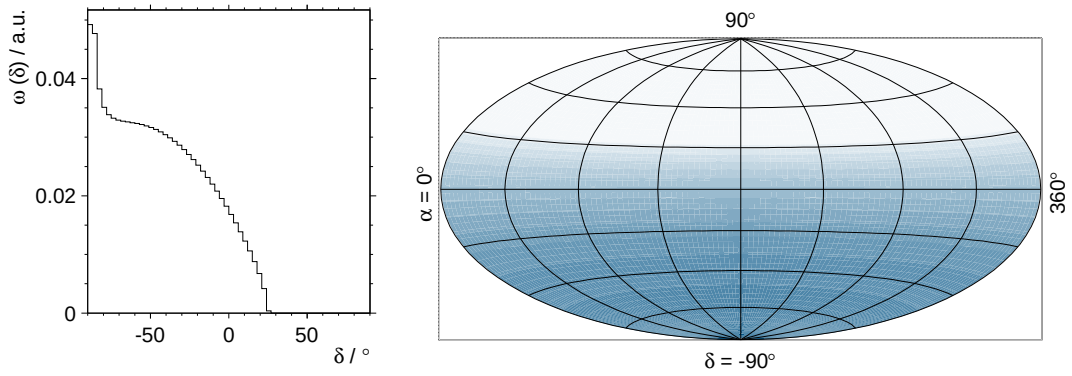

(a) (b)

Figure 3.7: Relative exposure ω of the PAO SD. The dependence on declination δ is shown on the left; for convenience, the weights $\omega(\delta)$ have been plotted on a projection of the full sky observing flatness in right ascension on the right. This equatorial map is what a perfectly isotropic sky would look like from the PAO's field of view in case of infinite statistics.

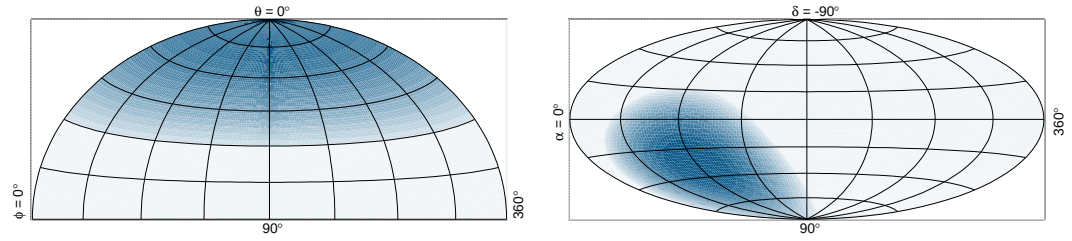

(a) (b)

Figure 3.8: Acceptance of the PAO SD. The locally available field of view of the SD weighted with $\cos\theta \cdot \sin\theta$ to account for geometric effects is plotted on the left; the corresponding transformation to equatorial coordinates is displayed on the right.

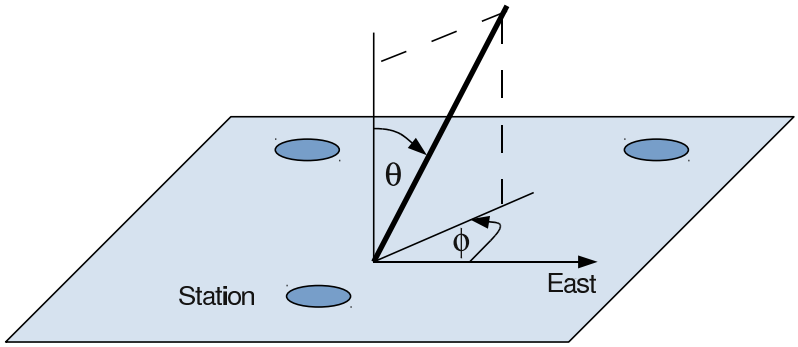

Figure 3.9: Coordinate system of the surface detector. Angle definitions relevant for the measurement of the arrival direction of an air shower with the SD: $0^\circ \leq \theta \leq 180^\circ$ = zenith angle, $0^\circ < \phi \leq 360^\circ$ = azimuth angle, similar to figure A.1.

Bad Periods

Next to the monitoring of the T2 triggers of SD stations another measurement is necessary to properly evaluate the exposure: It is possible that T2 triggers are continuously monitored but at the same time the CDAS does not operate accurately, i.e. it may not produce central triggers, which in turn would lead to an overestimation of the exposure. In order to correct for this kind of malfunction, an expectation for the rate of T5 triggers to be seen by the CDAS can be computed under the assumption that T5 triggers follow a Poisson distribution. Assuming a constant T5 rate $\lambda \approx 1000$ per day and hexagon, the probability P to measure an interval larger than T between two consecutive T5 triggers is

$$P(T) = e^{-\lambda T}. \tag{3.7}$$

The expectation can then be compared to the measurement and data taking periods are rejected in case P drops below a certain threshold value. The choice of the threshold value is obtained from the data itself [Bon06]. After accounting for bad periods, the integrated exposure of the SD array for the time from start of January 2004 to end of June 2010 using the strict (mild) T5 condition is

$$\Lambda^{SD} = 20,905 \ \ (25,806) \ \ \text{km}^2 \ \text{sr y} \tag{3.8}$$

3.2.3 Angular Reconstruction of the SD

The direction of an air shower is estimated by means of measurements of the arrival times of the shower front in the triggered SD stations. The shower front denominates the very first particles in the lateral spread of the particle cascade of the shower. In addition to this timing information the location of every triggered station i given by x_i, y_i and z_i in the coordinate system of the array is needed to reconstruct the arrival direction of the shower.

It is possible to predict the arrival times of the shower front in the stations, i.e. the time of the first particles of the particle cascade of the shower causing signal in the station electronics. To do so, several shower front models (plane, spheric, parabolic) may be used.

Assuming a plane shower front for the simplest case, a flat SD array and a particle velocity again close to the speed of light, the time difference between the measured arrival time t_i at station i and the expected arrival time with respect to the station's distance from the shower core can be written as [Pri03]

$$\triangle t_i = t_i - \left(T_0 - \frac{(x_i - x_{core})u + (y_i - y_{core})v}{c} \right), \tag{3.9}$$

where T_0 is the arrival time of the shower core at ground and $u = \sin\theta\cos\phi$ and $v = \sin\theta\sin\phi$ are the direction (co-)sines; x_{core} and y_{core} are the coordinates of the core position. In a first step the core position is determined by the barycenter of all triggered stations, weighted by the square root of each station signal. The typical accuracy is 150 m at 10 EeV [Dem09]. To be able to take into account the shower front curvature, the determination of the additional parameter of curvature necessitates at least 4 stations to be involved in the measurement. Furthemore, another term has to be added to the right of equation 3.9:

$$\Delta/c \approx r_i^2/(2Rc)\,, \qquad \Delta/c = \left(\sqrt{R^2 + r_i^2} - R \right)/c \tag{3.10}$$

in case of a spherical shower front or a parabolic shower front, respectively (with Δ the additional distance travelled, R the curvature radius and r_i the distance of station i to the core), see figure 3.10. Remember that the common nomenclature of the angles in local coordinates is $zenith = \theta$ and $azimuth = \phi$. These angles define the locally measured arrival direction of the shower. They can be extracted from equation 3.9, by minimization of

$$\chi^2 = \sum_i (\triangle t_i)^2/\sigma_{t_i}^2, \tag{3.11}$$

where σ_{t_i} is the uncertainty of the measured arrival time t_i at station i. It is worth noting that the χ^2 presented here can also be used as a goodness of fit estimator to find out which shower front model describes the data better. It can be shown, that using a curved shower front model, be it spherical or parabolic, produces adequate agreement between expectation and measurement [Bon09].

To have a handle on the spread of the expected first particles' arrival times in the detectors a Poisson model can be used to describe their longitudinal distribution within the shower front [Bon08]. Propagated from the time measurement to the shower direction estimation, this spread provides a measure of the precision of the angular reconstruction. Precisely speaking, the angular uncertainties in the locally measured direction, $\sigma(\theta)$ and $\sin(\theta)\sigma(\phi)$, are derived from the uncertainty of the time measurement.

It is possible to compute the order of magnitude of the angular resolution from the timing precision of the SD stations. The GPS clock accuracy is ~ 10 ns and the FADC trace resolution can be computed as $25\text{ ns}/\sqrt{12} \approx 7$ ns. The latter is limited by the sampling frequency of 40 MHz of the data taking electronics of the stations. The quadratic sum of the given uncertainties yields an expected total time precision of ~ 12 ns for the individual trigger times of the stations. Note that the intrinsic uncertainty of the locations of individual particles within the shower front can only be derived from data [Bon08]. From the comparison of trigger data in doublets, i.e. twin stations that are ~ 10 m distant from each other and thus measure different samples of the shower front at essentially the same time, a value of ~ 14 ns is derived [Bon09]. The time resolution estimates from the signal time measurements in doublets and from the examination of the electronics accuracy can be contrasted to

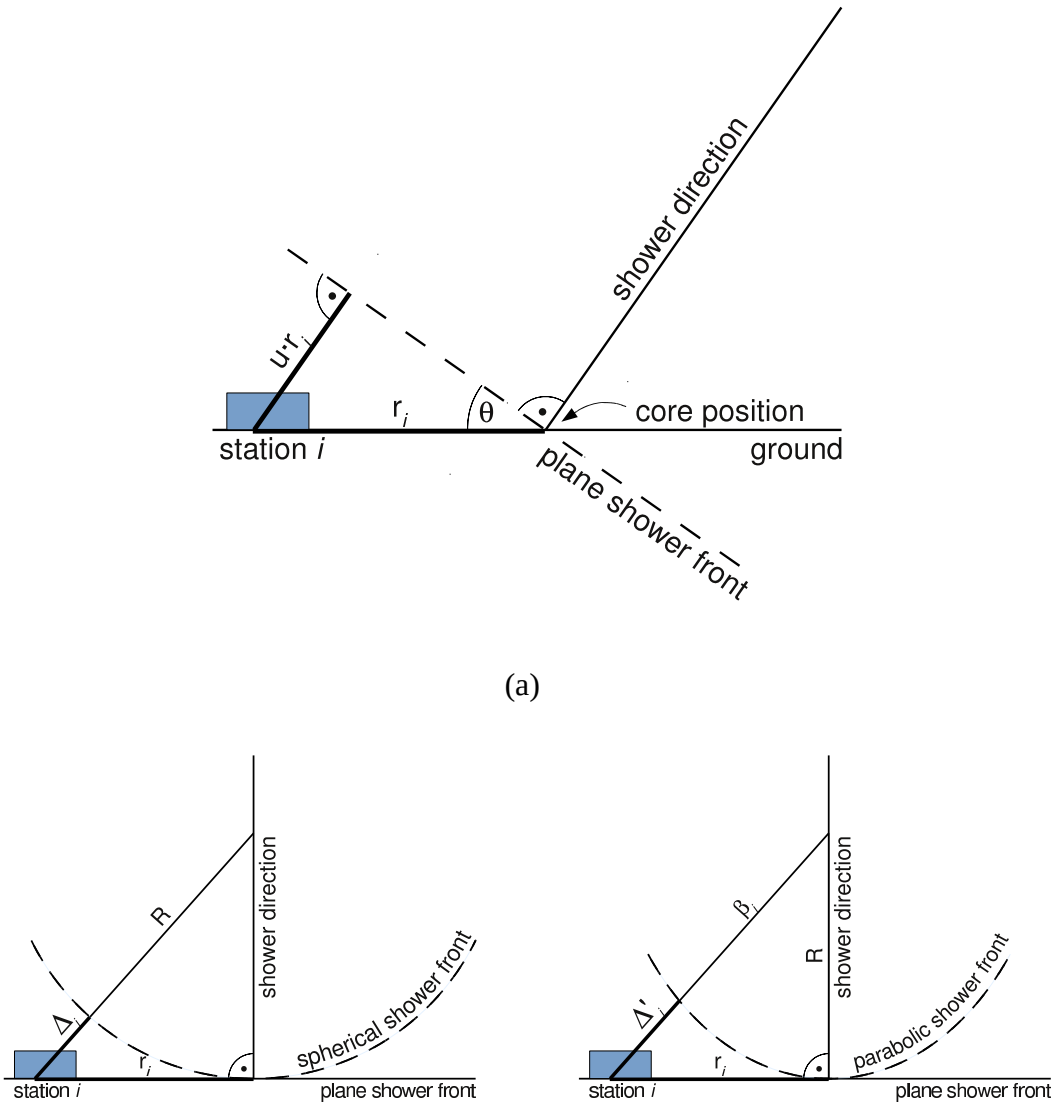

Figure 3.10: (a) Plane shower front. A shower arrives at zenith angle θ, the central point of impact of the particles is the core position. Compared to the core, the additional distance for the particles necessary to reach station i is $u \cdot r_i$ with r_i the station to core distance and $u = \sin\theta$. See text for details; note that, for the sake of simplicity, the problem has been projected from 3 to 2 dimensions. Figures (b) and (c) display the extra difference in travel distance for the shower to reach the same station i when assuming a spherical and a parabolic shower front instead of a plane one. Compared to a plane shower front, for (b) the extra travel distance is Δ_i and for (c) it is $\Delta'_i + \beta_i - R$.

each other: With the concept of the quadratic sum the intrinsic Poisson uncertainty of the particle times within the shower front can be estimated to be about $\sqrt{14^2 - 12^2}$ ns ≈ 7 ns. Assuming the shower particles travel with the speed of light the total time precision of ~ 14 ns corresponds to a length precision of ~ 4.2 m of distance travelled. Using the typical station distance in the hexagonal grid of 1500 m a crude estimate is obtained of the contribution to the total angular uncertainty of approximately $\arctan(4.2/1500) \approx 0.2^\circ$. This uncertainty estimate is meant to give an impression of how the accuracy of the hardware timing and fluctuations of the longitudinal distribution of particles within the shower front propagate to the precision of the reconstruction of angular information. In some sense it quantifies a lower limit on the possible angular resolution that is supposed to be only reached under ideal conditions. The angular resolution of the SD is discussed in more detail in chapter 4.

3.2.4 Energy Estimator of the SD

In this subsection the energy estimator of the SD is introduced and the principle of the calibration by means of data recorded in Golden Hybrid mode is explained. The technical subtleties of the reconstruction can be found in [Dem09] and [Veb05] and will not be covered here in detail.

The lateral distribution of secondary particles within the shower front is expected to be symmetric about the shower axis. In fact the axial symmetry is distorted by the geomagnetic deflection of the charged particles of the shower. While the resulting effect on the energy measurement is negligible for zenith angles θ below 60°, it induces a directional bias which is important to be considered when performing anisotropy studies at small signal to noise ratios, see chapter 5. One of the dominant sources of uncertainty concerning the measurement of the lateral profile of the shower is given by physical shower to shower fluctuations. These fluctuations occur in the very first steps of interactions during the development of a shower. It has been shown that the uncertainties due to shower to shower fluctuations can be minimized if a characteristic signal is measured at a shower core distance of $\gtrsim 600$ m [Hil71]. For the SD of the PAO with a station spacing of 1500 m the optimum distance for estimating the shower energy has been found to be at ≈ 1000 m [New06]. This is why the energy estimator of the SD has been chosen to be $S(1000)$, the signal at 1000 m distant from the shower core.

The energy estimate by the SD is obtained from the signal measurements by the stations which sample the lateral footprint of the shower. The signal sizes in the individual stations together with their distances to the shower core are used to fit the value of $S(1000)$. To do so, the lateral samples of the longitudinal particle density within the shower front, i.e. the station signals, are related to the core distances of the corresponding stations and modeled by an NKG-like lateral density function (LDF),

$$S(r) = S(1000) \left(\frac{r}{1000\text{m}}\right)^{\beta} \left(1 + \frac{r}{1000\text{m}}\right)^{\beta}, \tag{3.12}$$

with $S(r)$ the signal measured in an SD station at core distance r and the parameters β and $S(1000)$ for the slope and for the shower size, i.e. the energy estimator in this context [New05]. The basic shape of this LDF is similar to the parametrisation of the lateral distribution of the muonic (and electromagnetic) component of air showers given in equation 2.13 (2.5). It has proved to describe the signal data recorded with surface detectors of EAS experiments such as the PAO sufficiently well [New06].

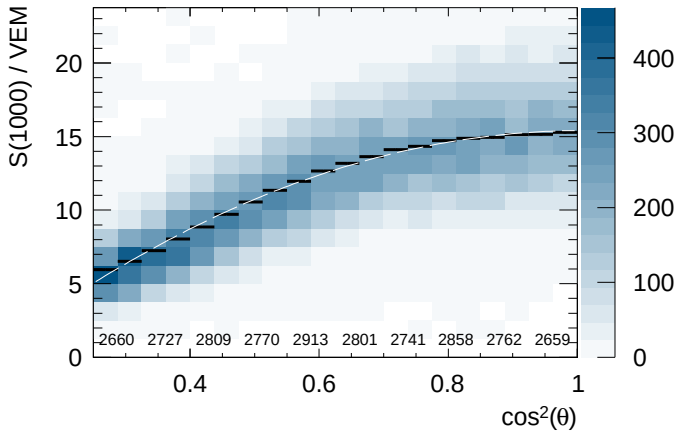

Figure 3.11: Dependence of the SD energy estimator measurement on the zenith angle for a set of simulated showers at an energy interval from $10^{18.5} < \mathrm{E}\,/\,\mathrm{eV} < 10^{18.7}$: $S(1000)$ decreases for increasing inclination of the shower. Mean and RMS are plotted (black solid) and a parabola is fitted (white dashed). The numbers in the plot indicate the number of entries in the respective bin pairs.

Since the shower front is only sampled at several discrete positions on the ground by the stations of the SD, it is intuitively clear that changes of the estimated direction lead to changes of the estimated position of the shower core and vice versa. More precisely, if the core position is moved, the inclination of the shower needs to be adjusted to fit the (relative) time information in the stations involved in the measurement. Consequently, the energy estimator is affected by changes of the estimates of direction and core position for the following reason: The core position defines the core distance r of the individual station with signal $S(r)$ which is essential for the LDF fit that in turn provides the energy estimator $S(1000)$. These correlations are typically accounted for by applying an iterative procedure in the reconstruction of core position, direction and energy estimator of the shower [Veb05]. Furthermore, another solution by means of a global fit has been proposed recently [Dem10].

Calibration of S(1000)

Another step in the process of the energy measurement with the SD is necessary before the final calibration can be performed. The particle density distributions observable at ground level are strongly affected by the zenith angle of the shower as the zenith angle determines the amount of atmosphere, or slant depth, the particles have to pass. Larger zenith angles mean longer travel distances within the atmosphere and stronger attenuation which in turn leads to a diminished number of secondary particles reaching the SD. This behaviour is displayed qualitatively in figure 3.11 for a set of simulated showers at an energy interval from $10^{18.5} < \mathrm{E}\,/\,\mathrm{eV} < 10^{18.7}$. From purely geometric considerations the amount of atmosphere to be traversed by the particles approximately goes like $1/cos(\theta)$ and thus is roughly a factor of two larger for a zenith angle of $\theta = 60^\circ$ compared to an exactly vertical shower ($\theta = 0^\circ$).

The zenith angle dependence of the energy estimator can be eliminated by means of the constant intensity cut (CIC) method. The basic ingredient to this method is the assumption that cosmic rays arrive isotropically at Earth, i.e. there is no preferred arrival direction and the primary energy distribution should be the same in every angular bin. The CIC method is

applied using data above full efficiency, $\log(E/\mathrm{eV}) > 18.5$. Thus, directional bins covering the same *solid angle* $\times$ *detector area* are supposed to measure the same number of showers of the same energies. For this task, azimuthal effects are negligible above full efficiency. The zenith angle axis can be scaled as $\cos^2(\theta)$ to achieve the adequate binning. Figure 3.11 illustrates the functioning of this approach, all bins in $\cos^2(\theta)$ contain the same (within the given statistics) number of entries.

It is necessary to define a reference zenith angle, $\theta_{ref} = 38^\circ$, to relate the measurement of the energy estimator $S(1000)(\theta)$ to a zenith angle independent quantity: S_{38° is defined as the signal expected at 1000 m distant from the shower axis in case the shower had arrived at a zenith angle of $\theta_{ref} = 38^\circ$. The connection between $S(1000)(\theta)$ and S_{38° is called the attenuation curve and must suffice the constant intensity conditions mentioned above. Therefore, it is reasonable to make use of a polynomial in $\cos^2(\theta)$. Currently, the following parabolic solution is implemented in the reconstruction of air showers with $\overline{\mathrm{Off}}\underline{\mathrm{line}}$[3] [Veb05]:

$$S(1000)(\theta) = S_{38^\circ}(1 + a \cdot (\cos^2(\theta) - \cos^2(\theta_{ref})) + b \cdot (\cos^2(\theta) - \cos^2(\theta_{ref}))^2) \ , \quad (3.13)$$

with the fit parameters given in [Mar08].

$$a = 0.919 \pm 0.055(stat)^{+0.02}_{-0.09}(sys) \quad (3.14)$$

$$b = -1.13 \pm 0.26(stat)^{-0.04}_{+0.19}(sys) \ . \quad (3.15)$$

Using this relation, the zenith angle independent quantity S_{38° can be obtained for any $S(1000)(\theta)$ measured at any θ. The unit of S_{38° is VEM and it has to be scaled to be assigned the correct energy. The details and properties of the energy calibration of SD data are thouroughly addressed in [Mar08]. Basically, this final calibration step is performed by making use of Golden Hybrid data, i.e. the set of showers which have been detected coincidently by both the FD and the SD. The energy measured with the FD, E_{FD}, and the corrected energy estimator of the SD, S_{38°, correlate and the relation between the two is well described by

$$E_{FD} = A \cdot S^B_{38^\circ} \quad (3.16)$$

with the parameters given in [Abr08b].

$$A = [1.49 \pm 0.06(\mathrm{stat}) \pm 0.12(\mathrm{sys})] \cdot 10^{17}\ eV \quad (3.17)$$

$$B = 1.08 \pm 0.01(\mathrm{stat}) \pm 0.04(\mathrm{sys}) \ . \quad (3.18)$$

Note that B is close to unity and the relation can be considered almost linear.The directional and energy reconstruction by $\overline{\mathrm{Off}}\underline{\mathrm{line}}$ of an example air shower is visualised in figure 3.12.

3.3 Further Detectors

The southern part of the Pierre Auger Observatory is designed to work efficiently in the EeV-range of cosmic ray primary particles. Enhancements of both the SD and the FD detector have recently been deployed in order to extend the efficiency down to energies of 0.1 EeV. With decreasing energy, air showers produce less fluorescence light and develop higher in

[3] $\overline{\mathrm{Off}}\underline{\mathrm{line}}$ is the detector simulation and reconstruction software used for the offline analysis of data taken by the Pierre Auger Observatory

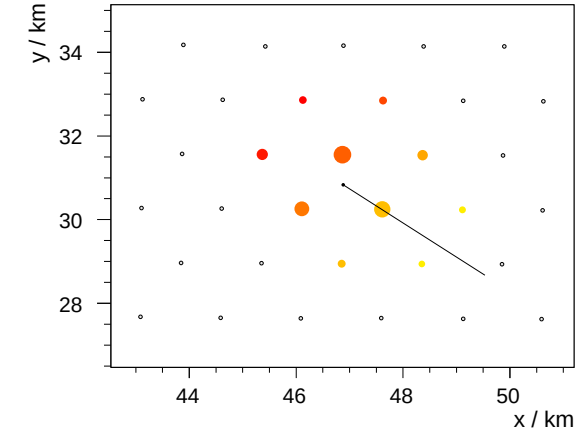

(a)

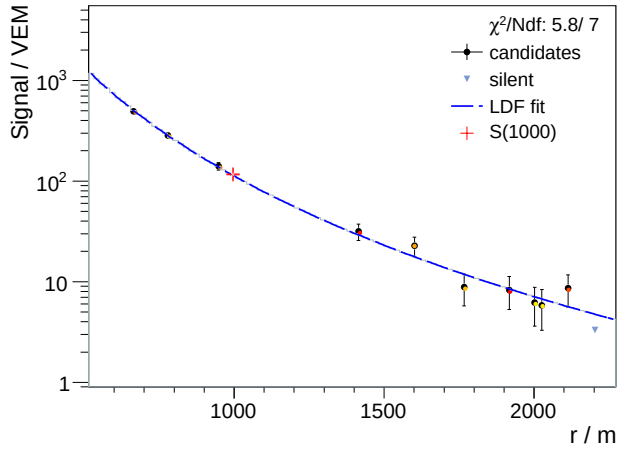

(b)

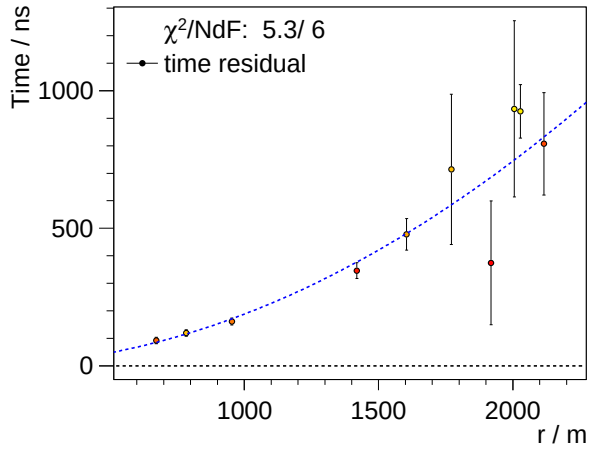

(c)

Figure 3.12: Visualisation of the main properties of an example air shower reconstructed by the SD with $\overline{\text{Off}}\underline{\text{line}}$: (a) shows the lateral footprint with triggered stations on ground level, the size of the circles is a measure of the detected signals, the line indicates the azimuthal incident direction of the shower. (b) shows an LDF fit to the signals at the respective core distances r and (c) gives an impression of the arrival direction reconstruction by means of the time residuals under the assumption of a curved (spherical) shower front. For all plots, the colour code of the data points indicates the arrival time, from light yellow (early) to dark red (late).

the atmosphere and their lateral spread becomes smaller. Good detection probabilities can only be maintained with fluorescence telescopes that look higher in the atmosphere and with surface detector arrays of smaller granularity. Furthermore, only near showers are detectable with the FD. Additionally, the properties of rather new (within the PAO) air shower detection techniques are presently investigated. All enhancements are described here briefly, their geographical position within the array is indicated on the map in figure 3.1 as described in the corresponding caption.

The High Elevation Auger Telescopes (HEAT) consist of three additional fluorescence cameras located close to the Coihueco FD building site [Abr09c]. Equipped with basically the same optical and technical properties as the standard cameras, the HEAT cameras are situated in small shelters. These shelters can be tilted by 30° to provide the cameras with an elevated field of view that directly borders on the f.o.v. of the standard FD installation at the Coihueco site. This combination allows for stereo detection of air showers with the standard cameras of Coihueco and those of HEAT.

The Auger Muon detectors and Infill for the Ground Array (AMIGA) is also located close to the Coihueco site [Abr09c]. In the context of the infill for the ground array, in a limited region within the regular grid stations are deployed with a smaller lattice constant of 750 m and partly even 433 m. Next to providing the basis for shower detections at lower energies, data taken with the infill array can be used for cross-checks and reliability tests of the standard SD up to EeV energies.
For the second part of AMIGA, muon detectors are buried close to selected SD stations. The increased attenuation in the earth shields the electromagnetic component and scintillation detectors measure the penetrating, almost purely muonic component of the air shower. This measurement is expected to provide a deeper understanding of the different components in the lateral distribution of the secondary particles of air showers.

In the densely instrumented area around Coihueco, another type of EAS detector is presently being installed: Air showers generate radiation at radio frequencies, which is commonly interpreted as synchrotron radiation of electrons and positrons deflected in the geomagnetic field. Given a shower disk of a thickness of the order of ~ 1 m, this radiation turns out to be coherent in a frequency range of $\sim 1\ldots100$ MHz [vdB09]. The first phase of deployment of the Auger Engineering Radio Array (AERA) has recently been finished. Measurements with an array of up to now 25 radio antennas are currently being performed.

The basic concept of the Pierre Auger Obserbatory of making use of hybrid and multiple detection techniques applies. It provides the opportunity of cross-checks and -calibration which are essential for an improved understanding of either technique and allows for achieving highly precise air shower measurements.

Chapter 4

Angular Resolution of the Surface Detector

In this chapter the angular resolution (AR) of the surface detector (SD) is studied. The precise reconstruction of the arrival directions of air showers is crucial to allow for anisotropy studies of Ultra High Energy Cosmic Rays (UHECRs). It is shown, that the AR of the SD is always better than $\sim 2^\circ$ and as good as $\sim 1^\circ$ at energies above 10^{19} eV. This makes the data set collected with the surface detector of the Pierre Auger Observatory well suited for all kinds of anisotropy studies at all angular scales down to the 2° - level. The work presented in this chapter has contributed to the understanding and the reduction of systematics of the angular resolution of the SD and the FD. Furthermore, part of this work is subject to publication in the context of a full author list paper that is currently being prepared for submission to Astroparticle Physics [Abr11a].

The angular reconstruction of the SD was discussed in section 3.2.3. Here, focus is put on the estimation of the AR of the SD in section 4.1. Two approaches are applied: Firstly, the AR is computed making use of the angular uncertainties estimated by the SD reconstruction. Secondly, the AR is derived by comparing the arrival direction measured with the SD to the one reconstructed by the FD. For this purpose, only a subset of events can be used, namely the Golden Hybrid ones which have been reconstructed independently by the SD and the FD.

Section 4.2 of this chapter is dedicated to the investigation of systematic distortions of the directional precision of the SD (and FD) measurements. Again, use is made of the Golden Hybrid subset of events to estimate systematic effects of the angular reconstruction.[1] The differences of the two reconstructed arrival directions are studied in the dimensions of the respective detector-specific coordinate system.

Data, Simulations and Cuts

Many of the analyses presented here, especially the study of systematic uncertainties in section 4.2 rely on Golden Hybrid events, i.e. showers that have been directionally reconstructed by both the SD and the FD. This is why for the sake of consistency in fact all analyses related to AR studies which are shown here have been performed on the Golden Hybrid data

[1] It is worth remembering that doing so, advantage is taken of the hybrid detection principle at the Pierre Auger Observatory: The possibility to cross-check one reconstruction with the other is a very remarkable feature of the experiment.

set. Note that in this context, FD reconstruction always means hybrid reconstruction: The information of the SD station with the largest signal (the *hottest station*) is adjoined to the information of the FD to produce the FD or equivalently hybrid reconstruction. Correspondingly, physical quantities obtained with the hybrid reconstruction will be denoted by *HY*.

The set of real Golden Hybrid events comprises data taken from January 2004 until December 2010. The reconstruction has been performed with $\overline{\text{Off}}\underline{\text{line}}$ `v2r6p4-AsterixObelix`. The simulation of air showers has been performed with CORSIKA making use of QGSJetII and Fluka. For these shower simulations, detector simulation and reconstruction have been performed with $\overline{\text{Off}}\underline{\text{line}}$ `2.2p4-mojo-svn trunk` (thanks to Ioana Mariş for making available the resulting event sets [Mar08]).

To obtain a proper event selection, the cuts agreed on within the angular resolution working group are applied, see table 4.1. The application of basic cuts is intended to remove events that do not fulfil the most fundamental requirements for a reliable reconstruction: Each event is required to have at least one triggered station to allow for FD hybrid detection mode, $N_{stat} > 0$. Note that in fact there is an implicit trigger allowing only events with at least 3 stations since the SD reconstruction is required to provide directional information. The axis of the shower measured with FD must have a non-zero shower impact parameter R_p (R_p is the distance of the shower axis to the FD eye), and a non-zero angle of inclination of the shower axis within the shower detector plane χ_0 (an illustration of the shower detector plane (SDP) and the angle definitions is shown in figure 3.3). Concerning the SD shower, in this study only showers with zenith angles below 60 degrees are taken into account (see figure 3.9 for the (SD) angle definitions, note that these follow the definitions of local coordinates in appendix A).

Geometrical cuts are applied in order to remove showers that were not reconstructed reasonably well: Events are only used in case the fitting procedure of the shower axis produces small reduced χ^2-values considering both the purely geometric fit of the SDP from the triggered camera pixel positions and the time fit from the trigger times of these pixels. Furthermore, the SD station used in the FD hybrid reconstruction (typically the hottest station, i.e. the station with largest signal) is required to be less than 2000 m distant to the shower axis and the time offset of SD and FD involved in the detection must be smaller than 200 ns.

In the end, one quality cut is applied: The angular track length (the trace of the triggered pixels in the FD eye camera) is required to be larger than 15° in order to use only showers with a large lever arm considering both the position and time information of the camera pixels.

4.1 Angular Resolution

The angular resolution (AR) of the surface detector of the Pierre Auger Observatory is typically obtained in two different ways [Bon09]. On the one hand it can be computed on an event by event basis from the angular uncertainty estimates of the directional reconstruction. Here, the precise knowledge of the timing resolution of the surface detector stations and an adequate shower front model is necessary. On the other hand, the AR can be obtained from the comparison of the reconstructed shower arrival directions by the FD and the SD measurement. For the latter method the AR of the FD reconstruction needs to be known. It can be reliably obtained from simulations of FD hybrid shower measurements.

Table 4.1: Cuts applied to both real and simulated events for angular resolution studies. These cuts are the 'standard' cuts agreed on within the angular resolution working group. Note that unfortunately, information on the angular track length was not provided in the simulation files available. However, all results concerning the data have been reproduced ignoring the quality cut essentially yielding the same results. Thus, results obtained from data and from simulations can be compared with each other.

Category	*Name*	*Value*	N_{dat}	N_{sim}
No cuts			110942	52259
Basic cuts	N_{stat}	> 0	110917	52259
	R_p/m	> 0	104369	49220
	$\chi_0/^\circ$	> 0	104317	49212
	$\theta/^\circ$	< 60	97173	49212
Geometrical cuts	SDP fit χ^2/Ndf	< 7	96057	49142
	Time fit χ^2/Ndf	< 8	94679	48639
	Hottest station to axis distance $/m$	< 2000	94507	48628
	SD-FD Time Offset $/ns$	< 200	94442	48620
Good quality cut	Angular Track Length $/^\circ$	> 15	71488	not available

It is natural to investigate the behaviour of the AR depending on several shower parameters. The dependence on the zenith angle, the energy and the number of stations (also *multiplicity*) involved in the reconstruction is studied in the course of this work.

4.1.1 AR from Angular Reconstruction Uncertainty Estimates

Technically, for the first case Gaussian distributions of the reconstructed angles θ and ϕ around the true values are assumed. For the sake of a simpler notation the true values are assumed to be zero in this section. Note that at these small angular scales, i.e. small values of the variances $\sigma^2(\theta)$ and $\sin^2(\theta)\sigma^2(\phi)$ of the angular distributions, the deviation from a Gaussian due to the curvature is neglected. The variance of the angular distance $\eta = (\theta^2 + \sin^2(\theta)\phi^2)/2$ of the measured direction compared to the true one can be obtained as

$$\sigma_\eta^2 = \frac{1}{2}(\sigma^2(\theta) + \sin^2(\theta)\sigma^2(\phi)), \tag{4.1}$$

with $\sigma^2(\theta) \approx \sin^2(\theta)\sigma^2(\phi)$. In this scenario, η follows a Rayleigh probability density function:

$$Rayleigh_{p.d.f.}(\eta) = \frac{\eta^2}{\sigma^2(\eta)} exp\left(-\frac{\eta^2}{2\sigma^2(\eta)}\right). \tag{4.2}$$

The AR is defined such that it contains 68 % of the shower directions diced from a 2D Gaussian around the true direction, which can be identified equivalently as the 68 % quantile of values of η diced from a Rayleigh, see figure 4.1. Assuming $\sigma^2(\theta) = \sin^2(\theta)\sigma^2(\phi) = 1$, σ_η needs to be scaled with a factor of ~ 1.5 to make it contain 68 % of the shower directions. Thus, the uncertainties of the reconstructed angles are combined in the following way to yield the AR:

$$AR_{SD} = 1.5 \cdot \sqrt{\frac{1}{2}(\sigma^2(\theta) + \sin^2(\theta)\sigma^2(\phi))}. \tag{4.3}$$

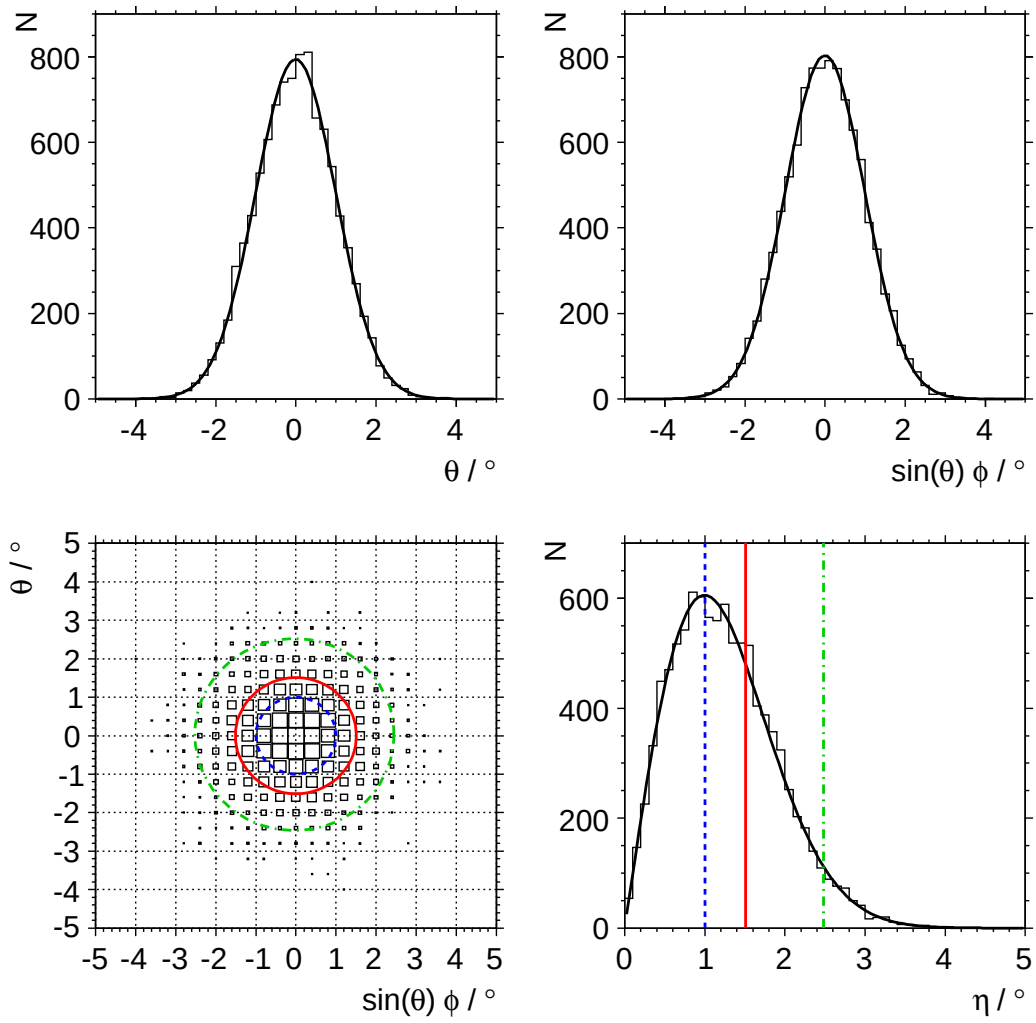

Figure 4.1: The upper plots show distributions of the horizontal angles θ and $\sin(\theta)\phi$ diced from Gaussians of mean $\mu = 0$ and variance $\sigma^2 = 1$. The two-dimensional Gaussian obtained from these independent processes is plotted on the lower left. The corresponding radial distribution of the angular distance η is presented on the lower right. The circles on the left and the lines on the right indicate the 39 % (1σ), 68 % (1.5σ) and the 95 % (2.5σ) quantiles (drawn in blue/dashed, red/solid and green/dotted-dashed) of the 2D Gaussian and the η distribution, respectively. The latter has been fit by a Rayleigh probability density function. The AR is defined as the 68 % quantile of the distribution of η which leads to a factor of ~ 1.5 with respect to the variance of the 1D Gaussians.

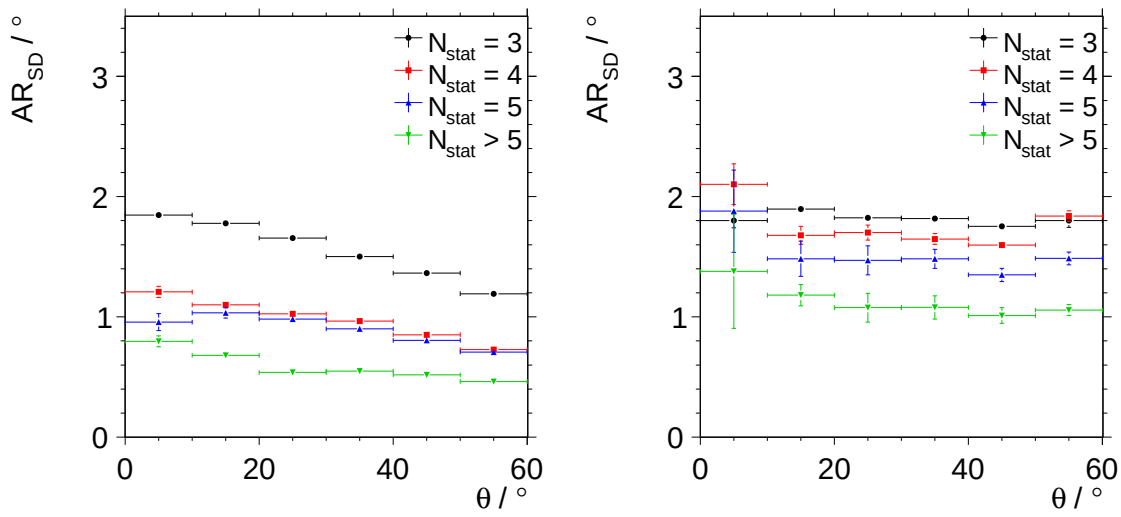

Figure 4.2: Angular resolution of the surface detector depending on the zenith angle computed with two different methods: (a) from the angular uncertainties of the reconstruction according to equation 4.3 and (b) from the comparison to the FD hybrid reference direction according to equation 4.4. The dependence on the zenith angle θ is given for various station multiplicities indicated by the value of N_{stat} in the legend.

It is worth emphasizing that this method is sensitive to statistical uncertainties of the time measurement in the stations as well as to the goodness of the model both of the lateral shape of the shower front and of the shape of the longitudinal particle distribution within the shower front. However, it may be conceivable that there are other systematics such as for example an asymmetry of the particle distribution within the shower front which the method is insensitive to; section 4.2 about systematics will shed light on this issue.

The results for AR_{SD} from the timing resolution estimates of the reconstruction according to equation 4.3 are shown in figure 4.2(a) and 4.3 (black circles). The angular resolution is plotted against the zenith angle and against energy, for the former use is made of the number of stations used in the reconstruction as a parameter of the number of samples taken from the shower front. The AR of the SD is always better than 1.9° and reaches down to 0.5°. It is worse for low station multiplicities and small zenith angles while being better for high multiplicities and large zenith angles. Both observations can be understood applying the following reasoning: Low multiplicity corresponds to less information about the shower front which can be expected to provide less certain angular results. Furthermore, small zenith angles correspond to small lever arms with respect to the arrival times of the first particles of the shower front measured in the stations. Note that for an exactly vertical shower the difference of the arrival times in the hit stations can be of the order of their timing resolution. This leads to comparably large uncertainties of the orientation of the shower front and thus, of the reconstructed direction.

4.1.2 AR from Comparison to Hybrid Direction

For the second approach to obtain the AR of the SD the arrival direction of the shower measured with the SD is compared to the one reconstructed in FD hybrid mode. Again, η is

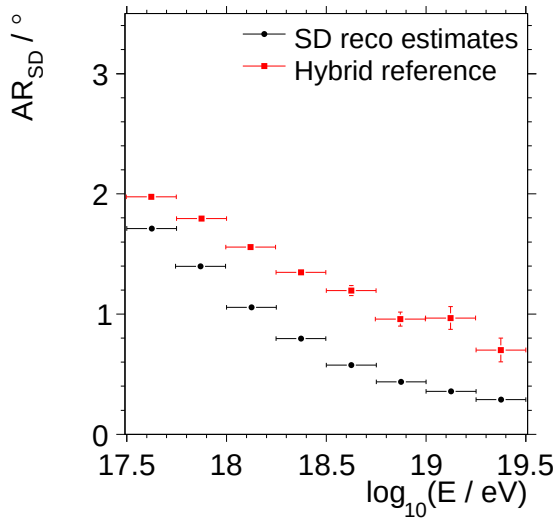

Figure 4.3: Angular resolution of the surface detector depending on the energy computed with two different methods: from the angular uncertainties of the reconstruction according to equation 4.3 (black circles) and from the comparison to the FD hybrid reference direction according to equation 4.4 (red squares).

the angular distance, in this case the distance between the two independently reconstructed directions; η_{68} is the 68 % quantile of the cumulative distribution of η. In order to derive the AR of the SD from η_{68}, the angular resolution of the FD hybrid measurement, AR_{HY}, has to be subtracted:

$$AR_{SD} = \sqrt{\eta_{68}^2 - AR_{HY}^2}. \tag{4.4}$$

Note that AR_{HY} has to be derived from simulations [Bon09]. It denotes the 68 % quantile of the cumulative distribution of the angular distance between reconstructed and true directions of these simulations. In figure 4.4, the results for AR_{HY} from FD hybrid simulations are presented. Figures 4.2(b) and 4.3 (red squares) show our results for AR_{SD} as computed from the FD hybrid reference according to equation 4.4.

The values of AR_{SD} obtained using the FD hybrid direction as a reference are larger by up to $\sim 0.5^\circ$ than those computed with the method that relies on the uncertainty estimates of the reconstruction. There are essentially two categories of possible reasons for this observation: Firstly, the uncertainty estimates of the reconstruction might be too small. However, this has been largely excluded in [Bon08]: It was shown that the lateral shape of the shower front is in fact adequately described by simple, curved models and that the longitudinal distribution of particles within the shower front follows a Poisson function. This proof has been achieved with goodness of fit tests. Secondly, there may be systematic biases of the angular reconstruction, be it from the SD or the FD part. This category of systematic distortions of the angular reconstruction is studied in the following section.

4.2 Angular Reconstruction Systematics

In the previous section the angular resolution was computed by two different methods, both being sensitive to the *statistical* uncertainty and different potential origins of *systematic* uncertainties of the angular reconstruction. The results given in figure 4.3 differ by up to

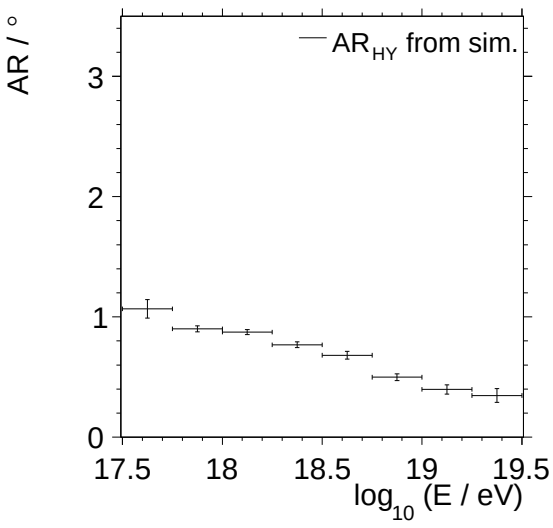

Figure 4.4: Angular resolution of the FD hybrid reconstruction as obtained from simulations. It is defined as the 68 % quantile of the cumulative distribution of the angular distance between the measured and the true directions.

$\sim 0.5^\circ$. In this section a method to study purely *systematic* biases in the measurement of arrival directions is presented.

In [Kue08] physical motivations and their implications concerning the impact of the application of idealising assumptions w.r.t. the propagation of the fluorescence light in the course of the FD reconstruction have been thoroughly investigated and discussed. However, this is not the scope of the present work. Instead, an approach that covers all possible sources of systematic deviations regardless of its physical origin is presented. The concept of the analysis is introduced in subsection 4.2.1. Some reasoning is provided how the systematic uncertainties observed may be assigned to the detector they are supposed to have been caused by. In subsection 4.2.2 the analysis is applied to data. After the presentation of the results and their implications some remarks are made related to work in progress in the field of directional reconstruction systematics in the angular resolution working group. Finally, conclusions are derived and presented.

4.2.1 Concept of the Analysis

In this analysis again use is made of the Golden Hybrid data set. Golden Hybrid air shower events have been detected and reconstructed by both the SD and the FD. Since the FD hybrid reconstruction only makes use of the signal time information of one single triggered SD station (the hottest station), the two reconstructions are considered independent[2]. Another study investigating the issue of systematics from the real data side including the systematics of the core position reconstruction can be found in [Cre08, Cre09].

In order to find a systematic shift in one reconstruction, both reconstructed directions will be compared within the corresponding detector-specific coordinate systems. The basic concept relies on the idea that systematics e.g. of the FD hybrid reconstruction are supposed to be uncovered at best when transforming the SD direction into the coordinate system of the

[2] in principle, this remains to be shown, but will not be covered in this work.

FD eye that has seen the same shower and comparing the resulting coordinates. Apparently, the fundamental assumption and necessary condition to allow attributing any systematic uncertainty to the FD detector is that the SD itself should not know a preferred direction within the eye-specific coordinate system of the FD. This basically means that the SD direction is regarded as the true one when investigating FD coordinates in the FD coordinate system. Therefore, the difference between the values of relevant coordinates reconstructed with the FD and the SD, $x_{FD} - x_{SD}$, is plotted against the value reconstructed by the SD x_{SD}. Vice versa, the same considerations apply and $x_{SD} - x_{FD}$ is plotted against x_{FD} in case the SD systematics are investigated in the SD coordinate system.

4.2.2 Systematics from Data

The angular distance of the directions of incoming air showers obtained from SD and FD reconstructions is investigated. In order to reveal systematic errors of each particular reconstruction, the directions obtained from the respectively other reconstruction are transformed into the detector-specific coordinate system of the former. The directions are compared by calculating the difference in each of the relevant coordinates in the respective detector-specific coordinate system.

SD Reconstruction Systematics

According to figure 3.9, SD specific coordinates are defined in relation to the ground plane of the array, i.e. a shower core centred horizontal plane. Note that this can be considered the "natural" reference frame of the SD, since all detector stations relevant for the reconstruction of an individual air shower are located on this plane, essentially. Considering the coordinate systems available in $\overline{\text{Off}}\underline{\text{line}}$ the *ePampaAmarilla* frame of reference is used. The direction of the shower is given by its zenith θ and azimuth ϕ angle. The zenith angle ranges from 0° (vertical) to 90° (horizontal) but is effectively cut at 60° according to table 4.1. The azimuth angle starts with 0° in eastern direction and is counted anticlockwise.

The reconstructed directions of SD and FD in this SD specific coordinate system shall be compared. Figure 4.5 shows the difference of the zenith angles obtained from SD and FD against the latter. Note that the results are not the same for all FD eyes, which may be an indication that systematic distortions by at least some of the FD eyes are involved. Small differences mostly in the extreme ranges of the zenith angle are observed; the SD reconstruction slightly underestimates the zenith angle at large inclination values especially for Los Leones and Los Morados. This behaviour has already been reported in [Cre08]: It is presumably caused by the fact that in the early part of the shower larger signals are found than in the late part. It was shown in [Cre08] that only low multiplicity events suffer this slight shift in inclination due to the SD reconstruction. This shift originates in the fact that the reconstructions of core position and direction are correlated. The early/late asymmetry in the signals measured at ground level leads to a bias of the reconstruction of the position of the shower core, which is obtained as the barycentre of the signals. This in turn causes a systematic tilt in the reconstruction of the direction of the shower. Since the signal asymmetry grows with the zenith angle of the showers, the directional bias also is supposed to be largest for the last bin, $55^\circ < \theta \leq 60^\circ$. However, the largest difference is less than 0.2°. Thus, it is well below the corresponding value of AR which is of the order of $\text{AR}_{\text{SD}} = 1.5^\circ$ for low multiplicities

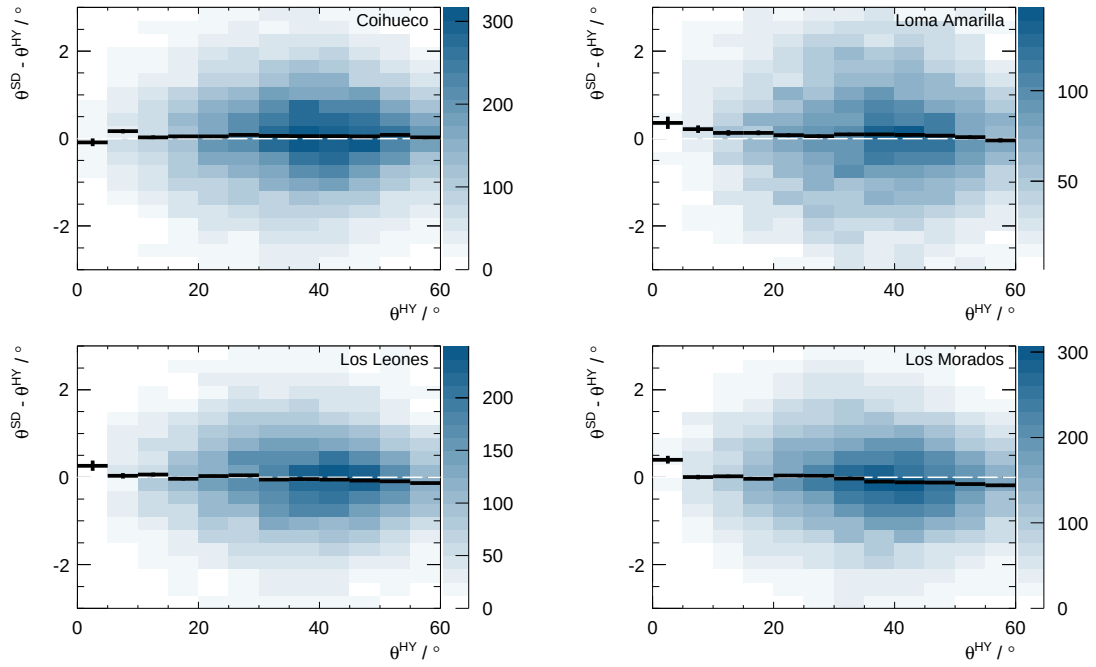

Figure 4.5: The zenith angle reconstructed with the FD (θ^{HY}) is subtracted from the zenith obtained with the SD (θ^{SD}) and plot the result against the former in a 2D histogram. The zenith angle is binned in 12 bins, the y-axis takes 20 bins; for each of these 12 slices the mean value and its error are computed and drawn in black. The white dashed line indicates zero and thus, the expectation of where to find the mean value in the absence of any systematic. This plot concept will be used throughout this section.

(see also figure 4.2(b).

The same analysis is applied to the azimuth angle (figure 4.6), observing a small systematic behaviour that appears to be slightly periodic with a maximum amplitude of $\sim 0.5°$. Apparently, the phase of this periodic behaviour depends on the FD eye involved in the reconstruction. This can be explained with the presence of a systematic distortion due to the FD reconstruction. Since the fields of view of the eyes correspond to different ranges of azimuth angle, each individual FD eye has a preferred direction in azimuth and therefore might translate an FD-caused systematic into the SD specific coordinate system.

This observation can be studied more deeply: In figure 4.7 the azimuth angle difference is plotted against the difference of azimuth angle of the shower ϕ^{HY} and the eye-to-core azimuth angle ϕ^{EC}. The definition of the latter angle is visualised in figure 4.8. Choosing this azimuthal difference for the abscissa should align the phases of the plots in figure 4.6 in case the periodic behaviour originates in the FD reconstruction.

Figure 4.7 indeed shows that the phases are aligned for all eyes when correcting for the azimuthal position of the shower core relative to the respective FD eye: A sine-like behaviour of the azimuthal systematic is clearly visible with a phase of $\sim 0°$ in all plots. This leads to the conclusion that a dominant fraction of the observed systematic in the azimuth angle originates in the FD hybrid reconstruction.

Note that the investigations of systematic errors of both the zenith and the azimuth angle have been performed in much more detail than is presented here. The dependency of the systematics on various quantities has been studied. No observations more prominent than

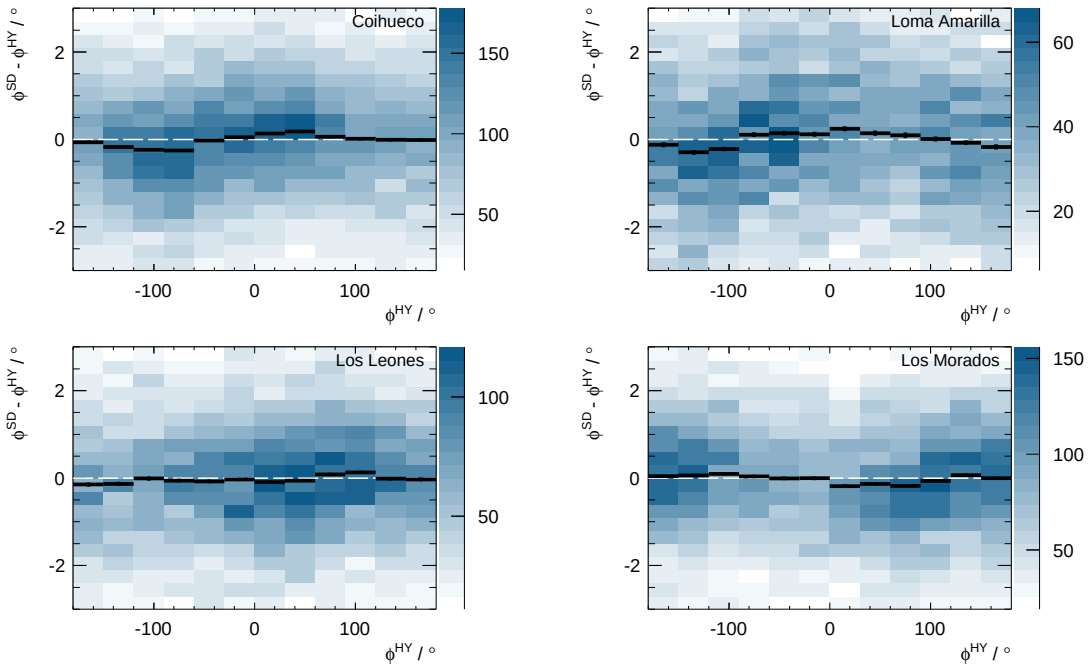

Figure 4.6: The plot shows the difference of the reconstructed azimuth angles $\phi^{SD} - \phi^{HY}$ against the azimuth ϕ^{HY}. The plot concept is identical to what is described in figure 4.5.

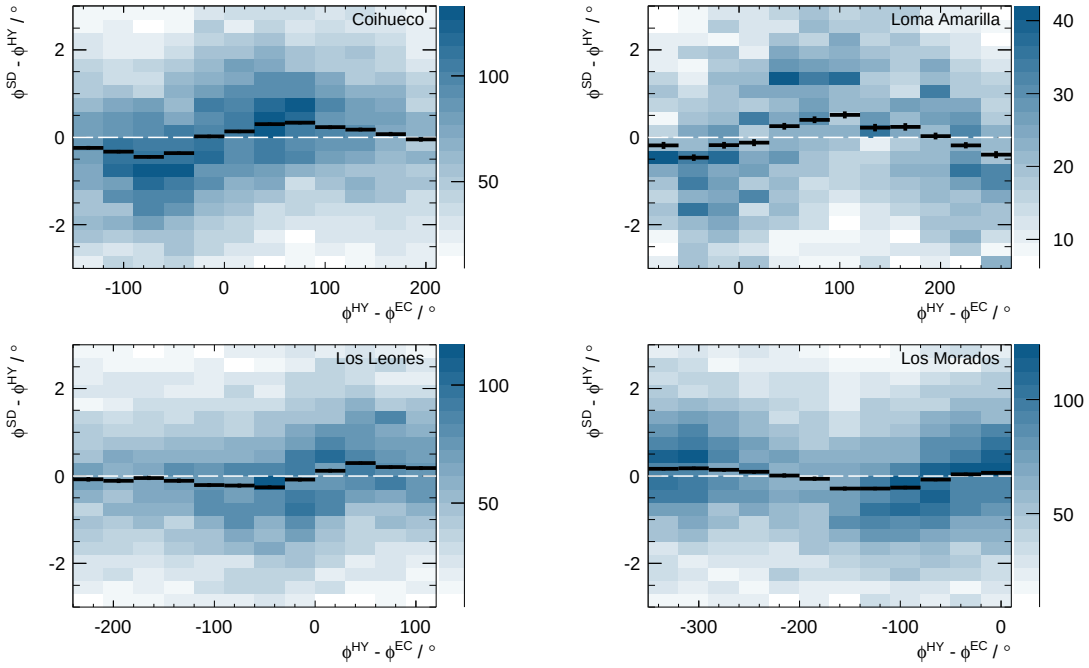

Figure 4.7: The plot shows the difference of the reconstructed azimuth angles $\phi^{SD} - \phi^{HY}$ against the eye-to-core azimuth ϕ^{HY}_{EC}. The plot concept is identical to what is described in figure 4.5.

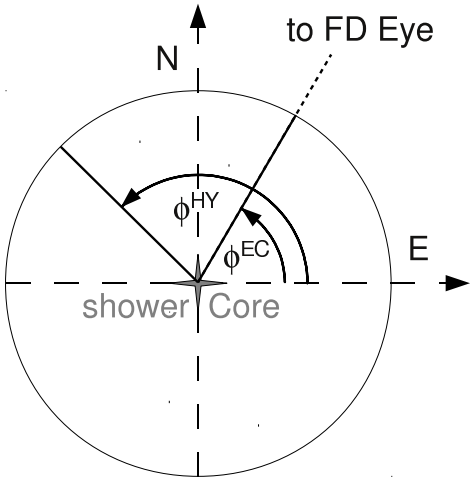

Figure 4.8: The figure visualizes the definition of the eye-to-core azimuth ϕ^{EC}. With the reconstructed angle ϕ^{HY} it is needed to align the phases measured in the azimuthal systematics in figure 4.6, see text for details.

those presented in this work have been made. The same is valid for the next subsection, where systematics originating in the FD are investigated.

FD Hybrid Reconstruction Systematics

FD-specific coordinates are defined in relation to the so-called Shower Detector Plane (SDP), i.e. the plane spanned by the direction of the shower and the position of the FD eye involved in the detection. Given the shower core and the eye position, the direction of the shower is given by the inclination θ_{SDP} of the SDP and the inclination χ_0 of the shower within the SDP. Both angles range from 0° to 180°, θ_{SDP} starts from zero on the right from the point of view of the eye, while χ_0 starts from zero for showers pointing to the eye (see figure 3.3 for visualisation). Note that due to the cut on the zenith angle (table 4.1), the range of θ_{SDP} and χ_0 is limited to 30° to 150°. The reconstructed directions of SD and FD in the FD eye specific coordinate system are compared. Note that now investigating FD systematics the SD reconstructed value will be subtracted from the FD one and the result is plotted against the former.

Figure 4.9 shows the difference of the FD and SD reconstructions of the inclination angle θ_{SDP} of the SDP. A slight shift can be observed, in such a way that the FD reconstruction on average underestimates the value of θ_{SDP} by $\sim 0.1^\circ$. The worst bin slices in terms of the biggest difference of $\sim 0.4^\circ$ can be found in the two upper plots for Coihueco and Loma Amarilla. In order to quantify the size of the systematic deviation it is possible to apply a flat fit and interpret the fit parameter. Restricting the fit to entries between $60^\circ < \theta_{SDP} \leq 120^\circ$ to make it cover the most populated bins in the histograms fit parameters ranging from 0.07° to 0.11° are obtained. All results are small and compatible with zero within their statistical uncertainties. The systematic differences in the reconstructions are within the AR of both detectors as presented in figures 4.2, 4.3 and 4.4.

When applying the same analysis to χ_0, i.e. the inclination of the shower within the SDP,

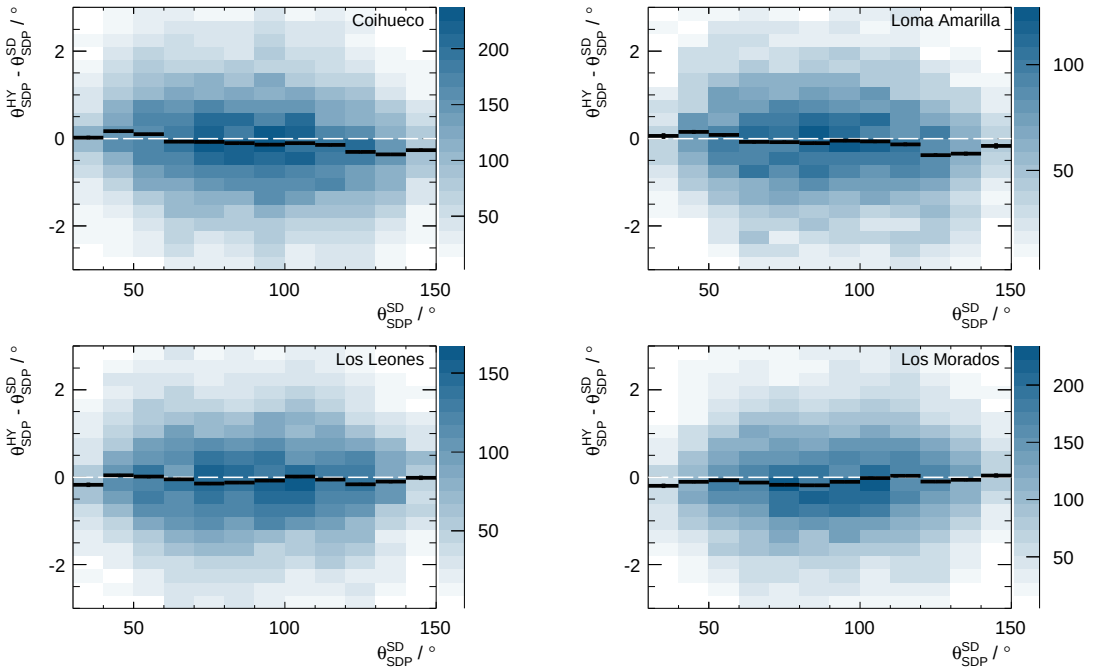

Figure 4.9: The plot shows the difference of the reconstructed angles of inclination of the SDP $\theta^{HY}_{SDP} - \theta^{SD}_{SDP}$ against θ^{SD}_{SDP}. The plot concept is identical to what is described in figure 4.5.

similar differences are observed (see figure 4.10). FD systematically underestimates χ_0 by up to 0.5°, which only occurs in a few bins at Loma Amarilla. Again restricting the analysis to entries between $60^\circ < \theta_{SDP} \leq 120^\circ$ the same flat fit procedure is applied as was done for θ_{SDP} and the fit parameter are interpreted. Values of about $\sim 0.05^\circ$ for Los Leones and Los Morados are obtained and $\sim 0.25^\circ$ for Loma Amarilla and Coihueco. While the latter two yield roughly constant differences at all angles, Los Leones and Los Morados show a slightly curved dependence on χ_0. However, these small offsets can be considered negligible with respect to the angular resolution values of $\sim 0.5^\circ$ at best, see section 4.1.

4.2.3 Remarks and Outlook

At the time this study was performed and made available to the angular resolution working group and the collaboration, the systematics of the angular reconstruction have been larger [Gri09]. It is worth noting that the concept of the analysis and the results have been taken serious. In fact, with Jose A. Bellido, the analysis has been used to tune a parameter of the hybrid reconstruction in order to make it match the SD result. It was possible to identify the cause of a major portion of the systematic as offsets in the timing of the different hardware systems used by the SD and the FD, respectively. Different absolute time measurements are obtained from the two detectors resulting in a systematic shift of the shower core position reconstruction which in turn affects the angular reconstruction, especially the χ_0 angle. The tuning in fact allowed to diminish the systematics found in the analysis of χ_0 by up to 0.5°, see figure 4.11 as an example.

In the same study [Gri09] Golden Hybrid simulations have been investigated. It has been shown that the results from applying the same analysis of angular reconstruction systematics to simulations does provide compatible results only in case of the zenith angle analysis. For

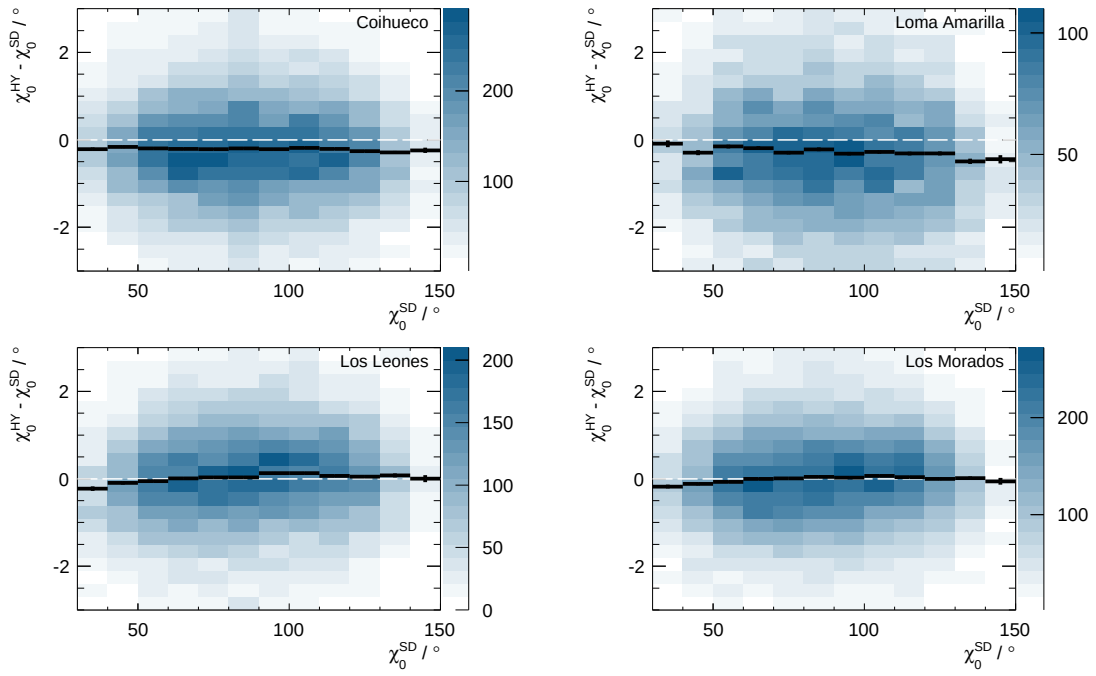

Figure 4.10: The plot shows the difference of the reconstructed angles of inclination of the shower within the SDP $\chi_0^{HY} - \chi_0^{SD}$ against χ_0^{SD}. The plot concept is identical to what is described in figure 4.5.

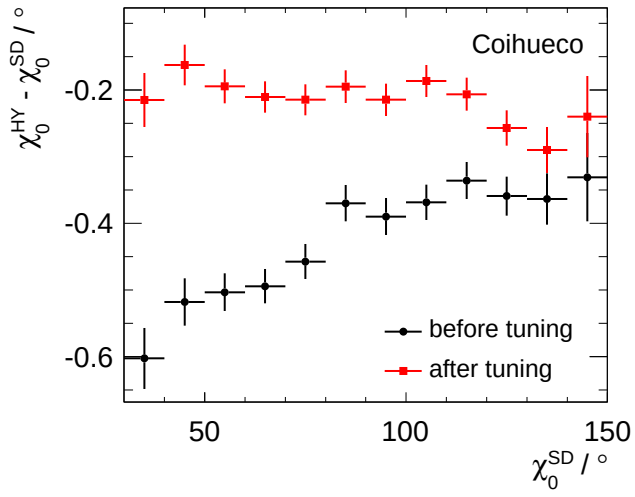

Figure 4.11: The plot shows the difference of the reconstructed angles of inclination of the shower within the SDP $\chi_0^{HY} - \chi_0^{SD}$ against χ_0^{SD}. It shows a comparison of the systematics measured at Coihueco before (black points) and after (red squares) the tuning of FD reconstruction parameters.

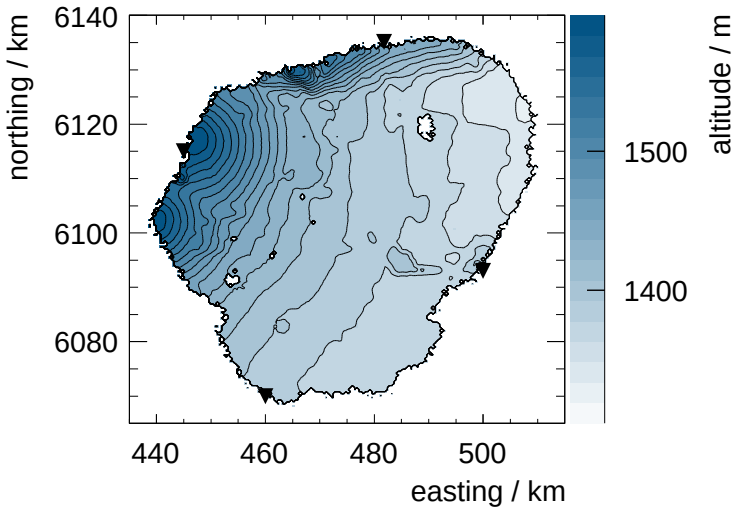

Figure 4.12: Altitude distribution of the SD array plotted in a 2D histogram in UTM coordinates [Abr05]. Every bin contains the average altitude of shower cores measured within its range. The black triangles indicate the positions of the FD buildings with the lowermost Los Leones and then anticlockwise Los Morados, Loma Amarilla and Coihueco. Open areas in the plot correspond to small spaces in the field which are not instrumented, compare to figure 3.1.

all other angles the results have been better for the simulations compared to the data. The origin of this discrepancy is still subject to further investigation in the *angular resolution* and the *data vs. simulations* working groups within the Pierre Auger Collaboration.

It has been suggested [Bel09] that there is one property of the Pierre Auger Observatory site which relates the surface and the fluorescence detectors to each other: The array is not completely plain in terms of altitude a.s.l.. On the one hand it is characterised by an overall inclination describing an increase of altitude towards the direction of the Andes mountains in the west-north-west. On the other hand, the FD buildings have been chosen to be positioned on slightly elevated points in order to guarantee optimum data transmission conditions amongst other criteria. Both characteristics are visualised in figure 4.12. The implication of the latter circumstance is that the SD actually is not completely unaware of the position of at least some of the FD buildings. The stations of the SD are located on increasing altitudes towards the FD eyes. Especially the Coihueco building on the upper left in the corresponding figure displays this fact rather well.

The possible impact on angular resolution issues can be estimated by quantifying the inclination of the array. It can be read from the plot that there is an increase of for example ~ 200 m (read from the colour axis) over a distance of ~ 30 km around the Coihueco building resulting in a slope of $0.67\,\% \mathrel{\hat{=}} 0.4^\circ$. Note that this crude estimate roughly matches the angular difference measured in the χ_0 analysis for Coihueco (and Loma Amarilla), figure 4.10. The intuitively first approach to identify the source of this difference would probably be to search its origin in wrong altitude assignments of the SD stations. Efforts have been taken to investigate the altitude assignments of SD stations via GPS measurements and contingently apply corrections. However, these ongoing studies have not identified wrong altitude assignments nor led to any improvement of the results of the χ_0 analysis, yet [Bel10].

Conclusions

In this chapter the angular resolution of the surface detector was analysed. The computation of the AR based on the estimates of the directional reconstruction of the SD has been described. It has been shown to be dependent on both zenith angle and energy and multiplicity ranging from $\sim 2^\circ$ for the worst combination (small values of zenith, energy and multiplicity) down to $\sim 0.5^\circ$ at highest energies. These observations have been qualitatively discussed and understood. Secondly, the AR of the SD has been derived from comparing the directions reconstructed with SD to the ones given by the FD. For this purpose, the AR of the FD events has been computed from simulations. This second method has been shown to produce an AR of the SD that is larger (than with the former method) over the full range of energy and zenith angle by up to $\sim 0.5^\circ$. This observation can be understood in the presence of systematic deviations in the directional reconstruction by either of the detectors. These would not show up in the former but in the latter method.

Systematic uncertainties in the reconstruction of arrival directions of air showers have been thoroughly investigated making use of Golden Hybrid events. The reconstructed directions of one detector have been transformed into the natural coordinate system of the other detector and have been used as the respective reference. The basic assumption behind this concept is, that the two detector systems can be considered independent and do not "know" the position / behaviour / directional preferences of each other. The expectation of finding a systematic uncertainty in the directional reconstruction of up to $\sim 0.5^\circ$ has been confirmed. According to the concept of the analysis, most of the systematic deviations have been attributed to being caused by the FD: They either occurred in the FD specific coordinate system (especially the χ_0 angle) or could be assigned to the FD due to showing a behaviour that is sensitive to the (position of the) FD eye involved in the reconstruction (the ϕ angle).

It has been shown that the precision of the directional reconstruction by the surface detector is $AR_{SD} \lesssim 2^\circ$ for all showers and better than $\sim 1^\circ$ at energies beyond 10^{19} eV. At the energy range of interest to make large scale anisotropy studies feasible, i.e. above full detection efficiency of the SD, $E > 10^{18.5}$ eV, the angular resolution amounts to 1.2° and less. Therefore, the distribution of arrival directions measured with the SD is well suited to perform anisotropy studies at all angular scales down to a few 1°.

Chapter 5

Local Effects Inducing False Anisotropy

In this chapter the effect of a varying area of the SD on the exposure of the SD and of changing atmospheric conditions over time will be discussed. A qualitative introduction into the topic can also be found in [Gri11]. Furthermore, the effect of the geomagnetic field on the energy measurement via the energy estimator of the SD will be presented. Each of these effects is capable of introducing systematic deviations into a potentially isotropic map of arrival directions and thus, must be carefully accounted for when performing anisotropy studies.

5.1 Varying Area of the SD over Time

The definition of the area of the surface detector was introduced in 3.2.2. The size of the area of the SD is determined by the number N_{cell} of elementary cells with one central station and its six closest neighbours active for the strict T5 condition (five of them for the mild T5). The activity, i.e. the availability of the station for data taking, is monitored by means of the local T2 triggers of every individual station. Every second, the positions of active stations are recorded. The data accumulated this way allows to compute the number of elementary cells at a given GPS second. In turn, the sum of these cell-seconds in a given time interval of n seconds is directly connected to the total exposure of the SD, see equation 3.3. Secondly, the identification of the GPS second with the part of the sky covered by the field of view of the SD at the corresponding time allows to compute the effective relative exposure in equatorial coordinates. In this section realistic origins of variations of the area of the SD will be discussed. Then the changing of the SD area over time will be visualised. The connection of the variation of the area over time to the variation of the relative exposure will be demonstrated by means of an example. The amount of false anisotropy induced when not accounting for the varying area of the SD will be estimated. Finally, a technique will be presented that accounts for the changing exposure. It should be applied to make anisotropy studies insensitive to variations of the area of the SD.

There are essentially three dominant origins of time-like variations of the size of the area of the SD: Firstly, single and multiple detector station or CDAS downtimes cause a random variation of the SD area over time. These downtimes may occur due to e.g. power outages and maintenance work. In case the CDAS is affected, data loss occurs and the according time intervals are tagged as bad periods which should not be used in anisotropy or exposure studies [Bon06]. Secondly, the overall number of stations has continuously increased in the

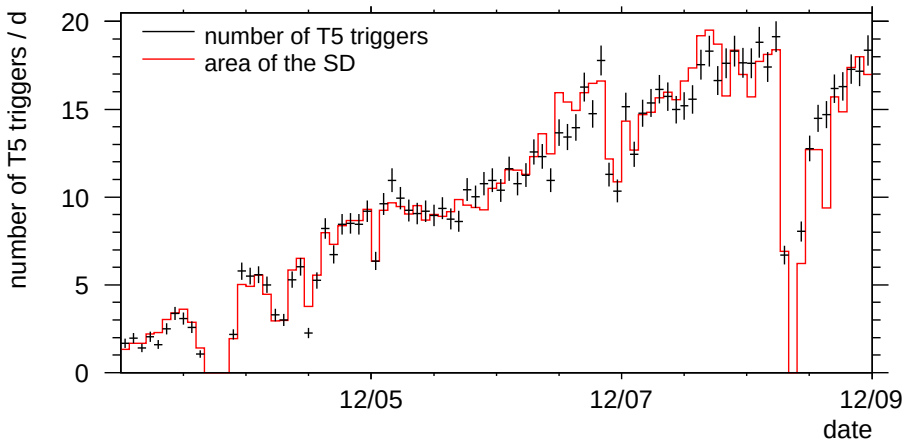

Figure 5.1: SD area growth and T5 trigger rate: The plot shows the SD area (red) and the T5 trigger rate (black) versus time after the subtraction of bad periods. While growing continuously during the construction phase starting in 2004, the area reaches its maximum corresponding to a T5 rate of ~ 18 triggers per day in the middle of 2007. The SD area has been scaled to match the numerical range of the T5 trigger rate, both agree well as expected.

construction phase from 2004 to mid-2007; this obviously leads to a systematically growing detector in that phase. The corresponding growth of the SD area is indicated in figure 5.1 alongside with the (compatible) growth of the T5 trigger rate. Thirdly, for optimization purposes single stations are still being moved. For example, stations are moved from the edge of the grid to fill up holes within the array which increases the sensitive area by reducing the length of the borderline of the compact grid of the SD.

The variation over time consequently leads to a variation over the viewing direction of the detector since time and direction are directly correlated due to the Earth's rotation. More precisely, the time is connected to right ascension, the equatorial longitude. A change of the area of the SD corresponds to a change of the absolute scale of the instantaneous acceptance cone of the SD which was displayed earlier in figure 3.8(a). Rotating this cone of varying scale about the Earth's axis during one sidereal day leads to a relative exposure $\omega_\alpha(\delta,\alpha)$ varying over right ascension α. This effect is displayed in figure 5.2 for the simple case of a sinusoidal modulation of the acceptance with the period of one sidereal day. The amplitude has been arbitrarily chosen to be 0.2 and the phase indicating the maximum acceptance over time is $\phi = 270°$. To compute the impact on the distribution of the individual equatorial coordinate δ and α the changed exposure $\omega_\alpha(\delta,\alpha)$ must be integrated over α and δ, respectively; technically, this is achieved by the projection of the sky map histogram in figure 5.2(b) along the respective axis. The figure shows that the variation of the area of the SD is directly promoted to a cosine modulation of the right ascension distribution of the same amplitude and phase. However, there is no impact of the variation of the area of the SD on the declination distribution.

In order to quantify the effect of the varying area of the SD on anisotropy studies use is made of another example. The information of the GPS second has to be transformed to equatorial coordinates, effectively. To be more precise, the cone representing the instantaneous field of view of the SD weighted with the acceptance of the detector (see figure 3.8(a)) can

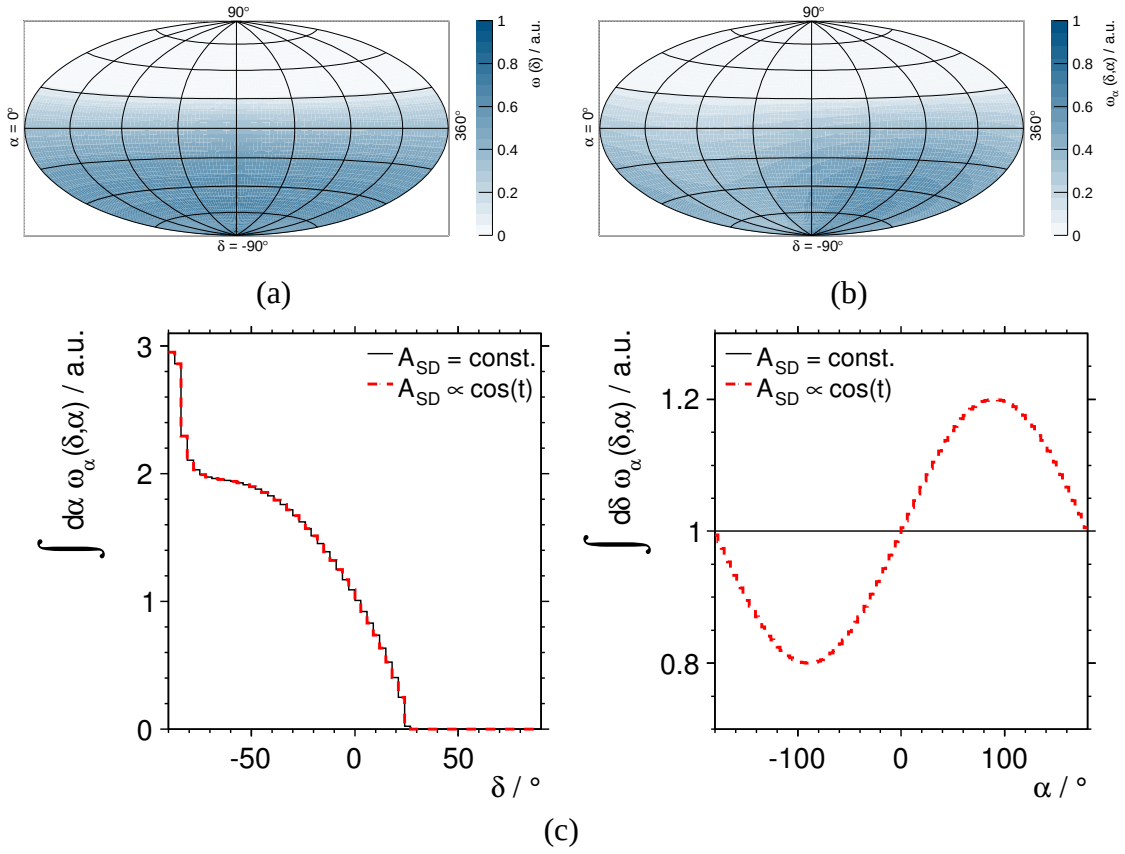

Figure 5.2: A cosine variation of the SD area of amplitude 0.2 and phase $\phi = 270^\circ$ within the period of one sidereal day of data taking is directly promoted to a cosine modulation of the right ascension distribution with identical parameters, see text for details. The top left plot shows the relative exposure $\omega(\delta)$ in equatorial coordinates in absence of a modulation of the area of the SD. The top right plot displays the changed exposure function $\omega_\alpha(\delta, \alpha)$ in the presence of the described cosine modulation of the area; it now shows a dependence on α. The bottom plots compare the two scenarios without (black solid) and with (red dashed) a modulation of the SD area in the declination and right ascension.

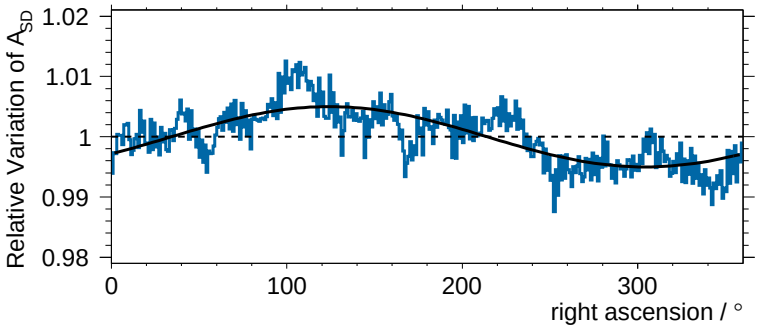

Figure 5.3: First harmonic modulation in the event rate induced by the variation of the SD area. The numbers of cell seconds have been filled into the corresponding bin in right ascension. To guide the eye, the resulting modulation has been fit by a cosine in order to quantify the effect of the changing area of the SD on searches of first harmonic modulations. The plot has been produced for the data period from 2004 until 2009.

be positioned on the equatorial sphere for a given point in time and the corresponding area of the SD available at that time. The corrected relative exposure map is then obtained by adding up these cones at all GPS seconds within the time interval of taking data considered for analysis. The resulting variation of the SD area accumulated in bins of right ascension is displayed in figure 5.3. It shows that for the example of the anisotropy search for a first order harmonic modulation the amplitude artificially induced by the changing size of the SD area is about ~ 0.5 %.

To dispose of the locally induced variation of the relative exposure in equatorial coordinates use can be made of the complete information contained in the histogram in figure 5.3 bin by bin. The data points taken within a certain period of time need to be divided by the SD area weights obtained for the same period. Doing so, account is taken of how often the detector has "looked" at a certain direction in the sky. In local coordinates the instantaneous local exposure for a given local direction, time and energy is given by [Abr11c, Som01]

$$\omega_{loc}(\theta,\phi,t,S_{38^\circ}) = N_{cell}(t) \times A_{cell}^{SD} \cos\theta \times \varepsilon(S_{38^\circ},\theta,\phi) \tag{5.1}$$

with N_{cell} the number of active elementary cells at time t, A_{cell}^{SD} the area of the SD, θ and ϕ the zenith and azimuth angle, S_{38° the energy measurement of the SD and ε the detection efficiency. With the given position of the observatory and the local direction and time the local exposure can be transformed to the exposure in equatorial coordinates by rotation, see appendix A. The integral over time of the resulting instantaneous equatorial exposure yields the expectation of what an isotropic sky would look like from the geographical position of the PAO, the corrected exposure $\omega_\alpha(\delta,\alpha)$.

Note that at full efficiency, $E > 10^{18.5}$ eV and $\theta < 60^\circ$, the local exposure does not depend on the azimuth angle and in case of a detector of constant size $\omega_{loc} \propto \cos\theta$ expresses the acceptance cone of the local field of view of the SD, see figure 3.8. Under these conditions the integration over time achieved by one rotation of the cone in equatorial coordinates around the axis through the poles yields the well-known $\omega(\delta)$ given in equation 3.4.

5.2 Varying Atmospheric Conditions over Time

The particle content measured at ground level depends on the properties of the atmosphere the air shower cascade develops in. These properties are relevant for meteorological studies and forecasts which is why the effects on the shower development are commonly referred to as weather effects. In this section, the connection between atmospheric conditions and shower cascade physics will be briefly illuminated. The impact of these conditions on the energy estimator of the SD will be discussed. Then the connection between systematically varying energy measurements with SD over time and anisotropy studies will be drawn. Finally, the correction for the energy estimator will be presented and the size of the effect on the event rate will be quantified.

The quantities describing the atmospheric conditions are pressure P, density ρ and temperature T; from the ideal gas law they are known to fulfil the relation $P \propto \rho T$, approximately, so that the choice of the two observables P and ρ suffices to basically characterise the atmosphere. Changes of these thermodynamical characteristics of the atmosphere affect the interaction lengths of hadrons and radiation lengths of the EM component of the shower. For example, a higher air density is expected to cause a smaller slant depth of the shower maximum and stronger attenuation of shower particles on their way to ground level. In turn, fewer particles reach the SD and the signals measured by the stations of the SD are systematically smaller. Thus, the energy estimator is smaller compared to a measurement of the same primary particle and energy in an atmosphere of less dense air.

Atmospheric conditions vary with time. Well-known features of this behaviour are seasonal and daily changes of the weather most commonly indicated by the temperature. Consequently, the measurement of the energy estimator with the SD varies over time, too. Consider a set of extensive air showers reconstructed successfully by SD measurements with assigned energies and arrival directions of the respective cosmic ray primary particle. Recalling the fact that time of measurement and direction of the shower (right ascension) are connected it becomes apparent that the variation of energies over time result in variations of energies over direction. For anisotropy studies on this set of events it is necessary to apply an energy cut; since the detection efficiency depends on energy, see equation 5.1, the exposure can by calculated correctly only if the energy of the particles is precisely known. Thus, after the application of an energy cut to a set of events whose energies vary systematically over direction the steeply falling energy spectrum causes a non-negligible fraction of this directional dependence to be propagated to the event rate.

The air pressure and density are continuously monitored at the SD of the PAO and recorded every 300 s. Figures 5.4(a) and (b) show the seasonal and daily variation of the air density ρ obtained from the monitoring files kindly provided by [Kei11]. In [Abr09a] it is shown that the signal $S(1000)$ measured with the SD at 1 km from the shower core impact position correlates with actual local values of pressure P and air density. Using the average values $P_0 = 862$ hPa and $\rho_0 = 1.06$ kg m^{-3} at the location of the observatory as a reference, the signal $S^0(1000)$ that would have been measured at these reference values is:

$$S^0(1000) = [1 - \alpha_P(\theta)(P - P_0) - \alpha_\rho(\theta)(\rho_d - \rho_0) - \beta_\rho(\theta)(\rho - \rho_0)]S(1000)\ . \qquad (5.2)$$

where ρ_d is the daily average air density at the time of the measurement of the air shower and θ is the zenith angle. The correlation coefficients α_P, α_ρ and β_ρ are reported in [Abr09a]. For the sake of visualisation of this effect, the correlation of air density and energy estimator

of the SD is plotted in figure 5.4(c). The correction is applied on the level of the energy estimator and has to be transferred to a correction of the energy in order to make typical energy cuts feasible. This transfer is achieved performing the known process of the constant intensity cut and energy calibration as described in chapter 3. The procedure is applied to the corrected estimator $S^0(1000)$ making use of the same CIC and calibration constants that are obtained for the original values of $S(1000)$.

In order to quantify and visualise the impact of the variation of the energy estimator of the SD over atmospheric conditions (and thus, over time) on anisotropy searches, a subset of real data events has been investigated. A comparison has been made of the raw data set and the energy corrected data set according to equation 5.2. After applying a lower energy cut, $E > 3$ EeV, to both data sets, the ratio of the event rates has been plotted versus right ascension in figure 5.5. From the cosine fit applied to guide the eye an amplitude of 0.5 % for first order harmonic modulations can be read. This modulation would directly be propagated to a search for sinusoidal anisotropies as a systematic effect if not corrected for.

5.3 Effect of the Geomagnetic Field

In this section the directional distortions of the event rate of cosmic rays induced by the geomagnetic field will be analysed. The charged secondary particles of extensive air showers are deflected in the geomagnetic field. This deflection affects the energy estimator $S(1000)$ of the SD. The resulting variation of $S(1000)$ depending on the direction of the air shower with respect to the direction of the B-field is propagated to the event rate indirectly when applying an energy cut, similar to what was already described in the previous section in the context of weather effects. Consequently, anisotropy studies may be sensitive to this modulation of the event rate that is induced by the geomagnetic field. If not corrected for, this local effect leads to false identification of anisotropy in the event rate distribution on the equatorial sphere of arrival directions.

In the simplest approach to quantify the influence of the B-field on the event rate distribution as described above one would want to make use of isotropic air shower simulations. These simulations are expected to describe the reality of magnetic deflections of secondary particles fairly well. After the detector simulation and reconstruction chain, an energy cut would be applied and the effect on the event rate could be obtained both qualitatively and quantitatively from the comparison to the isotropic expectation. Isotropic expectation in this context means the relative exposure which was described in chapter 3. However, without introducing a model a priori to restrict the shape and number of parameters of the influence a huge number of shower simulations would be necessary to allow for precise results.

This is why the effect will be modelled before being quantified by means of air shower simulations. In a first step, a qualitative model of the effect on the energy estimator will be derived on an intuitive basis. A more rigorous approach will show that this rather intuitive model was sensibly chosen and holds for quantitative considerations. Air shower simulations will be used to derive the parameters of the model. It will be shown that the modulation of the energy estimator results in a systematic distortion of the event rate distribution inducing false anisotropy at the ~ 1 % level. The work presented in this section has contributed to the understanding and quantification of the effect of the geomagnetic field on anisotropy studies. The aim of this work is to quantify the influence of the geomagnetic field on the

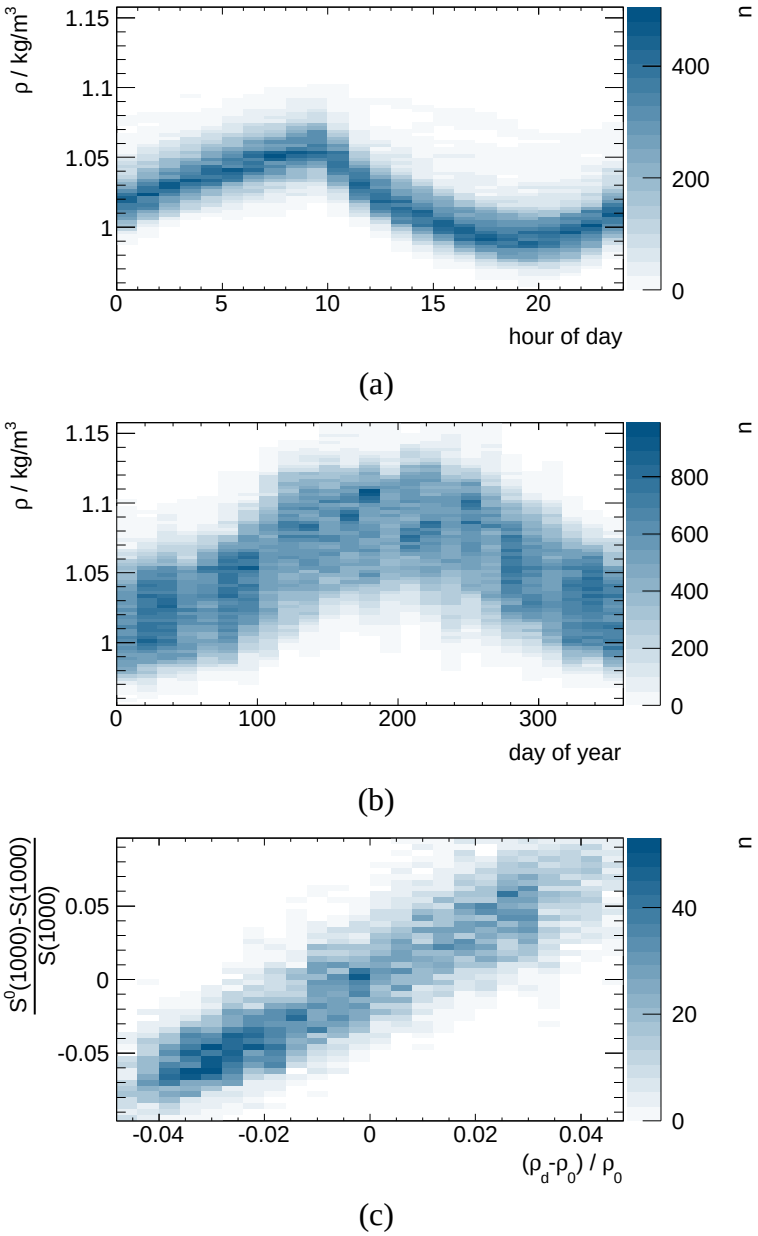

Figure 5.4: Variation of the weather conditions and correlation of the varying air density ρ and the energy estimator $S(1000)$. (a) displays the daily variation of the air density during southern summers (December - February), (b) shows the seasonal changes. As expected from fundamental physics the air is densest after cold periods, i.e. at about 10 o'clock in the morning and during southern winters. (c) gives an impression of the impact of the air density on the energy estimator: a variation of 5 % of the air density correlates to a change of 10 % of the energy estimator.

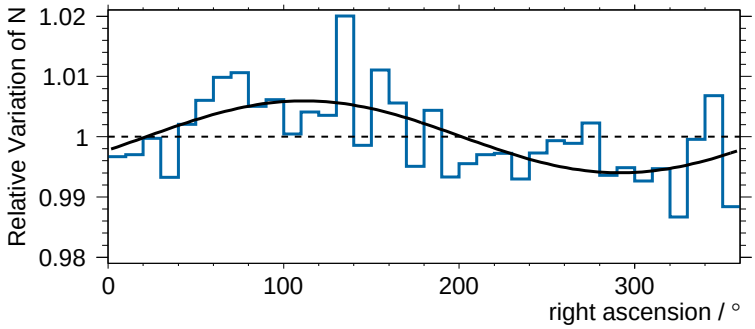

Figure 5.5: First harmonic modulation in the event rate induced by the variation of the conditions of the atmosphere. The raw set and the weather corrected set produce event rate distributions over the right ascension. The plot shows the bin-wise ratio of these event rates when applying an energy cut of $E > 3$ EeV. To guide the eye, the resulting ratio has been scaled to make the mean entry match unity and the modulation has been fit by a cosine in order to quantify the effect of the changing atmosphere on searches of first harmonic modulations. The plot has been produced for the data period from 2004 until 2009.

energy estimator measured with the SD; more precisely, the bias of the value of the energy estimator is obtained that is due to the presence of the geomagnetic field, a correction is derived. The corresponding results obtained in a collaborational effort with the Large Scale Anisotropy task force of the Pierre Auger Collaboration will be published soon [Abr11b].

5.3.1 Intuitive Approach

The following general considerations provide an idea of how the geomagnetic field affects the energy estimator $S(1000)$. A qualitative model of the variation of $S(1000)$ in local coordinates is derived from few fundamental assumptions.

Due to magnetic deflection the shower particles are subject to charge separation on their way to ground level. Thus, the lateral distribution of the particles in the plane perpendicular to the shower axis is distorted: While in absence of the field axial symmetry and a circular distribution is expected, the deflection by the geomagnetic field leads to an approximately elliptical distribution, see figure 5.6. In turn, this distortion is transferred to the signals measured in the individual stations detecting the shower at ground level. Since the measurement of the energy estimator $S(1000)$ by the SD assumes axial symmetry of these signals around the shower direction the estimator is subject to variation depending systematically on two quantities:

- On the one hand, it is affected by the angle $\Omega_B = \sphericalangle(\mathbf{S},\mathbf{B})$ between the shower direction $\mathbf{S}$ and the local direction of the B-field $\mathbf{B}$. The influence is large at $\Omega_B \approx 90^\circ$ and decreases for both smaller and larger angles until it vanishes at showers (anti-)parallel to the field direction, $\Omega_B = 0^\circ$ or $\Omega_B = 180^\circ$. Due to this symmetry of the influence around $\Omega_B = 90^\circ$ the simplest approach to model the influence on the energy estimator would be a quadrupolar function; it turns out that

$$f_B(\Omega_B) = (1 - \cos(2\Omega_B))/2 \tag{5.3}$$

  exactly matches the described properties. Note that in principle it is not clear a priori

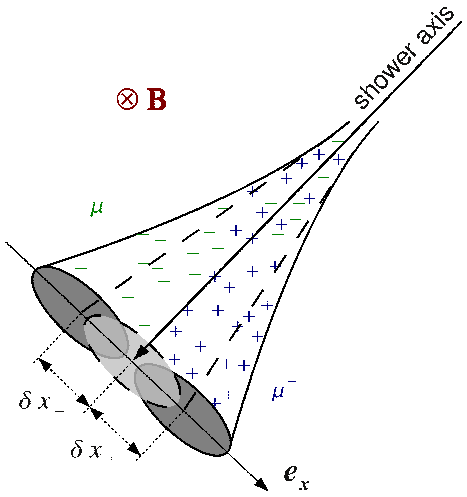

Figure 5.6: Separation of charged air shower particles in the Earth's magnetic field **B**: Muons $\mu^{\pm}$ are deflected by $\delta x_{\pm}$ on average according to their respective charge, the originally circular footprint of the lateral particle densities in the shower front (light grey) becomes distorted. In the drawing the separation is exaggerated and two circular footprints are generated (dark grey). In a more realistic scenario for non horizontal showers with typical particle deflections $|\delta x_{\pm}|$ of several 10 m and a lateral extent of the overall footprint of a few km large fractions of these circles will overlap thus leading to an approximately elliptical shape. See also figure A.4 for reference.

whether the effect is of positive or negative sign, i.e. whether the energy estimator will be larger or smaller due to the influence of the geomagnetic field.

- On the other hand, the influence depends on the distance d travelled by the particles through the B-field. There is a simple approximate connection between this distance d and the zenith angle θ of the shower as illustrated in figure 5.7. The distance d is given by the altitude h of particle generation divided by the cosine of the zenith angle θ,

$$d = h/\cos\theta \ ,$$

This relation is based on the assumption of a flat atmosphere. The spherical curvature of the atmosphere in fact leads to smaller values of d at large zenith angles than what

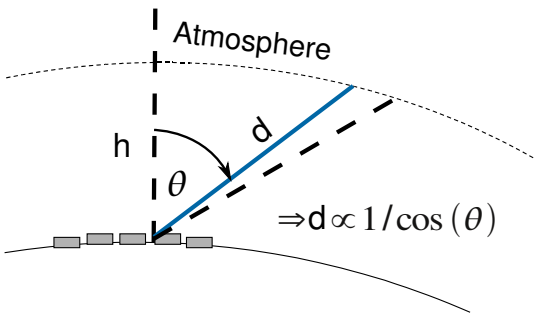

Figure 5.7: The travel distance d of secondary particles in the atmosphere depends on zenith angle θ. Approximately, it is inversely proportional to the cosine of the zenith angle, $d \propto 1/\cos\theta$.

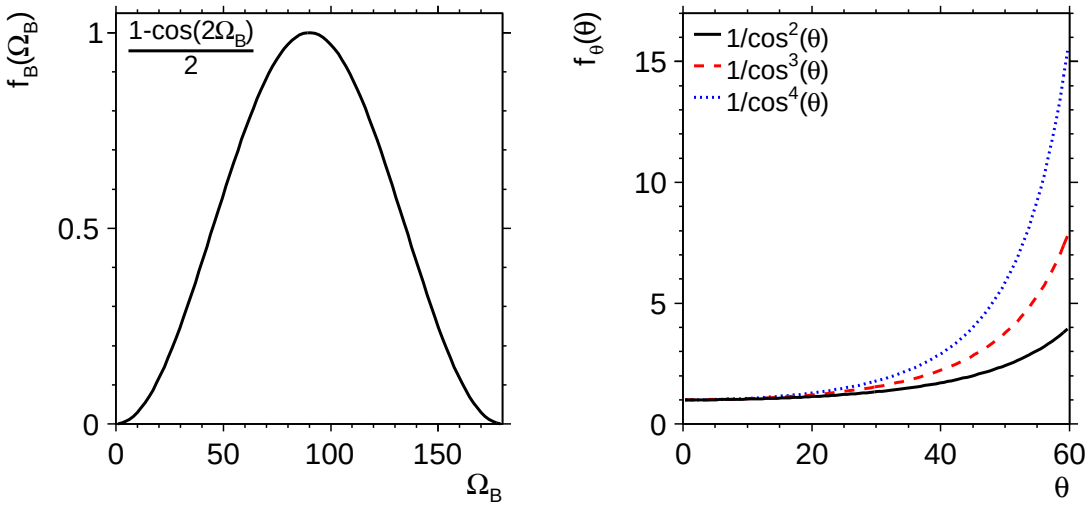

Figure 5.8: Parametrisation of the influence of the geomagnetic field depending on Ω_B and zenith angle θ, see equations 5.3 (left), 5.4 (right). The latter is displayed for different exponents $n = 2,3,4$ of the zenith angle dependence.

is predicted by the formula. However, this effect is partly compensated due to the fact that inclined showers are supposed to generate secondary particles at a higher altitude than vertical showers. This is because the former has penetrated a larger amount of air when reaching the same altitude. The path of particles travelling through the geomagnetic field is known to be bent by the Lorentz force to a circular orbit. For large gyroradii magnetic deflections are small and the circular path may be approximated by a parabola. Thus, the influence of the geomagnetic field on the energy estimator can be assumed to depend quadratically on the distance travelled,

$$f_\theta^{n=2}(\theta) = 1/\cos^2(\theta)\ . \tag{5.4}$$

Note that n is introduced as a parameter. This degree of freedom accounts for the fact that in the rigorous approach in the following subsection a steeper dependence on the zenith angle is predicted. The actual value of n will be derived from simulations. The functions $f_B(\Omega_B)$ and $f_\theta^{n=2}(\theta)$ are displayed in figure 5.8.

These functions model the effect of two properties of the shower which are essentially independent of each other, the combination of the two influences is described by the product. The model of the effect of the geomagnetic field on the energy estimator therefore becomes

$$\frac{\Delta S(1000)}{S(1000)} = R_B \frac{1-\cos(2\Omega_B)}{2\cos^n(\theta)}\ , \tag{5.5}$$

with the parameters n to describe the zenith angle dependence and R_B indicating the amplitude of the effect. According to this model, the expected variation of the energy estimator in the sky map of local coordinates is visualised in figure 5.9 for an exaggerated amplitude of $R_B = 0.2$ and $n = 2$. The projections of this map along x- and y-axes yield the distributions of $\frac{\Delta S(1000)}{S(1000)}$ in zenith and azimuth, respectively. In case of the large amplitude $R_B = 0.2$, the effect in the dimension of the individual coordinate is clearly visible and amounts to values of comparable order of magnitude, ~ 0.2.

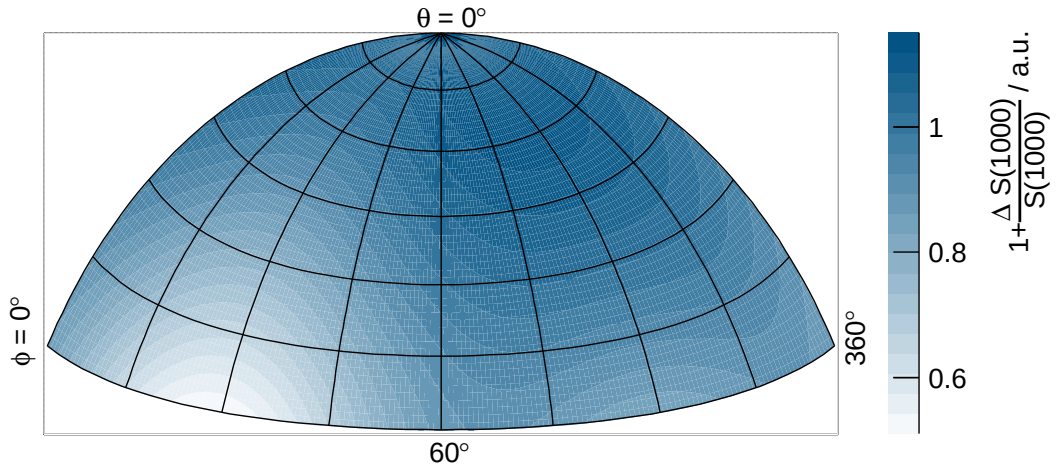

(a)

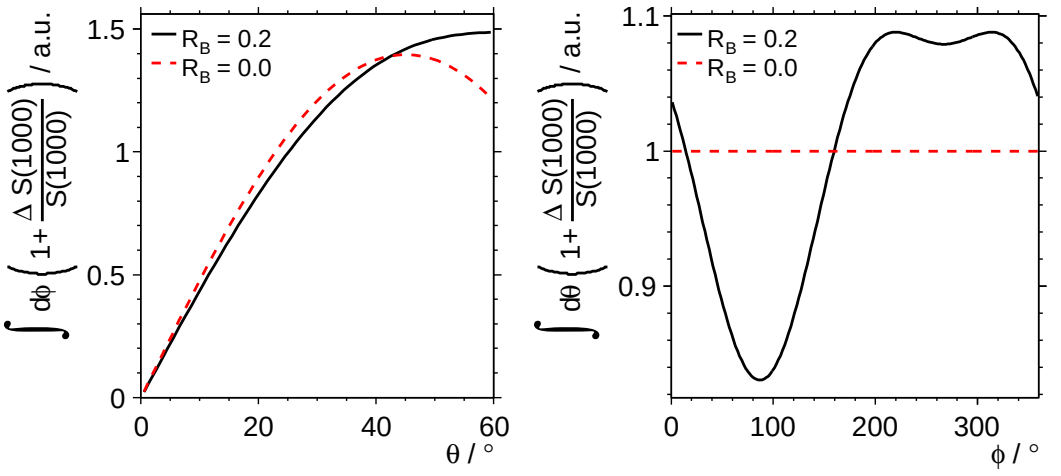

(b)

Figure 5.9: Model of the influence of the geomagnetic field on the energy estimator obtained from an intuitive approach, see equation 5.5 (top). The parameters used for the visualisation of the sky map in local coordinates are $R_B = 0.2$ and $n = 2$. The respective effect on the local coordinates zenith θ and azimuth ϕ (bottom) is obtained from the projection of the sky map along the corresponding axis (black solid). For comparison, the distributions expected in absence of a geomagnetic field ($R_B \equiv 0$) are plotted (red dashed).

The resulting variation of $S(1000)$ is propagated to the event rate indirectly when applying an energy cut. In the simplest scenario the model would remain unchanged qualitatively; equation 5.5 would hold and only the amplitude of the effect would possibly change.

With this solution the effect of the geomagnetic field on the event rate and thus, on anisotropy studies, is modelled from very basic ingredients and considerations. It can be quantified by obtaining the parameters in equation 5.5 from simulations. Note that it is not easily possible to derive the parameters from real data: The distribution of arrival directions in local coordinates may partly contain true anisotropy, e.g. a strong source above the south pole would result in an excess in the azimuth angle distribution at $\phi \approx 270^\circ$. While the technical details of the air shower simulations are given in appendix B, the results will be reported later on in this section. In the following subsection a more rigorous approach will be presented including more quantitative information on the geomagnetic field and the deflection of charged shower particles.

5.3.2 Rigorous Approach

Magnetic Field of Malargüe

The geomagnetic field at the site of the PAO near Malargüe is affected by the south Atlantic anomaly which results in a field strength that is roughly a factor of two smaller compared to typical values e.g. at locations in Central Europe. The International Geomagnetic Reference Field (IGRF) provides the following parameters defining the local geomagnetic field [Oce11]:

$$\mathbf{B} = (B, I_B, D_B) = (24.5\mu\mathrm{T}, -35.4^\circ, 3.1^\circ) \tag{5.6}$$

with I_B and D_B commonly referred to as the inclination and declination of the local field lines. Transformed to the coordinates of the local coordinate system as defined in appendix A, the magnetic field is

$$\mathbf{B} = (B, \theta_B, \phi_B) = (24.5\mu\mathrm{T}, 54.6^\circ, 86.9^\circ)\ . \tag{5.7}$$

The field strength and direction can be considered constant for the time scale of the data taking of the PAO which is shown in figure 5.10.

Magnetic Deflection

The deflection of charged shower particles in the magnetic field **B** is described by the Lorentz force,

$$|\mathbf{F}_L| = |q\mathrm{v}(\mathbf{S}\times\mathbf{B})| = |q|\mathrm{v}B\sin\Omega_B\ .$$

with q the charge of the particle and v**S** its velocity and direction. As before, the angle between particle direction **S** and direction of the magnetic field **B** is denoted as $\Omega_B = \sphericalangle(\mathbf{S},\mathbf{B}) = \arcsin((\mathbf{S}\times\mathbf{B})/(\mathrm{v}B))$. The component of **B** transverse to the direction of the particle is $B_T = B\sin\Omega_B$. Since **B** forces the particle on a circular track, together with the centrifugal force the gyroradius of the particle can be computed. The gyroradius of a shower muon of an energy of E_μ travelling perpendicular to the direction of the Earth's magnetic field is $r_g = E_\mu/(eB_T)$. The size of the magnetic deflection of the muon within the shower plane depends on the gyroradius r_g and the travel distance d of the muon in the B-field. The

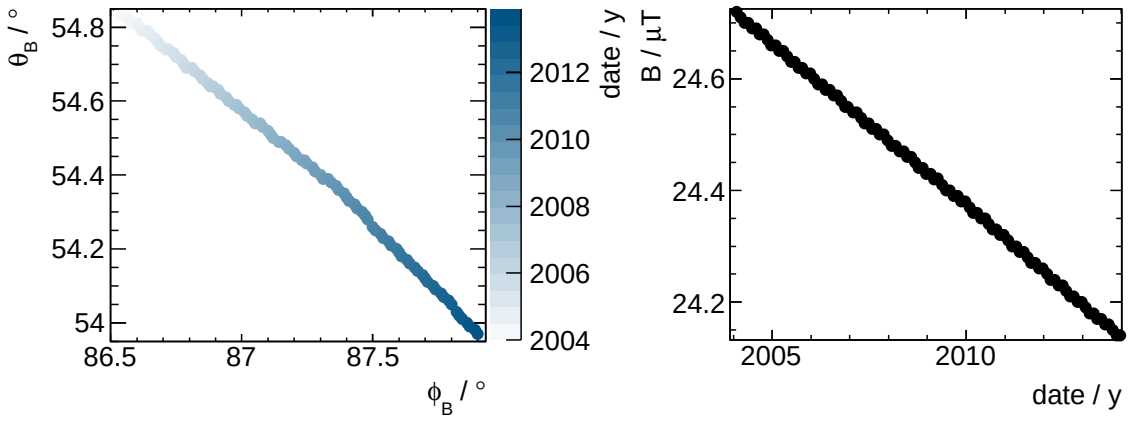

Figure 5.10: The change of the geomagnetic field during one decade according to the IGRF is negligible for the investigation of its effects on anisotropy studies. The change in direction amounts to $\sim 0.1^\circ$ per year (left plot) and the relative change in field strength is $\sim 0.6/24.4/10 \approx 0.25$ % per year (right plot). The values have been obtained for the IGRF from [Oce11]

shower coordinate system made use of is illustrated in appendix A. The magnetic deflection $\delta x_\pm$ of the muon along the x-axis in the shower plane can be estimated from purely geometrical considerations from r_g and d,

$$\delta x_\pm \approx \pm d \times \sin(\arctan(d/r_g)) - r_g \ .$$

This relation can be approximated by means of the expansion of the sine and arctangent function to first non-linear order in d/r_g resulting in $\delta x_\pm \approx d^2/(2r_g)$. With the gyroradius substituted again by the known formula the magnetic deflection becomes

$$\delta x_\pm \approx \pm \frac{ecB_T d^2}{2E_\mu} \ . \tag{5.8}$$

Lateral Muon Density and S(1000)

In the presence of the geomagnetic field a dominantly quadrupolar shape of the lateral muon density ρ_μ within the shower plane is generated by the charge separation caused by the magnetic deflections. Quantitatively, the density $\bar{\rho}_\mu(\bar{x},\bar{y})$ in presence of the magnetic field can be derived from the density $\rho_\mu(x,y)$ in absence of the field [Abr11b]. This is done by means of the following Jacobian transformation identical to what has been done in the context of horizontal air showers [Ave00]:

$$\bar{\rho}_\mu(\bar{x},\bar{y}) = \left|\frac{\partial(x,y)}{\partial(\bar{x},\bar{y})}\right| \rho_\mu(x(\bar{x},\bar{y}),y(\bar{x},\bar{y})) \ . \tag{5.9}$$

with the Cartesian coordinates in the shower plane fulfilling the simple relations

$$\bar{x} = x + \delta x_\pm(x,y) \ , \qquad \bar{y} = y \ . \tag{5.10}$$

The quadrupolar character of the modulation of the muon density in the shower plane affects the signals measured by the surface detector stations. The signal sizes are modulated

depending on the polar angle ψ in the shower plane like

$$S_{obs}/S_{exp} = 1 + r_\psi \cdot (1 - \cos(2\psi - \phi_\psi))/2 \; . \tag{5.11}$$

with r_ψ the amplitude and ϕ_ψ the phase of the modulation and S_{obs} the observed and S_{exp} the expected signal measured at an individual station. In this context, the expected signal is obtained from the LDF fit that assumes a circular symmetry of the muon density around the shower axis. Thus, the fit function yields the "average" signal size at a given shower axis distance. Isotropic air showers of energies above $E > 3$ EeV have been simulated with spectral index $\xi = 2.6$ with the geomagnetic field at Malargüe switched on (off). The number of air showers simulated with AIRES is 52086 (8637) and the number of individual tank signals included in the normalised average is 263783 (43422). The amplitude of the quadrupolar modulation estimated by the procedure described is $r_\psi = (0.48 \pm 0.05)$ % ($r_\psi = (0.10 \pm 0.12)$ %), see figure 5.11. Similarly, the ratio is plotted for real data above energies of 2 EeV from 336410 tank signals observing an amplitude of $r_\psi = (0.53 \pm 0.04)$ %. Both amplitude and phase of the modulation found in real data agree with simulations in the presence of the geomagnetic field while there is no significant amplitude in the absence of the field. Note that the phase aligns the maxima with the $\pm x$-axis direction which is where the maximum deflections and thus, the muon overdensities are expected. Consequently, the existence of an influence of the geomagnetic field on the data taken with the PAO SD is implied. Even more, the influence is described quantitatively with air shower simulations.

When focussing on changes of the muon density at a distance of 1000 m from the shower axis, the variation of the magnetic deflection $\delta x_\pm$ depending on x and y has been shown to be small [Abr11b] compared to the distance to the shower axis. Consequently, the muon density in presence of the field can be approximated by

$$\bar{\rho}_\mu(\bar{x},\bar{y}) \approx \rho_{\mu_+}(\bar{x} - \delta x_+, \bar{y}) + \rho_{\mu_-}(\bar{x} - \delta x_-, \bar{y}) \tag{5.12}$$

$$\approx \rho_\mu(\bar{x},\bar{y}) + \frac{(\delta x)^2}{2} \frac{\partial^2 \rho_\mu(\bar{x},\bar{y})}{\delta \bar{x}^2} \tag{5.13}$$

with the deflections $\delta x = \delta x_+ = -\delta x_-$ and muon densities $\rho_{\mu_+} = \rho_{\mu_-} = \rho_\mu/2$ differing only in the sign (of the muon charge), not in the absolute value. This is why the linear term is cancelled out in the approximation. Therefore, the muon density at the distance of 1000 m is changed in the magnetic field by a factor proportional to

$$(\delta x)^2 \propto B_T^2 d^4 \; . \tag{5.14}$$

Since the transverse component of the B-field depends on the individual shower direction, $B_T = B_T(\theta, \phi)$, the influence of the B-field on the energy estimator contains an azimuth angle and a zenith angle dependence. While the zenith angle θ dependence affects the travel distance d, see below, the azimuth angle ϕ dependence is indirectly derived from the dependence of the Lorentz force on the angle Ω_B between shower direction **S** and direction of **B**. Therefore, it is both intuitive and convenient to separately consider the dependence of the magnetic deflection on Ω_B and θ. The former is described by equation 5.14 with $B_T = B \sin \Omega_B$ leading to

$$(\delta x)^2 \propto B^2 \sin^2(\Omega_B) d^4 \; . \tag{5.15}$$

Again assuming a direct connection of the magnetic deflection with the variation of the energy estimator results in the following parametrisation:

$$\frac{\Delta S(1000)}{S(1000)} = R_B \frac{\sin^2(\Omega_B)}{\cos^4(\theta)} \; . \tag{5.16}$$

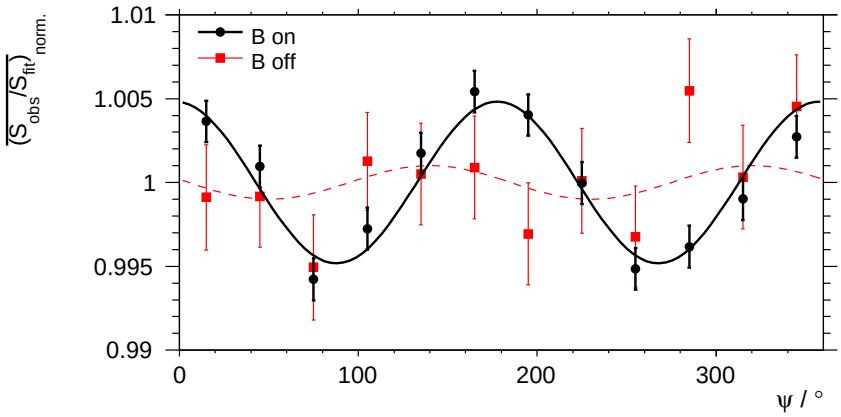

(a) Simulations

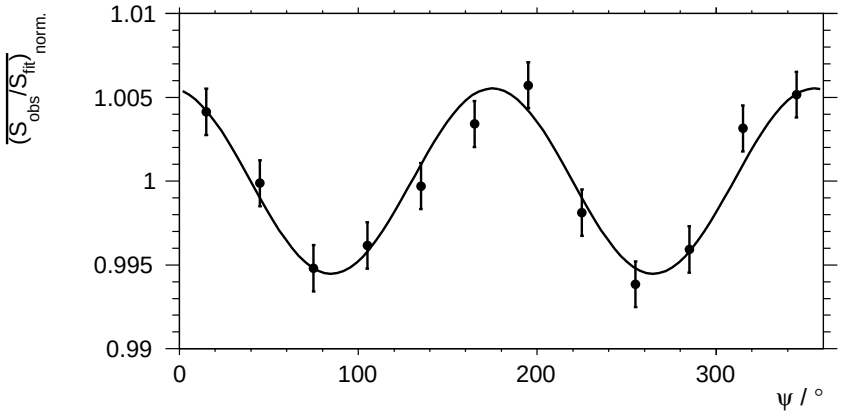

(b) Real Data of the PAO SD

Figure 5.11: Modulations of the ratio of observed and expected tank signals versus the polar angle ψ in the shower front. The top plot shows the modulations for simulated showers in the presence (black solid) and absence (red dashed) of the geomagnetic field. The bottom plot shows the modulation for real data above $E > 2$ EeV.

It is worth noting that this equation differs only slightly from equation 5.5: The dependence on Ω_B given here is identical to what has been obtained with the intuitive approach in equation 5.3, $\sin^2(\Omega_B) \equiv (1-\cos(2\Omega_B))/2$. However, the zenith angle dependence obtained from the intuitive approach assumed a quadratic behaviour, $n = 2$. Instead, the result from the rigorous approach claims a stronger dependence like $1/\cos^4(\theta)$. This apparent disagreement is softened when recalling that the propagation of the effect of the geomagnetic field on charged particles and the muon density to an effect on the energy estimator is a complex issue which cannot be modelled easily; as an educated guess, the actual value of n is supposed to lie somewhere in between the two results. In any event, the characterisation of the connection of the variation of the energy estimator and the cosine of the zenith angle by a power law is considered a reasonable ansatz. Simulations will be used to determine the power n and the overall amplitude of the modulation R_B.

In summary of and corresponding to the two presented approaches the parametrisation of the influence of the geomagnetic field on the energy estimator is defined in the following way:

$$s = \frac{S_{\text{on}} - S_{\text{off}}}{S_{\text{off}}} = R_B \frac{\sin^2(\Omega_B) \cdot \cos^n(\theta_B)}{\cos^n(\theta)} \tag{5.17}$$

with S_{off} and S_{on} denoting the energy estimator $S(1000)$ measured by the SD in absence (off) and in presence (on) of the B-field, respectively. Note that a factor of $\cos^n(\theta_B)$ has been introduced to renormalize the formula to the special case of showers coming in at the same zenith angle as the B-field direction. This will allow for the evaluation of R_B without interference by the zenith angle. Independently on whether the B-field is switched on or off, the lateral density function assumes axial symmetry about the shower axis. For this reason, the given definition of s corresponds to the amount the measurement of $S(1000)$ is over- or underestimated by due to the B-field. Contrariwise, the correction that has to be applied to every measured $S(1000)$ to make the data set insensitive to the effect is given by the permutation of S_{off} and S_{on} or essentially by $-s$. The uncertainty of s is obtained from the propagation of the uncertainties ΔS_{off} and ΔS_{on} of S_{off} and S_{on}, respectively.

$$\Delta s = \frac{\sqrt{\Delta S_{\text{on}}^2 S_{\text{off}}^2 + \Delta S_{\text{off}}^2 S_{\text{on}}^2}}{S_{\text{on}}^2} \,. \tag{5.18}$$

5.3.3 Model Parameters from Simulations of Air Showers

In order to derive the parameters of the model in equation 5.17, ideally two large sets of isotropic simulations would be generated with the magnetic field switched on and off, respectively. After the application of an energy cut to both sets, the event rate ratio of the resulting distributions of arrival directions in local coordinates would be fitted with the model and the parameters could be obtained. However, this approach would necessitate a huge number of simulated air showers. That is because in isotropic arrival directions the angular range at large zenith angles is under-represented. Large zenith angles, at the same time, are of major relevance to derive significant estimates of the parameter values; the ratio defined in equation 5.17 increases strongly with zenith angle as can also be observed in figure 5.8.

Basics on air shower simulations and the corresponding numbers and parameters used in this work are introduced in appendix B. The air showers produced in the course of this

Table 5.1: Isotropic air shower simulations generated with AIRES in the course of the study of the effect of the geomagnetic field. The primary particle type is proton, the energy has been diced above $E > 3$ EeV from an energy spectrum with realistic spectral index $\xi = 2.6$, the directions are distributed isotropically and the actual direction of the Earth's magnetic field has been used, see equation 5.7. The strength has been switched on and off, respectively, and a number N of showers has been simulated.

AIRES simulation parameters for isotropic showers

primary	E	θ	ϕ	B / μT	N
p	$\sim E^{-2.6}$	$\sim \cos\theta \sin\theta$	flat	24.5	52086
				0	8637

thesis are summarised in tables 5.1 and 5.2. Large sets of isotropic showers simulated with the AIRES program were already made use of for the plots in figure 5.11. Furthermore, a number of mono-energetic and mono-directional air showers have been simulated with the CORSIKA program and partly cross-checked with the AIRES program.

In order to quantify the geomagnetic field effect from the latter simulations, the mean values $\langle S(1000)\rangle$ of the energy estimators reconstructed with the B-field switched on and off in the respective set of showers are computed and compared with each other. The comparison consists of inserting the mean values into equations 5.17 and 5.18. Two scenarios are of major interest for the computation of the model parameters R_B and n.

Firstly, fixing the shower direction to a direction perpendicular to the B-field direction, $\Omega_B \equiv 90^\circ$, while at the same zenith angle, $\theta \equiv \theta_B = 54.6^\circ$, the measurement of the ratio s in equation 5.17 exactly becomes the amplitude R_B. The mean values of $S(1000)$ obtained with protons of energy 8 EeV are plotted in figure 5.12(a); additionally observing equation 5.18 for the uncertainty results in the following measurement of the amplitude:

$$R_B = (2.56 \pm 0.32)\% \,.$$

The amplitude is positive and thus, the energy estimator $S(1000)$ is overestimated due to the influence of the geomagnetic field on the shower particles. For the determination of the zenith angle dependence it makes sense to use directions perpendicular to the B-field direction, $\Omega_B \equiv 90^\circ$, and correspondingly produce sets of air showers at different zenith angles. With this approach the exponent n can be measured. Figure 5.12(b) shows the results obtained for s at four different zenith angles. A fit to the points with equation 5.17 produces the second parameter,

$$n = 2.99 \pm 1.06 \,. \tag{5.19}$$

Note that this value is compatible within its uncertainty with $n = 2$, i.e. the preliminary prediction made in the intuitive approach. It is also compatible with $n = 4$ predicted with the rigorous approach. In a similar study using AIRES (with QGSJetI) simulations a larger set of showers is produced and a value of $n = 2.8 \pm 0.3$ is obtained [Abr11b], compatible with the result in equation 5.19 but confirming neither approach. As mentioned before, the propagation of the effect of the geomagnetic field on individual particle level to the level of energy estimation with the SD is complex and both approaches can only provide a qualitative idea.

The amplitude R_B can be fitted from the zenith angle dependence plot as well, it is obtained

Table 5.2: This table shows a summary of all mono-energetic and mono-directional air shower simulations done in the course of the study of the effect of the geomagnetic field. The simulation input parameters are given starting on the left with primary, the type of the cosmic ray particle, followed by the energy E, the zenith angle θ, the azimuth angle ϕ (for completeness, the angle Ω_B of the shower relative to the local direction of the Earth's magnetic field, θ_B and ϕ_B, is given, too), the strength of the field B and the number N of showers simulated. On the right the result obtained when simulating the answer of the surface detector and reconstructing the air shower from the measurement of the simulated signals in the detector stations. As an estimator of the effect of the geomagnetic field use is made of the average value of the energy estimator $\langle S(1000)\rangle$ which is given with its statistical uncertainty. All results are obtained with CORSIKA except for the bottom case: A cross-check is performed with AIRES for protons of $E = 8$ EeV and zenith angle of 55° confirming the CORSIKA results.

Simulation Parameters							Result
primary	E / EeV	θ / °	ϕ / °	Ω_B / °	B / μT	N	$\langle S(1000)\rangle$ / VEM
CORSIKA							
p	8	55	86	90	0	5797	12.91 ± 0.03
			327		24.5	7621	13.24 ± 0.03
p	80	55	86	90	0	2573	116.87 ± 0.42
			327		24.5	2472	120.19 ± 0.42
Fe	8	55	86	90	0	6001	16.03 ± 0.03
			327		24.5	7754	16.23 ± 0.03
p	8	35	266	90	0	897	24.88 ± 0.16
		35	266		24.5	912	25.10 ± 0.15
		45	312		0	1752	18.36 ± 0.09
		45	312		24.5	1822	18.54 ± 0.08
		60	332		0	1953	10.84 ± 0.05
		60	332		24.5	1914	11.24 ± 0.05
AIRES							
p	8	55	86	90	0	998	12.78 ± 0.06
			327		24.5	971	13.08 ± 0.08

as

$$R_B = (2.43 \pm 0.27)\% \tag{5.20}$$

and thus agrees with the estimate produced when only using the measurement at one zenith angle.

5.3.4 Systematic Uncertainties

The dependence of the effect on energy and composition of the primary particle is investigated. For simulations of protons at $E = 80$ EeV and $\theta \equiv \theta_B$, $\Omega_B = 90°$ a compatible result is obtained, $R_B = (2.84 \pm 0.49)$ %, which implies that the influence of the geomagnetic field on the energy estimator is essentially independent of the primary energy. This can be understood because the energy spectra of the secondary particles show only little dependence on the primary energy: The primary energy rather affects the multiplicity, i.e. the number of

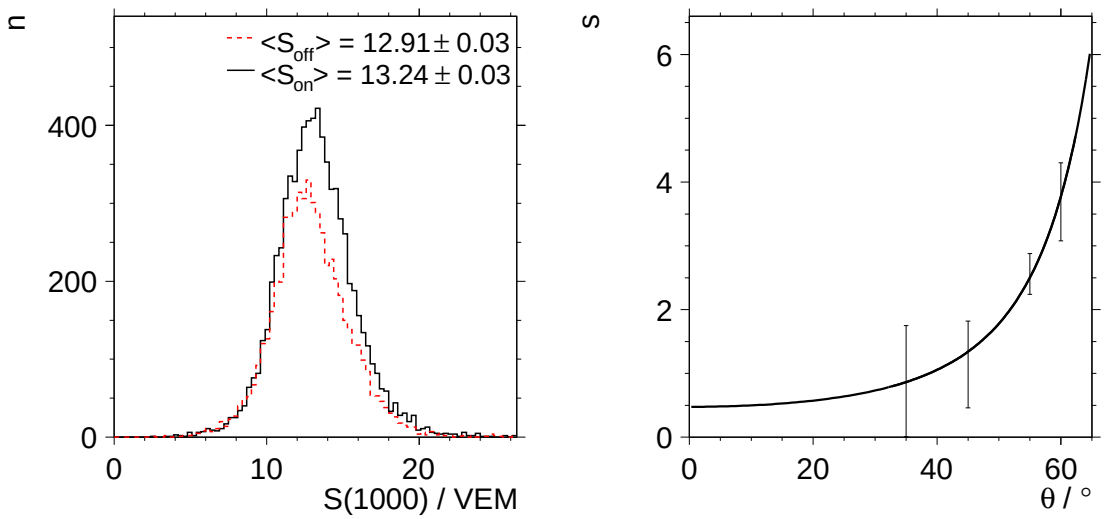

(a) (b)

Figure 5.12: Measurements of the mean values of $S(1000)$ from air shower simulations with the B-field switched on and off, respectively. With $\theta = \theta_B$ and correspondingly $\Omega_B = 90^\circ$ in the left plot the ratio defined in 5.17 becomes the amplitude, $s \equiv R_B$. In the right plot the zenith angle dependence of this ratio determined by the power n is investigated, see text for details. The plots show the results for proton simulations at $E = 8$ EeV.

secondary particles generated within the air shower cascade while the atmosphere regulates the typical energies of these particles after few steps of interaction. Since the gyroradius and thus, the magnetic deflection scales with the particle energy it is not surprising that even for primary energies differing by one order of magnitude the impact of the field on the energy estimator is roughly the same.

The same exercise is performed with iron primary particles at 8 EeV resulting in $R_B = (1.25 \pm 0.26)$ %. It is significantly smaller by a factor of ~ 2 compared to the result for protons. This is surprising since the energy spectra of the charged shower particles should be similar and in first order approximation no difference is expected at all. Moreover, iron nuclei initiate air showers earlier in the atmosphere; this in turn leads to larger track lengths of the secondary particles and therefore should rather cause larger deflections in the B-field and a larger impact on the energy estimator. The origin of this discrepancy is not clear.

The work presented in this thesis assumes that protons of energies in the single-digit EeV range can be considered to yield the dominant fraction of the flux of UHECRs. A cross-check with AIRES produces good agreement with the CORSIKA results for this case, $R_B = (2.43 \pm 0.60)$%. In the following the parameters of the model are fixed with the values given in equations 5.20 and 5.19.

5.3.5 Impact on Anisotropy Searches

The effect of the geomagnetic field on the energy estimator is propagated to the reconstructed energy and eventually, it affects the event rate expectation for different directions as soon as an energy cut is applied. In order to produce a reasonable estimate of the amplitude of the modulation of the event rate the step from $S(1000)$ to energy will be considered linear, i.e.

the assumption is made that the parameters found in equations 5.20 and 5.19 for the variation of $S(1000)$ can be taken as they are and used to describe the variation of the energy E. With it the amplitude transferred to a modulation of the even rate can be derived from the energy spectrum:

$$\frac{dN}{dE} \propto E^{-\xi} \tag{5.21}$$

with $\xi = 2.6$ in the range of energies of interest above $E > 3$ EeV. A variation of the energy leads to a variation of the event rate with an amplitude larger by a factor of $\xi - 1 = 1.6$. Therefore, the amplitude parameter of the model on event rate level becomes

$$R_B^N = 1.6 \times (2.43 \pm 0.27)\% = (3.89 \pm 0.43)\% \,. \tag{5.22}$$

With this amplitude the isotropic expectation of the distribution of arrival directions in local coordinates is changed. This changed local acceptance is transformed to equatorial coordinates by rotation as displayed in figure 3.8 and described in appendix A. Finally, the transformed acceptance cone needs to be rotated once about the axis of the equatorial system corresponding to the integration over one sidereal day. The resulting sky map is identified as the expected distribution of directions from isotropically arriving cosmic rays when affected by the B-field. It is compared to the isotropic expectation when neglecting the field, i.e. the relative exposure map of the SD according to equation 3.4.

The comparison is performed by computing and plotting the sky map of the ratio of the respective bin entries in the two maps, see figure 5.13. The ratio is plotted on both the full sky and in the projection to the declination coordinate. An increase of the rate of roughly 2 % at the south pole is obtained when not accounting for the influence of the geomagnetic field. As mentioned before, the effect is constant in time and thus, does not affect the right ascension distribution.

5.3.6 Correction of the Effect

With the previous subsection an estimate is given of the amplitude of the influence of the geomagnetic field effect on the event rate. However, the correction of the influence of the B-field will be performed on the reconstruction level closest to where the actual variation in terms of magnetic deflection occurs, i.e. on $S(1000)$ level. The correction of the energy estimator is obtained from the reorganisation of equation 5.17,

$$S_{\text{off}} = S_{\text{on}}(1+s)^{-1} = S_{\text{on}} \left(1 + R_B \frac{\sin^2(\Omega_B) \cdot \cos^n(\theta_B)}{\cos^n(\theta)} \right)^{-1} . \tag{5.23}$$

Following the principle in the section on weather effects, this relation produces the energy estimator that would have been measured in absence of the geomagnetic field. After correcting all records of S_{on} the known relative exposure can be made use of again in anisotropy studies.

5.4 Summary

Three local effects have been described in the previous sections. All of them can be considered properties of the (surface) detector in the broadest sense and all of them have been shown to induce significant modulations of the distribution of arrival directions.

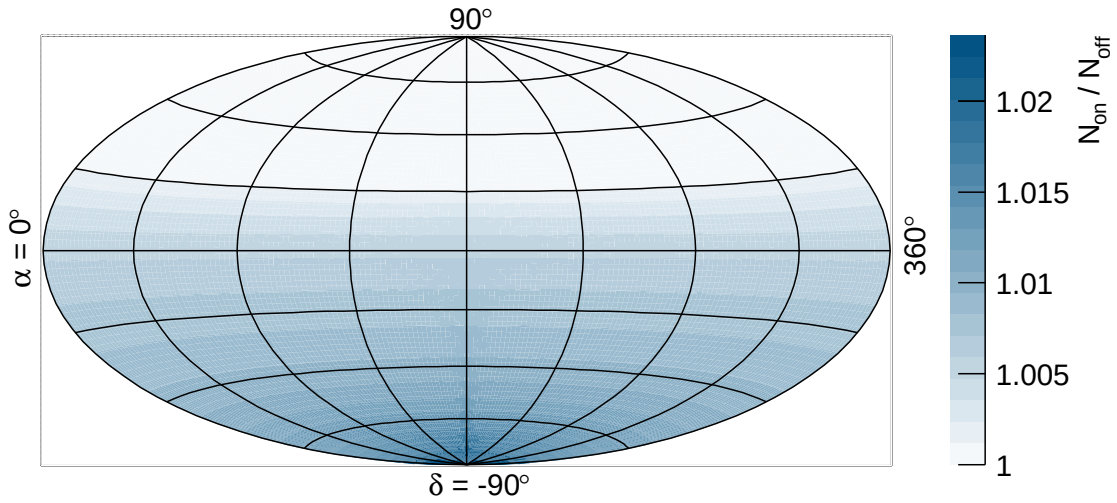

(a)

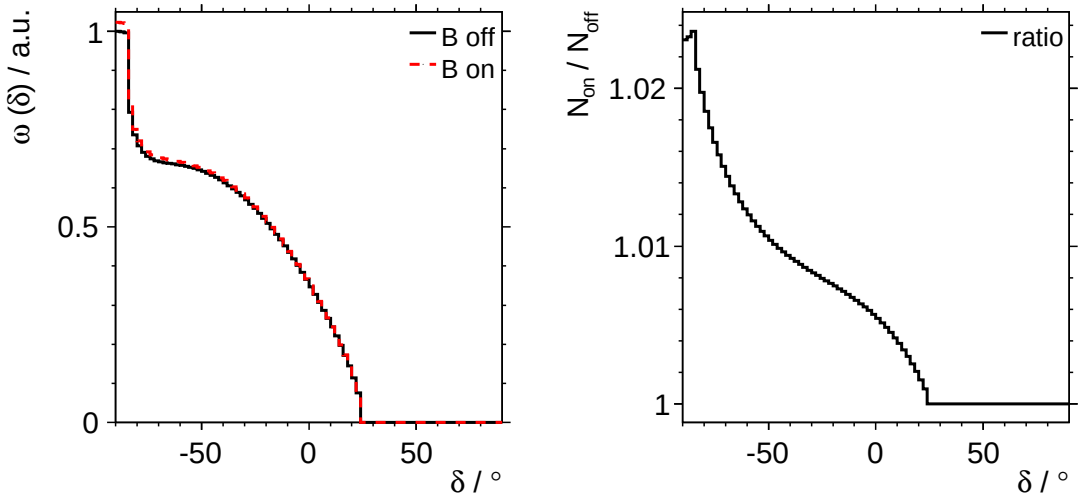

(b)

Figure 5.13: Estimate of the influence of the B-field on the event rate. The upper plot shows the ratio map of the scenarios with B-field switched on and off. The underlying distributions of the declination coordinate are given in the left lower plot and a declination projection of the ratio map, i.e. the ratio of the two curves on the left, is displayed on the right. See text for details.

1. The varying size of the SD over time immediately affects the expectation of the event rate over right ascension. The amplitude of the relative modulation of the event rate has been estimated to be of the order of ~ 0.5 %. A correction of this effect can be performed by inversely weighting the event rate with the cell seconds, i.e. the actual size of the exposure a certain region of the sky has been observed with.
   The concept of how to account for the variation of the area of the SD was presented in [Aub05, Mol05, Abr11c]. The correction has to be applied individually to the respective data set under study; in this work it will be performed on the data taken in the time interval from January 2004 until December 2010.

2. Daily and seasonal changes of the atmospheric conditions such as air density and pressure above the SD induce a modulation of the energy estimator $S(1000)$. This variation over time is propagated to the event rate as soon as an energy cut is applied. The amplitude of the corresponding modulation of the event rate over right ascension has been estimated to be ~ 0.5 %. The correction is applied on $S(1000)$ level by means of equation 5.2.
   The concept of how to account for the changing weather conditions was presented in [Abr09a, Abr11c]. The procedure of the corresponding correction is applied in this work.

3. The geomagnetic field deflects charged secondary shower particles. The resulting distortion of the lateral distribution of these particles in the shower plane measured at ground level affects the energy estimator. Correspondingly, the energy estimator of the SD is varied systematically depending on the arrival direction of the shower. Again, this variation is propagated to an event rate modulation. This time, the declination distribution is affected only, since the geomagnetic field can be considered constant in direction and strength. The amplitude of the modulation of the event rate has been estimated to be of the order of ~ 2 %. The correction is applied on $S(1000)$ level by means of equation 5.23.
   In this work a model of the influence of the geomagnetic field on the energy estimator has been derived from an intuitive approach. The parameters of the model have been obtained from the complete chain of simulations and reconstructions of air showers. Both the model and the results of the parameters agree with a study performed in parallel making use of a more rigorous approach within the Large Scale Anisotropy task force of the Pierre Auger Collaboration. The results of both approaches will be published soon [Abr11b].

Chapter 6

Methods to Study Large Scale Anisotropy

In this chapter, several approaches to investigate large scale anisotropy will be discussed. All studies will be restricted to largest angular scales, i.e. first order harmonic modulations in the distribution of the arrival directions of UHECRs. Motivation for dipole searches in general have been given in section 2.5.4. In addition to simple single source models, the Compton-Getting effect and galactic magnetic field models are supposed to be capable of causing dipolar patterns. The latter two are known to produce testable predictions concerning the dipole amplitude (and direction). In the following, a brief general introduction to standard methods for large scale anisotropy studies is given. Subsequently, four methods applied in the course of this work are presented alongside their individual properties.

Introduction

The multipole expansion can be considered the standard method for anisotropy studies at all angular scales. It is realised by spherical harmonic transforms comparable to the Fourier transform in Cartesian coordinates. While the Fourier transform makes use of sine and cosine functions of integral multiples of frequency in units of $1/2\pi$, the analogue transforms on the sphere take advantage of spherical harmonics which are obtained as the solution of the Laplacian equation in spherical coordinates. These functions are defined with the angles θ and ϕ on the unit sphere,

$$Y_{\ell m}(\theta,\phi) = \sqrt{\frac{2\ell+1}{4\pi}\frac{(\ell-m)!}{(\ell+m)!}}\, P_\ell^m(\cos\theta)\, e^{\mathrm{i}m\phi}, \tag{6.1}$$

with the associated Legendre polynomials P_ℓ^m and the coefficients $\ell = 0,\ 1,\ 2, \ldots$ and $m = 0,\ \pm1, \ldots,\ \pm\ell$. The zeroth order ($\ell = 0$) describes a monopole, the first order describes a dipole ($\ell = 1$), second order is quadrupole ($\ell = 2$), third is octupole ($\ell = 3$) and so on. An overview of the first orders of real spherical harmonics is given in figure 6.1. A projection of these excluding the monopole is displayed in figure 6.2 alongside the formulas computed from equation 6.1. Spherical harmonics are orthonormal,

$$\int_{\theta=0}^{\pi}\int_{\phi=0}^{2\pi} Y_{\ell m} Y^*_{\ell' m'}\, d\Omega = \delta_{\ell\ell'}\ \delta_{mm'}\ . \tag{6.2}$$

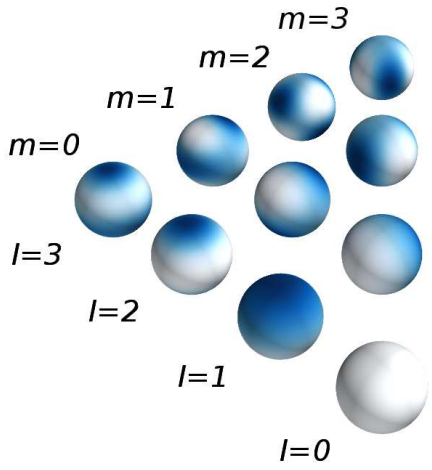

Figure 6.1: First orders of real spherical harmonics $Y_{\ell m}(\theta,\phi)$. The coefficient ℓ indicates the order of the multipole and is chosen so that the real functions for a monopole ($\ell = 0$), a dipole ($\ell = 1$), a quadrupole ($\ell = 2$) and an octupole ($\ell = 3$) are displayed for values of $m \leq \ell$.

The expansion in spherical harmonics of a distribution of (arrival) directions on the sphere is commonly referred to as the *multipole expansion*. This leads to a description of the original distribution function $f(\theta,\phi)$:

$$f(\theta,\phi) = \sum_{\ell=0}^{\infty} \sum_{m=-\ell}^{\ell} a_{\ell,m}\, Y_{\ell,m}(\theta,\phi) \tag{6.3}$$

with the multipole coefficients $a_{\ell,m}$ for the spherical harmonics $Y_{\ell,m}$. Truncation of this infinite sum provides an approximation of $f(\theta,\phi)$ for a desired angular precision. The range of angular scales the approximation comprises is determined by the values of ℓ considered in the sum. For example, a purely dipolar distribution will result in $a_{\ell,m} \neq 0$ only for $\ell \equiv 1$. In this case, there are three values available for $|m| \leq 1$ leading to three multipole coefficients $a_{\ell,m}$. All of them describe amplitudes of dipoles for different directions on the sphere, compare e.g. to figure 6.2, so that the combinations of these will allow for the description of a dipole of any direction and amplitude. Just to note the obvious: The number of parameters necessary to define a dipole also equals three, i.e. the polar and azimuthal angles θ_D and ϕ_D of the dipole axis and the amplitude D. In general, the parameter ℓ fixes the multipole order and thus, the angular range as displayed in figure 6.2. Together with the parameter m the orientation of the respective multipole is determined.

After the expansion in spherical harmonics, excesses and deficits (with respect to the monopole) of the contribution of angular scales to the distribution $f(\theta,\phi)$ can be quantified by means of the multipole moments C_ℓ,

$$C_\ell = \frac{1}{2\ell+1} \sum_{m=-\ell}^{\ell} |a_{\ell,m}|^2 \,. \tag{6.4}$$

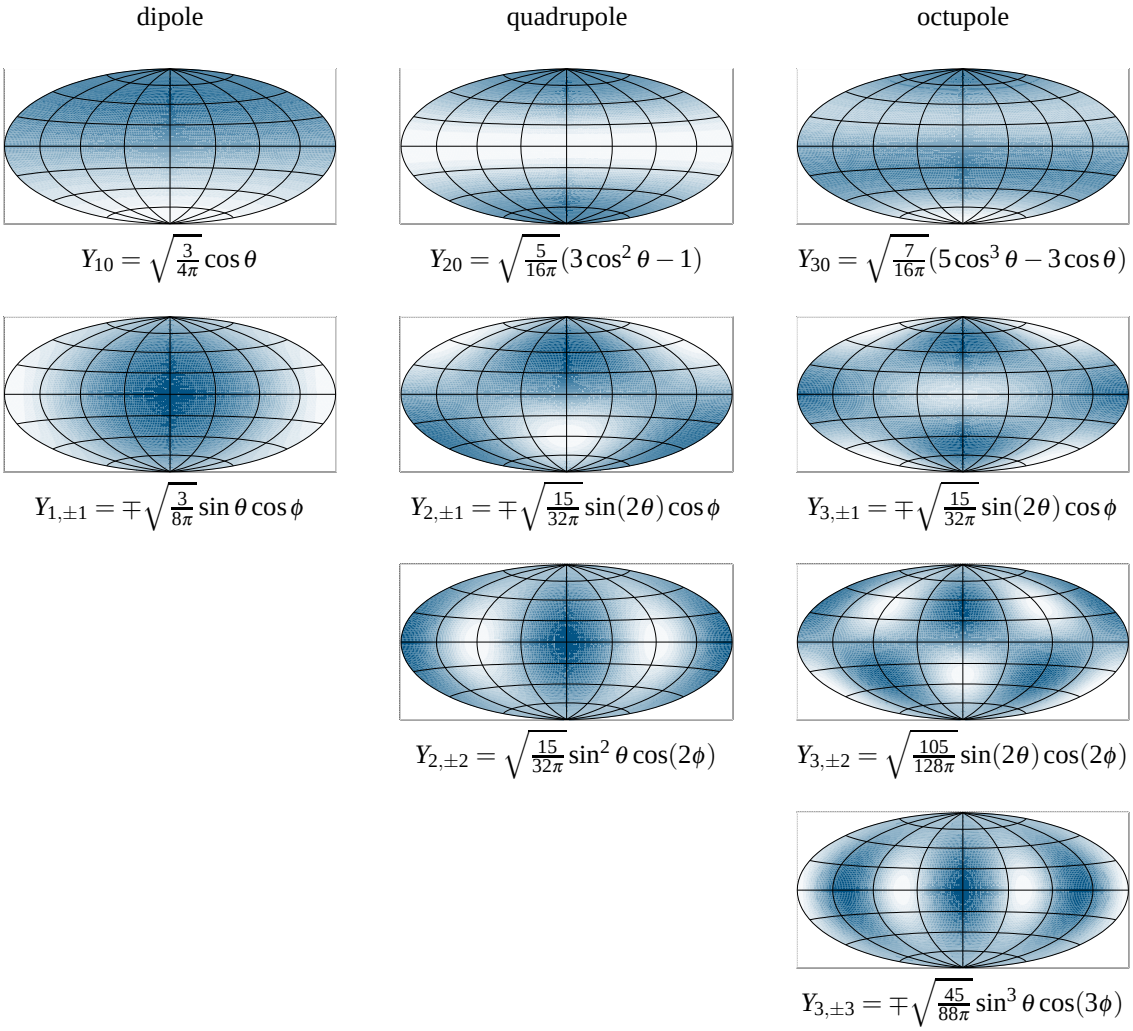

Figure 6.2: First orders of real spherical harmonics $Y_{\ell m}(\theta,\phi)$. Similar to figure 6.1, the functions are given for coefficients $\ell = 1,2,3$ and $|m| = 0,1,2,3$ in the Hammer projection of the sphere, see chapter A for details. The monopole at $\ell = 0$ is not shown here, it is defined by the constant $Y_{00} = \frac{1}{\sqrt{4\pi}}$.

Doing so, the orientation of the multipoles is ignored and a measure of the angular power of the underlying distribution is obtained.

Multipole expansions have been applied successfully by the CMB community to derive the angular power spectrum of the distribution of cosmic microwave background photons, e.g. by the COBE and WMAP experiments [Smo92, Hin07, Hin09, Lar11]. They work optimally in the case of full sky coverage, i.e. in the case where data is available and distributed on the complete sphere. However, they are applicable also to (weighted) fractions of the sky as they are typically observed by earth-bound EAS experiments such as the Pierre Auger Observatory which mainly covers the southern hemisphere. Its field of view within the typically applied zenith angle cut, $\theta \leq 60^\circ$, goes up to a declination of $\delta \approx 25^\circ$ in equatorial coordinates. Additionally, as already mentioned in chapter 3, the field of view is weighted by the coverage of the surface detector. The application of multipole expansions to the distribution of arrival directions as measured by the PAO will not be covered in this work and will be published by the Pierre Auger Collaboration soon.

Dipole

This chapter deals with first order harmonic modulations in the distribution of the right ascension on the circle ($\sim$ cosine) and in the distribution of both right ascension and declination on the sphere ($\sim$ dipole). The definition of the dipole in 2D is as simple as

$$f_{cos}(\alpha) = 1 + D_{2D}\cos(\alpha - \alpha_D) \,, \tag{6.5}$$

with α the known right ascension, D_{2D} the amplitude and α_D the phase of the cosine. For the definition of the dipole on the sphere it makes sense to switch over to vector notation: Let $\mathbf{D} = (D, \delta_D, \alpha_D)$ be the dipole vector of amplitude D and $\mathbf{u} = (1, \delta, \alpha)$ the unit vector on the sphere of the equatorial sky, then

$$f_{dip}(\delta, \alpha; \mathbf{D}) = 1 + \mathbf{D} \cdot \mathbf{u} \,. \tag{6.6}$$

To build the bridge to the 2D case, equation 6.5, and to make use of the axial symmetry of the pattern about the dipole direction it is useful to introduce the angle Ω between the direction $\mathbf{D}$ of the dipole peak and the unit vector $\mathbf{u}$ on the sphere,

$$\Omega = \sphericalangle(\mathbf{D}, \mathbf{u}) = \arccos\left(\frac{\mathbf{D} \cdot \mathbf{u}}{D}\right) \,. \tag{6.7}$$

Very similar to equation 6.5 the dipole expression then is

$$f_{dip}(\Omega; \mathbf{D}) = 1 + D\cos(\Omega) \,. \tag{6.8}$$

A full sky (i.e. full sphere) dipole f_{dip} according to equation 6.6 is given in figure 6.3 (top). It shows an example dipole with an amplitude and a direction of $(D, \delta_D, \alpha_D) = (0.2, 0^\circ, 270^\circ)$. To obtain an expectation of what this dipole looks like from the Pierre Auger Observatory's field of view the dipole must be multiplied with the coverage ω described in equation 3.4. This weighting produces the bottom plot of figure 6.3,

$$f_{dip}^{PAO}(\delta, \alpha; \mathbf{D}) = f_{dip}(\delta, \alpha; \mathbf{D}) \times \omega(\delta) \,. \tag{6.9}$$

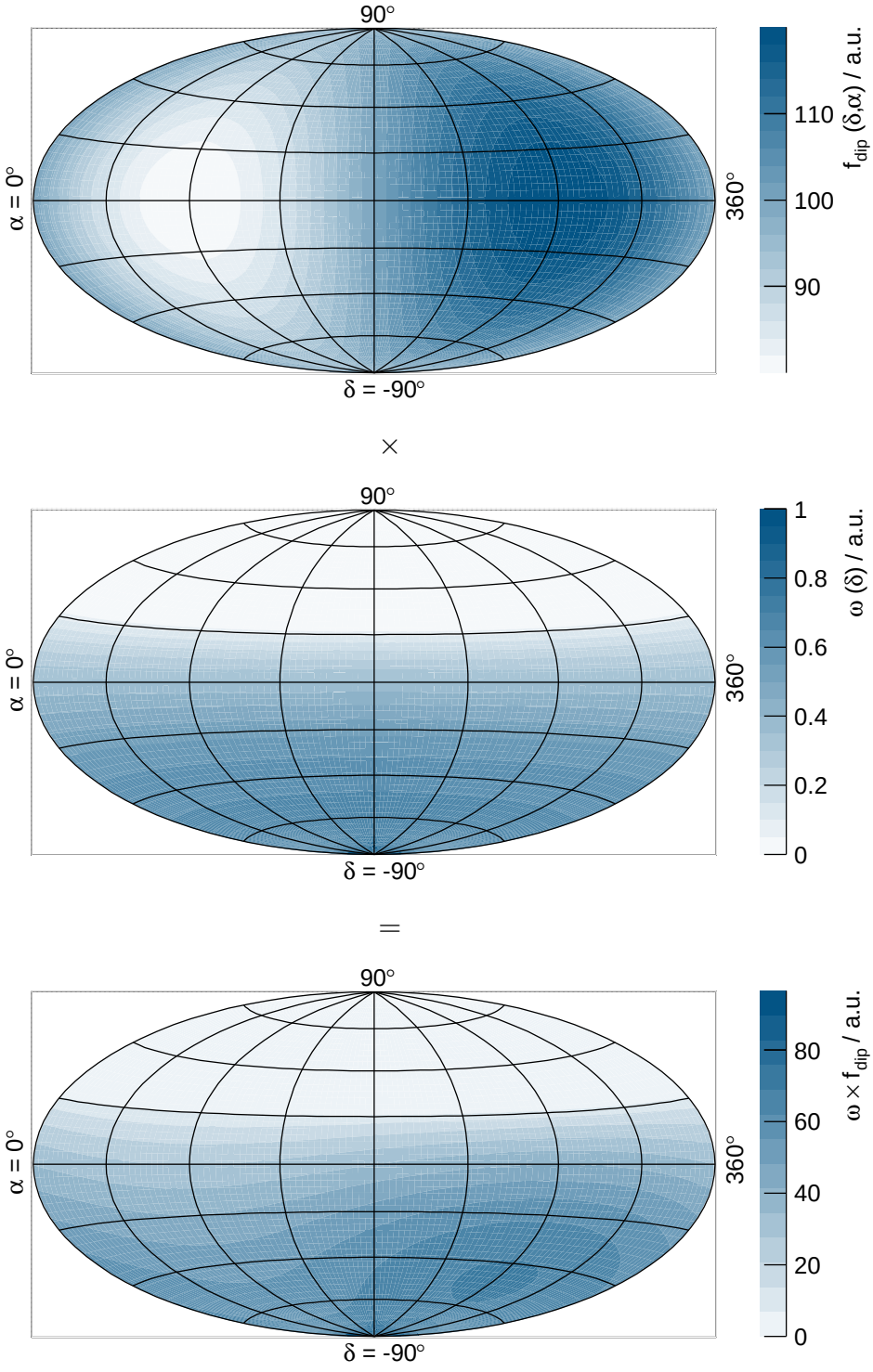

Figure 6.3: Full sky dipole as observed from the field of view of the PAO. The top plot shows the full sky dipole f_{dip} with parameters $(D, \delta_D, \alpha_D) = (0.2, 0°, 270°)$. It has to be weighted with the coverage ω of the PAO (middle plot) to obtain what the PAO will observe from this dipole ($f_{dip} \times \omega$, bottom plot).

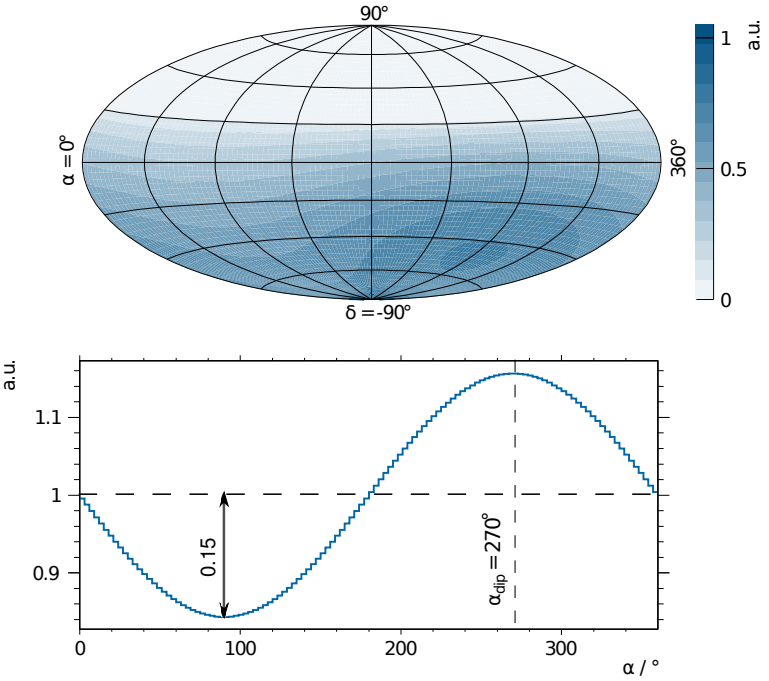

Figure 6.4: Dipole with parameters $(D, \delta_D, \alpha_D) = (0.2, 0°, 270°)$ observed from PAO and corresponding cosine in right ascension. The phase in right ascension is reproduced correctly. However, even though in this case the dipole points to the equator and $\cos\delta_D \equiv 1$, care has to be taken of the evaluation of the amplitude D_{2D} which scales with $\langle\cos\delta\rangle$ according to the preferred arrival directions caused by the coverage.

There are two general points to consider when going from a full sphere investigation of a dipolar pattern to a cosine pattern in the right ascension coordinate: Firstly, since the directional information of the declination component is ignored, the number of parameters describing a dipolar anisotropy decreases from three (D, α_D, δ_D) to two (D_{2D}, α_D). On the one hand, that improves the situation in terms of increased statistics per degree of freedom since the number of events remains the same. On the other hand, only dipolar patterns with a direction not too close to one of the poles of the equatorial coordinate system will be accessible. In principle, the amplitude D_{2D} reconstructible with the 2D study in right ascension scales with the cosine of the declination coordinate of the direction of the dipole, $\cos\delta_D$; similarly, it scales with the cosines of the average of the cosines of the measured declination values, $\langle\cos\delta\rangle$. The geometric reasoning addressing the latter statements is given in appendix C. Thus, an example dipole of amplitude $D = 0.2$ pointing to $(\delta_D, \alpha_D) = (0°, 270°)$ will result in a cosine in the right ascension distribution with correct phase $\alpha_D = 270°$ but a reduced amplitude of $D_{2D} \approx 0.15$ %, see figure 6.4. Secondly, time-independent local effects on the event rate distribution can introduce systematic distortions into the declination coordinate; however, these effects do not affect the study in right ascension. This aspect was covered in detail in chapter 5.

For the two-dimensional case of deriving the amplitude and phase of the right ascension distribution, two different methods will be discussed: The standard Rayleigh method [Lin75] and a new method making use of wavelet transforms. Then the three dimensional investigation of the complete sphere of arrival directions including the declination component will

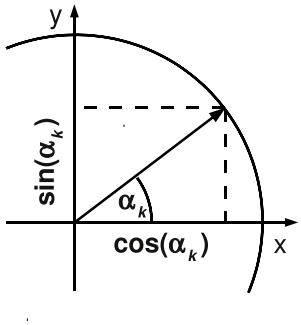

Figure 6.5: Principle of the Rayleigh method. To obtain the phase and amplitude of a given distribution of angles α_k on the unit circle the x and y components in Cartesian coordinates are averaged, see text for details.

be presented in terms of two new dipole fit methods. For the sake of consistency, the names of the angles will be the ones that make up the sky map of arrival directions of UHECRs in equatorial coordinates, i.e. right ascension α and declination δ.

6.1 Methods in Two Dimensions

6.1.1 Rayleigh Method

The Rayleigh method to study (first order) harmonic modulations is directly obtained from discrete Fourier analysis. Interpreting the right ascension α as the polar angle in the x,y-plane, arrival directions can be identified as unit vectors distributed on the unit circle. The distribution of these angles shall be given by the function $f_c(\alpha)$; it is also determined by the Fourier series with Fourier coefficients a_k:

$$f_c(\alpha) = \frac{a_0}{2} \sum_{k=1}^{n} \left(a_k \cos(k\alpha) + b_k \sin(k\alpha) \right) \ . \tag{6.10}$$

For the first order harmonic, $k \equiv 1$, the Fourier coefficients a_1 and b_1 are obtained as

$$a_k = \frac{1}{\pi} \int_0^{2\pi} f(\alpha) \cos\alpha \, d\alpha \quad \text{and} \quad b_k = \frac{1}{\pi} \int_0^{2\pi} f(\alpha) \sin\alpha \, d\alpha \ . \tag{6.11}$$

These coefficients can be identified as the x and y coordinate of the sum of the unit vectors that indicates the direction of the dipole, i.e. the amplitude and phase of the sine on the circle, see figure 6.5. The number of arrival directions, i.e. values of angles in right ascension α, is finite which makes it reasonable to express a_1 and b_1 in discrete terms

$$a_1 \approx X = \frac{2}{N} \sum_{k=1}^{N} f(\alpha_k) \cos\alpha_k \quad \text{and} \quad b_k \approx Y = \frac{2}{N} \sum_{k=1}^{N} f(\alpha_k) \sin\alpha_k \ . \tag{6.12}$$

Note that the factor $\frac{2}{N}$ is obtained from the approximation of the integrals with rectangular areas of equal width w,

$$\int_a^b g(x) \, dx \approx w(y_1 + y_2 + \ldots + y_N) \ . \tag{6.13}$$

The width is identified as $w = \frac{2\pi}{N}$ and observing equation 6.11 this leads to the factor of $\frac{2}{N}$.

In equation 6.12 the discrete versions X and Y of a_1 and b_1 have been introduced. In a sense, they are the averaged values of the x and y component, respectively, computed from the cosines and sines of the set of right ascension angles. The function $f(\alpha)$ describes the probability density of the distribution of α. It is not known a priori when investigating real data; it will be taken as constant, $f(\alpha) \equiv 1$, in the simplest case of the hypothesis of isotropy. This simplifies equation 6.12 to

$$X = \frac{2}{N}\sum_{k=1}^{N}\cos\alpha_k \quad \text{and} \quad Y = \frac{2}{N}\sum_{k=1}^{N}\sin\alpha_k \; . \tag{6.14}$$

From these averaged values of x and y components the amplitude D_{2D} and phase α_D can be computed as

$$D_{2D} = \sqrt{X^2+Y^2} \quad \text{and} \quad \tan\alpha_D = \frac{Y}{X} \; . \tag{6.15}$$

The uncertainties of the amplitude and phase measurements are determined by the statistics available, i.e. the number N of entries in the set of arrival directions. More precisely, they are propagated from the uncertainties of X and Y, $\sigma_X = \sigma_Y = \sqrt{\frac{2}{N}}$. This leads to

$$\sigma(D_{2D}) = \sqrt{\frac{2}{N}} \quad \text{and} \quad \sigma(\alpha_D) = \frac{1}{D_{2D}}\sqrt{\frac{2}{N}} \; . \tag{6.16}$$

The uncertainty of the amplitude is computed simply making use of $D_{2D}^2 = X^2 + Y^2$. Furthermore, it is intuitively clear that the uncertainty of the phase measurement relates to the size of the amplitude and should decrease for larger amplitudes: In fact, with the help of $\frac{d}{d\xi}\arctan(\xi) = \frac{1}{1+\xi^2}$, it turns out that the phase uncertainty is inversely proportional to the amplitude D_{2D}.

6.1.2 Wavelet Analysis

Next to standard Fourier transforms, wavelet transforms have been developed and adapted during the last few decades in many fields of digital signal processing, e.g. in the compression of image data and in electrocardiogram analysis. Furthermore, wavelet transforms have been proved useful for the testing of non-Gaussianity in the data of the CMB recorded by WMAP [Hob98, Vie04]. In this subsection the basic numerical principles of wavelets and wavelet transforms will be elucidated. Then their applicability to anisotropy studies will be demonstrated using the example of a cosine pattern in right ascension. The technical content of this subsection is based on the "practical guide to wavelet analysis" found in [Tor98]. The work presented in this subsection has provided a basis for the understanding and application of wavelet analyses in 2D and on the sphere of arrival directions. It aims at introducing the principle of wavelet transforms and the way how they can be applied successfully in anisotropy studies.

Wavelets are brief wave-like oscillations which either have finite length or are fast decaying. The latter is typically achieved by scaling with an exponentially decreasing term. In this work use is made of the well-known Mexican Hat wavelet; since wavelet transforms will be applied in the right ascension space, the argument in this 2D study will again be α:

$$\psi_{MH}(\alpha) \propto (1-\alpha^2)\exp(-\alpha^2/2) \; . \tag{6.17}$$

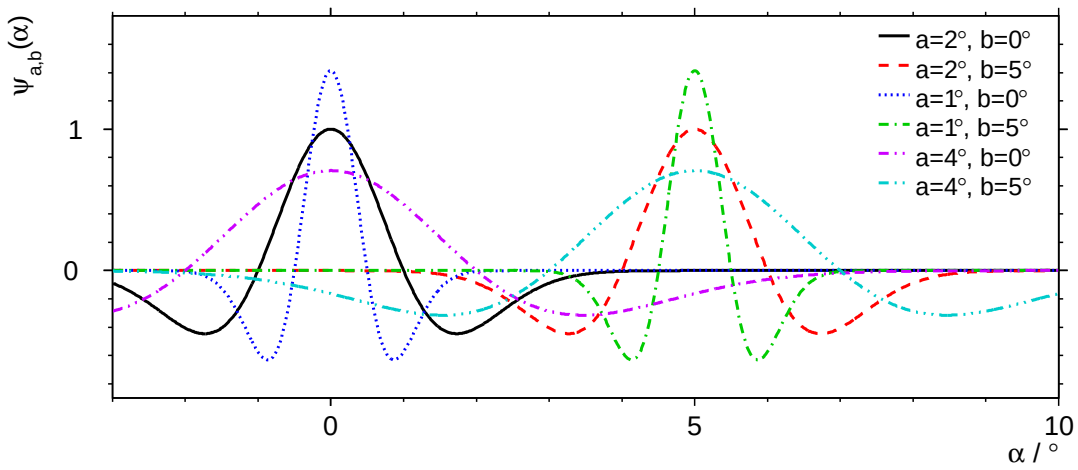

Figure 6.6: Mexican Hat wavelet examples: Some combinations of values for a and b are displayed. The fundamental mother wavelet with $(a,b) = (2^\circ, 0^\circ)$ is indicated by the black solid line. See text for further details.

This equation expresses the Mexican Hat as a *mother wavelet*. The mother wavelet can be adjusted in terms of a scaling of the width by the scale parameter a and a shift of the argument by the shift parameter b. Consequently, a family of wavelet functions is generated:

$$\psi_{MH}^{a,b}(\alpha) = \sqrt{\frac{2^\circ}{|a|}}\psi\left(\frac{2^\circ(\alpha-b)}{a}\right) . \tag{6.18}$$

This definition allows to identify the scale a of the wavelet as the width of the wavelet in terms of the distance between the two zero-crossings and the shift b as the position of the maximum of the wavelet. For $a \equiv 2^\circ$ and $b \equiv 0^\circ$ the mother wavelet is reproduced. All other cases are commonly referred to as daughter wavelets. Some combinations of values for a and b are illustrated in figure 6.6.

Wavelets can be combined with a signal trace to extract information from the unknown signal. This procedure is commonly referred to as the wavelet transform; it is the convolution of the wavelet functions ψ of different scales with the signal trace $f(\alpha)$ that is subject to analysis. Signal trace is another place holder for the distribution of angles in this context motivated by the original application of wavelet transforms in signal processing. The convolution can be realised by means of the Fast Fourier Transform (FFT) [Coo65], a numerically highly efficient version of the Discrete Fourier Transform (DFT). Before the discussion of convolutions and wavelet transforms, the basic properties of the DFT will be elucidated briefly.

The DFT provides a measure of to what extent a frequency, i.e. an angular scale, is contained in a signal trace. In the case of 2D anisotropy studies the signal trace is given by the right ascension distribution $f_k = f(\alpha_k)$:

$$F_j = \sum_{k=0}^{N-1} f_k \cdot \exp\left(-\frac{2\pi i}{N} jk\right) \qquad j = 0,\ldots,N-1 , \tag{6.19}$$

with i the imaginary unit and N the number of bins of the distribution in α. The $N-1$ values of F_j make up the discrete Fourier transform of f. Correspondingly, the inverse discrete

Fourier transform is given by

$$f_k = \sum_{j=0}^{N-1} F_j \cdot \exp\left(-\frac{2\pi i}{N} kj\right) \qquad k = 0, ..., N-1 \,, \tag{6.20}$$

The coefficients F_j are complex numbers that can be denoted by amplitude A_j and phase $\alpha_{D,j}$ similarly to what has been discussed in the previous subsection on the Rayleigh method:

$$A_j = |F_j| = \sqrt{\Re^2(F_j) + \Im^2(F_j)} \quad \text{and} \quad \tan\alpha_{D,j} = \frac{\Im(F_j)}{\Re(F_j)} \tag{6.21}$$

with $\Re(F_j)$ the real part and $\Im(F_j)$ the imaginary part of F_j. The numbers producing the right ascension distribution, f_k, are real numbers, $f_k \equiv \Re(f_k) \;\forall\, k \in [0, ..., N-1]$. In this case the DFT obeys the following symmetry:

$$F_j = F^*_{N-j} \,. \tag{6.22}$$

This means that the output of the DFT of a signal trace made up of real numbers is half redundant. E.g. for even N there are two real elements, F_0 and $F_{N/2}$, and $N/2-1$ non-redundant complex numbers, so that when accounting for both real and imaginary parts of the latter there are in total N independent real numbers (imaginary and real parts). Thus, the amount of information represented by the original N independent values of f_k is conserved. Consequently, both the information about typical angular scales of a signal and the information about the position where excesses at the respective scale are observed within the signal trace will be conserved and transferred from angle space to frequency space.

In this work, the implementation of the real FFT and inverse real FFT provided with the numerical python package `numpy` has been used. For *one* set of scale and shift parameters $a = a_0$ and $b = b_0$, the convolution of the signal trace f and the wavelet ψ^{a_0,b_0} comprises the following steps:

(a) Provide the binned signal trace $f(\alpha)$ and a binned version of the wavelet test function $\psi^{a_0,b_0}(\alpha)$

(b) Transform both f_k and $\psi_k^{a_0,b_0}$ into frequency space according to the rules of the DFT, see equation 6.19; this results in the complex coefficients F_j and $\Psi_j^{a_0,b_0}$, respectively.

(c) Multiply the coefficients in frequency space: $P_j = F_j \times \Psi_j$.

(d) Inversely Fourier transform P_j to angle space and obtain p_k according to equation 6.20.

p is a measure of **how well** and **where** the signal trace f, i.e. the right ascension distribution $f(\alpha)$, agrees with the wavelet representation ψ^{a_0,b_0} in terms of angular scales. As an example, in figure 6.7 a simulated signal is considered which is of a shape similar to the Mexican Hat wavelet (in fact it is a Mexican Hat with $a = 10^\circ$ and $b = 100^\circ$). The wavelet test function is $\psi^{20,0}$ and can be derived from equation 6.17. Note that in this example only one value for the scale parameter is used for the wavelet $a = 20^\circ$.

The scale of f is not perfectly recovered in p since the scales of f ($a = 10^\circ$) and ψ ($a = 20^\circ$) do not (perfectly) match. However, the convolution p correctly reproduces the position of the signal peak at 100°. Extrema of p can be interpreted as indicators of the

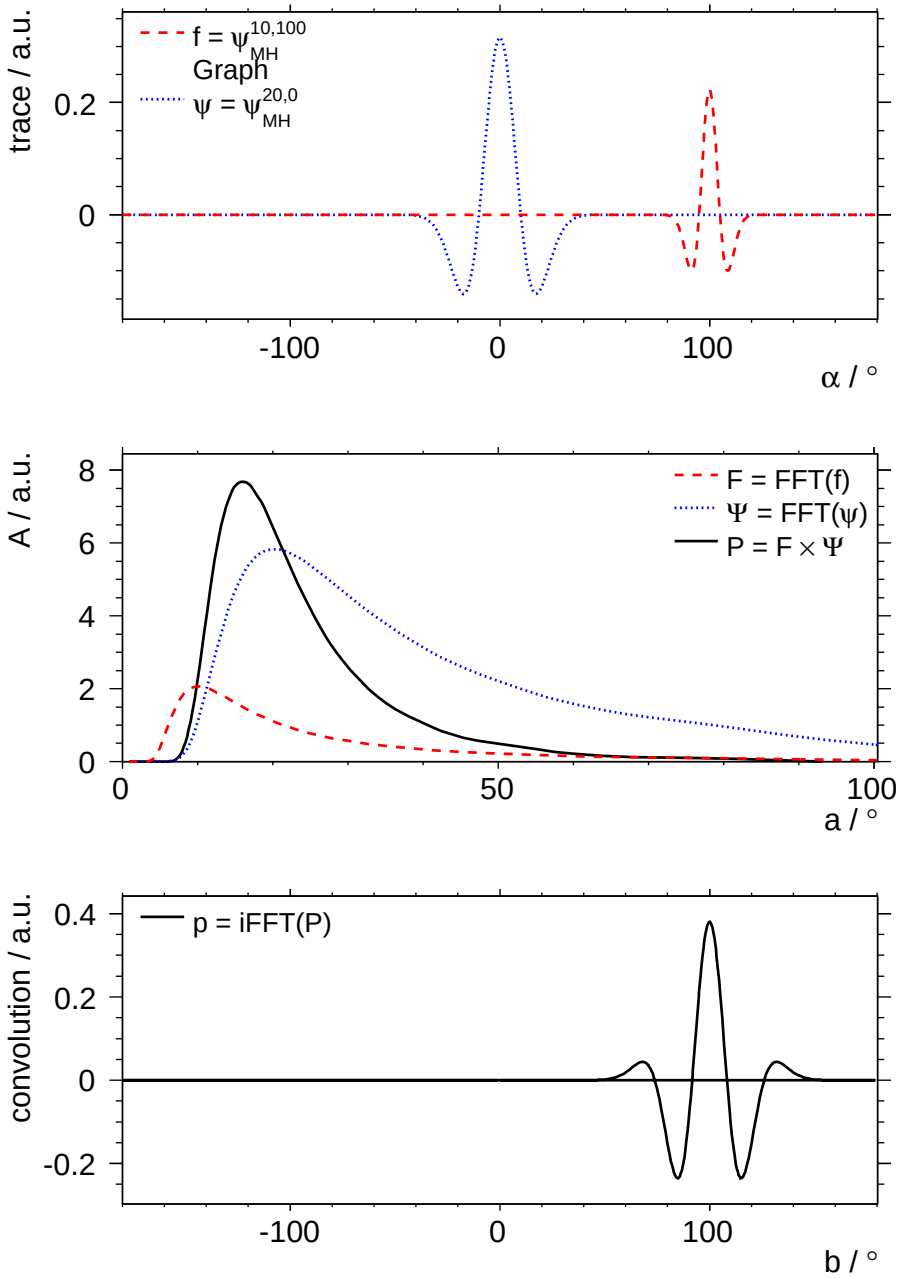

Figure 6.7: Example of wavelet transform at one angular scale. The top plot shows the wavelet function ψ and a signal trace f. For the sake of simplicity, in fact both are Mexican Hat wavelets with the wavelet $\psi = \psi_{MH}^{20,0}$ and the signal $f = \psi_{MH}^{10,100}$. The figure in the middle indicates the amplitudes A of the FFTs of the wavelet Ψ and the signal trace F. Also the product of the two transforms $P = F \times \Psi$ is shown and they are plotted against the angular scale. The bottom plot shows the result of the iFFT of the product, p, which is also referred to as the convolution of f and ψ.

positions where to move ψ, i.e. which value to assign to the shift parameter b to make extrema of f and ψ coincide. In this context maxima of p correspond to extrema of f and ψ of same sign while minima indicate the coincidence of extrema of opposite signs. The major peak of p is found at 100° which corresponds to the shift of ψ necessary to make the main maxima of f and ψ coincide. The two valleys of p indicate the positions of coincidences of extrema of opposite signs of f and $\psi^{20,0}$, respectively. Finally, two side peaks in p occur at positions where the wavelet needs to be shifted to cause the coincidence of two minima of f and ψ. In many applications the square of the convolution, p^2, is used to describe matches of angular scales of wavelet and signal regardless of the signs of matching extrema.

For a complete wavelet transform, the steps 2-4 described above have to be performed on each scale a out of a set of N_a values. In principle, an arbitrary choice of scale parameters is possible and the wavelet transform can become sensitive to (all) different angular scales sensibly accessible with the binning of the signal trace. The N_a convolutions obtained this way are then summed up and yield a complete picture of the presence and position of corresponding scales in the signal trace. The information on the position of the signal most adequately represented by the wavelet at a given scale is directly obtained from the procedure described above. This property is the most remarkable difference of wavelet transforms compared to standard Fourier transforms: Wavelet transforms are sensitive to both frequencies (angular scales) and shifts (positions) of features in the signal while for Fourier transforms only the former applies.

An example of a complete wavelet transform of simulated test data set drawn from a cosine signal with amplitude $D_{2D} = 0.03$ and phase $\alpha_D = 135°$ is shown in figure 6.8. The scale parameter range made use of is $a = 2°, ..., 360°$ in whole numbers. As expected, the convolution p of the signal trace f and the wavelets $\psi^{a,0}$ peaks at the scale of 180° which is the half period of the cosine. The most remarkable observation is the confirmation of the sensitivity of the wavelet transform to the position of the peak of the cosine, as displayed in the colour plot: The wavelet transform does reproduce both the position of the maximum (phase $\alpha_D = 135°$) and minimum ($\alpha_D + 180° = 315°$) of the cosine.

The phase α_D of the cosine modulation can be reconstructed from the position of the maximum of the convolution p at the scale of interest. However, it is more difficult to obtain the amplitude D_{2D}. In this work the following approach has been chosen to derive the amplitude value: A Monte Carlo data set is simulated from a cosine with variable amplitude, the phase is set to zero since it does not matter in this ansatz. The MC data set is convoluted with the wavelet in the same procedure that is applied to the simulated test data set. The amplitude of the MC data set is calibrated so that the value of the maximum of its convolution with the wavelet matches the value of the maximum of the convolution of the simulated test data set with the wavelet.

It must be emphasized that the technique of applying wavelet transforms in the field of anisotropy studies is rather new. Wavelet transforms in 2D as described in this section do not natively expand a signal trace into orders of harmonic modulations. This approach has been chosen in order to provide a method that is testable and comparable with respect to a method established for decades, the Rayleigh method. Eventually, many kinds of further questions should be answered prior to the establishment of this new technique. The type of the wavelet function to be employed, the estimator to derive amplitudes, phases and significances are only some of the issues that must be addressed. However, this is not the aim of this work which may rather be considered a feasibility study.

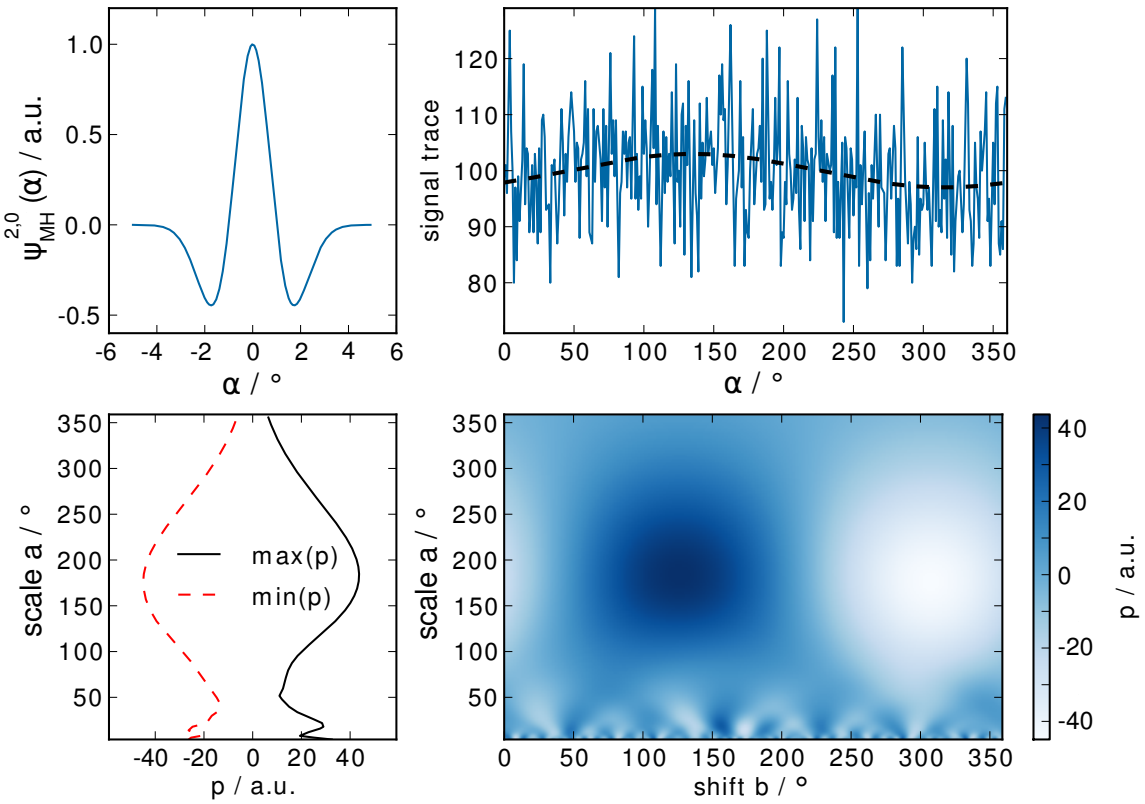

Figure 6.8: Example of a wavelet transform. The top right plot shows the signal trace of a cosine with amplitude $r = 0.03$ and phase $\alpha_D = 135°$ (black dashed). For a more realistic scenario the signal trace is randomised with Poisson uncertainties (blue solid). The top left plot shows the test wavelet $\psi^{a,0}_{MH}$ for the case of $a = 2°$. The bottom left plot indicates the maximum (black solid) and minimum (red dashed) values of the convolution p as obtained at various angular scales. The colour plot shows the convolution versus angular scale (y-axis) and direction α. It peaks largest at the correct angular scale of the half period of the cosine, 180°, and the position of the peak, i.e. the phase of the cosine.

6.2 Dipole Fit

In this subsection two possible realisations of a dipole fit method will be introduced. A dipole is the first order harmonic modulation in 3D, it is described on the equatorial sphere by equation 6.6. Figure 6.3 (bottom) shows what a dipole looks like in equatorial coordinates after being weighted with the coverage of the PAO, equation 3.4; it is described by the product given in equation 6.9: After normalisation to unity, this mathematical expression can be interpreted as the probability density function. For a given set of parameters of the dipole, (D, δ_D, α_D), it assigns the probability of occurrence to directions on the sphere. The dipole fit method presented here makes use of this p.d.f. in one out of two ways, respectively: The p.d.f. is either used for an unbinned maximum (log-) likelihood (LL) fit or for the preparation of reference distributions in a binned χ^2-fit. Both methods will be reviewed in the following.

6.2.1 Maximum Likelihood Method

In the course of the LL fit method the product of the individual probabilities of all N entries of arrival directions on the equatorial sky is computed for a given parameter set, i.e. dipole $\mathbf{D}$, from equation 6.9. This leads to the likelihood function

$$L(\mathbf{D}) = \prod_{i=1}^{N} f_{dip}^{PAO}(\delta_i, \alpha_i; \mathbf{D}) \; . \tag{6.23}$$

$$\ln L(\mathbf{D}) = \sum_{i=1}^{N} \ln f_{dip}^{PAO}(\delta_i, \alpha_i; \mathbf{D}) \; . \tag{6.24}$$

The main advantage of the LL method consists in its unbinned character; every single direction is immediately and precisely promoted to the p.d.f. and thus, to the likelihood function. This can be relevant especially for anisotropy searches at rather small angular scales where it makes a difference whether a couple of directions coincide within a solid angle of say 1° or in fact are distributed randomly within a solid angle of several degrees. This advantage is expected to play a minor role for models such as the dipole and other patterns of large angular scales which are rather insensitive to scales smaller than typical bin sizes.

6.2.2 χ^2 Method

The χ^2 fit method is a standard least squares method; it is applied on a binned equatorial sky map with N_B bins. The computation of the χ^2 is based on a binned reference map $f_{dip}^{PAO}(i_B; \mathbf{D})$ that yields the expectation for the respective dipole scenario and the binned map obtained from the data $f_{data}^{PAO}(i_B)$ with i_B the bin number and $f..(i_B..)$ the number of entries in the histograms of the data and model, respectively. The 2D histogram that contains the predicted distribution is filled from the probability density function in equation 6.9 for a given set of dipole parameters. This is done by setting the bin contents with the integral of the p.d.f. between the bin limits of the respective bin. After normalisation the contents of these maps are compared bin by bin,

$$\chi^2(\mathbf{D}) = \sum_{i_B=1}^{N_B} \frac{(f_{data}^{PAO}(i_B) - f_{dip}^{PAO}(i_B; \mathbf{D}))^2}{f_{dip}^{PAO}(i_B; \mathbf{D})} \; . \tag{6.25}$$

Note that in this context the uncertainty of the model given in the denominator is assumed to be Poissonian which is reasonable in case both histograms are normalised to the total number of entries N available in the data. The minimisation of $\chi^2(\mathbf{D})$ yields the dipole $\mathbf{D}$ that fits the data best. Computationally, the χ^2 fit is more efficient than the LL method since the amount of information that has to be processed is reduced due to the binning by a factor of $\mathcal{O}(10)-\mathcal{O}(100)$, typically. Furthermore, the value of $\chi^2(\mathbf{D})$ obtained from the minimisation process is a measure of the goodness of the fit, i.e. it quantifies how well the model describes the data. Technically, this is done through dividing by the number of degrees of freedom ndf which is given by the number of bins N_B minus the number of fit parameters, 3 in this case to determine a dipole, $ndf = N_B - 3$. The probability to find a χ^2 value larger than the one measured at the minimum is commonly referred to as the *p-value*. It is derived from the cumulative distribution function of the χ^2 distribution for a given value of ndf. Thus, the p-value is a measure of the probability that the data distribution originates from the fitted model.

6.2.3 Remarks

The dipole parameter set that describes the data distribution best, i.e. the solution to the maximisation of $\ln L(\mathbf{D})$ or minimisation of $\chi^2(\mathbf{D})$, respectively, is obtained numerically by means of an iterative procedure. In this work use has been made of the highly efficient tools of the MINUIT package [Jam75] provided with ROOT [Bru97]. It is worth repeating that for the correct assignment of the probabilities the dipole p.d.f. has to be normalised for every set of parameters; the integral will in general be affected by the choice of these parameters.

Brief Review of Other 3D Methods

Other 3D methods aiming at the reconstruction of dipoles in the distributions of arrival direction of UHECRs as recorded by earthbound experiments without full sky coverage have been studied and developed during the previous decade: It is possible to adapt the Rayleigh method to three dimensions for experiments of both full-sky [Som01] and partial-sky [Aub05] coverage. Furthermore, the two angular dimensions in equatorial coordinates can be analysed independently by applying the 2D Rayleigh method to the right ascension distribution and fitting the declination distribution with a relative exposure function which is adjusted to include a parametrised dipole [Mol05].

Chapter 7

Monte Carlo Studies

The properties of the large scale anisotropy methods described in chapter 6 are studied and compared. To this end, a large amount of Monte Carlo (MC) sets of arrival directions both in the absence (isotropy) and in the presence of a dipole of varying amplitude and direction has been produced. The arrival directions are diced from equation 6.9 and interpreted as devoid of local effects. The methods are applied to the resulting sky maps and the reconstruction precision is investigated. Furthermore, the significance of measured amplitudes is obtained from the comparison to isotropic results.

7.1 Monte Carlo Sky Maps

The parameters of the generated MC sets are given in table 7.1. The MC truth values of the parameters are denoted by $()^{true}$ while reconstructed values will be referred to as $()^{rec}$. The amplitude of the underlying dipole has been varied starting from the isotropic case, $D^{true} \equiv 0$, over small values up to rather large fractions of anisotropic contributions: It is of interest above which signal amplitude a method becomes sensitive to the underlying dipole parameters. Because of the rotational symmetry of the exposure of the PAO, no dependence of the behaviour of the respective method on the right ascension value of the dipole is expected; thus, it is fixed to $\alpha_D^{true} \equiv 0^\circ$ for all sets. On the contrary, the dependence of the methods on the dipole declination is investigated in more detail. The declination distribution of arrival directions recorded with the PAO is not flat but follows the relative exposure given in equation 3.4. The increasing exposure towards the southern range of declination values is likely to cause statistical fluctuations large enough to introduce a directional bias especially in case of the binned dipole fit method. This is studied by simulating sky maps with varying dipole declination in steps of 10° over the full range from north to south pole. The four methods are applied to every single MC sky map created this way. The results obtained with the two 2D methods are compared with each other as well as those obtained with the two 3D methods. However, it is not possible to directly compare the amplitudes reconstructed with the 2D methods to those of the 3D methods. A scaling of the 2D amplitudes is necessary as discussed in appendix C to account for the geographic latitude of the observatory as well as for the true declination of the dipole direction. Then, the amplitudes and right ascension phases reconstructed with 2D and 3D methods may be contrasted with each other.

Table 7.1: Parameters of the Monte Carlo simulations of sky maps. 190 combinations of parameters have been chosen. 500 maps have been produced for each of the parameter sets. 30000 directions have been diced for each map from the corresponding probability density function given in equation 6.9 with $\mathbf{D}^{true} = (D^{true}, \alpha_D^{true}, \delta_D^{true})$.

D^{true}	0, 0.005, 0.01, 0.02, 0.05, 0.07, 0.1, 0.15, 0.2
α_D^{true} / °	0
δ_D^{true} / °	0, ±10, ±20, ±20, ±30, ±40, ±50, ±60, ±70, ±80, ±90

7.2 Parameter Reconstruction Results

The precision of the reconstruction is computed from the comparison of the measured dipole parameters with the input parameters of the dipole which the respective MC sky maps have been generated with. Furthermore, the uncertainties of the reconstructed parameters as obtained in the fit procedures are investigated. Next to the reconstruction of the directional parameters of right ascension and declination the absolute pointing precision is of interest. It will be obtained from the angular difference Ω between the true direction of the dipole and the reconstructed one,

$$\Omega = \sphericalangle\left((\alpha_D^{true}, \delta_D^{true}), (\alpha_D^{rec}, \delta_D^{rec})\right) \ .$$

This quantity is especially useful because it is independent of the different properties and definitions of angular coordinates on the sphere.

The most probable value for a reconstructed parameter is given by the maximum of the corresponding distribution. The average uncertainty of a reconstructed value at a given set of input parameters has been chosen to be described by the width of the integral covering the 68 % most probable values. This measure is a reasonable indicator of the spread of the distribution of reconstructed values because it is unaffected by the potential skewness of the distributions. Reconstructed amplitudes follow a Rice distribution which is rather skew especially for small true amplitudes, see appendix C. Furthermore, the distribution of angular distances originating from Gaussian statistics in one dimension have been shown to be described by the Rayleigh p.d.f., see chapter 4. This is why an indicator that produces a symmetric uncertainty estimate in general, such as the RMS, is considered inadequate.

At first, the likelihood method for the dipole fit will be used to exemplify how the precision of the reconstruction of dipole parameters is quantified. Then, the results obtained from all methods are compared. Finally, isotropic maps are investigated and the significance potential of amplitude measurements is derived for the respective method.

7.2.1 Reconstruction Precision

Dipole Fit Likelihood Method

The reconstructed values are investigated with regard to their dependence on the varying input parameters. Figure 7.1 shows the distributions of the dipole parameters and their uncertainties reconstructed with the likelihood method for a fixed amplitude of $D^{true} = 0.05$ and varying declination. The colour code displays the normalised number n of entries in the corresponding bins and the black bars indicate the range of 68 % of the values most likely reconstructed. The true values are indicated by black dashed lines.

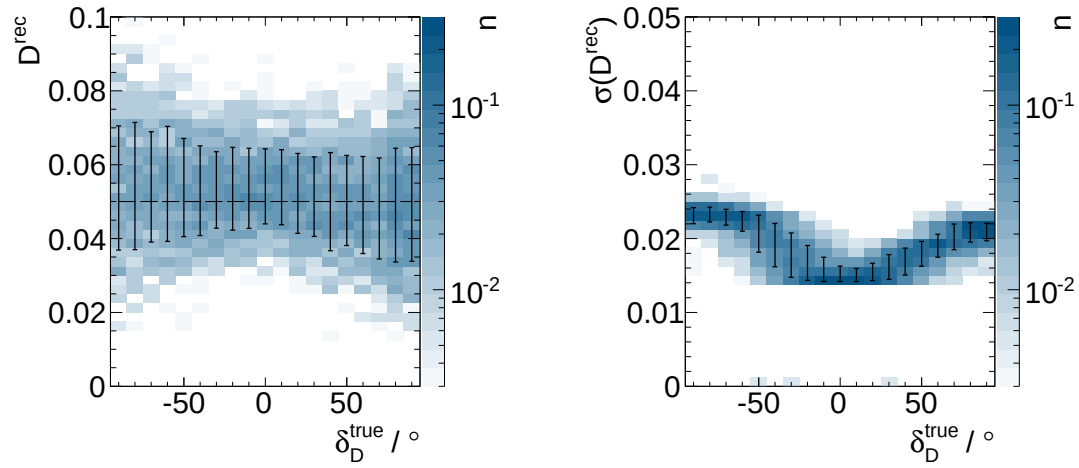

(a)

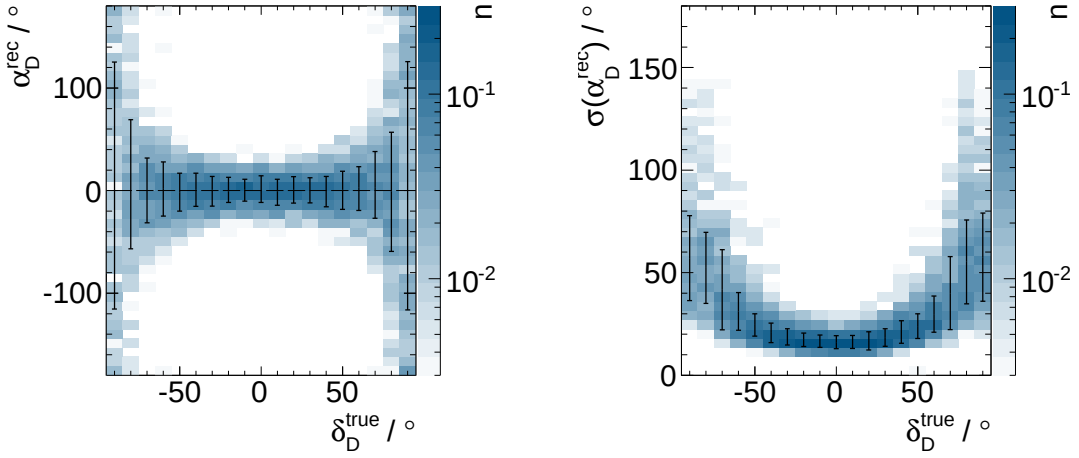

(b)

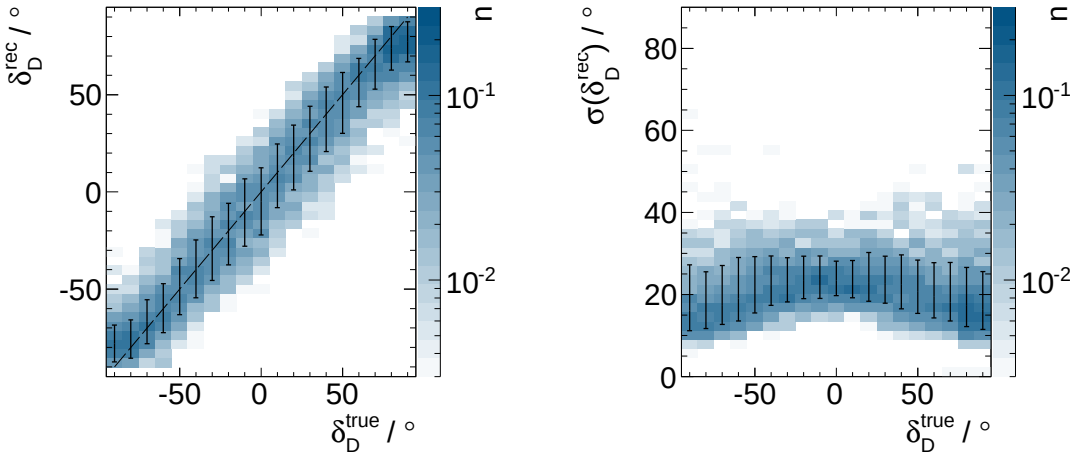

(c)

Figure 7.1: Dipole parameters and uncertainties reconstructed with the likelihood fit method for the MC scenarios of a fixed amplitude of $D^{true} = 0.05$ and varying declination δ_D^{true}. (a), (b) and (c) show the reconstructed dipole parameters amplitude D^{rec}, right ascension α_D^{rec} and declination δ_D^{rec} next to their uncertainties $\sigma(D^{rec})$, $\sigma(\alpha_D^{rec})$ and $\sigma(\delta_D^{rec})$, respectively. The (logarithmic) z-axis indicates the normalised number n of occurrences of corresponding values. The black dashed lines indicate the MC truth.

(a) 68 % of the reconstructed amplitudes D^{rec} match the true value D^{true} within less than ~ 0.02. The amplitude distributions become slightly wider for larger absolute values of the declination. A marginal systematic tilt is observed so that the amplitudes are reconstructed somewhat larger at negative declination values and smaller at positive ones. As a result of the corresponding shift of these 68 % bars, the distribution of reconstructed amplitudes at northern declination values is centred more closely on the true amplitude than it is at southern declinations. This dependence of the reconstructed amplitude on the true declination is not a bias of the method; it is caused by the fact that with a fixed number $N = 30000$ of events and a declination dependent field of view of the detector the statistical power of an amplitude measurement depends on the true declination of the dipole. This connection becomes clear when having a closer look at the number of events which is a measure of statistical power: 30000 events originating from a dipole ($D^{true} = 0.05$) pointing to the south, $\delta_D^{true} = -90^\circ$, correspond to 29341 events in absence of the dipole. Similarly, with the same dipole pointing to the north, $\delta_D^{true} = 90^\circ$, isotropy would yield 30689 events. Note that both estimates assume a constant time of data taking. Thus, since the number N of events is fixed a dipole pointing to the northern hemisphere can be detected with a larger statistical power on average. This aspect of dipole parameter reconstruction is also addressed in appendix D. Consequently, plot (a) in figure 7.1 shows that the distributions of reconstructed amplitudes more precisely match the true amplitude for larger values of the true declination.
These observations are both qualitatively and quantitatively consistent with what can be read from the plot of the amplitude uncertainties $\sigma(D^{rec})$: They are as small as ~ 0.014 at the equator while increasing to values of up to ~ 0.026 towards the poles. At northern declination values the amplitude uncertainties are a bit smaller on average than they are at southern declinations.

(b) The reconstruction of the right ascension parameter of the dipole is precise within $\pm 20^\circ$ for $|\delta_D^{true}| \lesssim 50^\circ$. It becomes worse for larger absolute values of δ_D^{true} since the solid angle of a unit step in right ascension decreases towards the poles. Thus, this observation does not necessarily imply a worse pointing precision for dipoles with directions close to the poles.
Correspondingly, the right ascension uncertainties $\sigma(\alpha_D^{rec})$ are small only at true declination values not too far from the equator.

(c) Similar to the right ascension parameter, the dipole declinations are reconstructed precisely within $\pm 20^\circ$ for $|\delta_D^{true}| \lesssim 50^\circ$. However, contrary to the former the spread of the distributions slightly decreases towards the poles. The absolute values of the reconstructed declination are limited to the defined declination range $\pm 90^\circ$. This leads to the bars not covering the dashed line of true values at the (extreme directions close to the) poles which in turn results in skew distributions. Note the similarity to what is discussed in appendix C in the context of the amplitude measurement that is always larger than zero.
Consistently agreeing with the spread of the declination parameter, also the declination uncertainties $\sigma(\delta_D^{rec})$ are larger close to the equator and decrease towards the poles.

Similarly, the dipole likelihood fit method has been chosen to exemplify results for the scenario of a fixed declination of $\delta_D^{true} = 0^\circ$ and varying amplitude D^{true} in figure 7.2.

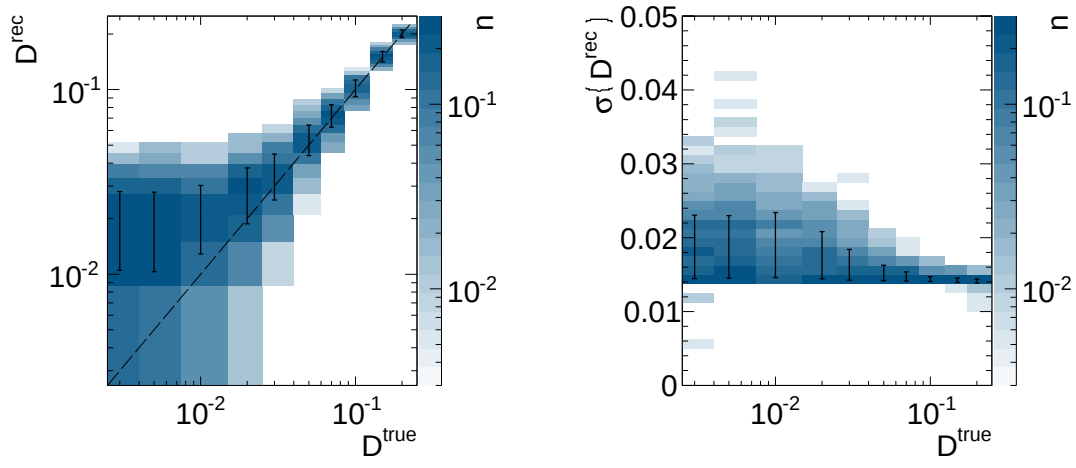

(a)

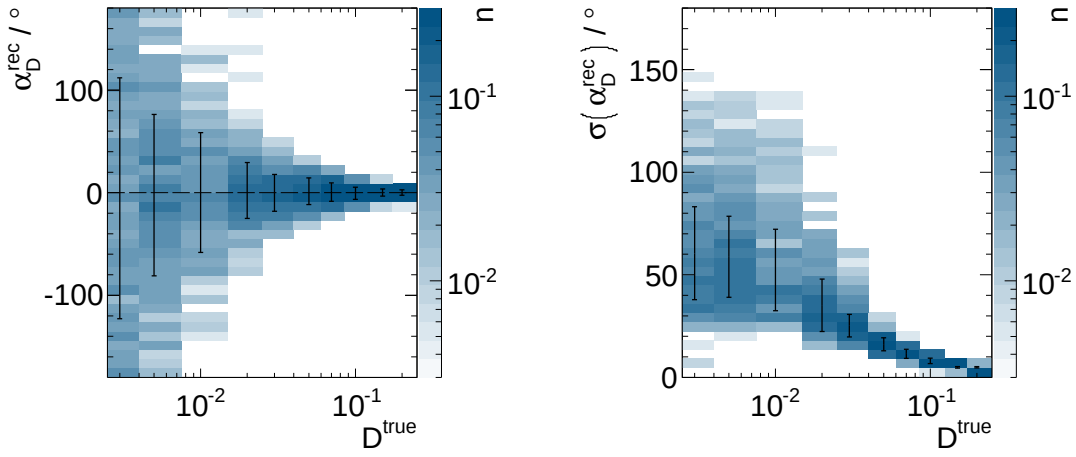

(b)

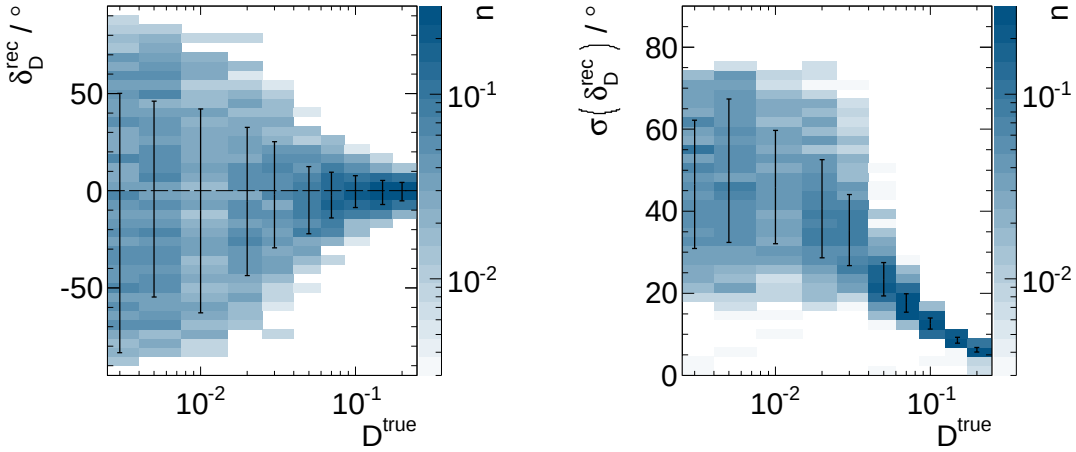

(c)

Figure 7.2: Dipole parameters and uncertainties reconstructed with the likelihood fit method for the MC scenarios of a fixed declination of $\delta_D^{true} = 0°$ and varying amplitude D^{true}. (a), (b) and (c) show the reconstructed dipole parameters amplitude D^{rec}, right ascension α_D^{rec} and declination δ_D^{rec} next to their uncertainties $\sigma(D^{rec})$, $\sigma(\alpha_D^{rec})$ and $\sigma(\delta_D^{rec})$, respectively. For the sake of visibility, the results obtained with $D^{true} \equiv 0$ are shown at the very left at $D^{true} = 3 \times 10^{-3}$. The (logarithmic) z-axis indicates the normalised number n of occurrences of corresponding values. The black dashed lines indicate the MC truth.

(a) The reconstructed amplitudes match the truth only for amplitudes larger than $D^{true} \gtrsim 0.02$. The spread is constant for all input values as somewhat expected in analogy to the Rayleigh method that states that the uncertainty of the amplitude does only depend on the statistics, see equation 6.16. For the given number $N = 30000$ of events the reconstruction by means of the likelihood method becomes insensitive to amplitudes smaller than ~ 0.02 which can be read from the asymptotic behaviour of the 68 % - bars in the corresponding range of $D^{true} \lesssim 0.02$.
The distributions of the amplitude uncertainties $\sigma(D^{rec})$ confirm this observation: While below $D^{true} \lesssim 0.02$ the 68 % bars hardly differ from isotropy, the amplitude is reconstructed more precisely for larger values of D^{true}. A sharp edge of smallest values of $\sigma(D^{rec})$ is observed at ~ 0.014 which again relates to the fact that the smallest possible amplitude uncertainty is determined by the statistics.

(b) The reconstructed right ascension values can be considered flatly distributed for amplitudes smaller than 0.01. While all values are equally likely in case of zero amplitude, distributions become more and more narrow around the respective true value for increasing D^{true}. At $D^{true} = 0.02$ they match the true value $\alpha_D^{true} = 0$ already within $\pm 30^\circ$.
Consistently, 30° is also the most probable value in the distribution of right ascension uncertainties $\sigma(\alpha_D^{true})$ at $D^{true} = 0.02$.

(c) The observations made for the right ascension parameter also apply for the declination parameter. Remarking that the range of the right ascension is two times larger than that of the declination, see the y-axes, the precision of the directional reconstruction indicated by the length of the black bars can be considered approximately equal in both coordinates above $D^{true} \gtrsim 0.02$.
Consequently, also the distribution of the uncertainties $\sigma(\delta_D^{true})$ of the declination peaks at 30° for $D^{true} = 0.02$.

The precision of the directional reconstruction of the likelihood fit method in terms of the angular difference Ω of reconstructed and true direction is studied in figure 7.3.

(a) The results from the scenario of a fixed amplitude are summarised in the left plot of figure 7.3. The distributions peak around $10^\circ - 15^\circ$ most likely with a bar of a length of $\sim 20^\circ$ covering the 68 % most probable values. This observation is mostly independent of the true declination input value and only a small systematic is observed: Ω tends to be larger by $\lesssim 5^\circ$ at the equator compared to the poles.

(b) The right plot of figure 7.3 was produced from the scenario of a fixed declination value. The directional precision given by Ω starts at 90° with a width of 80° for the case of isotropy. As soon as $D^{true} > 0$ the range of most probable angular distance values decreases to $20^\circ - 60^\circ$ at $D^{true} = 0.02$ and is better than $10^\circ - 30^\circ$ above $D^{true} \geq 0.05$. It is worth noting that the precision of the directional reconstruction of the dipole appears to be more sensitive and more immediately responding to a genuine signal amplitude larger than zero while the amplitude measurement itself is rather insensitive at $D^{true} \leq 0.02$, see figure 7.2. This observation is also addressed in appendix C.

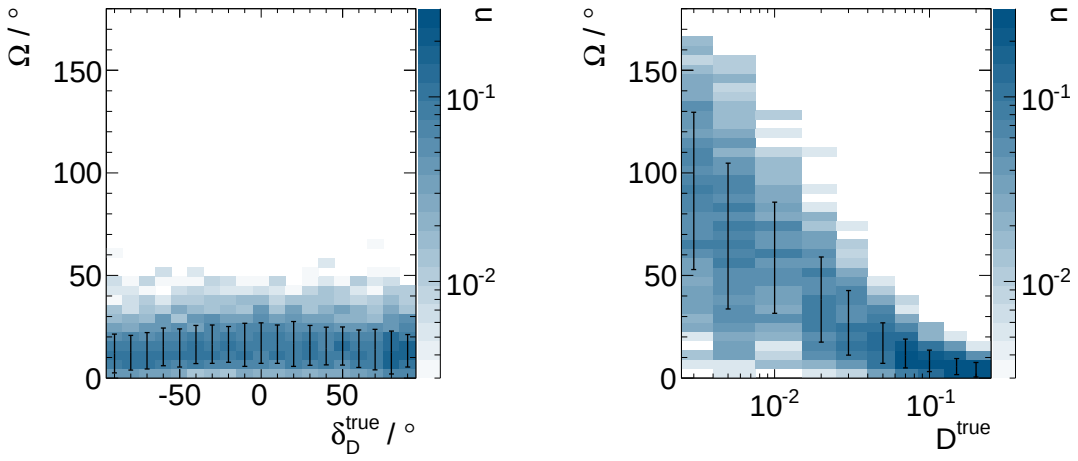

(a) (b)

Figure 7.3: Precision of the directional reconstruction of the likelihood dipole fit method. (a) is obtained from the scenario of a fixed amplitude $D^{true} = 0.05$ and a varying declination δ_D^{true} while (b) displays the results for the scenario of a fixed declination $\delta_D^{true} = 0^\circ$ and varying amplitude D^{true}. The (logarithmic) z-axis indicates the normalised number n of occurrences of corresponding values.

Comparison of Methods

In order to compare the performance of all methods their results obtained with the same approach as described in the previous paragraphs are displayed in figures 7.4 and 7.5. For the χ^2 fit method a binning of the sky maps of (12×6) has been chosen in (right ascension $\times$ declination). This choice is motivated in appendix D. Again, the cases of a fixed amplitude $D^{true} \equiv 0.05$ and varying declination as well as a fixed declination $\delta_D^{true} \equiv 0^\circ$ and varying amplitude are given. Instead of the 2D distributions only the bars are displayed that indicate the 68 % most probable values. At first, the former scenario is discussed. The amplitudes and their uncertainties obtained with the 2D methods are given for declination values below $|\delta_D| \leq 50^\circ$. Note that they have been scaled according to appendix C like $D^{rec} = D_{2D}^{rec}/(\cos\delta_D \langle \cos\delta \rangle)$ to match the 3D amplitudes.

(a) Compared to the likelihood method the χ^2 fit method shows slightly worse performance in terms of a larger spread in the amplitude reconstruction. It produces results which are systematically shifted in a comparably weak fashion as in case of the likelihood method: The amplitude is reconstructed slightly larger for negative declination values and smaller for positive ones. Again, this observation is not a bias of the method but can be assigned to the declination dependence of the statistical power the sky map pattern can be analysed with. The width in terms of the uncertainty of the measurements increases when moving the dipole direction to the poles. The Rayleigh method closely matches the true values in the given range of $|\delta_D^{true}| \leq 50^\circ$ while the wavelet transform results are systematically too large already at smallest declinations.
Larger widths are also observable in the amplitude uncertainty distributions of the χ^2 method compared to the likelihood method while the former produces smaller uncertainties on average. This observation is a bit counterintuitive, since larger spreads of the distribution of a parameter should correspond to larger values of its uncertainty and vice versa. Therefore, one of the methods is supposed to produce either too large

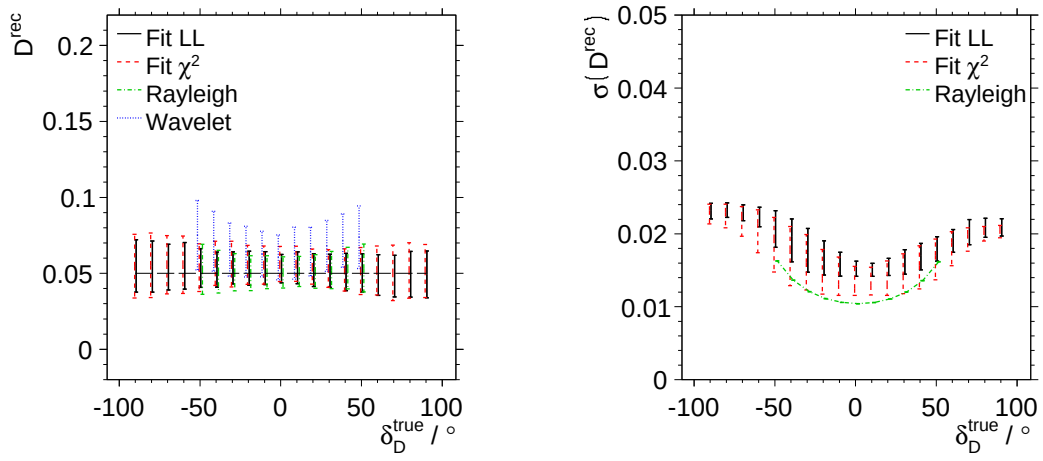

(a)

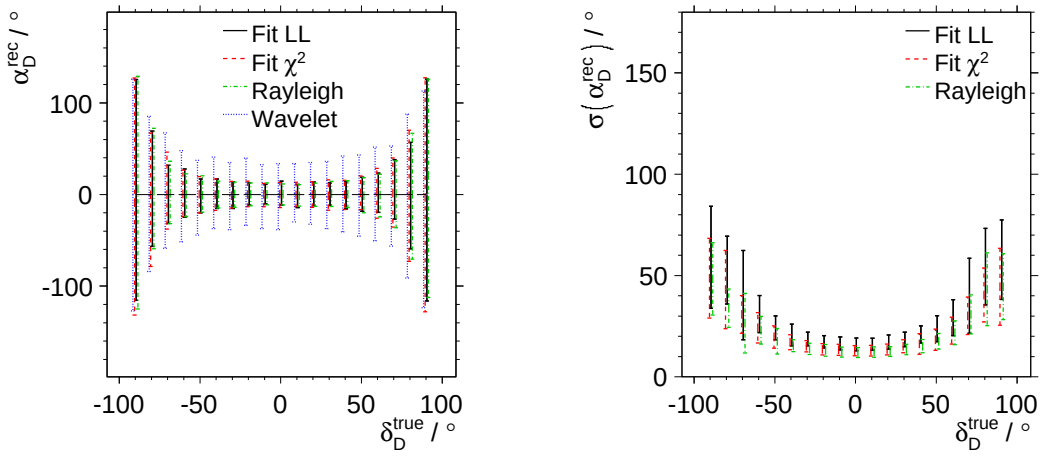

(b)

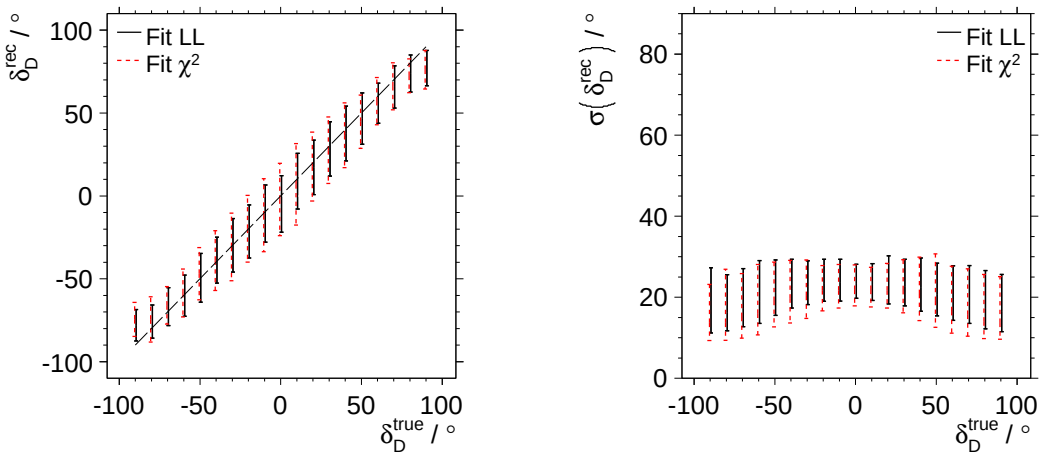

(c)

Figure 7.4: Dipole parameters and uncertainties reconstructed with the different fit methods for the MC scenarios of a fixed amplitude of $D^{true} \equiv 0.05$ and varying declination δ_D^{true}. (a), (b) and (c) show the reconstructed dipole parameters amplitude D^{rec}, right ascension α_D^{rec} and declination δ_D^{rec} next to their uncertainties $\sigma(D^{rec})$, $\sigma(\alpha_D^{rec})$ and $\sigma(\delta_D^{rec})$, respectively. The results for the amplitude obtained with the 2D methods are only shown for directions not too close to the poles, see text for details. The (logarithmic) z-axis indicates the normalised number n of occurrences of corresponding values. The black dashed lines indicate the MC truth.

(likelihood fit) or too small (χ^2 fit) parameter uncertainties. This issue is addressed in appendix D and it turns out that the likelihood fit method overestimates the parameter uncertainties such that around 80 % of the reconstructed parameters agree with the true value within their respective uncertainties. The qualitative behaviour of the methods is similar with small values of $\sigma(D^{rec}) \approx 0.014$ at the equator and increasing towards the poles. The Rayleigh method produces the smallest uncertainties. Note that the wavelet method does not produce uncertainties in its current implementation.

(b) The reconstruction of the right ascension parameter works equally well and bias-free with all methods. However, the statistical spread of values reconstructed with the wavelet method is always larger than about $\pm 30^\circ$. The spreads obtained with the other methods are always smaller and agree rather well with each other.
The distributions of the right ascension uncertainties produce a consistent picture again. The comparison shows that the Rayleigh method and the χ^2 fit method produce smaller uncertainties than the likelihood method.

(c) Similar to the amplitude reconstruction, the declination parameter obtained with the χ^2 method does match the truth less perfectly than that measured with the likelihood method. Again a larger width is observed with decreasing absolute value of the declination.
While showing the same behaviour qualitatively, the χ^2 fit again produces larger spreads and smaller values on average compared to the likelihood method in the distributions of declination uncertainties.

In the scenario of a fixed declination value at $\delta_D^{true} \equiv 0^\circ$ the parameter reconstruction of all methods are compared. Again, the amplitudes obtained with the 2D methods must be scaled appropriately with a factor of ~ 1.28 as described in appendix C.

(a) No method is sensitive to amplitudes smaller than $D^{true} \leq 0.01$, the Rayleigh method is the first to become sensitive to amplitudes larger than that. This is expected remembering the formula for the amplitude uncertainty calculation from the number of events $N = 30000$ as $\sigma_r = \sqrt{2/N} \approx 0.008$: Multiplied with ~ 1.28 this is about 0.01 and no true amplitude smaller than that can be (significantly) detected at all. The amplitude sensitivity of the dipole fit likelihood method is remarkably close to that of the Rayleigh method. On the one hand, this is expected due to the unbinned character of the method; on the other hand, the need to fit three parameters instead of two limits the performance of the 3D method. The binned χ^2 method reconstructs systematically larger amplitudes over the full range of D^{true}. However, the shift is small and the 68 % bars of both 3D methods match the truth above $D^{true} \geq 0.02$. Similar to the χ^2 method, the results obtained with the wavelet transforms also overestimate the amplitude on average; additionally, this method produces widths that are up to a factor of two times larger than with any other method. (Note the log-scale on the y-axis.)
As expected the Rayleigh method produces the smallest amplitude uncertainties at ~ 0.01. Both 3D methods produce larger uncertainties with the χ^2 (likelihood) fit reaching down to values of 0.012 (0.014) asymptotically for large true amplitudes.

(b) The reconstructions of the right ascension parameter $\alpha_D^{true} \equiv 0^\circ$ perform comparably well for the 3D methods and the Rayleigh method. The lengths of the 68 % bars

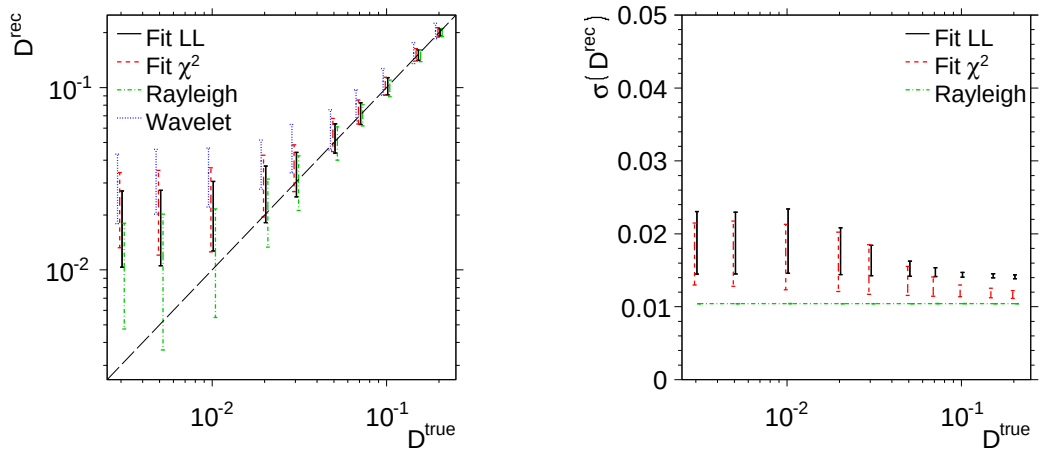

(a)

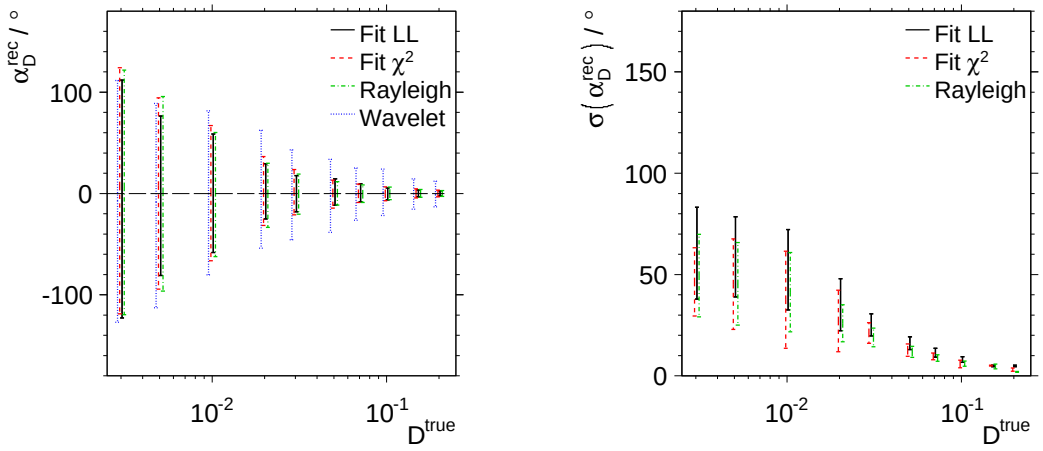

(b)

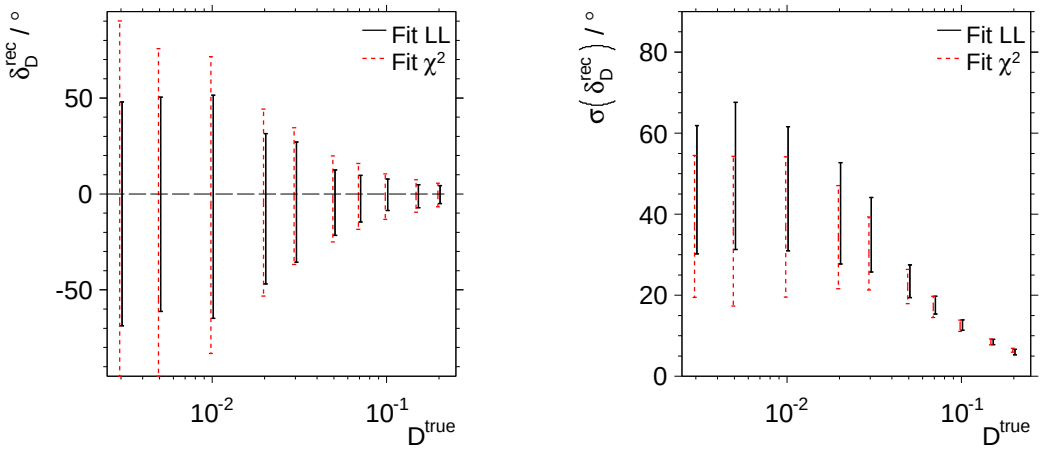

(c)

Figure 7.5: Dipole parameters and uncertainties reconstructed with the different fit methods for the MC scenarios of a fixed declination of $\delta_D^{true} \equiv 0°$ and varying declination D^{true}. (a), (b) and (c) show the reconstructed dipole parameters amplitude D^{rec}, right ascension α_D^{rec} and declination δ_D^{rec} next to their uncertainties $\sigma(D^{rec})$, $\sigma(\alpha_D^{rec})$ and $\sigma(\delta_D^{rec})$, respectively. For the sake of visibility, the results obtained with $D^{true} \equiv 0$ are shown at the very left at $D^{true} = 3 \times 10^{-3}$. The (logarithmic) z-axis indicates the normalised number n of occurrences of corresponding values. The black dashed lines indicate the MC truth.

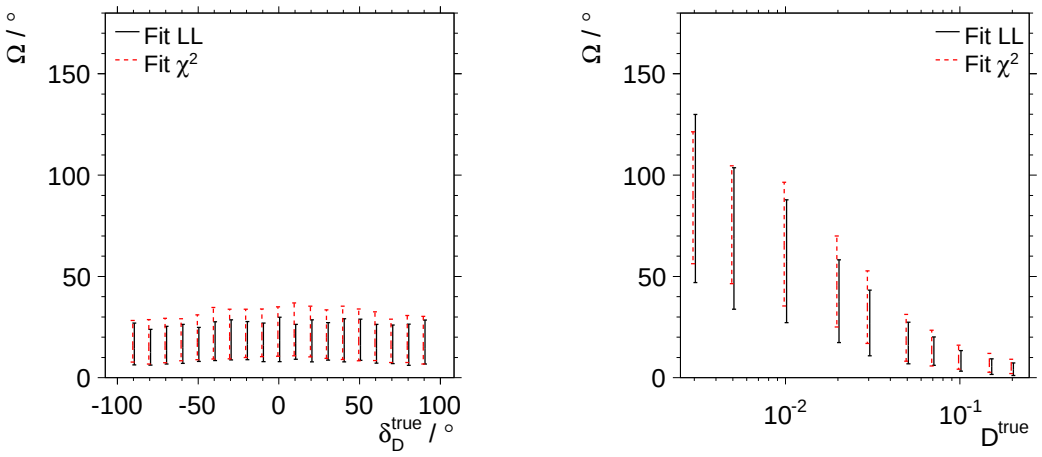

(a) (b)

Figure 7.6: Precision of the directional reconstruction of the 3D dipole fit methods. (a) is obtained from the scenario of a fixed amplitude $D^{true} = 0.05$ and a varying declination δ_D^{true} while (b) displays the results for the scenario of a fixed declination $\delta_D^{true} = 0^\circ$ and varying amplitude D^{true}. The (logarithmic) z-axis indicates the normalised number n of occurrences of corresponding values.

decrease quickly with increasing amplitude remarkably responding already to smallest values of $D^{true} \gtrsim 0.005$ and reaching values smaller than 10° for true amplitudes larger than ~ 0.1. Again, the wavelet transforms produce up to three times larger widths over the complete range of D^{true}.
The observations regarding the right ascension also apply for its uncertainty which is consistently smaller than 10° for true amplitudes larger than ~ 0.1.

(c) The declination parameter is reconstructed more precisely with the likelihood method. Both 3D fit methods show a slight preference for producing negative declination values. However, this bias is negligible compared to the statistical widths of the distributions.
Again, the observation is made that the likelihood method overestimates the declination parameter uncertainty, see appendix D. Nevertheless, both methods agree qualitatively and a precision of $\sim 15^\circ$ can be read from the distributions of both the declination and its uncertainty for amplitudes larger than $D^{true} \gtrsim 0.1$.

The precision of the directional reconstruction of the 3D methods in terms of the angular difference Ω of reconstructed and true direction is compared in figure 7.3.

(a) The results from the scenario of a fixed amplitude are summarised in the left plot of figure 7.6. The pointing precision of the χ^2 fit indicated by Ω is slightly worse (larger) on average than that of the likelihood method. This observation applies over the full range of δ_D^{true}. Furthermore, at true declinations around the equator, $|\delta_D^{true}| \lesssim 50^\circ$, the χ^2 fit produces larger widths than the likelihood method.

(b) The right plot of figure 7.6 was produced from the scenario of a fixed declination value. The angular distance of the reconstructed and true directions is smaller for the likelihood method than for the χ^2 method. Once more, it is worth noting that

the directional precision “improves” already at smallest amplitude values while the amplitude measurement is still compatible with noise.

The unbinned methods have proven to perform better than the binned ones both in the fields of amplitude and directional reconstruction. The parameters reconstructed with these methods are closer to the true values than those obtained with the binned methods. This agrees with the expectation that the larger amount of information processed by the unbinned methods leads to more precise results. However, compared to the likelihood method the χ^2 fit produces smaller uncertainties of all parameters in the scenarios considered. This observation is counterintuitive considering the fact that the χ^2 fit also produces wider distributions of the parameters. Small parameter uncertainties intuitively are supposed to correspond to small widths of the parameter distributions and vice versa. This observation is addressed in appendix D and assigned to an overestimation of the uncertainties obtained with the likelihood method.

Both 3D methods have shown to produce a bias depending on the true declination value. The methods reconstruct preferentially negative declination values which is probably caused by the shape of the relative exposure and its asymmetric dependence on declination. This bias is transferred to systematics in the precision of the directional reconstruction of these methods. The bias becomes smaller with increasing amplitude and always remains well within the estimated range of the 68 % most probable values around the MC truth. Therefore it is considered negligible compared to the statistical uncertainties.
A declination dependent shift in the amplitude measurement has been observed with both 3D methods as well. This is not considered a bias but an effect of the statistical power that changes with the true declination value.

The binned method by means of wavelet transforms performs worst of all methods. It shows the largest systematic overestimation of the amplitude and the largest widths describing the 68 % most probable values. Some of the properties of the method must be kept in mind when evaluating its characteristics. The wavelet function made use of does not natively match sinusoidal functions and the angular scale of a dipole at which the analysis is performed is at the edge of what a wavelet transform can resolve. Nevertheless, the method has proven to work in principle and further studies have been initiated towards a multi-scale implementation in 3D on the sphere.

7.2.2 Isotropy

A measurement obtained from real data with any of the methods discussed in the previous paragraphs can only be evaluated if the response of the respective method to isotropic distributions is known and understood. More precisely, the investigation of isotropic sky maps as observed by the PAO yields the necessary basis to derive significances from amplitude measurements. Isotropic maps are produced with $D^{true} \equiv 0$; since the parameter of the declination of the dipole does not affect the distribution of arrival directions in this scenario, the MC sets generated with zero amplitude at various declination values are merged to one isotropic set. The reconstructed dipole parameters obtained with the different methods are shown in figure 7.7. The amplitudes obtained with the 2D methods are scaled as described in appendix C by a factor of ~ 1.28.

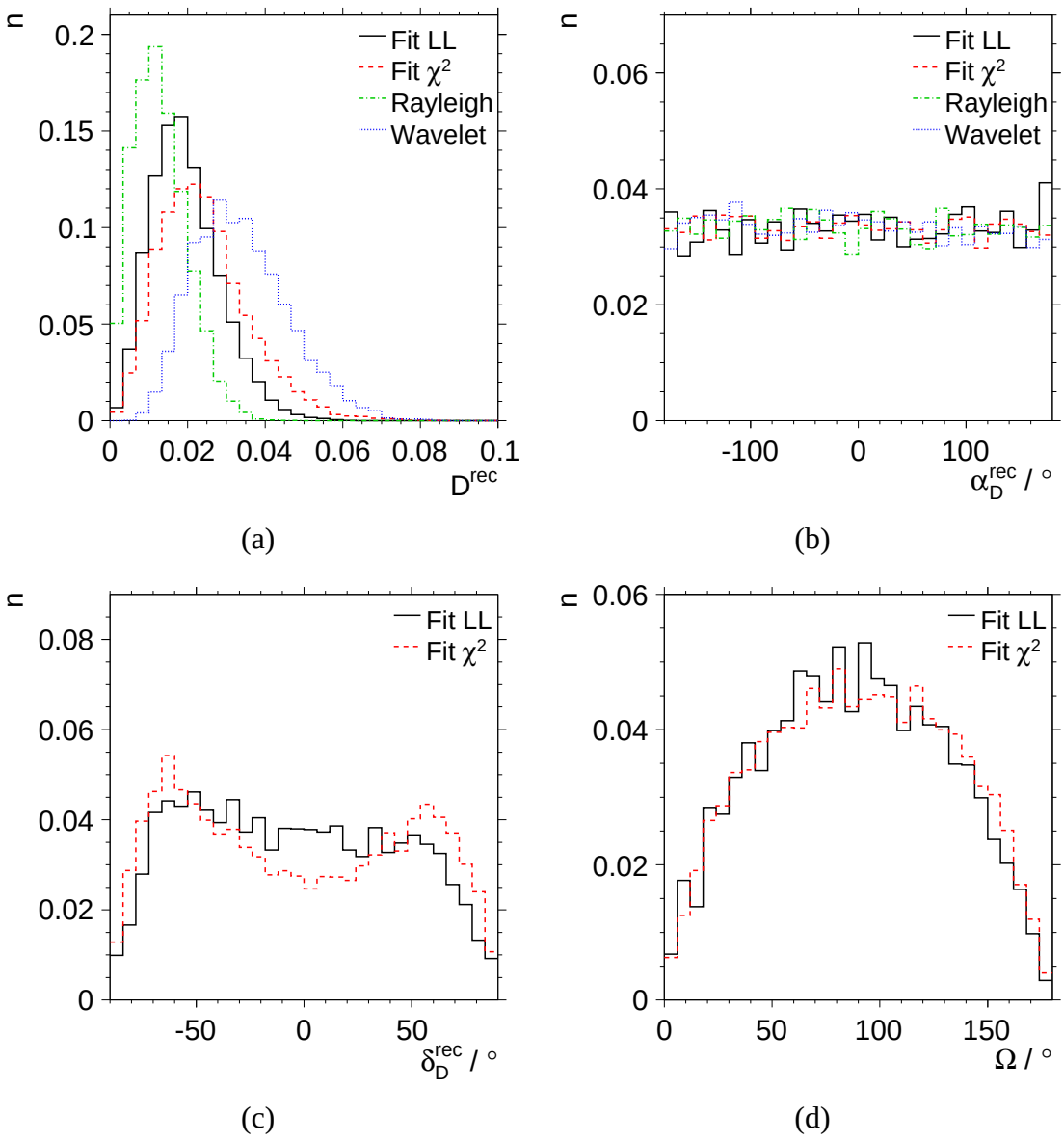

Figure 7.7: Normalised fraction n of dipole parameters obtained from isotropic maps with four different methods: The log-likelihood (black solid) and χ^2 method (red dashed) for a dipole fit and the Rayleigh (green dotted dashed) and Wavelet (blue dotted) method for a cosine fit in the right ascension coordinate. (a) shows the reconstructed amplitudes D^{rec}, (b) the reconstructed right ascension α_D^{rec} and (c) the declination δ_D^{rec} of the dipole; (d) indicates the pointing precision in absence of a dipole amplitude. 9500 isotropic sets have been analysed with each method.

(a) The distributions of amplitudes reconstructed with the four methods differ more or less strongly. The Rayleigh method performs best in terms of reconstructing amplitudes closest to zero. The method is considered a reference in this study in terms of producing the limit of what is achievable at best: Both the fact that only two parameters are fit and that it is an unbinned method lead to the smallest possible ratio of fit parameters per degrees of freedom. The wavelet transform technique produces amplitudes from the same isotropic data sets approximately a factor of two larger than those obtained with the Rayleigh method. The 3D dipole fit methods perform better than the Wavelet method but worse than the Rayleigh method. As already observed before, the unbinned likelihood fit produces smaller amplitudes than the binned χ^2 fit which is due to the larger amount of information made use of in the unbinned method.

(b) The distribution of the right ascension phase values α_D^{rec} is flat for all methods as expected in the absence of a dipole signal. All values of α_D^{rec} are reconstructed equally likely.

(c) The declination distribution δ_D^{rec} is expected to be symmetric about the equator. This symmetry is observed for both the likelihood and the χ^2 fit method. However, both distributions shows a little asymmetry preferring negative declination values. As stated before, this observation probably relates to the relative exposure of the SD of the PAO which dominantly covers the negative declination range.

(d) The pointing precision given by the angular difference Ω between the true direction of the dipole and the reconstructed one follows a sine. This is because the decreasing solid angle towards $\Omega \to 0^\circ$ and $\Omega \to 180^\circ$ must be accounted for. Both the likelihood method and the χ^2 method agree with this expectation.

7.2.3 Significance of Amplitude Measurements

As a measure of the power of a method with regard to the amplitude measurement the fraction n^{rec} of reconstructed amplitudes significantly larger than the expectation from isotropy is considered,

$$n^{rec}\left[D > D_{iso}^{\text{C.L.}}\right] \;=\; \frac{N^{rec}\left[D > D_{iso}^{\text{C.L.}}\right]}{N_{tot}^{rec}}\,, \tag{7.1}$$

with $D \equiv D^{rec}$ the reconstructed amplitude and N_{tot}^{rec} the total number of amplitudes in the respective set. $D_{iso}^{\text{C.L.}}$ is the amplitude that indicates the threshold below which a fraction of C.L. of amplitudes obtained from isotropy are distributed and $N^{rec}\left[D > D_{iso}^{\text{C.L.}}\right]$ is the number of amplitudes D in a given set that exceed this value. C.L. is identified as the confidence level indicating a measure of the significance of a reconstructed amplitude with regard to its distinctness from isotropy. The fraction n^{rec} is displayed in figure 7.8 as a function of the true amplitude D^{true}. The y-axis offsets of all methods are at $n^{rec} \approx 0.32$ (~ 0.05, ~ 0.01) directly corresponding to the chosen confidence level of significance of C.L. = 68 % (C.L. = 95 %, C.L. = 99 %).

For example, a true amplitude of $D^{true} = 0.03$ causes a significant measurement at a confidence level of C.L. = 68 % in ~ 90 % (~ 70 %) of all realisations with the unbinned (binned) methods, figure 7.8 plot (a). At $D^{true} = 0.05$, with the unbinned methods the measurement will be significant almost always even with a confidence of 95 %, plots (a), (b)

Table 7.2: Amplitudes obtained from isotropic sky maps corresponding to three different quantiles. E.g. an amplitude measured with the Rayleigh method must be larger than $D_{iso}^{0.95} = 0.0255$ to be significant at the 95 % level.

	Fit LL	Rayleigh	Fit χ^2	Wavelet
$D_{iso}^{0.68}$	0.0222	0.0157	0.0280	0.0386
$D_{iso}^{0.95}$	0.0354	0.0255	0.0460	0.0556
$D_{iso}^{0.99}$	0.0440	0.0318	0.0576	0.0663

while a level of 99 % is only reached above a true amplitude of 0.07. The values of $D_{iso}^{\mathrm{C.L.}}$ are summarised in table 7.2.

The two binned methods, wavelet transforms and dipole χ^2 fit method, perform comparably well. Note that the reconstructed amplitude enters only relatively to the isotropic distribution obtained with the same method in each case. This implies that the amplitude obtained with the wavelet method contains precise information when being interpreted rather relatively than absolutely: On the one hand, the absolute amplitude scale appears to be rather off when compared with the other methods, see figure 7.5. On the other hand, estimating the significance by relating the amplitude measurements within the method to each other shows that the method is competitive in this respect.

7.3 Summary

The performance of four methods to study potential dipolar patterns in the distribution of arrival directions of UHECRs recorded with the surface detector of the Pierre Auger Observatory has been investigated on simulated Monte Carlo sky maps generated in the absence and in the presence of a dipole of varying direction and amplitude.

Best results in terms of small systematic uncertainties and statistical spreads are achieved with the unbinned methods in 2D and 3D: The sensitivity of the amplitude measurement to a dipole underlying a distribution of $N = 30000$ arrival directions starts at a true amplitude of $D^{true} \gtrsim 0.03$ depending on the desired confidence level. Above this amplitude the direction is reconstructed correctly within $\Omega \approx 40^\circ$ with the 3D method and within a right ascension of $\pm 20^\circ$ with the 2D method. However, for the application to data it must be kept in mind that the likelihood method overestimates the parameter uncertainties such that it covers about ~ 85 % instead of ~ 68 % of the distribution around the true value of the respective parameter.

The results obtained with the Rayleigh method confirm the expectation as described by the distributions given in equations C.5 and C.6: The probability density functions are fitted to the distributions of amplitudes and phases (right ascension) obtained from isotropy. These distributions are displayed in figure 7.7. The fit to the amplitude distribution produces a signal amplitude of $D = 0.004$ compatible with isotropy and an uncertainty of $\sigma_D = 0.0077 \pm 0.0004$ compatible with the expectation of $\sigma_D = \sqrt{2/30000} \approx 0.008$. The fit to the right ascension distribution yields a tiny signal amplitude of $(0.5 \pm 5.0) \times 10^{-4}$ also compatible with flatness, i.e. isotropy.

The performance of the likelihood method is compared to the results of the 3D Rayleigh

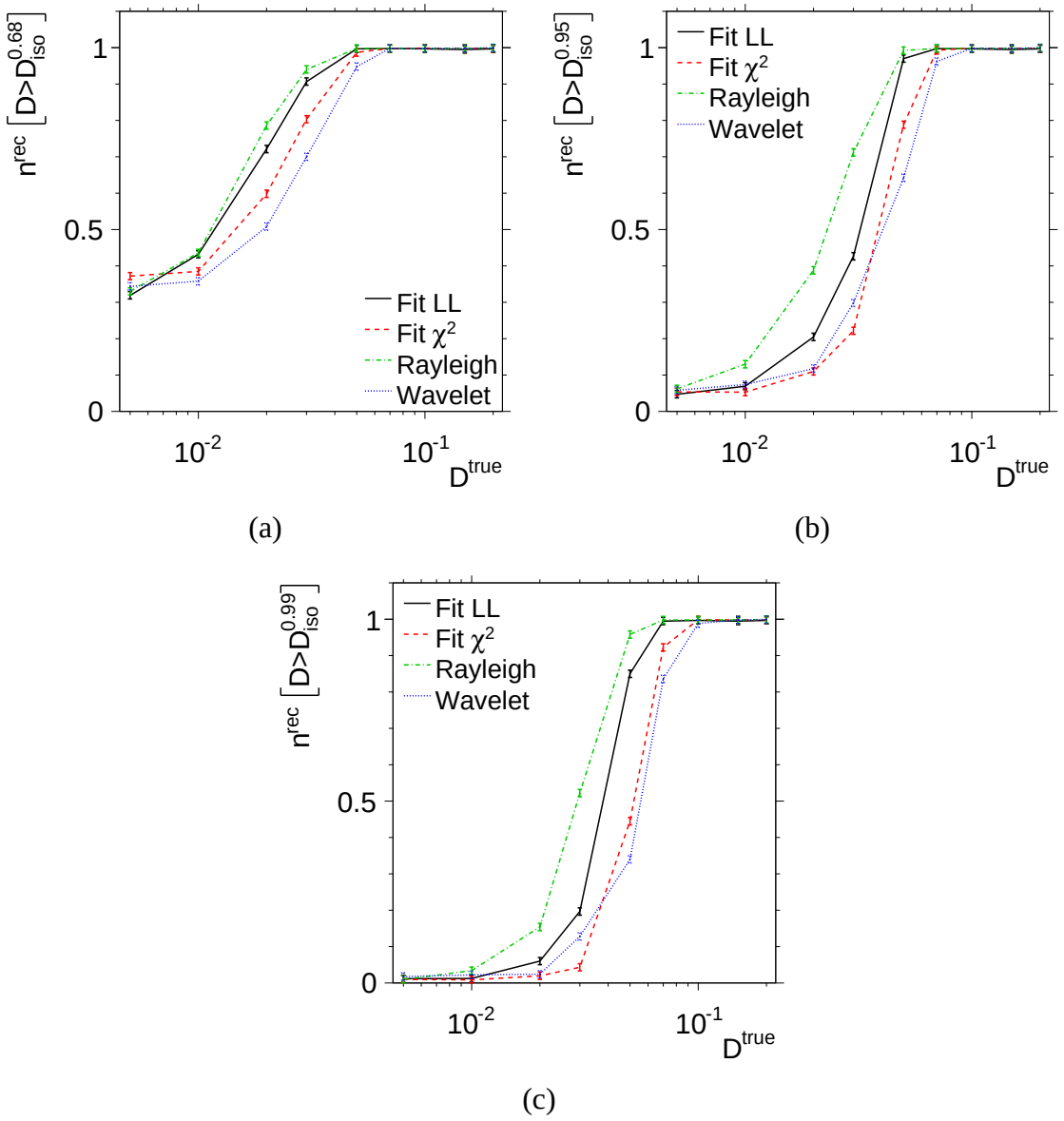

Figure 7.8: The fraction of reconstructed amplitudes significantly larger than the expectation from isotropy is displayed. The plots show the fraction of amplitudes larger than 68 % (a), 95 % (b) and 99 % (c) of the amplitudes expected from isotropic MC samples. For every true amplitude 500 sets are analysed and the reconstructed amplitudes are compared to those of the 9500 isotropic sets. Error bars are estimated conservatively as $\Delta n^{rec} = \pm 0.01$ accounting for the limited statistics.

Table 7.3: Example comparison of the reconstruction precision of two dipole fit methods. The likelihood fit method is contrasted to the method described in [Mol05] for the parameter set $(D^{true}, \alpha_D, \delta_D) = (0.05, 0^\circ, -45^\circ)$. Note that in case of the likelihood method the numbers have been estimated from the interpolation between the results obtained with the parameter sets for $\delta_D = -40^\circ$ and $\delta_D = -50^\circ$

	Fit LL	[Mol05]
$\sigma(D^{rec})$	$0.012 - 0.014$	0.013
$\sigma(\alpha_D^{rec})$ / $^\circ$	$17 - 19$	17.6
$\sigma(\delta_D^{rec})$ / $^\circ$	$15 - 16$	16.1

method given in [Som01, Aub05]: The directional precision of the latter method is stated to be better than 10° for true amplitudes larger than 0.1. The results of the likelihood method compare well with these numbers as can be read from the Ω-plot in figure 7.5 (d). The amplitude reconstruction precision with the 3D Rayleigh method is obtained to be as good as 0.01 and mostly independent of the true amplitude with a statistic of 32000 events. Again this compares well to the results found with the likelihood fit method as can be verified from figure 7.5 (a).

Similarly, the results obtained with the 3D method that derives the dipole parameters for each dimension independently [Mol05] agree very well with the likelihood method. As an example, table 7.3 compares the dipole parameter reconstruction precision for $(D^{true}, \alpha_D, \delta_D) = (0.05, 0^\circ, -45^\circ)$.

The likelihood method performs competitively well when compared to existing dipole fit methods. All methods described in this chapter are approximately bias-free. In the next chapter the four methods are applied to real data taken with the SD of the PAO. The results will be evaluated by relating them to the performance of the respective method as obtained from MC sky maps.

Chapter 8

Application to Data

In this chapter the four large scale anisotropy methods presented in chapter 6 and tested in chapter 7 are applied to data taken with the surface detector of the Pierre Auger Observatory. Firstly, the data set, cuts and periods of data taking adequate for the analysis are introduced. Then, the corrections freeing the data from local effects as described in chapter 5 are briefly recapitulated and performed step by step on the data set in order to get rid of artificial modulations of the event rate. In the subsequent section the dipole parameters obtained with each of the four methods are given after being reconstructed at different steps of the complete chain of corrections. Eventually, the final results in terms of directions and amplitudes of the dipole after the application of all corrections are given alongside their uncertainties and significances, respectively.

8.1 Data Set

The data set comprises all air shower events detected with the SD between January 2004 and December 2010 that have been reconstructed with $\overline{\text{Off}}\underline{\text{line}}$ version `v2r6p4-AsterixObelix`. To allow for full trigger efficiency only events passing the zenith angle cut $\theta \leq 60^\circ$ and the energy cut $E > 10^{18.5}$ eV are applied. All air shower measurements are required to fulfil the quality trigger T5 condition.

Bad periods are always excluded. Time intervals in which no records of measurements of the atmospheric parameters are available are excluded when the weather dependent energy correction is applied. The time intervals of non bad periods and of when weather data was available as well as the conjunction of the two are displayed in figure 8.1. The sum of bad periods amounts to 313 days corresponding to a fraction of 12 % of the total time of data taking. Weather data is missing for a fraction of another 12 % of that time. The conjunction of bad periods and intervals of time without atmospheric data records produces a fraction of data of 78 % that can be used when applying the weather correction. The records of atmospheric parameters made use of in this work have been obtained from the weather monitoring database kindly provided by [Kei11].

The number of events surviving the different cuts and remaining posterior to the corrections are summarised in table 8.1. After the application of cuts, 37407 events survive. This number remains unchanged when account is taken of the varying area of the SD. Different from that, the procedure of the correction of atmospheric effects impacts the number of events in two aspects: On the one hand, the data set is restricted to intervals of time where

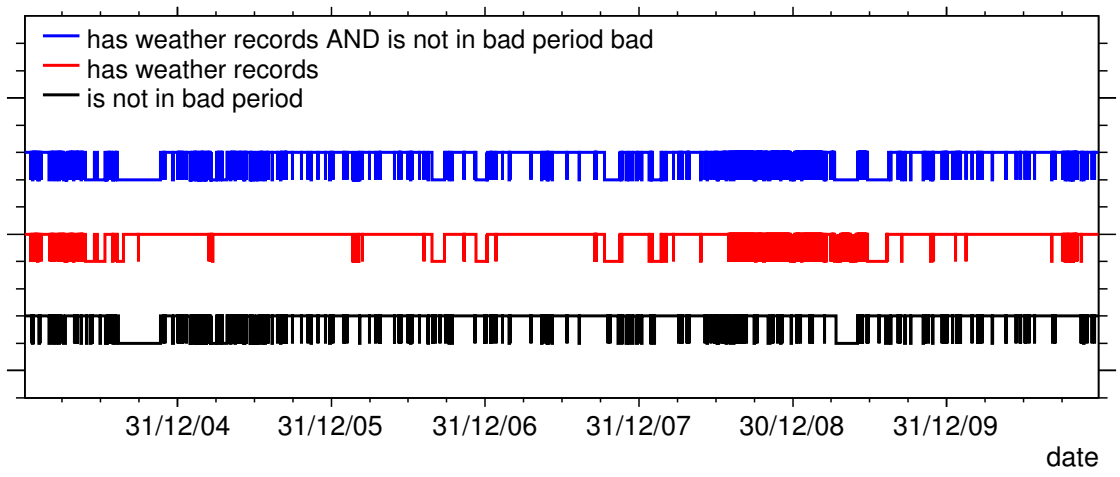

Figure 8.1: Availability of weather data and periods of data taking not tagged as bad over time. The bottom black line indicates the periods of data taking not tagged as bad, the red middle line displays the times where data records of the weather conditions have been available and the blue top line shows the conjunction of the two. Upper values indicate *true* and lower values indicate *false* for the respective statement and the corresponding line.

records of the atmospheric conditions are available. On the other hand, the correction of the energy causes events to pass or fail the energy cut. The latter statement is also valid with regard to the energy correction according to the geomagnetic field effect. The arrival directions of these events are analysed by means of the four methods to study potential large scale anisotropy in the data.

8.2 Correction of Local Effects

SD Area Correction

The correction necessary due to the varying area of the surface detector is performed by means of a weighting technique. Following the order of magnitude of the angular resolution

Table 8.1: Cuts applied to real data for anisotropy studies on the zenith angle θ, on the energy E and the T5 trigger. The number of events depends on the corrections applied, e.g. on whether or not measurements of the atmospheric parameters are available. It is also subject to variation when correcting the energy for atmospheric or geomagnetic effects since more or less events will survive the energy cut, consequently.

Category	*Name*	*Value*	N
Internal cuts	$\theta/^\circ$	< 60	
	$\log(E/\mathrm{eV})$	> 18.5	
Quality cut	T5 trigger	6T5	37407
External conditions	SD area	apply correction	37407
and corrections	Atmosphere	has records & apply correct.	31875
	Geomagnetic field	apply correction	31295

of the SD, the right ascension range is divided into $N_{bins} = 360$ bins each containing the accumulated area with regard to this directional sector as a weight w_i with $i = 1,...,N_{bins}$. The width of each sector i in right ascension is 1°, consequently. The weights are normalised in such a way that they match the condition $N_{bins} = \sum_{i=1}^{N_{bins}} \frac{1}{w_i}$ so that every weight is close to unity, compare to figure 5.3. The corrections of the binned methods are simply given by scaling the bin entries with the attributed inverse weight $1/w_i$. In case of the 3D unbinned likelihood method the weights are passed on to the probability density function of the dipole as additional factors depending on the right ascension value of the individual arrival direction. For the unbinned Rayleigh method the weighting is applied at the level of the basic parameters X and Y from which the amplitude and phase measurements are derived, following equation 6.14:

$$X = \frac{2}{N} \sum_{k=1}^{N} \frac{1}{w_i(k)} \cos \alpha_k \quad \text{and} \quad Y = \frac{2}{N} \sum_{k=1}^{N} \frac{1}{w_i(k)} \sin \alpha_k \; . \tag{8.1}$$

The connection between w_i and k is drawn from the histogram containing the weights in the corresponding bin in right ascension.

Atmospheric and Geomagnetic Corrections

As described in chapter 5, the energy needs to be corrected to get rid of modulations induced by changing atmospheric conditions and distortions caused by the geomagnetic field. This correction is performed on the level of the energy estimator $S(1000)$ as given by equations 5.2 and 5.23, respectively. In order to unbias the energy correspondingly the corrected energy estimators are reprocessed in the procedure of the CIC method and the energy calibration with the same parameters as given in equations 3.15 and 3.18 in chapter 3.

8.3 Dipole Parameters from Application to Data

The results of the reconstruction of dipole parameters with the four methods are summarised in tables 8.2 and 8.3. The reconstructed amplitudes and directions are indicated as obtained for different states of corrections. The case of performing no corrections is considered as well as the scenario of correcting the exposure for effects of a varying SD area. Then, the corrections of the energy due to modulations induced by atmospheric variations as well as by the geomagnetic field are applied. The corrections are performed inclusively, i.e. every line includes the correction stated in the line itself as well as those given in the previous lines. Consequently, the bottom line indicates the final results disentangled from all local effects.

Dipole Parameters and Uncertainties

The amplitudes reconstructed with every individual method remain essentially constant within their respective uncertainties regardless of the corrections applied. With the given statistics of $N \approx 30000$ events the predicted uncertainty of the amplitude is $\sigma(r_D) = \sqrt{2/N} \approx 0.008$ for the Rayleigh method. The values of the right ascension of the dipole direction found with the 3D and the 2D method at about $\alpha_D \approx 90^\circ$ agree well within their uncertainties. This value remains the same independent of the corrections performed. The declination parameter of the direction of the dipole obtained with the likelihood

Table 8.2: Dipole amplitudes D reconstructed with four methods given as obtained after performing the different corrections. The results in one line are inclusive with regard to the corrections indicated in and on top of it. Consequently, the results displayed in the bottom line are obtained after applying all corrections.

	Fit LL $D/10^{-2}$	Rayleigh $D/10^{-2}$	Fit χ^2 $D/10^{-2}$	Wavelet $D/10^{-2}$
No correction	3.6±2.0	1.7±0.7	7.5±2.1	3.1
SD area	3.6±1.8	1.4±0.7	7.4±2.1	2.7
Atmosphere	4.0±1.6	2.5±0.8	7.5±2.2	3.7
Geomag. field	3.5±1.4	2.3±0.8	5.3±2.1	3.6

Table 8.3: Dipole directions α_D (and δ_D) reconstructed with four methods. See also table 8.2.

	Fit LL		Rayleigh	Fit χ^2		Wavelet
	$\alpha_D/^\circ$	$\delta_D/^\circ$	$\alpha_D/^\circ$	$\alpha_D/^\circ$	$\delta_D/^\circ$	$\alpha_D/^\circ$
No correction	89±32	−51±28	84±35	103±32	−76±9	117
SD area	89±32	−51±27	77±42	100±42	−79±9	118
Atmosphere	93±22	−24±30	86±26	96±23	−68±10	107
Geomag. field	91±23	5±35	84±28	95±25	−60±16	105

(χ^2) method changes more apparently from $\delta_D = -51^\circ$ (-76°) in case of no correction to $\delta_D = 5^\circ$ (-60°) after applying all corrections. The uncertainty of the declination parameter amounts to $\pm 35^\circ$ ($\pm 16^\circ$). The results do not perfectly match but are compatible within two sigmas. The uncertainties obtained with the likelihood method is larger which partly can be explained by the fact that they correspond to ~ 85 % quantile rather than 68 %, see chapter 7 and appendix D.

Without applying any correction the amplitudes found with the two unbinned methods differ by a factor of two, approximately. This factor can be identified as the geometric correction necessary to scale an amplitude measurement of a 2D method to the 3D amplitude,

$$2 \approx \left[\cos(-51^\circ) \cdot \langle \cos(\delta) \rangle\right]^{-1} \ . \tag{8.2}$$

$\langle \cos(\delta) \rangle \approx 0.78$ is the mean of all cosines of the observed declination values in the distribution of arrival directions and $\cos(-51^\circ)$ is the fraction of the 3D amplitude that is visible in the projection on right ascension, see appendix C for further details. The geometric correction assumes the declination parameter of $\delta_D \approx -51^\circ$ found with the 3D likelihood method, see table 8.3. This characterisation roughly holds for all the other lines and steps of corrections, respectively, which implies consistency of the results obtained with the two methods.

Amplitude Measurements and Significance

Quantitatively, the absolute results obtained from the unbinned methods are trusted preferably because of the smaller statistical spreads and the mostly unbiased behaviour observed in Monte Carlo studies. Nevertheless, again all four methods are investigated with regard to

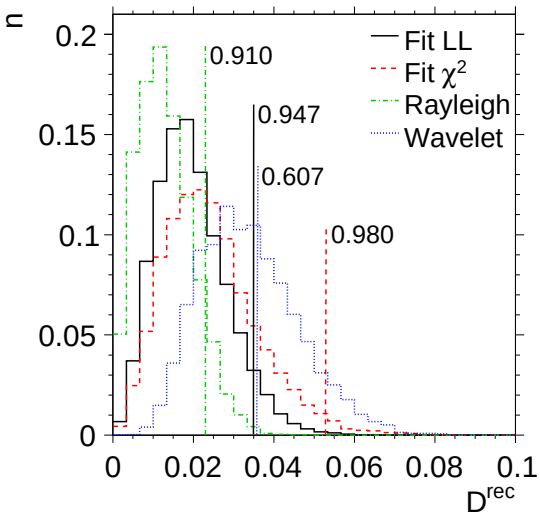

Figure 8.2: Significance of the amplitudes reconstructed from data with the four methods. The values found in the data are indicated by vertical lines and are compared to isotropic expectation. The number next to a line displays the significance of the respective measurement.

the significance of their reconstructed amplitudes. Here, advantage is taken of the fact that the significance is derived from every method inherently without need to relate the absolute amplitude measurements of the different methods to each other. The distinctness of the reconstructed amplitude found in the data from isotropy is displayed in figure 8.2 for the final values obtained after the application of all corrections.

The significances of the measured amplitudes with regard to their statistical distinguishability from isotropy vary from 61 % to 98 %. The likelihood method cannot exclude isotropy at the 95 % level. Thus, with the number of events currently at hand no conclusive anisotropy statement is possible. Assuming that the amplitude measured with the likelihood method is the true one, $N \approx 50000$ events need to be recorded in total to allow for the exclusion of isotropy at the 99 % level. This number of air showers will have been detected in another ~ 3 years of data taking with the surface detector. In the same scenario for the χ^2 fit only $N \approx 37000$ are needed to reach the 99 % level.

It is worth remarking that the amplitudes measured with e.g. the likelihood method without having applied all corrections is larger and thus, more significant. This observation becomes even more apparent noting that in the corresponding scenarios more events are available and consequently, the amplitude distributions obtained from isotropy are narrower. The computation of the significance does not take into account the statistical uncertainty of the amplitude parameter obtained from the fit. Therefore, the uncorrected event sets may contain artificial anisotropy mimicked by local effects that could cause a significant amplitude measurement.

Systematic Uncertainties

The uncertainties of the parameters determining the energy corrections corresponding to atmospheric variations on the one hand and the effect of the geomagnetic field on the other hand are propagated to the reconstructed dipole parameters. This is achieved by varying the

parameters normally within their uncertainties. The uncertainties of the parameters of the influence of the geomagnetic field are given in equations 5.20 and 5.19. The uncertainties of the parameters of the atmospheric energy corrections are obtained from [Abr09a]. The cuts described in table 8.1 are then performed "as usual" and the dipole methods are applied to the resulting set of events. This procedure is repeated 300 times and the RMS of the resulting distributions of the dipole parameters is used as a measure of the systematic uncertainty of the respective parameter. These systematic uncertainties are given in table 8.4. They are smaller than the statistical uncertainties by at least a factor of two.

Dependence on Energy Threshold

Air shower detection with the SD works fully efficient above an energy threshold of $E > E_{th} = 10^{18.5}$ eV. In this subsection the energy cut is increased from $10^{18.5}$ eV to $10^{19.2}$ eV in steps of $10^{0.1}$ eV. The dipole methods are applied to the resulting event sets and the reconstructed dipole parameters are shown in figure 8.3. Both the dipole direction and the significance of the measured amplitude show to be essentially independent of the energy threshold E_{th}. The significances obtained with the two unbinned methods, likelihood fit and Rayleigh, agree well. Note that the results obtained with the (binned) χ^2 method must be considered carefully at large values of E_{th} since with increasing energy cut the bins run out of statistics.

8.4 Summary

In this chapter, the four large scale anisotropy methods introduced in chapter 6 have been applied to real data taken with the SD of the PAO. A slight preference has been attributed to the unbinned methods, i.e. the dipole likelihood fit and the Rayleigh method, which have proven to perform better on Monte Carlo sky maps as studied in chapter 7. In table 8.4 the results are summarised.

The significances obtained for the amplitude measurements are statistically inconclusive. The statistical significances are smaller than 99 %, but close. Thus, they might be due to fluctuations as well as due to a genuine dipole signal. A larger number of events is necessary to provide the basis for a more definite answer to this issue. The right ascension of the dipole reconstructed consistently with all four methods at $\alpha_D \approx 90^\circ$ agrees with the phases measurement in the energy range above 3 EeV, see appendix C and [Abr11c]. The declination parameter has been shown to change slightly after the energy corrections. However, the dipole direction obtained with this single measurement is not meaningful as long as the amplitude is not considered significantly larger than the expectation from isotropy.

The systematic uncertainties of the dipole parameters have been estimated from the uncertainties of the parameters of the energy corrections corresponding to the effects of the atmosphere and the geomagnetic field. They are smaller by at least a factor of two compared to the statistical uncertainties estimated from the respective method.

The dipole parameter results obtained in this analysis are essentially independent of the energy threshold above which cosmic rays are allowed to enter into the analysis. This observation has been made with energy cuts up to $E > E_{th} = 10^{19.2}$ eV.

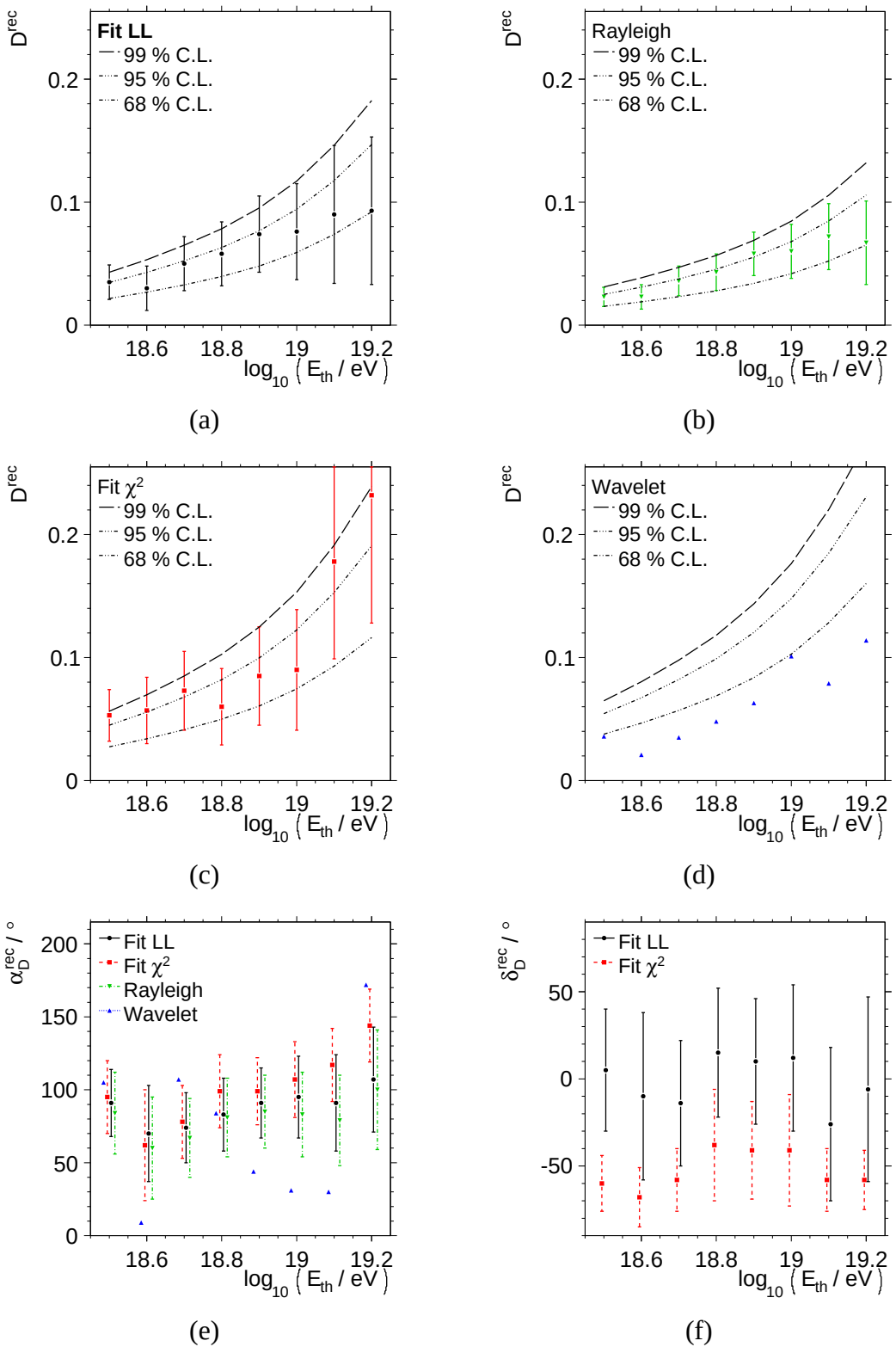

Figure 8.3: Dependence of the dipole parameters on the energy threshold E_{th}. (a), (b), (c) and (d) display the amplitudes of the dipole and the confidence levels for the likelihood, Rayleigh, χ^2 and Wavelet method, respectively. (e) and (f) indicate the reconstructed direction of the dipole in terms of right ascension and declination, respectively.

Table 8.4: Summary of dipole parameters with statistical uncertainties from the respective method and systematic uncertainties from the corrections, see text for details. Furthermore, the significances of amplitudes found in the data are indicated as the confidence level C.L. in terms of the fraction of amplitudes expected from isotropy below the measured amplitude value.

	$\alpha_D/^\circ$	$\delta_D/^\circ$
Fit LL	$91 \pm 23\ (stat)\ \pm 2\ (sys)$	$5 \pm 35\ (stat) \pm 14\ (sys)$
Rayleigh	$84 \pm 28\ (stat)\ \pm 2\ (sys)$	
Fit χ^2	$95 \pm 25\ (stat)\ \pm 2\ (sys)$	$-60 \pm 16\ (stat) \pm 3\ (sys)$
Wavelet	$105 \quad 1\ (sys)$	
	$D/10^{-2}$	C.L.
Fit LL	$3.5 \pm 1.4\ (stat) \pm 0.5\ (sys)$	0.947
Rayleigh	$2.3 \pm 1.1\ (stat) \pm 0.1\ (sys)$	0.910
Fit χ^2	$5.3 \pm 2.1\ (stat) \pm 0.4\ (sys)$	0.980
Wavelet	$3.6 \quad 0.1\ (sys)$	0.607

Chapter 9

Summary

In this thesis, large scale anisotropy studies of the distribution of arrival directions of ultra high energy cosmic rays recorded with the surface detector of the Pierre Auger Observatory have been focussed on. With this intention, three major topics have been investigated.

Firstly, the angular resolution of the surface detector has been studied thoroughly. Systematic uncertainties have been quantified by means of the comparison of arrival directions measured by the surface detector and the fluorescence detector. The difference of the angular coordinates obtained with the two reconstructions has been found to be less than 0.5° in any case. The angular resolution of the surface detector has been obtained to be better than 1.2° for the energies of interest, i.e. energies above the full efficiency threshold of the detector, $E > 10^{18.5}$ eV. In the course of this work, systematic uncertainties of the fluorescence detector have been discovered and quantified. It is worth remarking that with the results of this analysis a basis has been provided for the improvement of the directional reconstruction of the fluorescence detector.

Secondly, systematic local effects capable of mimicking anisotropy in the distribution of arrival directions have been studied. These effects are caused by properties of the detector which are typically not accounted for in the standard reconstruction of events. The varying area of the surface detector and the changing atmospheric (weather) conditions modulating the energy measurement over time systematically affect the right ascension distribution modifying the relative event rate to an extent of ~ 0.5 %, in each case. The corrections of both effects have been elucidated.

The main focus was put on the investigation of the influence of the geomagnetic field on the energy estimated with the surface detector. Via charge separation the lateral distribution of the particles of the air shower becomes spatially distorted with the extent of the distortion depending on the arrival direction of the shower. This systematic is directly transferred to the energy estimator $S(1000)$ of the surface detector measured at ground level and indirectly propagates to the event rate as soon as an energy cut is applied to the data set. A spatial model in local coordinates has been introduced to parametrise the effect on the level of $S(1000)$. By means of the complete chain of air shower simulations and detector simulations and reconstructions the parameters of the model have been fitted. The amplitude of the modulation of the relative event rate has been estimated to be of the order of ~ 1 %. The correction of the energy estimator necessary to make the measurement independent of the geomagnetic field is given by the introduced model and the fit parameters.

Thirdly, methods to study first order harmonic large scale anisotropies, i.e. dipoles, in the distribution of arrival directions have been investigated. The standard Rayleigh forma-

lism has been applied to the right ascension distribution and has been contrasted to a new binned method based on wavelet transforms. Furthermore, two new methods of fitting the 3D parametrisation of a dipole as detectable from the position of the Pierre Auger Observatory have been introduced: An unbinned likelihood method and a binned χ^2 fit.
Tested on Monte Carlo sky maps diced from the dipole parametrisation for different amplitudes and directions of the dipole the performance of the methods has been quantified.

- The Rayleigh method produces results perfectly agreeing with the expectation: E.g. it produces amplitudes that follow a Rice distribution in the presence and a Rayleigh distribution in the absence of a dipole signal.

- The wavelet transform has proved its applicability in the course of anisotropy studies though producing comparably large statistical uncertainties. This drawback is understood since the wavelet test function is not natively described by sinusoidal functions and there may also be room for improvement of the procedure of how the amplitude and phase are fitted.
  The wavelet method is currently being generalised for 3D anisotropy studies on the sphere by Matthias Plum based on the groundwork introduced in this thesis. With its application to distributions of arrival directions recorded with the surface detector of the Pierre Auger Observatory, a multi-scale approach is intended. Basically, this ansatz is similar to the standard spherical harmonics transform; a central aim of this work will be to evaluate whether or not advantage can be taken of the fact that wavelets provide a larger variety of possible shapes given by the wavelet test function that is made use of in the respective application.

- The unbinned likelihood method performs extraordinarily well in terms of small statistical uncertainties and negligible systematics. It is competitive to existing dipole reconstruction methods.

- The χ^2 fit shows qualitative agreement with the likelihood method. However, a rather coarse binning is necessary to get rid of a systematic dependence of the reconstruction precision on the declination parameter of the dipole; therefore, it produces slightly larger statistical uncertainties.

The application of the large scale anisotropy methods to real data taken with the surface detector of the Pierre Auger Observatory reveals two conclusions, essentially.
Firstly, as expected, the corrections applied to the data affect the significance of the amplitude measurements; amplitudes may be measured significantly at a confidence level of beyond 99 % at earlier stages of the chain of corrections. The amplitudes of the modulations of the relative event rate due to local effects are of the same order as the statistical uncertainties of the reconstructed dipole amplitudes, ~ 1 %. Therefore, the corrections to get rid of an artificially induced anisotropy caused by local effects are necessary especially for the computation of the significances of amplitude measurements.
Secondly, the amplitudes obtained after the application of the complete chain of corrections cannot be distinguished from isotropy at a confidence level of 99 % with neither method. This is the quintessential statement concerning anisotropy searches obtained in this thesis: Isotropy cannot be excluded with a probability larger than 99 %.

Appendix A

Coordinate Systems

The frame of reference for the geographically local measurement of arrival directions of cosmic rays and extensive air showers, respectively, is time dependent. Because of the Earth's rotation, a pair of locally measured angles of a celestially fixed object determines a point on the sphere, that seems to travel. It takes the period of a sidereal day, i.e. 23 h, 56 min and 4.099 s, or simply 360°, until the object will be visible again in the same direction and from the same geographic position. This time is different from the mean solar day (24 h), as the Earth's travel around the sun yields an additional rotation interval of $\sim 1^\circ$ per day. Thus, the number of sidereal days (366.25636042) within a year exceeds the number of mean solar days (365.25636042) in the same period by exactly 1 day. The Earth's axis can be assumed as fixed within a period of 50 years, as only little precession of $1^\circ/180$ y is observed. Thus, epochs are defined referring to the standard equinox (see below for explanation) every 50 years, with the actual period being named J2000.0. Furthermore, considering galactic and intergalactic distances, the instantaneous position of the Earth relative to the sun is negligible, too.

In order to specify a celestial position from the point of view of the earthbound observer, several different coordinates are needed. Obviously, the *local* position of the apparent source of the cosmic ray on the celestial sphere has to be known. Furthermore, this directional information depends on both the *geographic position* of the observer and the *time* of the observation. Two fixed reference frames are conventionally used, in order to specify a point on the celestial sphere: Both the *equatorial* and the *galactic* coordinate system are independent of time, observer position and locally measured arrival direction of a shower.

In this thesis, the local and equatorial coordinate systems were chosen for the display of directional information of cosmic rays. Both frames of reference as well as transformations between the two are given in the following sections. They are used within this thesis in order to transform the directional information locally measured by the SD into an equatorial position. Furthermore, the projection of spherical data by means of the so-called Hammer projection is introduced. The detector specific coordinate systems are not addressed here but are discussed in chapter 3.

A.1 Geographic Coordinates

A geographic position can be specified by a pair of spherical coordinates, i.e. geographic longitude *lon*, with $lon = 0^\circ$ at the Greenwich prime meridian, and geographic latitude *lat*,

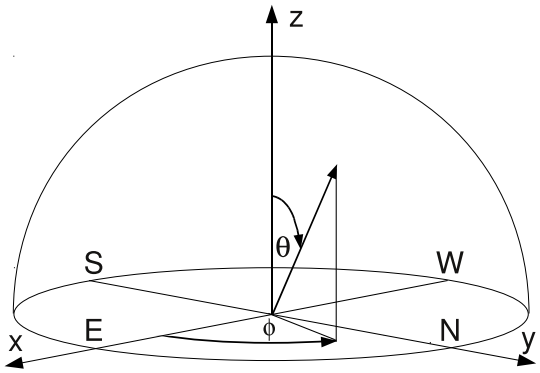

Figure A.1: The local coordinate system is a spherical coordinate system with the latitude being called altitude and the longitude known as azimuth angle. It covers a half space, as the azimuth angle can take only positive values. It is centred on the observer and the reference plane is defined by the observer's horizon. If in addition to the pair of local coordinates time and observer position are known, the celestial position of an object can be determined.

with $lat = 0^\circ$ at the equator and $lat = \pm 90^\circ$ at north and south pole, respectively. For the complete determination of the position of an object in geographic coordinates, the radius w.r.t. the Earth's center, alternatively the altitude a.s.l., needs to be known. The center of the PAO SD array expressed in geographic coordinates then is located at

$$lon_{\mathrm{PAO}} = -69.25^\circ \ , \quad lat_{\mathrm{PAO}} = -35.25^\circ \ , \quad alt_{\mathrm{PAO}} \approx 1400 \text{ m a.s.l.} \tag{A.1}$$

A.2 Local Coordinates

The incoming directions of air showers are measured in spherical coordinates of zenith angle θ, with $\theta = 0^\circ$ in case of a vertical shower, and azimuth angle ϕ, starting with $\phi = 0^\circ$ in the east and counting counter-clockwise, see figure A.1. Local coordinates, however, may also be given in altitude *alt* and azimuth angle, where the altitude is the elevation of an object above the horizon, $alt = 90^\circ - \theta$. The reference plane, called the horizontal plane, is a plane tangential to the Earth's surface through the observer's position. The measured arrival direction of an air shower does not point into the heading of the cosmic ray, but instead faces 'upwards' to where the cosmic ray apparently came from. The positions of celestial objects depend on the observer position and the time of observation. Thus, the local reference frame is inappropriate as a coordinate system for determining celestial positions.

A.3 Equatorial Coordinates

The position of a celestial object can be specified independently of time and observer position in an equatorial reference frame, see figure A.2. Equatorial coordinates are spherical and the reference plane is given by the Earth's equatorial plane. Consequently, the geographic latitudes are simply projected onto the sky (along the local zenith direction), defining the equa-

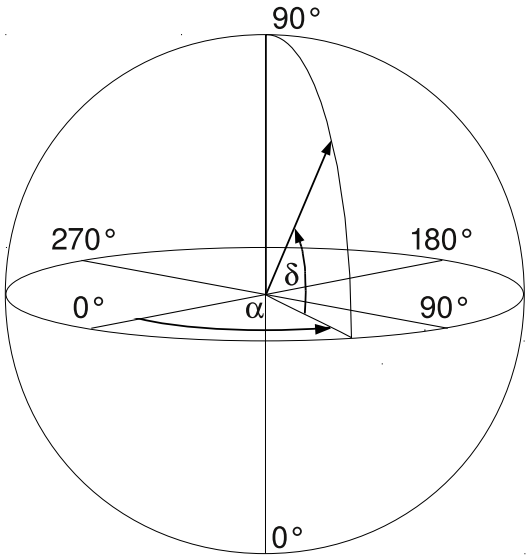

Figure A.2: The equatorial reference frame is a spheric coordinate system in declination (latitude) and right ascension (longitude). It is centred on the Earth and the reference plane is given by the equatorial plane of our planet; correspondingly, the Earth and the equatorial system share the directions of the poles as well. Celestial directions can be specified independently on time (neglecting epochal conventions, see text), without providing information about distances.

torial latitude, called declination. The declination δ corresponds to the spherical latitude, giving the angular distance of a star to the equatorial plane, while the spherical longitude is called right ascension α; the reference point for α is chosen conventionally as the vernal equinox which is defined as the point on the equatorial plane that coincides with the position of the sun at the beginning of spring. In order to find α it is necessary to introduce the local time information. The hour angle h is defined as the difference in geographic longitude between the positions of observer and the point on the Earth's surface where the object appears at zenith ($\theta = 0$); α then is simply given by the difference between local sidereal time *LST* and hour angle h, which can be converted from time to angular units ($360^\circ \hat{=} 2\pi \approx 23.9344719$ h)

$$LST - \alpha = h \; . \tag{A.2}$$

Finally, the transformation from local coordinates to equatorial coordinates is given by the following set of equations (note that the observer's longitude, lon_{PAO} enters indirectly via the hour angle h):

$$\cos\delta \sin h = \sin\theta \; \sin\phi \tag{A.3}$$

$$\sin\delta = \sin lat_{\mathrm{PAO}} \; \cos\theta \; - \; \cos lat_{\mathrm{PAO}} \; \sin\theta \; \cos\phi \tag{A.4}$$

$$\cos\delta \cos h = \cos lat_{\mathrm{PAO}} \; \cos\theta \; - \; \sin lat_{\mathrm{PAO}} \; \sin\theta \; \cos\phi \tag{A.5}$$

Note that the orientation and position of the equatorial plane are fixed, neglecting the relative position of our planet to the sun. The precession of the Earth's axis slightly alters the orientation of the equatorial reference frame with respect to the position of fixed stars. Thus,

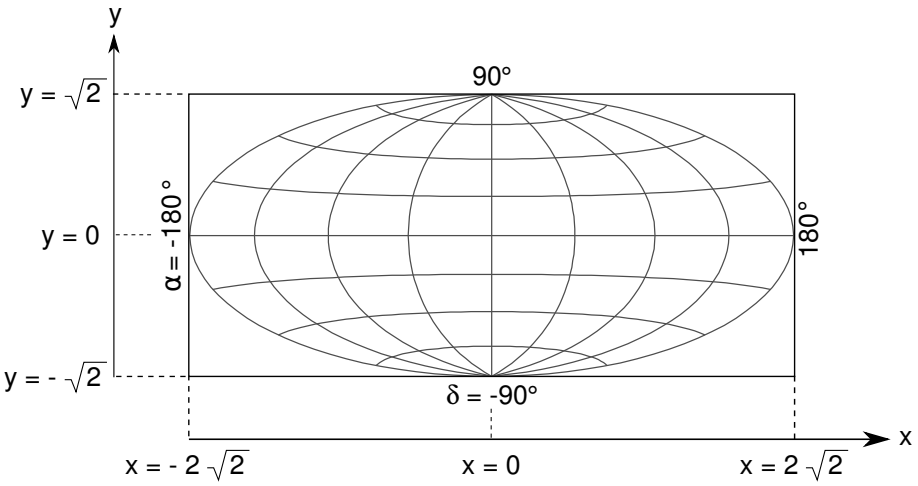

Figure A.3: Hammer projection of spherical coordinates for the example of the equatorial frame of reference, see equation .

when considering observations separated by long intervals of time it is necessary to specify an epoch (e.g. J2000.0 now, B1950.0 for older data) to determine the equatorial coordinates of celestial positions.

A.4 Hammer Projection of Spherical Coordinates

The application of projections of data distributed on the sphere is often useful both for the purpose of displaying and analysing these data. Whenever two-dimensional visualisations of spherical coordinates are needed in this work, the Hammer projection will be used (unless otherwise stated). It has the advantage of illustrating distributions on the surface of a sphere by means of an equal-area projection on the plane which is especially reasonable for the analysis of binned data. As an example, figure A.3 displays the coordinate grid for the equatorial frame of reference. The projection is realised by applying the following equations [Sny93]:

$$x = \frac{2\sqrt{2}\cos\delta\sin\left(\frac{\alpha}{2}\right)}{\sqrt{1+\cos\delta\cos\left(\frac{\alpha}{2}\right)}}\,, \quad y = \frac{\sqrt{2}\sin\delta}{\sqrt{1+\cos\delta\cos\left(\frac{\alpha}{2}\right)}} \tag{A.6}$$

A.5 Shower Coordinates

It is natural and useful to define a reference frame for the air shower itself. Shower coordinates can be determined in a Cartesian system, see figure A.4. The shower direction $\mathbf{e}_s$ defines the negative z-axis $-\mathbf{e}_z$ and the perpendicular plane that includes the shower core position defines the x,y-plane. In this *shower plane*, the y-axis direction $\mathbf{e}_y$ is chosen so that it coincides with the component of the geomagnetic field direction perpendicular to the shower direction, $\mathbf{B}_T$. Corresponding to the essentially cylindrical symmetry of the shower development and the particle densities, a cylindrical reference frame is equivalently applicable with r the distance to the shower axis and ψ the azimuthal angle in the x,y-plane of the shower coordinate system.

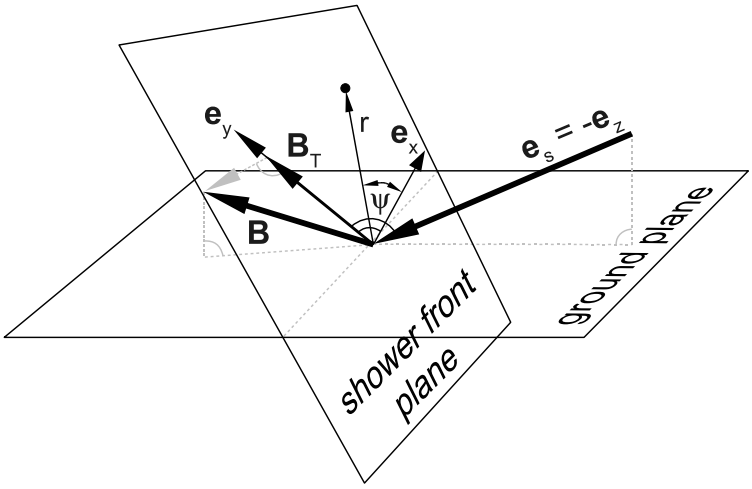

Figure A.4: The shower coordinate system is a Cartesian coordinate system with the z-axis $\mathbf{e}_z$ anti-parallel to the direction of the momentum of the shower $\mathbf{e}_s$ [Ave00]. The x,y-plane includes the shower core position and the y-axis is defined by the projection of the direction of the geomagnetic field $-\mathbf{B}$ on the x,y-plane, $\mathbf{B}_T$. Equivalently, cylindrical coordinates can be used with r the distance to the shower axis and ψ the azimuthal angle in the shower plane.

Appendix B

Extensive Air Shower Simulations

In order to generate air showers from primary particles of predefined properties and under predefined conditions two simulation programs have been made use of in this thesis, AIR-shower Extended Simulations (AIRES), version 2-8-4a [Sci02], and COsmic Ray SImulations for KAscade (CORSIKA), version 6.9.00 [Hec09]. Both are the most suitable and most commonly used air shower simulation programs for the production of EAS initiated by UHECRs.

The simulation of extensive air showers consists of the full space-time propagation of the primary particle in the uppermost layers of the atmosphere and the secondary particles generated in the cascade from the point of first interaction down to ground level. In a probabilistic approach the programs account for the different cross-sections of a variety of possible interactions with atmospheric constituents as well as the decay, fragmentation and attenuation of particles.

The CORSIKA program is a complete set of standard Fortran routines and consists of four parts. The first part handles the input of parameters of the cosmic ray primary particle such as particle type, energy and direction as well as the output of the secondary particles at a desired level of observation. It also performs the decay of unstable particles and the paths of the particles taking into account energy loss due to ionization and deflection by multiple scattering and the geomagnetic field. The second part is dedicated to the strong interactions of hadrons and nuclei with atmospheric nuclei at highest energies above ~ 100 GeV. The third part treats the hadronic interactions at lower energies and the fourth part describes the propagation of the electromagnetic component of the shower.

It lies outside the scope of this thesis to illuminate the complex details or advantages and drawbacks of the various interaction and propagation models that are available for the simulation of air showers. Therefore, only some brief statements and the choice of models for the showers simulated in the context of studies of the geomagnetic field effect are given in the following. At particle energies above $E \gtrsim 100$ GeV several models for the hadronic interaction cross-sections are available. These models tend to disagree more or less strongly as already mentioned in the context of X_{max} and composition studies in chapter 2. At moderate particle energies of up to some $E \approx 10$ GeV a number of phenomenological hadronic interaction models have been tested on and tuned with or verified by data recorded in collider experiments. The propagation of the electromagnetic component is modelled by means of analytical equations derived from Quantum chromodynamics.

The models made use of in this work for high and low energy hadronic and electromagnetic interactions are QGSJet-II [Ost06a, Ost06b], FLUKA [Fas03] and EGS4 [Nel85],

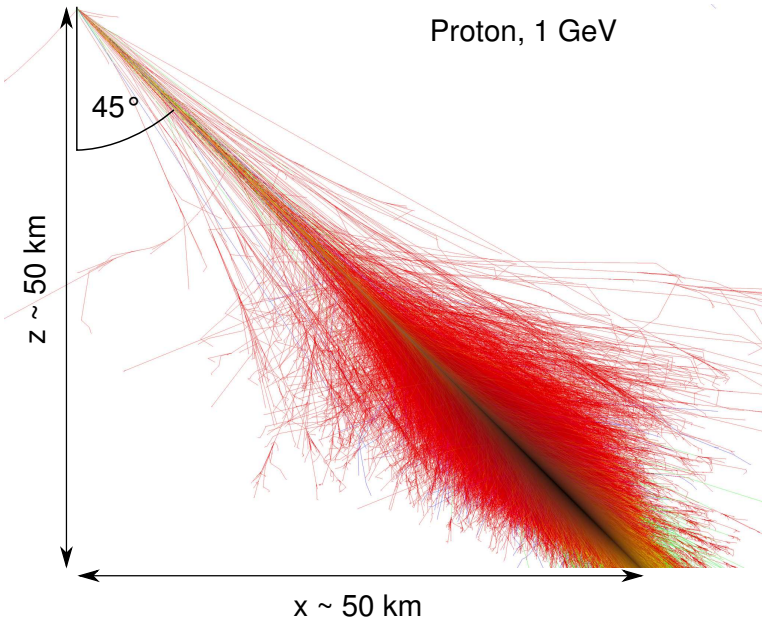

Figure B.1: Tracks of secondary particles as obtained from the simulation of an air shower with the CORSIKA program. The primary particle is a proton of energy $E = 10^{15}$ eV and the paths of hadrons (blue), muons (green) and electrons / positrons (red) are indicated. Taken from the CORSIKA homepage, *http://www-ik.fzk.de/corsika/*

respectively. While this is valid for the simulations produced with CORSIKA, in the AIRES simulations QGSJet-II and the extended Hillas Splitting Algorithm (HSA) [Sci02, Hil81] are used. The main reason to make use of the latter program for the large set of isotropic air showers is the smaller computation time; with AIRES, the CPU time consumption is reduced by about a factor of five for typical showers simulated in this work.

Both simulation programs offer the option of thinning. Again very useful in terms of the reduction of computational complexity, this option allows for the propagation of a huge number of secondary particles by essentially tracking only leading particles. Weights are assigned to all particles below a certain fraction of the primary energy. This allows to keep track of the relevant particles of the cascade development and to neglect the bunch of particles of lower energies which are supposed to at most affect the shower development only weakly and contribute few to the signal at ground level. An unthinning has to be performed by the program to produce a realistic particle content at ground level that can be passed on to the detector.

The simulations are steered by means of a simple text file that contains keywords and assigned values to fix the parameters of the shower and the conditions under which the simulation should be performed. An example steering card for the simulation with CORSIKA of a shower of fixed direction and energy is given in table B.1.

The shower simulation output is put into the detector simulation available with the Offline framework. Making use of GEANT4 [Ago03] the responses of the surface detector stations to the particle content of the air shower at ground level are simulated; thus, the same types of signals are produced in the SD stations that are also generated by real air showers. Consequently, simulated and real air showers can be reconstructed with identical reconstruction chains, the details of which have been elucidated in chapter 3 and are documented in the

Table B.1: Example of a steering card as used in an air shower simulation with CORSIKA. For the sake of compactness, not all keywords actually used are shown. The run number (RUNNR) is used to assign a number to every shower simulated. A random seed (SEED) has to be set and remembered for the sake of reproducibility of results. The primary particle (PRMPAR) is a proton encoded by the number 14. The energy range (ERANGE), zenith angle range (THETAP) and azimuth angle range (PHIP) of the primary is fixed to a number 8×10^9 GeV $\equiv$ 8 EeV, 55° and 61°. The altitude of observation (OBSLEV) of the surface detector is 1452 m. The transition between high and low energy hadronic interaction model (HILOW) is fixed to take place at 200 GeV. Thinning (THIN) is switched on as soon as the energy of a secondary particle drops below the millionth part of the primary energy. The magnetic field (MAGNET) parameters are given by x and z-components in μT of the local field vector in the CORSIKA coordinate system.

RUNNR	100000		
SEED	100001		
PRMPAR	14		
ERANGE	8.0000E+09	8.0000E+09	
THETAP	55.00	55.00	
PHIP	61.	61.	
OBSLEV	1452.e2	870.00g/cm2	
HILOW	200.		
THIN	1.e-06		
MAGNET	20.0	-14.2	Auger

$\overline{\text{Off}}\underline{\text{line}}$ reference manual and framework [Veb05].

Appendix C

Amplitude and Phase Measurements

Anisotropy Studies in 2D

In this appendix the following naming conventions apply for the amplitude and phase: Generically, the parameters of an individual distribution derived from any scenario will be denoted r and ϕ. The parameters of a genuine signal a distribution is potentially obtained from will be r_0 and ϕ_0. The random variables describing the distributions of r and ϕ will be denoted R and Φ. These parameters then describe the potential deviation in first harmonic space from the hypothesis of isotropy by the following expression

$$f(\alpha) = 1 + r\cos(\alpha - \phi) \ . \tag{C.1}$$

In this appendix some general aspects of measurements of the parameters of a cosine function from a distribution of polar angles on the unit circle will be discussed.

C.1 Probability Density Functions - Isotropy

The measurements of amplitude and phase from isotropic realizations observe the following properties: As intuitively clear, the phase obtained from an isotropic sample is supposed to be randomly distributed. However, amplitude measurements independently of the method they are obtained with will not be zero in the case of isotropy. This is because purely statistical fluctuations will make the distribution be not perfectly homogeneous.
The distribution of amplitudes derived from a set of realisations of isotropy is described by the Rayleigh probability density function (p.d.f.),

$$f_{p.d.f.}^{Rayleigh}(r, \sigma(r)) = \frac{r}{\sigma^2(r)} \cdot \exp\left(-\frac{r^2}{2\sigma^2(r)}\right) \ , \tag{C.2}$$

with $f_{p.d.f.}^{Rayleigh}$ the probability to find an amplitude r for a given number N of directions; note that this number enters via $\sigma(r) = \sqrt{2/N}$ as derived in chapter 6. The fact that an amplitude of exactly zero, $r \equiv 0$, is prohibited by the Rayleigh p.d.f. and will only occur in the limit of $N \to \infty$ is not surprising; it is a consequence of both the finite statistics and the infinitely small solid angle about the center of the coordinate system.

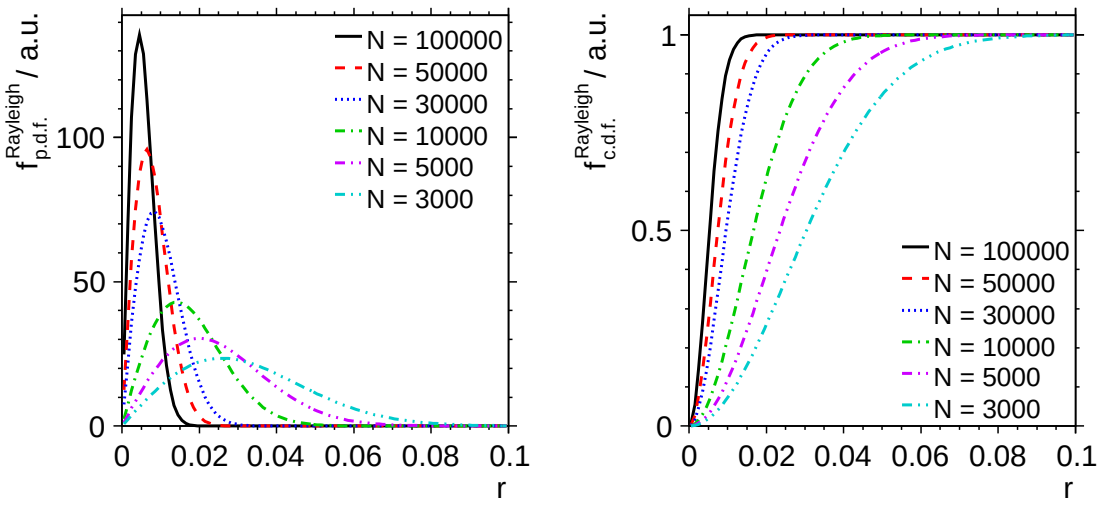

Figure C.1: Rayleigh probability density functions (p.d.f.) on the left and Rayleigh cumulative distribution functions (c.d.f.) on the right for various N, see text for details.

A cumulative distribution function (c.d.f.) $f^{Rayleigh}_{c.d.f.}$ of the amplitude is obtained from equation C.2 via integration,

$$f^{Rayleigh}_{c.d.f.}(r,\sigma(r)) = 1 - \exp\left(-\frac{r^2}{2\sigma^2(r)}\right) . \tag{C.3}$$

It defines the probability to measure an amplitude smaller than r from an isotropic distribution; consequently, $1 - f^{Rayleigh}_{c.d.f.}(r,\sigma(r))$ produces the probability to observe an amplitude of size r in an isotropic distribution. Both the Rayleigh p.d.f. and c.d.f. are displayed in figure C.1 for various values of N.

C.2 Probability Density Functions - Signal

In case of a genuine signal of amplitude $r_0 \neq 0$ and phase ϕ_0 anisotropic samples of polar angles are produced. The joint p.d.f. of the couple of random variables (R,Φ) is

$$p_{R,\Phi}(r,\phi) = r\, p_{X,Y}(r\cos\phi - r_0\cos\phi_0, r\sin\phi - r_0\sin\phi_0) . \tag{C.4}$$

The x and y components can be considered as independent random variables which are normally distributed about $(x_0 = r_0\cos\phi_0, y_0 = r_0\sin\phi_0)$ with variances $\sigma^2 = 2/N$, see section 6.1.1 for comparison. The p.d.f.s of the amplitude and phase are obtained by marginalisation, i.e. integration, over the respectively other parameter. Amplitudes r obtained from the corresponding anisotropic realisations follow the Rice distribution with the additional parameter r_0 indicating the true amplitude underlying the realisation. The phase ϕ follows a more complicated p.d.f.:

$$f^{R}_{p.d.f.}(r) = \frac{r}{\sigma^2}\exp\left(-\frac{r^2+r_0^2}{2\sigma^2}\right) I_0\left(\frac{r r_0}{\sigma^2}\right) \tag{C.5}$$

$$f^{\Phi}_{p.d.f.}(\phi) = \frac{1}{2\pi}\exp\left(-\frac{r_0^2}{2\sigma^2}\right) + \frac{r_0\cos(\phi-\phi_0)}{2\sqrt{2\pi}\sigma}\left(1+\mathrm{erf}\left(\frac{r_0\cos(\phi-\phi_0)}{\sqrt{2}\sigma}\right)\right)\exp\left(\frac{r_0^2\sin^2(\phi-\phi_0)}{2\sigma^2}\right) . \tag{C.6}$$

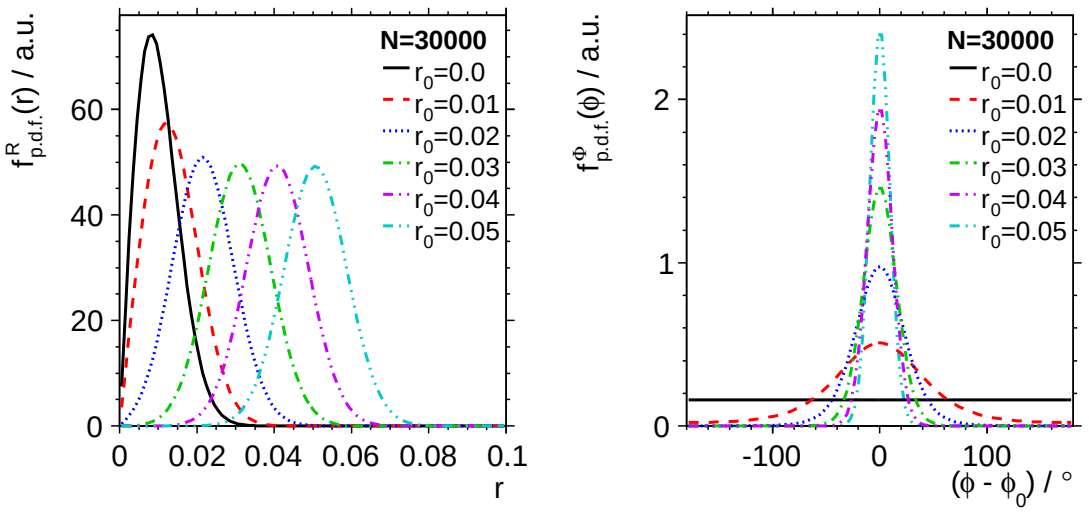

Figure C.2: Probability density functions of amplitude r and phase ϕ for $N \equiv 30000$. Both the distributions of r and ϕ are approximately Gaussian in case the genuine signal amplitude r_0 is large enough.

These probability density functions are displayed in figure C.2. As an example a number of $N = 30000$ entries in the distributions of polar angles is assumed. The uncertainty of the amplitude amounts to $\sigma = \sqrt{2/N} \approx 0.0082 \equiv 0.82$ %. This uncertainty estimate of the amplitude measurement implies that any method searching for first order harmonic anisotropies in a distribution of 30000 angles is supposed to be rather insensitive to genuine signal amplitudes of $r_0 \lesssim 1$ %. Concerning the phase measurement, the following considerations apply: On the one hand, the phase obtained from a genuine signal does contain information. On the other hand, it not clear a priori whether or not a genuine signal underlies the recorded distribution of polar angles. However, it will be shown later that the phase measurements from uncorrelated data sets indeed contains useful information with respect to potentially underlying anisotropy.

How significantly anisotropy can be distinguished from isotropy depends on the amplitude r_0 of the genuine signal and the number N of polar angles available. To get a quantitative impression, again the case of $N = 30000$ will be considered in the following. The left plot in figure C.3 shows a comparison of the p.d.f.s of the measured amplitudes r as obtained from isotropic and anisotropic samples with corresponding amplitudes of $r_0 = 0$ and $r_0 = 0.02$, respectively. The vertical lines correspond to amplitudes r that indicate upper limits for the integration of the isotropic p.d.f., $f^{Rayleigh}_{p.d.f.}$, to make it contain the fraction p of the area. These values will be called r^p_{iso} in the following, they can be computed from equation C.3 as

$$r^p_{iso} = \sigma\sqrt{2\ln(1/(1-p))}\,. \tag{C.7}$$

The quantity p can be identified as a confidence level in the following context: The fraction of measured amplitudes r found to be larger than r^p_{iso} is defined as

$$n\left[r > r^p_{iso}\right] \;=\; \frac{N\left[r > r^p_{iso}\right]}{N_{tot}}\,, \tag{C.8}$$

with $N\left[r > r^p_{iso}\right]$ the absolute number of amplitudes r larger than r^p_{iso} and N_{tot} the total num-

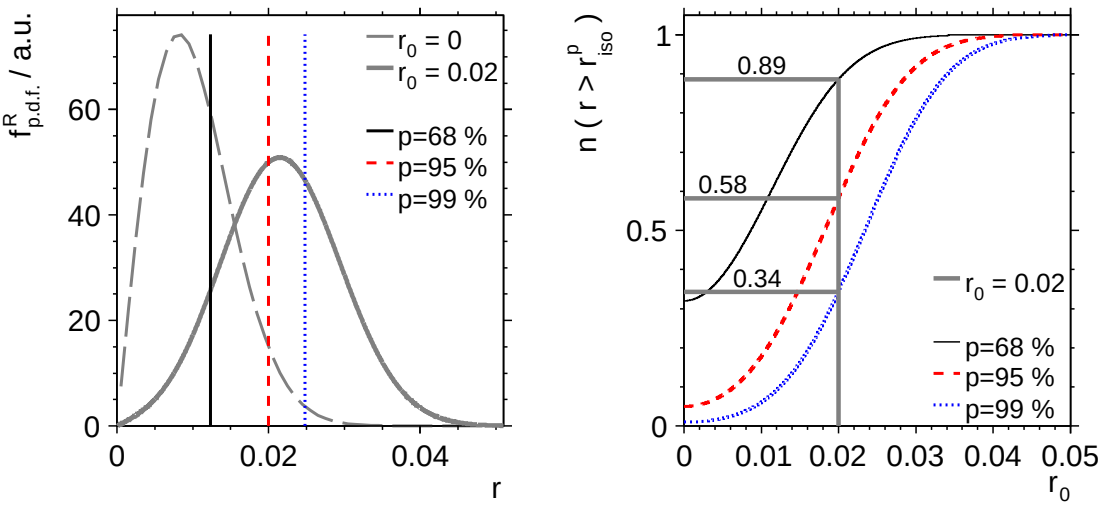

Figure C.3: Probability to find a significant amplitude depending on the genuine signal. Left: The overlap of the p.d.f.s of isotropic (grey dashed) and anisotropic (grey solid) amplitude measurements can lead to misidentifications of isotropy. The integral of the isotropic p.d.f. is given by the Rayleigh c.d.f., equation C.3, and upper limits of the integral are given by vertical lines. Right: A measured amplitude r from a distribution diced from a genuine signal of $r_0 = 0.02$ is distinguishable from isotropy in a fraction of $n(r > r^p_{iso}) = 0.89$ (0.58, 0.34) measurements with a confidence of $p = 68$ % (95 %, 99 %) (straight grey lines).

ber of amplitudes measured; $n\left[r > r^p_{iso}\right]$ depends on the size of the signal amplitude r_0 and is plotted on the right of figure C.3 for different values of p. The plot shows that a measured amplitude r from a distribution diced from a genuine signal of $r_0 = 0.02$ is distinguishable from isotropy in a fraction of $n(r > r^p_{iso}) = 0.89$ (0.58, 0.34) of all measurements with a confidence of $p = 68$ % (95 %, 99 %).

The basic message of this example is that amplitudes of small genuine signals are likely to be considered noise. Therefore, it is of interest whether and how a measurement can be improved by making use of the phase information as well. Figure C.4 shows the distributions of amplitudes and phases obtained from 1000 MC data samples each containing 10000 entries that are produced either from random noise (black) or from a genuine signal with $r_0 = 0.01$ and $\phi_0 = 180^\circ$ (blue): The probability to find a significant amplitude at a confidence level of 99 % is 10 %. The probability to find the phase within 40° of the true phase ϕ_0 is 66 %. While the significance of the amplitude can be derived directly from the value compared to isotropic expectation, phase value show a concentration around the true phase value that cannot be interpreted immediately as a significance.

It is remarkable that Linsley exemplified the different behaviour of phase and amplitude measurements already more than three decades ago; the statement can be found in [Edg78]:

Linsley has given a useful example of the behaviour of amplitude and phase estimates in different experiments. If the number of events available in an experiment is such that the RMS value of r is equal to the true value of r_0, then in a sequence of experiments r will only be significant (say at 99 % C.L.) in one experiment out of ten whereas the phase will be within 50° of the true phase in two experiments out of three.

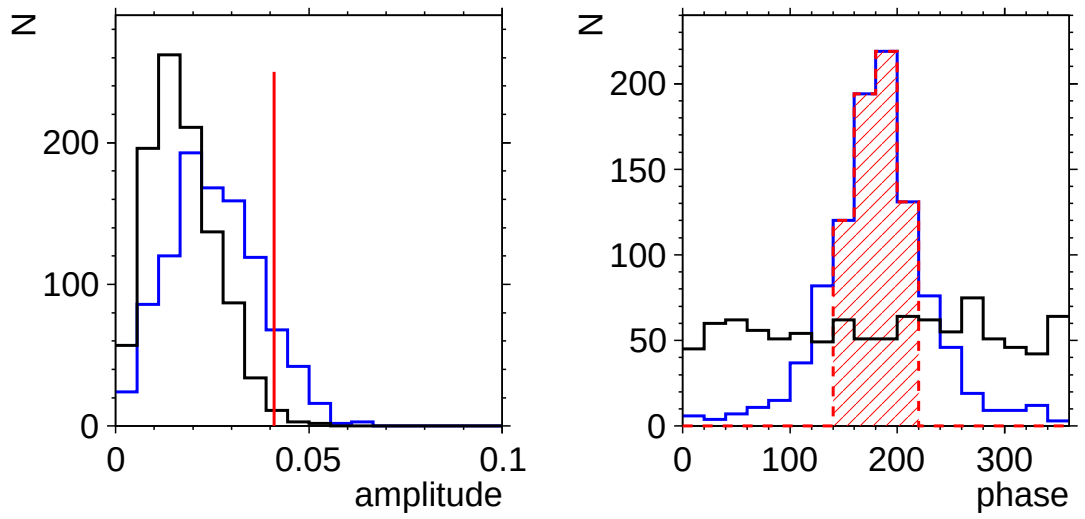

Figure C.4: Amplitude (left) and phase (right) distributions at noise level: The black histograms indicate isotropy and the blue ones display the distributions for a genuine signal of amplitude $r_0 = 0.02$ and phase $\phi_0 = 180°$. The red lines indicate the limits of arbitrarily chosen levels of confidence, see text for details.

C.3 Sensitivity to Anisotropy

The aim of this section is to compare amplitude and phase measurements with respect to their sensitivity to anisotropies. For a single measurement the meaningfulness of the phase depends directly on the significance of the amplitude. In case more measurements are made available e.g. by sensibly subdividing the data into independent samples aligned phases would provide a hint to a genuine signal even in case the amplitudes of the individual samples are mostly compatible with isotropy. This statement is evaluated in the following by means of tests introduced on both the amplitudes and the phases of a certain number of N_{bins} independent measurements. The tests presented here are largely based on [Bon10] and references therein.

C.3.1 Test on Amplitude

The Rayleigh cumulative distribution function, equation C.3, gives the probability for a single measurement of an amplitude that the same or a smaller amplitude is found in an isotropic sample. The quantity of interest for the case of two or more independent measurements is the probability that all of the N_{bins} measured amplitudes are compatible with isotropy. Since the amplitude r is obtained from the two normally distributed variables x and y, the sum over the squares of the N_{bins} measured amplitudes follows a χ^2 distribution with 2 degrees of freedom:

$$\sum_{i=1}^{N_{bins}} \left(\frac{r_i}{\sigma(r_i)} \right)^2 \sim \chi^2_{2N_{bins}} \,. \tag{C.9}$$

The probability to reject the hypothesis of isotropy therefore is calculated by integrating $\chi^2_{2N_{bins}}$ below the value of $\sum_{i=1}^{N_{bins}} (r_i/\sigma(r_i))^2$ obtained from the amplitudes r found in the data.

C.3.2 Test on Phase and Amplitude

Phases measured from isotropic data sets are randomly distributed over the complete range of 360°. Therefore, without the partner of a significant amplitude a phase measurement is not meaningful even in the presence of a genuine signal. However, phases measured from N_{bins} subsets of the data can be tested with respect to their alignment. In the simplest case the alignment hypothesis H_1 says the phases of all measurements should be the same, $\phi_0 = const$. In this case as well as in any other case it is clear that whatever parametrisation is used to describe the measured phases the prediction must not be tuned on the measurements but must be defined a priori. The isotropy hypothesis H_0 expects randomly distributed phases as obtained from equation C.6, $f^{iso}_{p.d.f.}(\phi) = 1/2\pi$. The likelihood functions of the two hypotheses are built as

$$L_0 = \prod_{i=1}^{N_{bins}} f^{iso}_{p.d.f.}(\phi_i) \; , \quad L_1 = \prod_{i=1}^{N_{bins}} f^{\Phi}_{p.d.f.}(\phi_i; r_0, \phi_0) \; . \tag{C.10}$$

By means of the likelihood ratio the probability to accept or reject the hypothesis H_0 compared to an alternative hypothesis H_1 is derived,

$$\lambda = \frac{L_0}{L_1} \; . \tag{C.11}$$

The distribution of $-2\ln\lambda$ is generated by 10000 simulated isotropic data samples. The value of $-2\ln\lambda$ that is found in the data is used as the upper limit of an integral over the normalised distribution obtained from isotropy. The value of the integral then gives the probability to reject isotropy, i.e. to distinguish between a true signal and expected fluctuations.

Note that a priori the genuine signal amplitude r_0 entering into the factors of L_1 indirectly via the phase p.d.f., equation C.6, is unknown. It is therefore set to the measured amplitude in the corresponding bin. Doing so, both the information of the phase and the amplitude measurement enter into the test. Furthermore, an expectation for the phase ϕ_0 must be entered. It is also of interest how a test on only the phase information performs compared to the test on the amplitude and the test on both quantities. For this scenario the amplitude can be fixed to the true signal amplitude when comparing the powers of the different tests on Monte Carlo simulations. The two options for r_0 are referred to as *test on phase and amplitude* and *test on phase* in the following.

C.3.3 Power of the Tests

A set of N_{bins} independent data samples of $N = 30000$ events is simulated with a genuine signal amplitude of $r_0 \equiv 0.01$ and phase of $\phi_0 \equiv 0°$. In figure C.5 the powers of the three tests are compared for different values of N_{bins}. The test on the combined information of phase and amplitude performs best being roughly a factor of two times more sensitive than the test on the amplitude. Remarkably, the test on the phase performs competitively well: As argued before, the power is confirmed to be zero at $N_{bins} = 1$ but increases and becomes larger than the power of the test on the amplitude as soon as the number of measurements exceeds a value of five, $N_{bins} \gtrsim 5$.

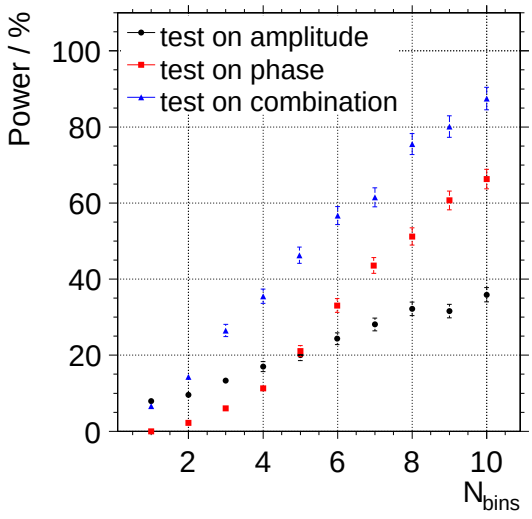

Figure C.5: Test on amplitude (black dots), phase (red squares) and both (blue triangles): Power of the tests as a function of the number of measurements N_{bins} for the example of a genuine signal of amplitude $r_0 \equiv 0.01$ and with $N = 30000$ polar angles in every bin.

C.3.4 Conclusion

Both phase and amplitude measurements are well understood. The comparison of the power of the described tests has confirmed what has been intuitively expected: The most valuable and significant result from a number of independent measurements can be obtained when making use of as much information available as possible; the test on both amplitude and phase has shown that given an a priori parametrisation of the predicted alignment of the phases the corresponding measurements can be taken advantage of successfully.

This approach has been made use of in [Abr11c] but with an a posteriori defined parametrisation of the alignment of phases: Phase and amplitude measurements from the right ascension distribution of the arrival directions recorded with the SD of the PAO in adjacent energy bins have been analysed, in this appendix the data are taken from the results given in [Gri11]. The alignment of the phases has been observed to agree with an a posteriori defined function that describes the transition of the phase from $-100^\circ (\hat{=} 260^\circ)$ at lower energies to $+100^\circ$ at higher energies,

$$\phi_0(E) = \phi_0 + \phi_E \arctan\left(\frac{\log_{10}(E) - \mu}{\sigma}\right) . \tag{C.12}$$

The data points agree extraordinarily well with the fit function, the parameters are

$$\phi_0 = (-11 \pm 37)^\circ , \qquad \phi_E = (97 \pm 52)^\circ \tag{C.13}$$

$$\mu = 0.16 \pm 0.20 , \qquad \sigma = 0.36 \pm 0.38 . \tag{C.14}$$

The agreement of the data with the given parametrisation shall be compared to the agreement of the same function with sets of phases diced from isotropic distributions. For the comparison to be fair, the parameters of the function are obtained by a fit not only in case of the data but also for every single set of random phases that enters into the isotropic histogram of likelihood ratios in figure C.6. The result from the fit to data is indicated by a vertical line. By means of this approach isotropy is rejected with a probability of 99.97 %.

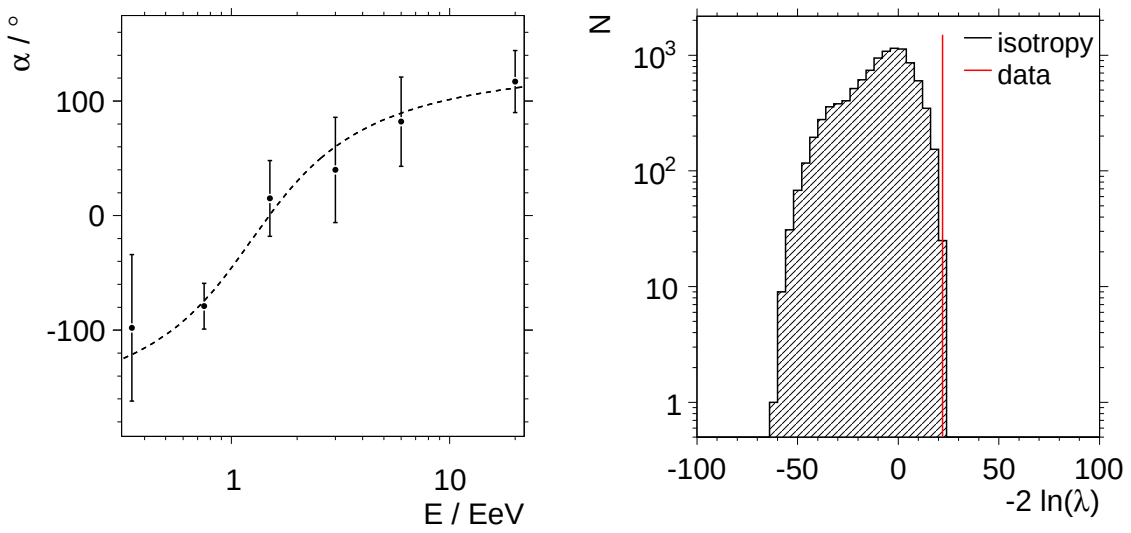

(a) (b)

Figure C.6: Phases obtained from measurements in adjacent energy bins (left). The phases agree remarkably well with an a posteriori defined function based on $\alpha(E) \sim \arctan(\log_{10} E)$. From the likelihood ratio method isotropy is accepted with a probability of 0.03 % (right). However, no significance can be derived from this observation, see text for details.

Unfortunately, no significance can be derived from this observation since the mathematical parametrisation of the alignment was defined a posteriori. Nevertheless, interesting implications e.g. on the energy dependent spatial distribution of sources would have been derivable if the function had been defined a priori. This is why the definition of a prescription to be applied to new data is discussed in this context. In case the observation is made from a genuine signal 1.6 times the amount of data already used is necessary to reach an efficiency of 90 % to verify the genuineness at 99 % C.L. as estimated in [Abr11c].

C.4 Transfer of Results in 2D to Sphere

Amplitudes obtained with a 2D method cannot directly be interpreted as dipole amplitudes on the sphere. On the one hand, it is expected that the sensitivity of 2D methods to dipole amplitudes decreases with increasing absolute value of the declination of the direction of the dipole. A dipole pointing to one of the poles in equatorial coordinates will not be visible at all for a 2D method. On the other hand, the detector does not observe the full sky but a spherical sector weighted according to the relative exposure mentioned earlier. This leads to the fact that even a dipole pointing to the equator, $\delta_D \equiv 0°$, will be reconstructed with a systematically smaller amplitude by a 2D method. Both cases are discussed in the following.

- With the true declination value at hand e.g. in case of simulations it is possible to scale the amplitude D_{2D} of a measurement by a 2D method with the inverse cosine of the true δ_D.

$$D \propto D_{2D} / \cos\delta_D \ . \tag{C.15}$$

  The result can be compared to the amplitude parameter D obtained with a 3D method. However, with a 2D method applied to real data the declination value of the dipole

direction is not known. Thus, only the reconstructed value of the dipole declination obtained with a 3D method applied on the same data might be used for the scaling in this case. In any event, it must be kept in mind that the more the dipole direction tends to one of the poles, the smaller the fraction of the dipole modulation will be that is transferred to the right ascension distribution. In the extreme case of a dipole pointing exactly e.g. to the south the measured amplitude must be zero, $D_{2D} \equiv 0$ to allow for the meaningfulness of equation C.15. As is known from the first paragraphs in this appendix, the amplitude measurement will never be zero. Consequently, with the given relation the 3D amplitude will be overestimated as soon as the true declination value is close to the poles. The declination value at which equation C.15 produces unreasonable results depends on the true amplitude itself and consequently, the scaling must be applied carefully especially when dealing with real data.

- The partial-sky coverage of a typical earthbound detector can be accounted for when considering the scenario of a dipole pointing somewhere to the equator, $\delta_D \equiv 0°$. The amplitude obtained with a 2D method on the right ascension distribution is scaled with the inverse of the mean of the cosines of the declination values in the respective MC data set,

$$D \propto D_{2D} / \langle \cos\delta \rangle \approx 1.28 D_{2D} \; . \tag{C.16}$$

  Doing so, the scaled amplitudes correspond to the full sky dipole amplitude expected to cause the given right ascension distribution e.g. measured with a detector located at the site of the PAO. Thus, the scaled amplitudes are directly comparable to amplitudes reconstructed with 3D methods for the same dipole declination parameter. It is common practice to indicate amplitudes of anisotropy results of 2D methods after having applied the scaling described here: The advantage is that typically, predictions for amplitudes of a right ascension modulation are made independently on the site of a specific detector and after the corresponding correction the measurements by observatories located at sites of different geographical latitudes may be compared directly both with these predictions as well as with each other. Of course, the comparisons of results obtained with different observatories have to be made carefully knowing full well that they do not necessarily have to agree: Different fractions of the sky are covered and it is not guaranteed that the measurement obtained with an observatory covering only one hemisphere is in fact caused by a full sky dipole. However, they of course have to agree to confirm a certain model prediction on the entire sky.

Appendix D

Dipole Fit Methods

Dependence of Statistical Power on Declination of Dipole

The statistical power of the measurement of a dipole from a sky map as observed by the SD of the PAO depends on the true declination of the dipole. A dipole pointing to the south will cause the accumulation of a fixed number N of events earlier in time than in absence of this dipole. In contrast, in the case of a dipole pointing to the north the same number of events will be accumulated later in time. In other words: Fixing the number of events to say $N = 30000$ causes the statistical power of the dipole measurement depend on its true declination. As a measure of this statistical power the number $\widetilde{N}$ of events is considered that would have been measured in the absence of an existing (in MC) dipole of given amplitude D^{true} and declination δ_D^{true}. This number $\widetilde{N}$ corresponds to the number of events expected from the isotropic background underlying the dipole; it is supposed to be smaller when the true declination of the dipole lies in the field of view of the SD and larger if it points to the northern hemisphere. For the sake of visualising this dependence, figure D.1 displays $\widetilde{N}$ as a function of δ_D^{true} for various amplitudes D^{true}. A dipole of an amplitude $D^{true} = 0.2$ causes a relative difference $(\widetilde{N} - N)/N$ of up to 10 %. More realistic amplitudes D^{true} still lead to values up to the ~ 1 % level.

The described connection between the true declination of the dipole and the statistical power of the measurement is expected to affect the reconstruction of the dipole amplitude. Amplitudes are supposed to be reconstructed more closely matching the true value when the dipole direction does point to positive declination values. This is valid especially for small amplitudes. This agrees with the expectation in 2D analyses: The left plot in figure C.1 displays for the extreme case of isotropy how the amplitude distribution is shifted to larger values with decreasing statistics.

Binning of Sky Maps for χ^2 Fit Method

For the χ^2 fit method the distribution of arrival directions is binned. In this appendix the appropriate binning of the corresponding rectangular 2D histogram is determined. Three binnings are analysed in a way similar to what is described in chapter 7.

Table D.1 shows these binnings and the average number $\langle n \rangle$ of entries per bin for the scenario of $N = 30000$ events. The number N_b of populated bins is also given; note that the

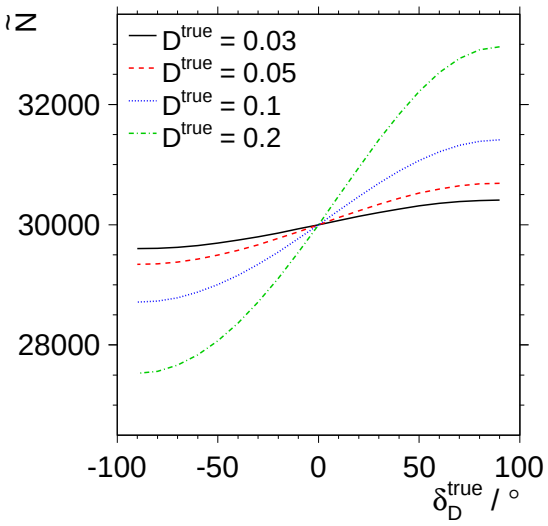

Figure D.1: The statistical power of dipole measurements depends on the true declination δ_D^{true} of the dipole, see text for details. The number $\widetilde{N}$ of events expected in absence of the dipole is plotted for various true dipole amplitudes D^{true}.

Table D.1: Binnings, number N_b of bins populated and average number $\langle n \rangle$ of entries per bin for the χ^2 fit method for the scenario of $N = 30000$ events. N_b^α and N_b^δ are the number of bins in *right ascension* and **declination**, respectively

N_b^α	N_b^δ	N_b	$\langle n \rangle$
36	18	432	69
18	9	108	278
12	6	48	625

PAO is no full sky observatory and thus, not all bins N_b^δ in the dimension of the declination are filled.

In case the bin size is chosen too small, a systematic bias is introduced resulting from small entries in the bins at the edges of the non flat relative exposure function given in equation 3.4: As displayed in figure D.2 (c) isotropic sky maps are preferentially reconstructed with negative declination values. This preference is transferred to plot (d) of the angular distance Ω between true and reconstructed direction and leads to the slightly flattened distribution about the equator. The described effect in δ_D^{rec} and Ω becomes smaller at coarser binnings.
Furthermore, the plot (a) in the same figure indicates that the amplitude D^{rec} is reconstructed smallest for the coarsest binning. Small amplitudes are desired in case of isotropy for intuitively obvious reasons when interpreting the amplitude on absolute scales as it is done when comparing it to other methods.
The binning does not visibly affect the distribution of α_D^{rec}, see plot (d).

The coarse binning of 12×6 shows to produce the smallest bias in the comparison. At the same time the spread of the distributions is not considerably affected by the variation of the binning.

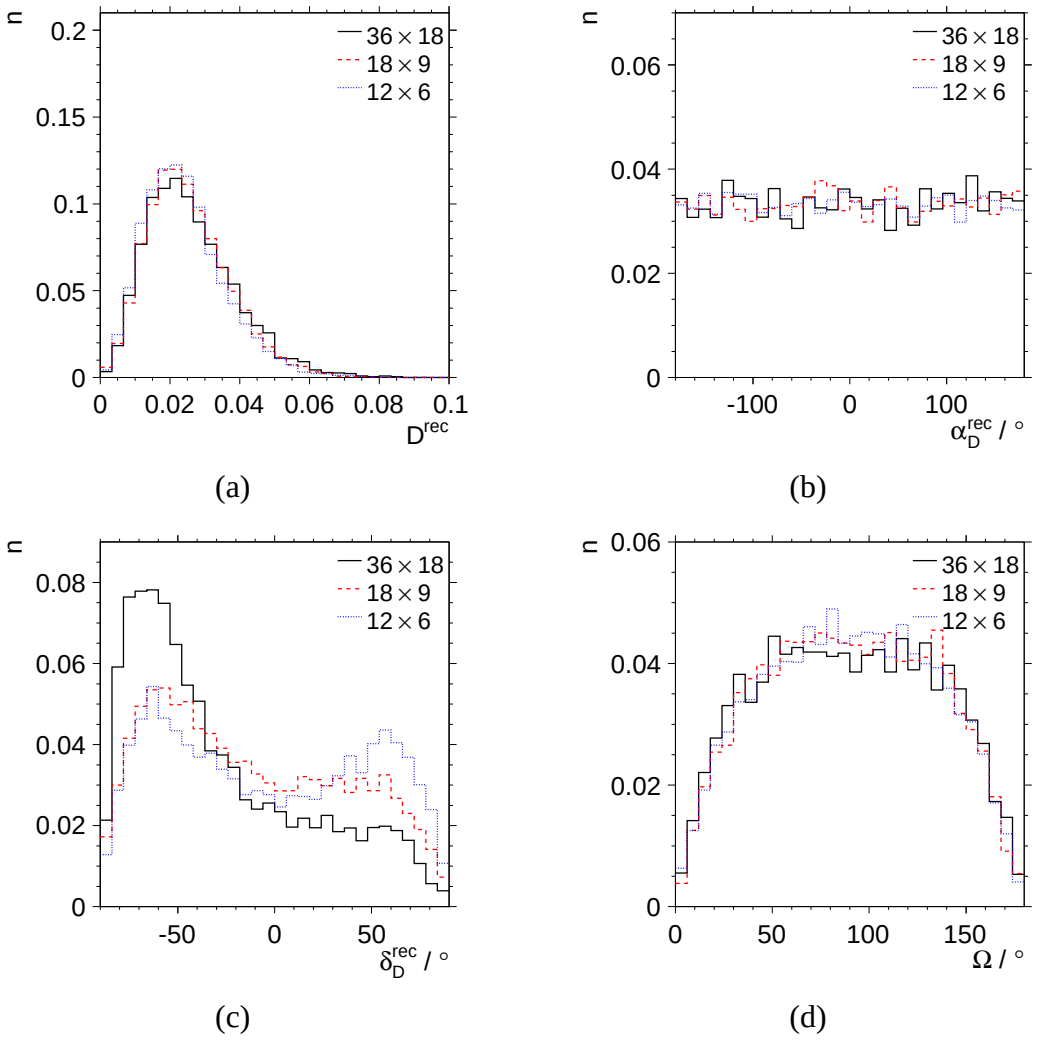

Figure D.2: Dipole parameters reconstructed from isotropic MC sky maps with the χ^2 fit method for different binnings. Similar to figure 7.7, (a), (b), (c) and (d) show the distributions of the amplitude D^{rec}, the right ascension α_D^{rec}, the declination δ_D^{rec} and the directional precision Ω.

Consistency of Parameter Uncertainties and Spreads

The observation that smaller spreads of the parameters obtained with the likelihood method compared to the χ^2 fit correspond to larger uncertainties of the respective parameter at the same time is counterintuitive. Either the likelihood method overestimates the parameter uncertainties or the χ^2 fit underestimates them. The answer to this question is given in figure D.3. The relative fraction $n_{1\sigma}$ of the number of reconstructed parameters that match the true value within one sigma is plotted versus the true declination and the true amplitude, respectively.

The Rayleigh method produces parameter uncertainties that are both quantitatively and qualitatively consistent with what is shown in chapter 7, figures 7.4 and 7.5: On the one hand, $n_{1\sigma}$ equals the expected value of 68 % over a large range of true values. On the other hand, this range is restricted to true declinations not too close to the poles and amplitudes not too small where the 2D method becomes insensitive. Essentially, the same observations apply for the χ^2 fit method. In contrast, the likelihood method produces uncertainties that are larger; consequently, the true value is matched by a fraction of $n_{1\sigma} \approx 85$ % of the parameters reconstructed with the likelihood method within one sigma. In other words, the uncertainties obtained with this method correspond to a ~ 85 % quantile rather than to the expected 68 % quantile.

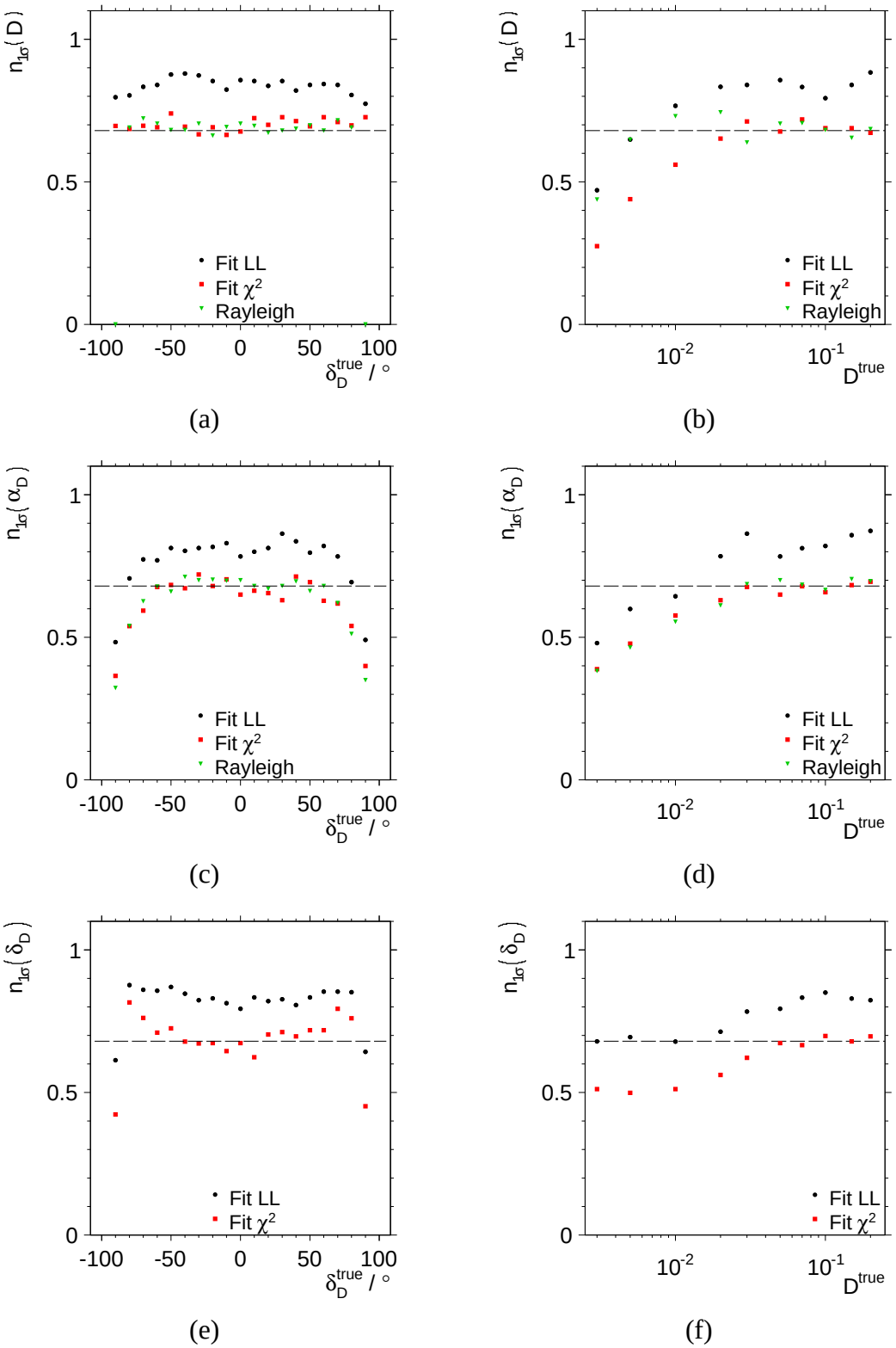

Figure D.3: $n_{1\sigma}$ is the fraction of reconstructed parameters that match the true value within one sigma. From top to bottom $n_{1\sigma}$ is displayed for the amplitude, right ascension and declination paramter, the left plots show the scenario of a fixed amplitude and the right ones indicate the case of a fixed declination, compare to the analyses in chapter 7. To guide the eye, the black dashed lines indicate the (expected) value of $n_{1\sigma} = 68$ %.

List of Figures

List of Tables

Acronyms

Acronym	Explanation
ADC	Analog-to-Digital Converter
ADST	Advanced Data Summary Tree (event data format)
AGN	Active Galactic Nuclei
AIRES	AIR-shower Extended Simulations (air shower simulator)
AMIGA	Auger Muon-detectors and Infill for the Ground Array
AR	Angular Resolution
a.s.l.	above sea level
BP	Bad Period
CDAS	Central Data Acquisition System
CIC	Constant Intensity Cut
C.L.	Confidence Level
CLF	Central Laser Facility
CMB	Cosmic Microwave Background
CORSIKA	COsmic Ray SImulations for KAskade (air shower simulator)
DAQ	Data AQuisition
EA	Engineering Array
EAS	Extensive Air Shower
EM	electromagnetic
Eye	One building of the FD typically consisting of six cameras
f.o.v.	field of view
FADC	Fast/Flash Analog-to-Digital Converter
FD	Fluorescence Detector (FD reconstruction means hybrid reconstruction)
FLUKA	FLUktuierende KAskade (german for fluctuating cascade)
FPGA	Freely Programmable Gate Array
GPS	Global Positioning System
GZK	Greisen-Zatsepin-Kuzmin
HEALPix	Hierarchical, Equal Area, and iso-Latitude Pixelisation (of the sphere)
HEAT	High Elevation Auger Telescope
HSA	Hillas Splitting Algorithm
IGRF	International Geomagnetic Reference Field
IR	Infrared
JD	Julian Day
LDF	Lateral Density (Distribution) Function
LSA	Large Scale Anisotropy
LST	Local Sidereal Time
LTP	Lateral Trigger Probability

continued on next page

continued from previous page

Acronym	**Explanation**
MC	Monte Carlo
ML	Maximum Likelihood
NKG	Nishimura-Kamata-Greisen
ndf	number of degrees of freedom
PAO	Pierre Auger Observatory
p.d.f.	probability density function
PMT	Photo Multiplier Tube
QGSJet-II	Quark-Gluon-String model with JETs
PMT	Photo Multiplier Tube
RMS	Root Mean Square
SD	Surface Detector
SDP	Shower Detector Plane, defines the eye-specific coordinate system
ToT	Time over Threshold (local SD station trigger level)
UHECR	Ultra High Energy Comic Ray
UTC	Universal Time Coordinated
UTM	Universal Transverse Mercator
UV	Ultraviolet
VEM	Vertical Equivalent Muon
XLF	eXtreme Laser Facility

Bibliography

[Abb04] R. Abbasi et al. (The High Resolution Fly's Eye Collaboration (HiRes) Collaboration), *A Search for arrival direction clustering in the HiRes-I monocular data above 10**19.5 eV*, Astropart.Phys. **22** (2004), 139–149, astro-ph/0404366.

[Abb08a] R. Abbasi, T. Abu-Zayyad, M. Allen, J. Amman, G. Archbold, et al., *Search for Correlations between HiRes Stereo Events and Active Galactic Nuclei*, Astropart.Phys. **30** (2008), 175–179, 0804.0382, * Brief entry *.

[Abb08b] R. Abbasi et al. (HiRes Collaboration Collaboration), *First observation of the Greisen-Zatsepin-Kuzmin suppression*, Phys.Rev.Lett. **100** (2008), 101101, astro-ph/0703099.

[Abb09] R. Abbasi, P. Desiati, and f. t. I. Collaboration, *Large Scale Cosmic Ray Anisotropy With IceCube*, 0907.0498, * Brief entry *.

[Abr05] Abraham, J. *et al.*, *Conventions for the Pierre Auger Observatory*, revised draft, https://edms.cern.ch/document/317390/1, 2005.

[Abr07] Abraham, J. *et al.* (Pierre Auger Collaboration Collaboration), *Correlation of the highest energy cosmic rays with nearby extragalactic objects*, Science **318** (2007), 938–943, 0711.2256.

[Abr08a] Abraham, J. *et al.* (Pierre Auger Collaboration Collaboration), *Correlation of the highest-energy cosmic rays with the positions of nearby active galactic nuclei*, Astropart.Phys. **29** (2008), 188–204, 0712.2843.

[Abr08b] Abraham, J. *et al.* (Pierre Auger Collaboration), *Observation of the suppression of the flux of cosmic rays above $4x10^{19}eV$*, Phys. Rev. Lett. **101** (2008), 061101,1–7, 0806.4302.

[Abr09a] Abraham, J. *et al.* (The Pierre Auger Collaboration Collaboration), *Atmospheric effects on extensive air showers observed with the Surface Detector of the Pierre Auger Observatory*, Astropart.Phys. **32** (2009), 89–99, 0906.5497.

[Abr09b] Abraham, J. *et al.* (Pierre Auger Collaboration Collaboration), *Limit on the diffuse flux of ultra-high energy tau neutrinos with the surface detector of the Pierre Auger Observatory*, Phys.Rev. **D79** (2009), 102001, 0903.3385.

[Abr09c] Abraham, J. *et al.* (The Pierre Auger Collaboration), *Operations of and Future Plans for the Pierre Auger Observatory*, 2009.

[Abr09d] Abraham, J. *et al.* (The Pierre Auger Collaboration Collaboration), *Upper limit on the cosmic-ray photon fraction at EeV energies from the Pierre Auger Observatory*, Astropart.Phys. **31** (2009), 399–406, 0903.1127.

[Abr10a] Abraham, J. *et al.* (Pierre Auger Collaboration), *Measurement of the energy spectrum of cosmic rays above* 10^18 *eV using the Pierre Auger Observatory*, Phys. Lett. B **685** (2010), 239–246, 1002.1975.

[Abr10b] Abraham, J. *et al.* (The Pierre Auger Collaboration), *The Fluorescence Detector of the Pierre Auger Observatory*, Nucl. Instr. Meth. **A620** (2010), 227–251, 0907.4282.

[Abr10c] Abreu, P. *et al.* (Pierre Auger Observatory Collaboration Collaboration), *Update on the correlation of the highest energy cosmic rays with nearby extragalactic matter*, Astropart.Phys. **34** (2010), 314–326, 1009.1855.

[Abr11a] Abraham, J. *et al.*, *Angular Resolution of the Pierre Auger Observatory*, to be submitted to Astropart. Phys. (2011).

[Abr11b] Abraham, J. *et al.*, *Azimuthal Distortions of the Cosmic Ray Event Rate Induced by the Geomagnetic Field*, in preparation (2011).

[Abr11c] Abraham, J. *et al.*, *Search for First Harmonic Modulation in the Right Ascension Distribution of Cosmic Rays Detected at the Pierre Auger Observatory*, Astropart. Phys. **34** (2011), 627–639.

[Agl96] M. Aglietta et al. (EAS-TOP Collaboration), *A Measurement of the solar and sidereal cosmic ray anisotropy at E(0) approximates 10**14-eV*, Astrophys.J. **470** (1996), 501–505.

[Agl07] M. Aglietta et al. (Pierre Auger Collaboration Collaboration), *Anisotropy studies around the Galactic Centre at EeV energies with the Auger Observatory*, Astropart.Phys. **27** (2007), 244–253, astro-ph/0607382.

[Ago03] S. Agostinelli et al. (GEANT4 Collaboration), *GEANT4: A Simulation toolkit*, Nucl.Instrum.Meth. **A506** (2003), 250–303.

[Alk75] O. C. Alkhofer, *Introduction to Cosmic Radiation*, Verlag Carl Thiemig, 1975.

[All06] D. Allard, M. Ave, N. Busca, M. Malkan, A. Olinto, et al., *Cosmogenic Neutrinos from the propagation of Ultrahigh Energy Nuclei*, JCAP **0609** (2006), 005, astro-ph/0605327.

[Ame06] M. Amenomori (Tibet AS-gamma Collaboration Collaboration), *Anisotropy and Corotation of Galactic Cosmic Rays*, Science **314** (2006), 439–443, astro-ph/0610671, * Brief entry *.

[Ant04] T. Antoni et al. (The KASCADE Collaboration Collaboration), *Large scale cosmic - ray anisotropy with KASCADE*, Astrophys.J. **604** (2004), 687–692, astro-ph/0312375.

[Ant05] T. Antoni et al. (The KASCADE Collaboration Collaboration), *KASCADE measurements of energy spectra for elemental groups of cosmic rays: Results and open problems*, Astropart. Phys. **24** (2005), 1–25, astro-ph/0505413.

[Aub05] J. Aublin and E. Parizot, *Generalized 3D-reconstruction method of a dipole anisotropy in cosmic-ray distributions*, Astron.Astrophys. (2005), astro-ph/0504575.

[Aug38] P. Auger, P. Ehrenfest, R. Maze, J. Daudin, Robley, and A. Fréon, *Extensive Cosmic-Ray Showers*, Rev. Mod. Phys. **11** (1938), 288–291.

[Ave00] M. Ave, R. Vazquez, and E. Zas, *Modeling horizontal air showers induced by cosmic rays*, Astropart.Phys. **14** (2000), 91, astro-ph/0011490.

[AZ00] T. Abu-Zayyad, K. Belov, D. Bird, J. Boyer, Z. Cao, et al., *Evidence for Changing of Cosmic Ray Composition between 1017 and 1018 eV from Multicomponent Measurements*, Phys.Rev.Lett. **84** (2000), 4276–4279.

[Bec09] R. Beck, *Galactic and Extragalactic Magnetic Fields*, AIP Conf.Proc. **1085** (2009), 83–96, 0810.2923, * Brief entry *.

[Bel01] J. Bellido, R. Clay, B. Dawson, and M. Johnston-Hollitt, *Southern hemisphere observations of a 10**18-eV cosmic ray source near the direction of the galactic center*, Astropart.Phys. **15** (2001), 167–175, astro-ph/0009039, Submission to journal is a revised version.

[Bel09] J. A. Bellido, *Study of the SD/FD axis systematics observed in Loma Amarilla*, 2009, Presentation given during the collaboration meeting in November 2009.

[Bel10] J. A. Bellido, 2010, private communication.

[Ber05] G. Bertone, D. Hooper, and J. Silk, *Particle dark matter: Evidence, candidates and constraints*, Phys.Rept. **405** (2005), 279–390, hep-ph/0404175.

[Ber06a] V. Berezinsky, S. Grigoreva, and B. Hnatyk, *Extragalactic UHE proton spectrum and prediction of flux of iron-nuclei at 10**8-GeV - 10**9-GeV*, Nucl.Phys.Proc.Suppl. **151** (2006), 497–500.

[Ber06b] Bertou *et al.* (Pierre Auger Collaboration), *Calibration of the surface array of the Pierre Auger Observatory*, Nucl. Instrum. Meth. **A568** (2006), 839–846.

[Blu09] J. Bluemer, R. Engel, and J. R. Hoerandel, *Cosmic Rays from the Knee to the Highest Energies*, Prog. Part. Nucl. Phys. **63** (2009), 293–338, 0904.0725.

[Bon06] C. Bonifazi and P. L. Ghia (Pierre Auger Collaboration), *Selection of data periods and calculation of the SD geometrical acceptance*, GAP-Note 2006-101, internal report, not for public display, 2006, http://www.auger.org/admin/GAP_Notes/GAP2006/GAP2006_prot/GAP2006_101.pdf.

[Bon08] C. Bonifazi, A. Letessier-Selvon, and E. M. Santos, *A model for the time uncertainty measurements in the Auger surface detector array*, Astropart.Phys. **28** (2008), 523–528, 0705.1856.

[Bon09] C. Bonifazi (Pierre Auger Collaboration), *The angular resolution of the Pierre Auger Observatory*, Nuclear Physics B (Proc. Suppl.) **190** (2009), 20–25.

[Bon10] R. Bonino, O. Deligny, and H. Lyberis (Pierre Auger Collaboration), *Sensitivity to large scale anisotropies: phase versus amplitude measurements*, GAP-Note 2010-057, internal report, not for public display, 2010.

[Bro10] J.-A. Brown, *The Magnetic Field of the Milky Way Galaxy*, 1012.2932, * Temporary entry *.

[Bru97] R. Brun and F. Rademakers, *ROOT: An object oriented data analysis framework*, Nucl.Instrum.Meth. **A389** (1997), 81–86.

[Can02] J. Candia, E. Roulet, and L. N. Epele, *Turbulent diffusion and drift in galactic magnetic fields and the explanation of the knee in the cosmic ray spectrum*, JHEP **0212** (2002), 033, astro-ph/0206336.

[Can03] J. Candia, S. Mollerach, and E. Roulet, *Cosmic ray spectrum and anisotropies from the knee to the second knee*, JCAP **0305** (2003), 003, astro-ph/0302082.

[Com35] A. Compton and I. Getting, *An Apparent Effect of Galactic Rotation on the Intensity of Cosmic Rays*, Phys. Rev. **47** (1935), 817.

[Coo65] J. W. Cooley and J. W. Tukey, *An algorithm for the machine calculation of complex Fourier series*, Math. Comp. **19** (1965), 297–301.

[Cre08] A. Creusot and D. Verberič, *SD-Hybrid Reconstruction Systematics*, GAP-2008-047, 2008.

[Cre09] A. Creusot and D. Verberič, *Update on the SD-Hybrid Reconstruction Systematics*, GAP-2009-095, 2009.

[Dem09] H. Dembinski, *Measurement of the flux of ultra high energy cosmic ray flux using data from very inclined air showers at the Pierre Auger Observatory*, Ph.D. thesis, RWTH Aachen University, 2009, Ph.D. thesis.

[Dem10] H. D. Dembinski, 2010, private communication.

[DM05] D. De Marco and T. Stanev, *On the shape of the UHE cosmic ray spectrum*, Phys.Rev. **D72** (2005), 081301, astro-ph/0506318.

[Edg78] D. Edge, A. Pollock, R. Reid, A. Watson, and J. Wilson, *A Study of the Arrival Direction Distribution of High-Energy Particles as Observed from the Northern Hemisphere*, J.Phys.G **G4** (1978), 133–157.

[Erl02] A. Erlykin and A. Wolfendale, *Properties of cosmic ray interactions at PeV energies*, Astropart.Phys. **18** (2002), 151–164, astro-ph/0112553.

[Fas03] A. Fasso, A. Ferrari, S. Roesler, P. Sala, F. Ballarini, et al., *The Physics models of FLUKA: Status and recent developments*, MOMT005, hep-ph/0306267.

[Fer49] E. Fermi, *On the Origin of the Cosmic Radiation*, Phys.Rev. **75** (1949), 1169–1174.

[Fix96] D. Fixsen, E. Cheng, J. Gales, J. C. Mather, R. Shafer, et al., *The Cosmic Microwave Background spectrum from the full COBE FIRAS data set*, Astrophys.J. **473** (1996), 576, astro-ph/9605054.

[Gai77] T. Gaisser and A. Hillas, vol. 8, Proc. ICRC 1977, August 1977, p. 353.

[Gai90] T. Gaisser, *Cosmic Rays and Particle Physics*, vol. 1, Cambridge University Press, 1990.

[Glu01] A. Glushkov and M. Pravdin, *Correlations between the arrival directions of ultrahigh energy cosmic rays and the large scale structure of the universe*, J. Exp. Theor. Phys. **92** (2001), 887–894.

[Gre56] K. Greisen, *Progress in Cosmic Ray Physics*, vol. 3, 1956.

[Gre60] K. Greisen, *Cosmic ray showers*, Ann.Rev.Nucl.Part.Sci. **10** (1960), 63–108.

[Gre66] K. Greisen, *End to the Cosmic-Ray Spectrum?*, Phys. Rev. Lett. **16** (1966), 748.

[Gri09] M. Grigat, *Angular Reconstruction Systematics*, GAP-2009-094, 2009.

[Gri11] M. Grigat, *Large Scale Anisotropy Studies with the Pierre Auger Observatory*, vol. Special Issue ECRS 2010, Arbeitsgemeinschaft Extraterrestrische Forschung e.V., 2011.

[Gru00] C. Grupen, *Astroteilchenphysik - Das Universum im Licht der kosmischen Strahlung*, Friedr. Vieweg & Sohn Verlagsgesellschaft mbH, Braunschweig/Wiesbaden, 2000.

[Gru05] C. Grupen, *Astroparticle Physics*, Springer-Verlag Berlin Heidelberg, 2005.

[Han09] J. L. Han, *Magnetic structure of our Galaxy: A review of observations*, 0901.1165.

[Har10] D. Harari, S. Mollerach, and E. Roulet, *Effects of the galactic magnetic field upon large scale anisotropies of extragalactic Cosmic Rays*, JCAP **1011** (2010), 033, 1009.5891, * Temporary entry *.

[Hau09] A. Haungs and K.-G. Collaboration, *The Cosmic Ray Energy Spectrum Measured with KASCADE-Grande*, 2009, * Brief entry *.

[Hay96] N. Hayashida, K. Honda, M. Honda, N. Inoue, K. Kadota, et al., *Possible clustering of the most energetic cosmic rays within a limited space angle observed by the Akeno Giant Air Shower Array*, Phys.Rev.Lett. **77** (1996), 1000–1003.

[Hay99] N. Hayashida, K. Honda, M. Honda, N. Inoue, K. Kadota, et al. (AGASA Collaboration Collaboration), *The Anisotropy of cosmic ray arrival directions around 10**18-eV*, Astropart.Phys. **10** (1999), 303–311, astro-ph/9807045.

[Hec09] D. Heck and T. Pierog, *Extensive Air Shower Simulation with CORSIKA*, Institut für Kernphysik - Forschungszentrum Karlsruhe GmbH, Karlsruhe, Germany, Version 6.9xx ed., April 2009, A Users Guide distributed with the CORSIKA code.

[Hei36] W. Heitler, *The Quantum Theory of Radiation*, 1st edition ed., OXFORD AT THE CLARENDON PRESS, 1936.

[Hes12] V. F. Hess, *Über Beobachtungen der durchdringenden Strahlung bei sieben Freiballonfahrten*, Phys. Z. (1912), no. 13, 1084–1091.

[Hil67] A. M. Hillas, *The energy spectrum of cosmic rays in an evolving universe*, Phys. Lett. **24** (1967), 677.

[Hil71] A. M. Hillas (Pierre Auger Collaboration), *Measurement of Primary Energy of Air Showers in the Presence of Fluctuations*, vol. 3, Proc. ICRC 1971, 1971, p. 1001.

[Hil81] A. M. Hillas (Pierre Auger Collaboration), vol. 8, Proc. ICRC 1981, 1981, p. 193.

[Hil84] A. M. Hillas, *The Origin of Ultra-High-Energy Cosmic Rays*, Annual Review of Astronomy and Astrophysics **22** (1984), no. 1, 425–444, http://www.annualreviews.org/doi/pdf/10.1146/annurev.aa.22.090184.002233.

[Hil06] A. M. Hillas, *Cosmic Rays: Recent Progress and some Current Questions*, astro-ph/0607109.

[Hin07] G. Hinshaw et al. (WMAP Collaboration Collaboration), *Three-year Wilkinson Microwave Anisotropy Probe (WMAP) observations: temperature analysis*, Astrophys.J.Suppl. **170** (2007), 288, astro-ph/0603451.

[Hin09] G. Hinshaw et al. (WMAP Collaboration Collaboration), *Five-Year Wilkinson Microwave Anisotropy Probe (WMAP) Observations: Data Processing, Sky Maps, and Basic Results*, Astrophys.J.Suppl. **180** (2009), 225–245, 0803.0732.

[Hob98] M. Hobson, A. Jones, and A. Lasenby, *Wavelet analysis and the detection of non-gaussianity in the cmb*, astro-ph/9810200, * Brief entry *.

[HR09] J. J. Hernandez-Rey, f. t. A. Collaboration, and f. t. K. Consortium, *Neutrino Telescopes in the Mediterranean Sea*, J.Phys.Conf.Ser. **171** (2009), 012047, 0904.4011, * Brief entry *.

[Hul11] K. Hultqvist, *IceCube: physics, status, and future*, Nucl.Instrum.Meth. **A626-627** (2011), S6–S12, 1003.2300.

[Jam75] F. James and M. Roos, *Minuit: A System for Function Minimization and Analysis of the Parameter Errors and Correlations*, Comput.Phys.Commun. **10** (1975), 343–367.

[Jon04] M. H. Jones, R. J. Lambourne, and D. J. Adams, *An Introduction to Galaxies and Cosmology*, 2004.

[Kac06] M. Kachelriess and D. Semikoz, *Clustering of ultrahigh energy cosmic ray arrival directions on medium scales*, Astropart.Phys. **26** (2006), 10–15, astro-ph/0512498.

[Kam58] K. Kamata and J. Nishimura, Prog. Theo. Phys. **6** (1958), 93.

[Kei11] B. Keilhauer, *Auger DB Tables*, 2011, data obtained as of 2011.03.04, http://www.auger.de/~keilhaur/.

[Kif86] T. Kifune, T. Hara, Y. Hatano, N. Hayashida, M. Honda, et al., *ANISOTROPY OF ARRIVAL DIRECTION OF EXTENSIVE AIR SHOWERS OBSERVED AT AKENO*, J.Phys.G **G12** (1986), 129.

[Kue08] D. Kuempel, K. H. Kampert, and M. Risse, *Geometry reconstruction of fluorescence detectors revisited*, Astropart. Phys. **30** (2008), 167–174, 0806.4523.

[Lar11] D. Larson, J. Dunkley, G. Hinshaw, E. Komatsu, M. Nolta, et al., *Seven-Year Wilkinson Microwave Anisotropy Probe (WMAP) Observations: Power Spectra and WMAP-Derived Parameters*, Astrophys.J.Suppl. **192** (2011), 16, 1001.4635.

[Lhe03] I. Lhenry, E. Parizot, D. Allard, P. Ghia, J. Aublin, and T. Suomijarvi (Pierre Auger Collaboration), *The Lateral Trigger Probability function (LTP) for UHE Showers detected by the Pierre Auger Observatory Surface Detector*, GAP-Note 2003-088, internal report, not for public display, 2003.

[Lin63] J. Linsley, *Primary cosmic rays of energy 10**17 to 10**20-eV: The energy spectrum and arrival directions*, Proceedings of the 8th International Cosmic Ray Conference (ICRC 63).

[Lin75] J. Linsley, *Fluctuation effects on directional data*, Phys.Rev.Lett. **34** (1975), 1530–1533.

[Lon92] M. S. Longair, *High energy astrophysics*, vol. 1, Cambridge University Press, 1992.

[LY05] I. Lhenry-Yvon (Pierre Auger Collaboration), *The trigger system of the Pierre Auger Surface Detector: operation, efficiency and stability*, Proc. ICRC 2005, 2005.

[Maj37] E. Majorana, *Theory of the Symmetry of Electrons and Positrons*, Nuovo Cim. **14** (1937), 171–184.

[Mar08] I. C. Maris, *Measurement of the Ultra High Energy Cosmic Ray Flux using Data of the Pierre Auger Observatory*, Ph.D. thesis, February 2008.

[Mat05] J. Matthews, *A Heitler model of extensive air showers*, Astropart. Phys. **22** (2005), 387–397.

[Mol05] S. Mollerach and E. Roulet, *A New method to search for a cosmic ray dipole anisotropy*, JCAP **0508** (2005), 004, astro-ph/0504630.

[Mol09] S. Mollerach and f. t. P. A. Collaboration, *Search for clustering of ultra high energy cosmic rays from the Pierre Auger Observatory*, Nucl.Phys.Proc.Suppl. **190** (2009), 198–203, 0901.4699, * Brief entry *.

[Nel85] W. Nelson, H. Hirayama, and D. W. Rogers, *THE EGS4 CODE SYSTEM*, Send all requests for copies to W.Ralph Nelson, MS 48. He provides the updates. 10/23/97.

[Nel04] L. Nellen and V. V. Elewyck (Pierre Auger Collaboration), *How to determine the Surface Detector T3 probability from the local T2 probabilities*, GAP-Note 2004-069, internal report, not for public display, 2004.

[New05] D. Newton, J. Knapp, and A. Watson (Pierre Auger Collaboration), *The Optimum Ground Parameter, $S(r_{opt})$*, GAP-Note 2005-013, internal report, not for public display, 2005.

[New06] D. Newton, J. Knapp, and A. Watson (Pierre Auger Collaboration), *The Optimum Distance at which to Determine the Size of a Giant Air Shower*, GAP-Note 2006-045, internal report, not for public display, 2006.

[Nit10] D. Nitz (Pierre Auger Collaboration Collaboration), *Instrumentation for the northern site of the Pierre Auger Observatory*, Nucl. Instr. and Meth. A (2010).

[Not09] Nothing *et al.*, 2009, private communication.

[Oce11] N. Oceanic and A. Administration, *National Geophysical Data Center*, 2011, data obtained as of 2011.02.19, http://www.ngdc.noaa.gov/ngdc.html.

[Ost06a] S. Ostapchenko, *QGSJET-II: Towards reliable description of very high energy hadronic interactions*, Nucl.Phys.Proc.Suppl. **151** (2006), 143–146, hep-ph/0412332.

[Ost06b] S. Ostapchenko, *QGSJET-II: Results for extensive air showers*, Nucl.Phys.Proc.Suppl. **151** (2006), 147–150, astro-ph/0412591.

[Oya06] Y. Oyama (Super-Kamiokande Collaboration), *Anisotropy of the primary cosmic-ray flux in Super- Kamiokande*, astro-ph/0605020.

[Par05] E. Parizot, D. Allard, I. Allekotte, E. Armengaud, J. Aublin, X. Bertou, A. Chou, P. L. Ghia, M. G. Berisso, J. Hamilton, I. Lhenry-Yvon, C. Medina, G. Navarra, and A. Tripathi (Pierre Auger Collaboration), *Aperture Calculation of the Pierre Auger Observatory surface detector*, Proc. ICRC 2005, 2005.

[Pen65] A. Penzias and R. W. Wilson, *A Measurement of Excess Antenna Temperature at 4080 Mc/s*, Ap. J. **142** (1965), 419–421.

[Per03] D. Perkins, *Particle Astrophysics*, Oxford University Press Inc., 2003.

[Pri88] J. R. Primack, D. Seckel, and B. Sadoulet, *Detection of Cosmic Dark Matter*, Ann.Rev.Nucl.Part.Sci. **38** (1988), 751–807, Revised version.

[Pri03] P. Privitera (Pierre Auger Collaboration), *The Angular Reconstruction and Angular Resolution of Air Showers Detected at the Auger Observatory*, Proc. ICRC 2003, 2003.

[Ptu93] V. S. Ptuskin, S. I. Rogovaya, V. N. Zirakashvili, L. G. Chuvilgin, G. B. Khristiansen, E. G. Klepach, and G. V. Kulikov, *Diffusion and drift of very high energy cosmic rays in galactic magnetic fields*, Astronomy and Astrophysics **268** (1993), 726–735.

[Ptu05] V. Ptuskin and V. N. Zirakashvili, *On the spectrum of high-energy cosmic rays produced by supernova remnants in the presence of strong cosmic-ray streaming instability and wave dissipation*, Astron.Astrophys. **429** (2005), 755–765, astro-ph/0408025.

[Rao98] M. V. S. Rao and B. V. Streekantan, *Extensive Air Showers*, World Scientific Publishing Co. Pte. Ltd., 1998.

[Rou11] E. Roulet, *Latest results from the Pierre Auger Observatory*, 1101.1825, * Temporary entry *.

[Rov03] A. Rovero and P. Bauleo (Pierre Auger Collaboration), *Trigger Efficiency from Hybrid Data*, GAP-Note 2003-056, internal report, not for public display, 2003.

[Sci02] S. J. Sciutto, *AIRES - A system for air shower simulations*, Departamento de Fisica - Universidad Nacional de La Plata, C. C. 67 - 1900 La Plata, Argentina, Version 2.6.0 ed., July 2002, Users guide and reference manual distributed with the AIRES code.

[Smo92] G. F. Smoot, C. Bennett, A. Kogut, E. Wright, J. Aymon, et al., *Structure in the COBE differential microwave radiometer first year maps*, Astrophys.J. **396** (1992), L1–L5.

[Sny93] J. P. Snyder, *Flattening the Earth: Two Thousand Years of Map Projections*, no. ISBN 0-226-76747-7, 1993.

[Som01] P. Sommers, *Cosmic ray anisotropy analysis with a full-sky observatory*, Astropart.Phys. **14** (2001), 271–286, astro-ph/0004016.

[Sta09] T. Stanev and f. t. I. Collaboration, *Status, performance, and first results of the IceTop array*, Nucl.Phys.Proc.Suppl. **196** (2009), 159–164, 0903.0576, * Brief entry *.

[Swo01] S. P. Swordy, *THE ENERGY SPECTRA AND ANISOTROPIES OF COSMIC RAYS*, Space Science Reviews **99** (2001), 85–94.

[Tor98] C. Torrence and G. P. Compo, *A Practical Guide to Wavelet Analysis*, Bull. Amer. Meteor. Soc **79** (1998), 61–78.

[VC06] M.-P. Veron-Cetty and P. Veron, *A catalogue of quasars and active nuclei: 12th edition*, Astron.Astrophys. **455** (2006), 773–777.

[vdB09] A. M. van den Berg, *Radio detection of cosmic rays at the southern Auger Observatory*, 2009.

[Veb05] D. Veberič and M. Roth (Pierre Auger Collaboration), *Offline Reference Manual - SD Reconstruction*, GAP-Note 2005-035, internal report, not for public display. An updated version is distributed with Offline, 2005.

[Vie04] P. Vielva, E. Martinez-Gonzalez, R. Barreiro, J. Sanz, and L. Cayon, *Detection of non-Gaussianity in the WMAP 1 - year data using spherical wavelets*, Astrophys.J. **609** (2004), 22–34, astro-ph/0310273.

[Wul09] T. Wulf, *Über die in der Atmosphäre vorhandene Strahlung von hoher Durchdringungsfähigkeit*, Phys Z. **10** (1909), 152–157.

[Zat66] G. Zatsepin and V. Kuzmin, *Upper limit of the spectrum of cosmic rays*, JETP Lett. **4** (1966), 78–80.

[Zwe97] E. G. Zweibel and C. Heiles, *Magnetic fields in galaxies and beyond*, nature **385** (1997), 131–136.

Acknowledgements

My gratefulness goes out to everybody who made this thesis possible. Firstly, I would like to thank my supervisor Prof. Dr Thomas Hebbeker for the opportunity to take part in the research in his group and at the Pierre Auger Observatory as well as for scrutinising my work and the course of my research. I am thankful to Prof. Dr Martin Erdmann for agreeing to revise this thesis and for asking challenging questions.

I would like to thank the collaboration members which contributed to discussions related to topics involved in this thesis. Especially, I want to thank Prof. Dr Pierre Billoir, Dr Jose Bellido, Dr Carla Bonifazi, Dr Raffaella Bonino, Dr Alexandre Creusot, Prof. Dr Bruce Dawson, Dr Olivier Deligny, Dr Hans Dembinski, Dr Piera Luisa Ghia, Prof. Dr Antoine Letessier-Selvon, Prof. Dr João de Mello Neto, Moritz Münchmeyer, Stephan Schulte, Dr Mariangela Settimo Prof. Dr Ricardo Vázquez and Prof. Dr Darko Veberič.

I wish to thank the Auger group in Karlsruhe for providing high level reconstruction data in a comfortable format, Michael Bontenackels and Dr Thomas Kress and Alain Cordier for the user support at the computing clusters at Aachen and Lyon.

Many thanks to the current and former members of the “cosmics” group at the physics institute III A of the RWTH Aachen University for feedback, criticism and teamwork: Dr Hans Dembinski, Christoph Genreith, Stefan Fliescher, Dr Christine Meurer, Gero Müller, Anna Nelles, Matthias Plum, Nils Scharf, Peter Schiffer, Stephan Schulte, Oliver Seeger, Maurice Stephan, David Walz, Klaus Weidenhaupt, Tobias Winchen.

I am deeply indebted to Stephan Schulte for countless discussions and proofreading of papers, mutual support and co-night-shifting, darkest humour and short periods of loud music (especially for the shortness). My gratitude goes to Dr Christine Meurer, Nils Scharf and Maurice Stephan for proofreading parts of this thesis. Special thanks to Nils Scharf, Stephan Schulte and Maurice Stephan for encouraging comments and valuable advices concerning scientific and technical aspects of this work and how they are presented.

Thanks to Dr Markus Merschmeyer for immediately solving any `fortran` and `C` programming issue occurring in the course of this work; thanks also for sharing the same sense of humour, chocolate, hot water and black tea.

My gratitude is also due to Prof. Dr Claus Grupen for arousing and encouraging my interest in astroparticle physics during my time at Siegen university. Thanks to Dr Thomas Bäcker, Dr Marc Brüggemann and Dr Dirk Kickelbick; for sure I would not be at this point at this time without your straight tips and encouragement.

Thanks to the administrative staff at the physics institute III A, especially to Adriana Del Piero for all those extra cookies and a willing ear.

This work was funded in parts by the German Federal Ministry for Education and Research BMBF and the German Research Foundation DFG.

Last but not least, I am proud to express my gratefulness to my family: Julia, Paula and Till, it’s you who provided a base of tranquillity during the sometimes tough course of this work. Thanks to my parents and brothers for your criticism, encouragement and pride. Thanks for your support!